



THE DOWN-CONVERSION SYSTEM FOR
THE MUONIC HYDROGEN HYPERFINE
SPLITTING EXPERIMENT AT PSI

Ahmed Ouf

THE DOWN-CONVERSION SYSTEM FOR THE MUONIC HYDROGEN HYPERFINE SPLITTING EXPERIMENT AT PSI

Dissertation submitted
for the award of the title
"Doctor of Natural Sciences"
to the Faculty of Physics, Mathematics, and Computer Science
of Johannes Gutenberg University Mainz
in Mainz



JOHANNES GUTENBERG
UNIVERSITÄT MAINZ

by
Ahmed Ouf
born on 5 May 1992
from Sharkia, Egypt

1st Examiner : Prof. Dr. Randolph Pohl
2nd Examiner : Prof. Dr. Aldo Antognini
3rd Examiner : Prof. Dr. Sonia Bacca
4th Examiner : Prof. Dr. Lucia Masetti

Date of the Oral Examination : January 31, 2025

Eidesstattliche Erklärung

Eidesstattliche Erklärung zur Doktorarbeit

Ich versichere, die von mir vorgelegte Arbeit selbstständig verfasst zu haben. Alle Stellen, die wörtlich oder sinngemäß aus veröffentlichten oder nicht veröffentlichten Arbeiten anderer entnommen sind, habe ich als entnommen kenntlich gemacht. Sämtliche Quellen und Hilfsmittel, die ich für die Arbeit benutzt habe, sind angegeben. Die Arbeit hat mit gleichem Inhalt bzw. in wesentlichen Teilen noch keiner anderen Prüfungsbehörde vorgelegen.

Unterschrift: 

Ort, Datum: Mainz, 13.01.2025

"A student of science is a seeker of truth."

– Ali Mostafa Mosharafa

*Dedicated to my beloved grandparents, Amal and Metwally
whose memories continue to live within me.*

ABSTRACT

THE DOWN-CONVERSION SYSTEM FOR THE MUONIC HYDROGEN HYPERFINE SPLITTING EXPERIMENT AT PSI

January 2025

This thesis focuses on the development of the laser system for the HyperMu experiment, conducted by the CREMA collaboration at the Paul Scherrer Institute (PSI), Switzerland. The experiment aims to measure the ground-state hyperfine splitting (HFS) in muonic hydrogen (μp) with 1 ppm precision using pulsed laser spectroscopy. This accuracy allows for a precise extraction of the proton structure contributions, including the Zemach radius and the proton polarizability.

In the HFS experiment, a muon beam stops in a cryogenic H_2 gas target, forming μp atoms. These atoms are excited from the $(1S, F = 0)$ state to the $(1S, F = 1)$ state by a laser pulse at $6.8 \mu\text{m}$ wavelength. A subsequent inelastic collision with an H_2 molecule de-excites the μp atom back to the $(1S, F = 0)$ state, transferring the de-excitation energy into kinetic energy. The additional kinetic energy causes the μp atoms to diffuse to gold-coated walls, where they form μAu atoms in an excited state. X-rays from μAu de-excitation are detected as a signature of a successful transition. The resonance is obtained by recording the number of μAu de-excitations versus laser frequency.

The primary challenge of the HyperMu experiment lies in developing a laser system capable of delivering pulses with a few mJ of energy at the target wavelength of $6.8 \mu\text{m}$, corresponding to the hyperfine splitting transition energy. This pulse energy is dictated by the weak transition matrix element of the HFS. The pulses need to be single-frequency with a narrow bandwidth below 100 MHz due to the transition linewidth and have a pulse length of 50 ns. A tunability range of 50 GHz is required to account for the uncertainty in the theoretical prediction. Additionally, the $6.8 \mu\text{m}$ pulses should exhibit good beam quality to ensure efficient incoupling into an enhancement cavity surrounding the cryogenic muon stopping volume.

This thesis centers on the nonlinear frequency down-conversion stages to generate mid-infrared light at $6.8 \mu\text{m}$, starting from a 1030 nm thin-disk laser. The system uses two parallel branches: optical parametric oscillators (OPOs) followed by optical parametric amplifiers (OPAs). Their outputs at $2.1 \mu\text{m}$ and $3.1 \mu\text{m}$, respectively, are combined in a difference

frequency generation (DFG) stage to produce pulses with the required properties for HFS measurement.

We realized a novel OPO cavity layout with variable reflectivity achieved through the use of polarization elements. This design allowed control of the outcoupling of the OPO cavity, enabling the optimization of nonlinear conversion efficiency. A total of 1.4 mJ pulse energy at 3.1 μm with 44% conversion efficiency was achieved. Single-frequency operation was achieved by locking the OPO cavity to the injection seeding laser via a modified Pound-Drever-Hall lock with an “infinite” capture range. Injection seeding at 1532 nm was validated through optical heterodyne measurements, showing a frequency chirp below 10 MHz. Temperature tuning of the OPO provided wavelength control over a range of 10 nm.

An OPA boosted the OPO pulse energy to 3.4 mJ at 3.1 μm with a pulse length of 50 ns. Long-term pulse energy RMS stability of 1.5% was demonstrated, with a beam quality of $M^2 = 1.3$. Methane absorption spectroscopy confirmed 20 GHz tunability and a laser bandwidth below 100 MHz, meeting experimental requirements.

The search for the resonance is critical to the experiment, requiring a precise theoretical prediction for the HFS transition. We provided an updated theoretical prediction for the HFS energy shift, incorporating new values from chiral perturbation theory and the data-driven approach for the proton structure contribution.

Keywords: Muonic hydrogen, Zemach radius, Parametric down-conversion, Nanosecond OPO.

Zusammenfassung

Diese Dissertation konzentriert sich auf die Entwicklung des Lasersystems für das HyperMu-Experiment, das von der CREMA-Kollaboration am Paul Scherrer Institut (PSI), Schweiz, durchgeführt wird. Das Experiment zielt darauf ab, die hyperfeine Strukturaufspaltung (HFS) im Grundzustand von myonischem Wasserstoff (μp) mit einer Präzision von 1 ppm mittels gepulster Laserspektroskopie zu messen. Diese Genauigkeit ermöglicht eine präzise Bestimmung der Protonenstrukturbeiträge, einschließlich des Zemach-Radius und der Protonenpolarisierbarkeit.

Im HFS-Experiment wird ein Myonenstrahl in einem kryogenen H_2 -Gasziel gestoppt, wodurch μp -Atome gebildet werden. Diese Atome werden durch einen Laserimpuls mit einer Wellenlänge von $6.8 \mu\text{m}$ vom Zustand $(1S, F = 0)$ in den Zustand $(1S, F = 1)$ angeregt. Eine anschließende unelastische Kollision mit einem H_2 -Molekül de-exzitert das μp -Atom zurück in den Zustand $(1S, F = 0)$, wobei die De-Exzitationsenergie in kinetische Energie umgewandelt wird. Die zusätzliche kinetische Energie bewirkt, dass die μp -Atome zu den goldbeschichteten Wänden diffundieren, wo sie μAu -Atome im angeregten Zustand bilden. Röntgenstrahlung aus der De-Exzitation der μAu -Atome dient als Nachweis für eine erfolgreiche Übergangsanregung. Die Resonanz wird durch die Aufzeichnung der Anzahl der μAu -De-Exzitationen in Abhängigkeit von der Laserfrequenz bestimmt.

Die Hauptherausforderung des HyperMu-Experiments liegt in der Entwicklung eines Lasersystems, das Impulse mit einigen mJ Energie bei der Zielwellenlänge von $6.8 \mu\text{m}$ liefert, die der Übergangsenergie der hyperfeinen Struktur entspricht. Diese Pulsenergie wird durch das schwache Übergangsmatrixelement der HFS bestimmt. Die Impulse müssen einzelmodig sein, eine schmale Bandbreite von weniger als 100 MHz aufweisen (bedingt durch die Linienbreite des Übergangs) und eine Pulsdauer von 50 ns haben. Eine Abstimmbarkeit von 50 GHz ist erforderlich, um die Unsicherheit der theoretischen Vorhersage zu berücksichtigen. Zudem sollten die $6.8 \mu\text{m}$ -Impulse eine gute Strahlqualität aufweisen, um eine effiziente Einkopplung in eine Verstärkungs-kavität um das kryogene Myonenstoppvolumen zu gewährleisten.

Diese Arbeit konzentriert sich auf die nichtlinearen Frequenzwandlungsstufen zur Erzeugung von Licht im mittleren Infrarotbereich bei $6.8 \mu\text{m}$, ausgehend von einem Dünnscheibenlaser mit 1030 nm Wellenlänge. Das System verwendet zwei parallele Zweige: optische parametrische Oszillatoren (OPOs) und nachfolgende optische parametrische Verstärker (OPAs). Die Ausgänge bei $2.1 \mu\text{m}$ und $3.1 \mu\text{m}$ werden in einer Differenzfrequenzerzeugungsstufe (DFG) kombiniert, um Impulse mit den erforderlichen Eigenschaften für die HFS-Messung zu erzeugen.

Ein neuartiges OPO-Resonatorlayout mit variabler Reflexion, realisiert durch Polarisationskomponenten, wurde entwickelt. Dieses Design ermöglichte die Kontrolle der Auskopplung aus dem OPO-Resonator und optimierte die Effizienz der nichtlinearen Konversion. Es wurde eine Pulsenergie von 1.4 mJ bei 3.1 μm mit einer Konversionseffizienz von 44% erreicht. Einzelmodige Operation wurde durch Verriegelung des OPO-Resonators an den ein-speisenden Laser mittels einer modifizierten Pound-Drever-Hall-Technik mit “unendlichem” Erfassungsbereich erreicht. Die Einspeisung bei 1532 nm wurde durch optische Heterodynmessungen validiert, die eine Frequenzchirp von weniger als 10 MHz zeigten. Eine Temperaturabstimmung des OPO ermöglichte eine Wellenlängenregelung über einen Bereich von 10 nm.

Ein OPA verstärkte die Pulsenergie des OPO auf 3.4 mJ bei 3.1 μm mit einer Pulsdauer von 50 ns. Eine langfristige RMS-Stabilität der Pulsenergie von 1.5% wurde demonstriert, bei einer Strahlqualität von $M^2 = 1.3$. Methanabsorptionsspektroskopie bestätigte eine Abstimmbarkeit von 20 GHz und eine Laserbandbreite unter 100 MHz, die die experimentellen Anforderungen erfüllt.

Die Suche nach der Resonanz ist entscheidend für das Experiment und erfordert eine präzise theoretische Vorhersage der HFS-Übergangsenergie. Eine aktualisierte theoretische Vorhersage wurde erstellt, die neue Werte aus der chiralen Störungstheorie und dem datengesteuerten Ansatz für den Protonenstrukturbeitrag einbezieht.

Contents

Eidesstattliche Erklärung	ii
1 Introduction	2
1.1 The muonic hydrogen atom	2
1.2 The HyperMu experiment	5
1.3 Summary of the experiment	6
1.4 Structure of the thesis	7
2 The hyperfine splitting theory	9
2.1 Introduction	9
2.2 The origin of the hyperfine splitting	9
2.3 Definition of corrections and the framework for their calculation	12
2.3.1 Relativistic corrections	13
2.4 Radiative non-recoil corrections	13
2.4.1 The muon anomalous magnetic moment	13
2.4.2 Vacuum polarization corrections	14

<i>CONTENTS</i>	x
2.4.3 Radiative binding non-recoil corrections	20
2.4.4 Next-to-leading order muon self-energy and muon vacuum polarization	22
2.5 Electroweak corrections	25
2.6 Hadronic vacuum polarization	26
2.7 Recoil corrections with proton anomalous magnetic moment	26
2.8 Proton structure corrections	26
2.8.1 The finite size contribution	29
2.8.2 Recoil correction	30
2.8.3 The polarizability contribution	30
2.8.4 Radiative corrections to the two photon exchange	32
2.9 Theory comparison	33
2.9.1 Comparison with heavy-baryon effective field theory	35
2.9.2 Comparison with the data driven approach	37
2.9.3 Theory prediction for the HFS measurement	38
Appendices	40
2.A The Uheling potential	40
2.B The Källen-Sabry potential	42
3 The experimental principle	44
3.1 The experimental sequence	44

<i>CONTENTS</i>	xi
3.1.1 Collisional processes	46
3.1.2 Thermalization of the μp atoms	47
3.1.3 Diffusion after laser excitation	49
3.2 The multi-pass cell	52
3.3 Detection system and background	53
4 Spectroscopy aspects of the HFS experiment	57
4.1 The transition probability	57
4.1.1 Excitation probability from the fluence distribution	60
4.2 Rates of signal and background	62
4.3 Time needed to search for the resonance	63
5 The HyperMu laser system	66
5.1 The general scheme	66
5.1.1 Tunability and frequency control	67
5.2 Down-conversion scheme	68
5.2.1 Difference frequency generation (DFG)	68
5.2.2 Phase matching and nonlinear coefficient	70
5.2.3 Conversion efficiency	73
5.2.4 Laser beam quality	74
5.2.5 The ZGP crystal	75

<i>CONTENTS</i>	xii
5.2.6 Simulation of the DFG in the ZGP crystal	77
5.2.7 Optical parametric amplification	78
5.2.8 The PPKTP crystal	80
5.2.9 Simulation of the OPA at 2148 nm	82
Appendices	88
5.A DFG simulation	88
5.B Down conversion optical layout	92
6 OPO and OPA at 3142 nm	96
6.1 Optical parametric oscillator at 3142 nm	97
6.2 OPO cavity optical layout	98
6.2.1 Gaussian beam propagation using ABCD-matrices	99
6.2.2 OPO cavity mode	100
6.3 Realization of a variable outcoupling cavity	102
6.3.1 The principle of operation of the variable outcoupling OPO cavity . .	104
6.4 PDH locking of the OPO cavity	114
6.4.1 Realization of a PDH lock with infinite capture range	117
6.5 Optical parameteric oscillator with variable conversion efficiency	120
6.5.1 Experimental setup	123
6.5.2 Beam quality meaurment	127

<i>CONTENTS</i>	xiii
6.5.3 OPO wavelength tuning	127
6.6 Heterodyne measurement of the frequency chirp	130
6.6.1 Fourier transform method	132
6.6.2 Quadrature demodulation	143
6.7 Optical parametric amplifier at 3142 nm	150
6.7.1 Energy, stability and beam quality of the OPA	153
6.8 Tunability and frequency calibration	157
Appendices	164
6.A Derivation of the reflectivity of the variable outcoupling OPO cavity	164
6.A.1 Reflection	164
6.B Active mixer for the PDH locking	168
List of Publications	171
List of Publications	185

List of Figures

1.1	Compilation of r_p values extracted from hydrogen, muonic hydrogen, deuterium and elastic electron proton scattering. Figure is reprinted from [1].	4
1.2	Energy level scheme of muonic hydrogen highlighting the Lamb shift (2S-2P transition) and the ground state hyperfine splitting (1S-HFS). The pair of arrows of the 1S-state indicates the muon and proton spins.	5
1.3	The 1S-HFS transition in μp , where the purple and the blue arrows are a representation of the spin of the muon and the proton, respectively.	7
2.1	Hyperfine energy levels of the ground state in μp	11
2.2	Vacuum polarization corrections to the hyperfine splitting at first order. Diagram (a) illustrates the correction arising from the one-loop polarization insertion into the exchanged photon. Diagram (b) depicts the first-order correction to the wave function at the origin. The double line represents the non-relativistic reduced Green's function for a muon bound to a proton in a Coulomb field.	16
2.3	Second-order vacuum polarization corrections to the hyperfine interaction. (a) Reducible two one-loop polarization insertion (b) The one loop irreducible polarization insertion.	18
2.4	Second-order vacuum polarization corrections to the wave function at the origin resulting from: (a) the reducible two one-loop polarization potential and (b) the irreducible two-loop Källén–Sabry potential.	19

2.5	Second-order vacuum polarization corrections to the wave function at the origin, arising from the quadratic inclusion of the Uehling potential.	20
2.6	The muon self energy. (a) Radiative insertion into the muon line. (b) Mass renormalization term.	21
2.7	One-loop muonic vacuum polarization: (a) polarization insertion into the hyperfine interaction, and (b) one-loop polarization correction to the wave function. A^M represents the proton anomalous magnetic moment.	22
2.8	Six gauge invariant sets of diagrams for corrections of order $\frac{\alpha^2}{\pi}(Z\alpha)$	23
2.9	Weak interaction through the Z-boson exchange between the muon and the proton.	25
2.10	Two photon exchange diagrams: (a), (b) represent the elastic contributions to $2 - \gamma$ giving rise to $\delta_Z + \delta_{\text{recoil}}$. (c) represents the inelastic contribution to $2 - \gamma$, leading to the polarizability term δ_{pol}	28
2.11	One loop electronic vacuum polarization insertion into the elastic two photon exchange.	32
2.12	Theory predictions of the 1S hyperfine splitting in muonic hydrogen with uncertainties.	38
2.13	The 1S-HFS theory predictions with and without scaling from H hydrogen HFS measurements.	39
2.A.1	Vacuum polarization insertion in the photon propagator to first order in α	40
2.A.2	Vacuum polarization corrections to the electrostatic coulomb potential. (a) V_{VP}^1 One loop Uehling potential. (b) $V_{VP}^{1,1}$ reducible two-loop Uehling potential.	41
2.B.3	Irreducible two-loop potential (the Källén-Sabry potential).	43
3.1	Schematic of the HFS experimental setup. A detailed description is given in the text.	45

- 3.2 Collisional rates Γ_{if} of the different scattering processes of $\mu p - \text{H}_2$ for H_2 at temperature of 22 K and a liquid hydrogen density ($\varphi = 1$). The rates are calculated for two different distribution for rotational states of H_2 , the Boltzman distribution and the 3:1 mixture of rotational states $k = 0, k = 1$. We see there is only a relevant difference in the total rates Γ_{11}, Γ_{10} below the kinetic energy of ~ 0.1 eV for different distributions of rotational states in the hydrogen gas. Figure is reprinted from [2]. 48
- 3.3 Time evolution of the average kinetic energy (in the LAB frame) of the μp atoms simulated for two different target conditions each of temperature and density. Figure is reprinted from [2]. 49
- 3.4 Kinetic energy distributions for thermalized μp atoms (blue), and for μp atoms immediately after a cycle of laser excitation and collisional quenching from the triplet to the singlet state (orange). The amplitude of the blue curve is scaled by a factor of 1/5. The black curve represents the mean free path of the μp atoms in H_2 versus the kinetic energy of μp atoms. Here the target conditions are a temperature of 22 K and a pressure of 0.6 bar. Figure is reprinted from [2]. 50
- 3.5 Time distribution of the laser excited μp atoms reaching one of the target walls (orange). The time distribution of all the μp atoms including those which did not undergo a laser excitation is shown in (blue). The event time window is highlighted by the grey band, and the horizontal line spanning times $t = 1100$ to $t = 1400$ ns. Here the target conditions are a temperature of 22 K and a pressure of 0.6 bar in addition to accounting for the muon lifetime. Figure is adapted from [2]. 51
- 3.6 (a) Schematic of the toroidal multi-pass cell under development. The red rays represent the in-coupled beam. Upon each reflection, the colour of the rays is changed to illustrate the spreading of the light in the $x - y$ plane. (b) Simulation of the two dimensional fluence distribution inside the toroidal multi-pass cell in the transverse plan for an injection at an angle $\theta = 2^\circ$, a laser pulse energy of 1 mJ, and a reflectivity of 99.2 % of the multi-pass cell. The green circle represents the size of the muon beam with a diameter of 15 mm. Figure is adapted from [3]. 53

3.7	Schematic of a muonic gold event produced in the target region detected using a large high-Z scintillator (light blue).	54
3.8	(a) Schematic of a Bremsstrahlung process where the decay-electron is falsely identified as an X-ray (muonic gold cascade event). The Bremsstrahlung photon deposit energy in the X-ray detector but none in the plastic scintillator (yellow colour) which are used to identify these false X-ray events. (b) Examples of uncorrelated background events due to electrons coming with the muon beam, cosmic particles and neutrons produced at the radiation zone. These events as well deposit energy in the X-ray detector and are rejected through non correlation with events timed by the muon entrance detector.	55
4.1	Three-level system described by the Bloch equations. The thermalised singlet and triplet states are described by ρ_{11}, ρ_{22} , respectively. ρ_{33} describes the level where the μp atom goes through a laser excitation followed by a collisional de-excitation, acquiring an average kinetic energy of 100 meV. Figure is reprinted from [4].	58
4.2	Line-shapes of the excitation probability around the resonance for two laser fluence (\mathcal{F}) values, each at two laser bandwidths Δ_l . Courtesy of Miguel Ferro.	59
4.3	(a) Representation of the fluence distribution along the thickness of the target volume (z direction) in blue. The dotted curve represents the transition probability corresponding to the fluence. (b) Same as (a) but showing the fluence distribution and corresponding transition probability for the transverse x-direction. The simulation presented in (b) and (c) are for a laser pulse energy of 1 mJ, reflectivity of 99.2% of the multi-pass cell, target pressure of 0.5 bar and temperature of 22 K. Figure is reprinted from [5] and [3].	61
4.4	Combined laser excitation probability followed by collisional de-excitation against the average fluence for a volume diameter of 10 mm, cell reflectivity of 99.2%, laser bandwidth of 10 MHz and a 50 ns pulse length. Courtesy of Miguel Ferro.	62

4.5	Monte Carlo simulation of resonance measurements assuming two weeks of data collection. (a) Line shape for a laser pulse energy of 1 mJ and bandwidth of 100 MHz. (b) Statistical uncertainty of the resonance position for various laser system energies and bandwidths. Figure is reprinted from [5].	65
5.1	The HyperMu laser system. A detailed description is given in the text.	67
5.2	Conservation principles in the DFG process [6]: (a) Energy conservation. (b) Momentum conservation: collinear phase matching.	70
5.3	An example of the monotonic relation between the refractive index (n) and the frequency (ω) in lossless materials. Figure is reprinted from [7].	71
5.4	(a) The index ellipsoid of a uniaxial crystal, illustrating the optical axis and the two principal refractive indices. (b) Angle tuning by varying the angle θ relative between \vec{k}_e and the optical axis. \vec{E}_e and \vec{E}_o correspond to the light polarized in the extraordinary and the ordinary direction. The figure in (b) is reprinted from [7].	72
5.5	The Gaussian beam intensity profile. Beam waist (w_0) and the FWHM beam diameter are indicated.	75
5.6	Nonlinear figure of merit d_{eff}^2/n^3 plotted against the transparency range of various mid-infrared nonlinear crystals. Figure is reprinted from [8].	76
5.7	Simulated idler energy at 6788 nm from the DFG simulation in a ZGP crystal, plotted against FWHM beam diameter for pump energies of 15 mJ, 20 mJ, and 25 mJ, with a fixed input signal energy of 2.5 mJ.	78
5.8	(a) Simulation of the energy evolution of the 3 different wavelengths for the DFG process along the propagation length inside the ZGP crystal. (b) The corresponding beam quality given by M^2 for the 3 different wavelengths is shown.	79

- 5.9 Schematic of the optical parametric amplification (OPA) process. (a) Illustration of the nonlinear medium showing input photons (signal and pump) and output photons (signal, pump, and idler) with their respective frequencies. (b) and (c) Energy diagrams demonstrating the regeneration of the signal photon, highlighting the parametric amplification mechanism at the required frequencies and corresponding wavelengths for OPA2. 81
- 5.10 Amplified signal energy at 2148 nm as a function of crystal length for two different pump energies at 1030 nm. The input signal energy was 700 μJ , with a pulse length of 50 ns and a beam waist of 0.84 mm for both the signal and pump. 83
- 5.11 Simulation results of the output signal energy at 2148 nm as a function of input pump energy for a single OPA stage using a 12 mm PPKTP crystal. The simulation assumes an input signal pulse energy of 0.7 mJ with a 50 ns duration. Results are shown for three beam waist configurations: the orange line represents a fixed beam waist of 1 mm, the blue line adjusts the beam waist at each pump energy to reach the damage threshold intensity, and the gray line uses a beam waist 1.4 times larger than the corresponding values of the blue line. 84
- 5.12 Simulation results of the beam quality, expressed as M^2 , and the pulse energy evolution along the crystal length for OPA2. Plots (a) and (b) correspond to an input pump energy of 120 mJ with a beam waist w_0 of 564 μm for both the signal and pump input beams. Plots (c) and (d) present similar results for the same input pump energy but with a larger beam waist of 1 mm for the input signal and pump beams. For both simulations, the input signal pulse energy was 700 μJ with a pulse duration of 50 ns. 85
- 5.13 Simulation results for two consecutive OPAs, each using a 12 mm long PPKTP crystal. (a) shows the output signal energy of the preamplifier, OPA2.1, as a function of pump energy, with an input signal energy of 0.7 mJ at 2148 nm. (b) displays the output signal energy of OPA2.2 for two different seed energies at 2148 nm, 7.7 mJ and 11.4 mJ. The simulations were performed for a pulse length of 50 ns, with w_0 representing the beam waist of both the signal and pump beams. 86

5.A.1	Phase-matching parameters for the ZGP crystal extracted using the SNLO program. (a) displays the effective nonlinear coefficient $d_{\text{eff}} = 80.6 \frac{\text{pm}}{\text{V}}$ and phase-matching angle of 51.5° . (b) shows the refractive index for the pump wavelength (2148 nm), and (c) provides the refractive index for the signal wavelength (3142 nm) under the same phase-matching conditions.	89
5.B.2	Scheme of the complete optical layout of the laser system. Detailed description is given in the text.	94
6.1	Scheme of the pulsed optical parametric oscillator CW seeded at the signal wavelength. Detailed description is given in the text.	98
6.2	Gaussian beam propagation parameters. Z_R is the rayleigh length.	99
6.3	(a) The L shaped cavity layout with a $\lambda/4$, TFP and the nonlinear crystal indicated. CM1 is the flat end mirror and CM2 is the plano concave mirror with $R = 1000$ mm. The reference plane used to calculate the laser mode is indicated by the red line. (b) Mode matching between the fiber coupled seed laser and the OPO cavity. d_1 represents the distance between the output of the fiber and the aspheric lens of the collimator. d_2 represents the distance from the aspheric lens to the position at which the beam waist should be collimated to the value of $w_0 = 362 \mu\text{m}$	102
6.4	Schematic of an optical cavity consisting of two mirrors M1, M2, with a cavity length L. (a) shows the field amplitudes circulating within the cavity. (b) The cavity response to the input field is shown. $E_{\text{inc}}, E_{\text{ref}}, E_{\text{tr}}$ and E_{circ} are the incident, reflected, transmitted and circulating fields, respectively.	103
6.5	Sketch of polarization plane \vec{k}^\perp perpendicular to the propagation direction.	105
6.6	Jones vectors and representations for specific polarization states. θ is the angle w.r.t the horizontal direction. The propagation vector direction is out of the page.	106
6.7	Linear polarizer: The lines on the polarizer indicate the permitted field direction for the transmitted light.	107

- 6.8 A wave plate with its fast axis aligned to the x-direction, and its slow axis aligned to the y-direction. 108
- 6.9 Transmission of light through several polarizing optical elements. J_1, J_2 represent the Jones vector of the input and output wave, respectively. The output vector is related to the input vector by the matrices product given in Eq. 6.22. 108
- 6.10 Beam incoupling and propagation within the OPO cavity for two special angles of the $\lambda/4$ – plate. (a) $\theta = 0^\circ$, (b) $\theta = 45^\circ$ shown in (b). 110
- 6.11 (a) Layout of the OPO optical cavity with the polarization elements. $\lambda/4$ refer to the quarter wave plate, TFP is the thin film polarizer. CM1 and CM2 are the end mirrors of the cavity. L_1 and L_2 correspond to the distance from the TFP to CM1 and CM2, respectively. (b) An equivalent representation in terms of a linear two mirror cavity. 112
- 6.12 Measured intra-cavity resonances for various effective reflectivities $\sqrt{R_{\text{eff}}}$ and its corresponding finesse \mathcal{F} values. The free spectral range FSR as well as the linewidth $\delta\nu$ of the resonances are indicated. 113
- 6.13 The finesse \mathcal{F} versus angle of $\lambda/4$ – plate extracted from the measured intra-cavity resonances. A fit of the data using Eq. 6.29 was carried out, where the uncertainty comes from the cavity losses L_{loss} , for details see text. 113
- 6.14 Schematic of the PDH locking. Detailed description is given in the text. . . . 115
- 6.15 a) The modulated intra-cavity intensity is shown. The carrier corresponds to the central frequency of the longitudinal mode resonant with the cavity. The frequencies $f_c + f_{\text{mod}}$ and $f_c - f_{\text{mod}}$ represent the two sidebands generated by the phase modulation and are made visible by scanning the cavity length. b) The PDH error signal obtained for $f_{\text{mod}} = 300$ MHz. The black arrows indicate the direction in which the cavity is pulled to lock on resonance. The green arrows indicate the direction in which locking occurs between resonances, referred to as "Anti-locking". 116

- 6.16 The high-stability mirror mount designed for the combination of the piezo-electric element and the mirror CM1. The mirror has a diameter of 0.5 " and a thickness of 6 mm. 118
- 6.17 a) Modulated intra-cavity resonances, with the sidebands at 760 MHz visible when scanning the cavity length. b) The PDH error signal generated at a modulation frequency of $FSR/2$. c) The intra-cavity intensity and error signal when the cavity is locked to the laser frequency. 119
- 6.18 The stabilized error signal, intra-cavity power, and piezo feedback voltage (which controls the cavity length) are shown as functions of time during pulse generation. In this case, a pulse energy of 500 μ J at 3142 nm was extracted. 120
- 6.19 Sketch of the singly resonant OPO and the corresponding energy level diagram for the parametric down-conversion process. 121
- 6.20 Picture of the OPO setup we built. The pump beam, shown in blue, is coupled through the TFP, which is HT for the pump wavelength. The signal light, shown in green, is resonant within the cavity. The (PPLN) text refers to the nonlinear crystal inside the home-built oven used to control the crystal temperature. The generated pulses at the idler wavelength are coupled through the mirror (CM2), which is HT for this wavelength. 124
- 6.21 Total output pulse energies (solid lines, left axis) at the signal and idler wavelengths, along with their corresponding conversion efficiencies (dashed lines, right axis), are plotted as functions of the input pump energy at a wavelength of 1030 nm. The data is presented for four different outcoupling values, represented by $r_{\text{eff}} = \sqrt{R_{\text{eff}}}$. E_{thr} refers to the threshold pump energy. The signal and idler wavelengths are 1532 nm and 3142 nm, respectively. 125
- 6.22 Measured pulse shapes at the signal wavelength for the seeded and free-running OPO cavity. The area under the pulses is calculated between 15% of the maximum pulse amplitude on both the rising and falling edges. This measurement was performed at $r_{\text{eff}} = 71\%$ and $E_p = 8$ mJ. 126

- 6.23 Measurement of the OPO beam radius W along the distance z . The extracted M^2 values in both the x and y directions are shown. The measurement was carried out for $r_{\text{eff}} = 71\%$ at an idler energy of $E_i = 1$ mJ. A sample beam profile image at the waist position is included. 128
- 6.24 The top panel displays temperature scans conducted at three distinct wavelengths, while the bottom panel presents the corresponding extracted phase-matching temperature values. The temperature scan was performed with a resolution of 0.01°C , and the measured power was normalized relative to the baseline value recorded by the power meter. Measurements were carried out at $r_{\text{eff}} = 71\%$ with an idler energy of approximately $E_i = 900 \mu\text{J}$ 129
- 6.25 An example of the electric field envelope of the pulse radiation without and with a chirp. 130
- 6.26 Scheme of the optical heterodyne measurement from which we extract the instantaneous frequency of the OPO pulses. Detailed description is given in the text. 131
- 6.27 (a) A synthesized pulse with a Gaussian envelope is compared to a measured output pulse at $r_{\text{eff}} = 71\%$ and a pulse energy of $E_{\text{signal}} = 1$ mJ. (b) The synthesized OH waveform generated by beating the synthesized pulse with CW light at $f_{\text{seed}} + f_{\text{mod}}$, where $f_{\text{seed}} = 1532$ nm and $f_{\text{mod}} = 760$ MHz. (c) The power spectrum of the OH beat waveform (left scale), with a Butterworth filter (right scale) applied to isolate the interference term at the frequency $f_{\text{seed}} + f_{\text{mod}}$. (d) The extracted instantaneous frequency of the synthesized pulse. 134
- 6.28 (a), (b), and (c) correspond to their counterparts in Fig. 6.27, but with an induced linear chirp added to the phase of the synthesized pulse. (d) The extracted instantaneous frequency of the synthesized pulse is shown, demonstrating a frequency variation consistent with the induced linear chirp of approximately 30 MHz. 135

- 6.29 (a) The amplitude envelope of the optical output pulse measured at $r_{\text{eff}} = 96\%$ and $E_{\text{signal}} = 700 \mu\text{J}$. (b) The OH beat waveform generated by combining the pulse in (a) with the CW light output of the FP cavity at a frequency $f_{\text{seed}} + f_{\text{mod}}$ 136
- 6.30 The power spectral density (PSD) of the beat waveform, obtained via Fourier transform, is shown in blue (left scale). A Butterworth filter, applied to isolate the positive-frequency interference term, is shown in red (right scale). 137
- 6.31 a) The amplitude of the positive-frequency interference term as a function of frequency. b) The power spectral density (PSD) of the positive-frequency interference term, corresponding to a), shown in dB. 138
- 6.32 The extracted instantaneous frequency of the beat waveform, shown in MHz, corresponds to the beat waveform presented in Fig. 6.29. 138
- 6.33 a, b) The pulse envelope and corresponding beat waveform recorded at a signal energy of $E_{\text{signal}} = 800 \mu\text{J}$ and reflectivity $r_{\text{eff}} = 84\%$. c) The extracted instantaneous frequency corresponding to the beat waveform is shown. 140
- 6.34 a, b) The pulse envelope and corresponding beat waveform recorded at a signal energy of $E_{\text{signal}} = 1 \text{ mJ}$ and reflectivity $r_{\text{eff}} = 71\%$. (c) The extracted instantaneous frequency corresponding to the beat waveform is displayed. 141
- 6.35 a) The pulse envelope recorded from the misaligned OPO. (b) The corresponding beat waveform generated by combining the pulse with the CW light. (c) The extracted instantaneous frequency showing frequency deviation, attributed to the misalignment between the seed and pump beams in the OPO cavity. 142

- 6.36 Diagram of the quadrature demodulator. The LO corresponds to the RF signal driving the electro-optic modulator (EOM), which generates the $f_{\text{mod}} = 760$ MHz modulation frequency. The cross symbols represent electronic mixers, while the LPF blocks indicate low-pass filters used to remove high-frequency components. The HPF eliminates low-frequency signals below f_{mod} , enabling the extraction of the in-phase ($I \propto A \cos(\phi)$) and quadrature ($Q \propto A \sin(\phi)$) components of the optical heterodyne (OH) beat signal. . . . 144
- 6.37 The OH beat waveform measured at a signal energy of $E_{\text{signal}} = 700 \mu\text{J}$ and $r_{\text{eff}} = 96\%$ is shown in a). Panel b) presents the resulting I and Q components extracted from the quadrature demodulator, representing the in-phase and quadrature signals of the beat waveform. In c), the directly measured output pulse is compared with the reconstructed pulse derived from the I and Q components, shifted by 26 ns to ensure temporal alignment. Panel d) illustrates the extracted instantaneous frequency, where the time domain coincides with the pulse duration derived from the quadrature demodulator components. . . 146
- 6.38 a) The OH beat waveform measured at a seed energy of $E_{\text{signal}} = 800 \mu\text{J}$ and $r_{\text{eff}} = 84\%$. b), c), and d) share the same explanation as provided in Fig. 6.37, illustrating the quadrature demodulator components, reconstructed pulse compared to the measured pulse, and the extracted instantaneous frequency, respectively. 147
- 6.39 a) The optical output pulse and (b) the corresponding OH beat waveform recorded at a seed energy of $E_{\text{signal}} = 1 \text{ mJ}$ and $r_{\text{eff}} = 71\%$. c) and d) share the same explanation as provided in Fig. 6.37, illustrating the reconstructed pulse compared to the measured pulse, and the extracted instantaneous frequency, respectively. 148
- 6.40 a) The OH beat waveform recorded for the misaligned OPO. (b) The I and Q components extracted from the quadrature demodulator, showing the in-phase ($\cos(\phi)$) and quadrature-phase ($\sin(\phi)$) signals. (c) The directly measured pulse and the reconstructed pulse obtained from the I and Q components, with a time shift applied for temporal alignment. (d) The extracted instantaneous frequency, showing an induced frequency deviation due to the misalignment between the seed and pump beams. 149

- 6.41 Sketch of the optical parametric amplification process. A PPLN crystal with a period of $30.3 \mu\text{m}$ is used as the gain medium. 150
- 6.42 The temporal overlap of the OPA pump pulse and the input pulse at 3142 nm. The left scale refers to the OPO, OPA pump pulses while the right scale refers to the OPA input pulse. 151
- 6.43 Scheme of the implemented OPA for amplifying the $3.1 \mu\text{m}$ Pulses. Detailed description is given in the text. 152
- 6.44 Gain of the OPA and output pulse energy for two different crystal lengths: 50 mm and 25 mm, shown in (a) and (b), respectively. The input signal pulse energy was $770 \mu\text{J}$ and $500 \mu\text{J}$ for the 50 mm long and the 25 mm long crystals, respectively. For details, see the text. 154
- 6.45 RMS stability of the OPA pulse energies at 3142 nm (red) compared to the input pump pulse energies (blue). For details, see text. 155
- 6.46 Measurement of the OPA beam radius W along the distance z . The extracted M^2 values for both x and y directions are given. The measurement was carried out at an output pulse energy of 2 mJ for a 25 mm-long crystal. A sample of the beam profile image near the waist position is also shown. 156
- 6.47 Schematic of the frequency calibration and tunability measurement. For detailed description, see text. 158
- 6.48 Measured CH_4 absorption lines at 95.1796 THz and 95.1789 THz, labeled as A and B, respectively. The Voigt fits to the measured absorption peaks are shown in blue. Measurements were conducted over a 2 m path length at two pressures: (a) 1.2 mbar and (b) 17 mbar. 160
- 6.49 Simulated CH_4 absorption lines at 95.1796 THz and 95.1789 THz, labeled as A and B, respectively, using the HITRAN database. Simulations were performed for a 2 m path length at pressures of 1.2 mbar (red) and 17 mbar (blue). 161

6.50	Pressure dependence of the Lorentzian linewidth extracted from Voigt fits to the CH ₄ absorption lines at 95.1789 THz (red, labeled as A) and 95.1796 THz (blue, labeled as B). The linewidth values were obtained at pressures of 1.2 mbar and 17 mbar, with error bars representing the uncertainties in the fit parameters. The linear trend reflects the broadening due to pressure effects.	162
6.A.1	Sketch of the beam propagation within the OPO cavity. L_1 and L_2 correspond to the distance from the TFP to CM1 and CM2, respectively. The symbol $\lambda/4@{\theta}$ corresponds to the $\lambda/4$ - plate being set to an arbitrary angle.	165
6.B.2	Circuit diagram of the PDH active mixer.	169
6.B.3	PCB layout of the PDH active mixer. The evaluation board is mounted using a set of screws through the holes (H1-4).	170

List of Tables

2.1	Physical constants used in this thesis.	11
2.2	Values of the Zemach radius r_Z in fm extracted using different methods. For μp and H, two r_Z values are given based on two values of δ_{pol} , one from the data-driven [9,10] and the other is from chiral perturbation theory [11]. . . .	29
2.3	Comparison of the different theory update of the 1S μp HFS from various authors. All the numerical values are in meV. The final HFS value in the column labeled ‘Ruth’ combines their calculation for the 2PE with our selected values for all other corrections.	34
4.1	A comparison of the different values of the excitation probability obtained through numerical integration of the Bloch equations $\bar{\rho}_{33}$. The table shows the experimental conditions at different sets of temperature (T), pressure (p), laser bandwidth (Δ_l) and fluence (\mathcal{F}). Γ is the full width at half maximum (FWHM) of $\bar{\rho}_{33}$ which estimates the line-shape around the resonance frequency ω_r . The table values were adapted from [4].	60
4.2	Time needed to expose a 4σ statistical significance of signal over background ($t_{4\sigma}$) at various experimental conditions. A target thickness d below 1 mm can lead to smaller $t_{4\sigma}$ but can not be realized practically due to diffraction losses. These numbers were obtained assuming a laser pulse of a 1 mJ energy and 50 ns length coupled into the multi-pass cell which has a reflectivity of 99.2%. The table is adapted from [5].	63

5.A.1 Simulation results for DFG output idler energy at $6.8 \mu\text{m}$ as a function of the FWHM beam diameter and pump energy, for a fixed signal input energy of 2.5 mJ at 3142 nm.	90
5.A.2 Simulation results for the DFG output idler energy at $6.8 \mu\text{m}$ as a function of the FWHM beam diameter and pump energy, with a fixed input signal energy of 1 mJ at 3142 nm.	91

Chapter 1

Introduction

“Who ordered that?” is attributed to physicist Isidor I. Rabi. Rabi made this remark humorously because the discovery of the muon seemed unexpected and puzzling. It did not fit into the theoretical framework of the time, as physicists were trying to understand particle interactions, and the muon didn’t seem to belong in the context of the known forces. Decades after Rabi’s remark, the muon, bound with a nucleus to form muonic atoms, is used as a tool to investigate the fundamental interactions, and to probe the properties of the nuclei [12–16].

1.1 The muonic hydrogen atom

A muonic hydrogen atom is formed when a muon, which is about 207 times heavier than an electron, replaces the electron in a hydrogen atom. In muonic hydrogen, the Bohr radius, given by $(Z\alpha m_r)^{-1}$, is around 186 times smaller due to the muon’s much larger mass relative to the electron. Here α is the fine structure constant, Z is the atomic number and m_r is the reduced mass of the μp atom. This smaller Bohr radius causes the muon to be tightly localized near the proton which, on the one hand, enhances the quantum electrodynamics (QED) effects at small scale, specifically the electronic vacuum polarization. On the other hand, for the S states, the probability density of the atomic wave function at the origin, $|\psi(0)|^2$, is proportional to m_r^3 . As a result, the overlap between the muon wavefunction and the proton is greatly increased, thereby enhancing sensitivity to nuclear structure effects such as the proton finite size. The atomic energy shift due to the finite size of the charge

distribution is, to leading order, given by

$$\Delta E_{\text{finite size}} = \frac{2\pi Z\alpha}{3} r_p^2 |\Psi(0)|^2, \quad (1.1)$$

where r_p is the root mean square of the proton charge radius, and we neglect higher moments of the charge distribution. For the Lamb shift (2S-2P) in μp , the correction due to the proton charge radius amounts to 3.7 meV, accounting for about 2% of the total energy.

In 2010, the CREMA (Charge Radius Experiment with Muonic Atoms) collaboration at Paul Scherrer institute (PSI) measured the Lamb shift (2S-2P) in muonic hydrogen, which led to a surprising result. The proton charge radius extracted from the Lamb shift measurement in μp [17] was an order of magnitude more precise, but significantly deviated from the previous determinations obtained from regular hydrogen spectroscopy [18, 19] and electron-proton scattering [20, 21]. At that time, the value of the proton charge radius from the muonic Lamb shift was around 4% smaller, or 7 standard deviations, than the value obtained from the electronic results. This striking discrepancy, referred to as the proton radius puzzle [22], has sparked extensive research across nuclear, particle, and atomic physics, extending into explorations of physics beyond the Standard Model. More than a decade after the emergence of the puzzle, 5 out of the last 6 experiments [23–27] using hydrogen spectroscopy resulted in smaller determination of r_p . Only the measurement of 1S-3S [28] transition in hydrogen resulted in a 3σ tension with the muonic results calling for further experimental investigation.

On the side of the electron-proton scattering experiments, the latest measurement from the PRad experiment [29] at Jefferson lab has reported a smaller value for the charge radius in agreement with the muonic results. This also agrees with several other r_p determination from modern analyses of proton electric form factor data [30–33]. Now, there seems to be an agreement that the value of r_p from μp measurement is not only 10 times more precise but it is also accurate, as illustrated in Fig. 1.1. For these reasons, the Committee on Data for Science and Technology (CODATA) has updated its recommended value for r_p in 2018 to include the μp Lamb shift measurement.

Moving beyond the puzzle, the precise value of r_p could be used in combination with other precise experiments in hydrogen to extract the most precise value of the Rydberg constant and to verify the bound-state QED prediction in hydrogen. Combined with the measurement of the isotope shift of the 1S-2S transition in atomic hydrogen and deuterium, it has led to the most precise extraction of the deuteron charge radius r_d . Going the other way by combining the r_d value from muonic deuterium μD with the H-D(1S-2S) isotope shift measurement, an

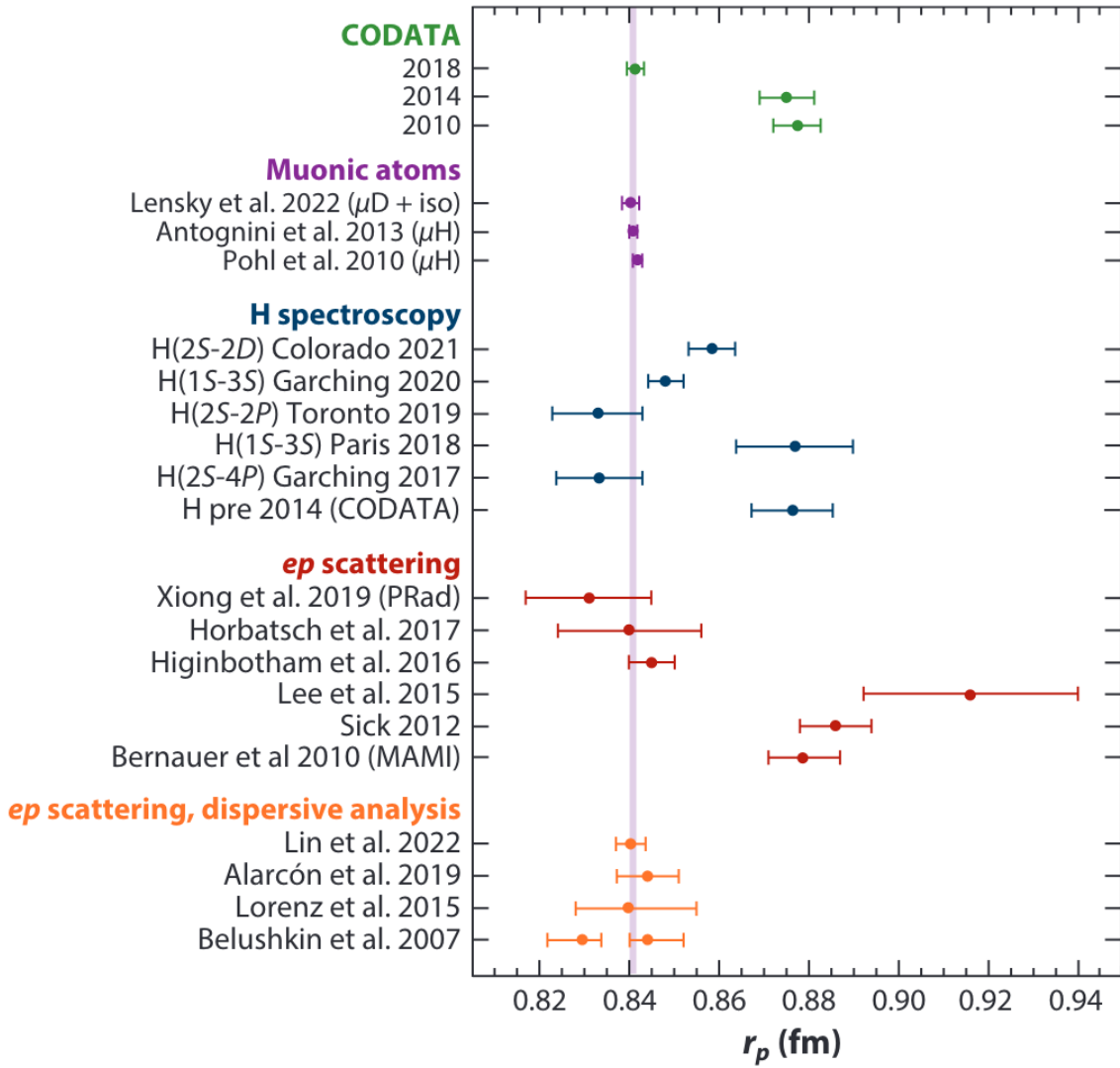


Figure 1.1: Compilation of r_p values extracted from hydrogen, muonic hydrogen, deuterium and elastic electron proton scattering. Figure is reprinted from [1].

r_p value can be extracted. This is in perfect agreement with the value directly extracted from the direct measurement in μp . This means that the two measurements in μp and μD are consistent with each others.

Until now we have been concerned with the charge aspects of the finite size of the proton that was accessed through the Lamb shift 2S-2P. As the next step, the CREMA collaboration is addressing the magnetic properties of the proton through the planned measurement of the ground state (1S) hyperfine splitting in muonic hydrogen, see Fig. 1.2, which is given by the interaction between the magnetic moment of the proton and that of the muon.

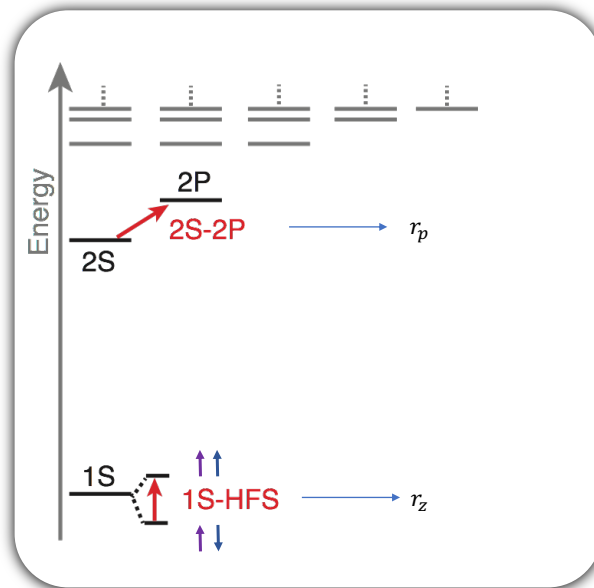


Figure 1.2: Energy level scheme of muonic hydrogen highlighting the Lamb shift (2S-2P transition) and the ground state hyperfine splitting (1S-HFS). The pair of arrows of the 1S-state indicates the muon and proton spins.

1.2 The HyperMu experiment

The CREMA collaboration aims at the first ever measurement of the ground state hyperfine splitting (1S-HFS) in muonic hydrogen by means of laser spectroscopy. The goal of the measurement is to achieve a relative accuracy of 1 ppm. The 1S-HFS transition shown in Fig. 1.3 corresponds to an energy of approximately 182 meV or a laser frequency of 44.3

THz. The 1S-HFS can be written as

$$\Delta E(1S - \text{HFS}) = E_F (1 + \Delta_{\text{QED}} + \Delta_{\text{weak}} + \Delta_{\text{str}}), \quad (1.2)$$

where E_F is the Fermi energy arising from the magnetic moment interaction of the muon and the proton, $\Delta_{\text{QED}}, \Delta_{\text{weak}}$ are the quantum electrodynamics and the weak interaction contributions to the hyperfine interaction, respectively. The proton structure contribution Δ_{str} arises from the composite structure of the proton and is attributed in the leading order to the two photon exchange (2PE) contribution.

The 2PE can be divided into three components, the finite size contribution parametrized by the Zemach radius (δ_Z), the recoil correction to it (δ_{recoil}) and the dynamical part called the polarizability contribution δ_{pol} .

$$\Delta E_{1S-\text{HFS}}^{(2\gamma)} = E_F (\delta_Z + \delta_{\text{recoil}} + \delta_{\text{pol}}). \quad (1.3)$$

The Zemach radius r_Z can be seen as the convolution of the charge and the magnetization distribution of the proton. The anticipated experimental accuracy of a 1 ppm will enable the extraction of the proton structure contribution to the 1S-HFS with a 10^{-4} relative accuracy. The Zemach and the polarizability contributions can be disentangled in two ways. The first is by combining the precise measurement from the 1S-HFS in μp and the value of r_Z from the precise 1S-HFS measurement in H to extract the polarizability contribution with a relative accuracy of $< 10\%$. The second method is to use the value of δ_{pol} calculated from the theory and combine it with our precise measurement of the 1S-HFS in μp , to extract the Zemach radius with a relative accuracy of 10^{-3} .

1.3 Summary of the experiment

The hyperfine splitting experiment is shortly summarized here. A muon beam of 11 MeV/c passes an entrance detector triggering the laser system and is stopped in an H_2 target of 22 K and 0.5 bar, where a μp atom is created. While the laser pulse is generated, the μp atom de-excites from a highly excited state to the singlet $F = 0$ ground state and thermalizes to the surrounding H_2 gas. After 1 μs , a laser pulse of around 6.8 μm in wavelength and few mJ in energy is coupled into a multi-pass cell surrounding the gas target, and excites the μp atoms from $F = 0$ singlet to $F = 1$ triplet state. After excitation, the μp atoms collide with

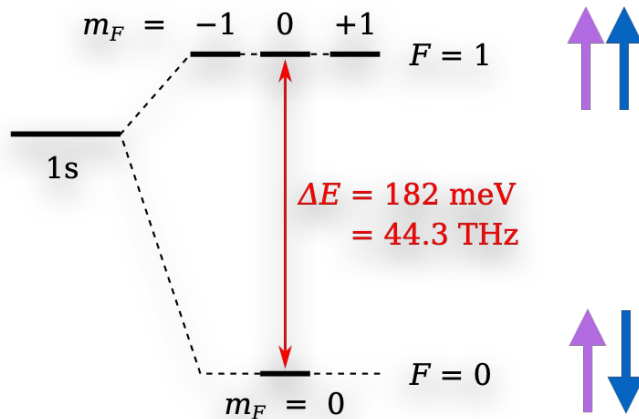


Figure 1.3: The 1S-HFS transition in μp , where the purple and the blue arrows are a representation of the spin of the muon and the proton, respectively.

the surrounding H_2 molecules and de-excite back to the singlet $F = 0$ state converting the 0.18 eV energy into kinetic energy of the μp atom and the H_2 molecule. Due to this additional kinetic energy, the μp atoms diffuse to the gold coated target walls where the muons transfer to the gold atoms creating muonic gold atoms μAu . A cascade of de-excitation from the highly excited states in the μAu takes place producing X-rays. We obtain the resonance by counting the number of μAu X-ray events as a function of laser frequency.

1.4 Structure of the thesis

A precise theoretical prediction for the 1S-HFS in μp is crucial for the success of the experiment. First and foremost, it helps narrow down the frequency search range scanned by the laser, which is particularly important given the expected low event rate and the limited beam time available to the collaboration at PSI. Secondly, it is essential for interpreting the results, particularly in disentangling and quantifying the various contributions from proton structure. Chapter 2 of this thesis is dedicated to the discussion of the different theoretical contributions to the 1S-HFS. We improve on the previous theoretical compilation by adding the missing higher order QED contributions as well as including the newest results for the proton structure contribution calculated from chiral perturbation theory (χ PT) and from the data driven approach. A theoretical prediction for the HFS is given, taking into account

discrepancy between the different methods used to calculate the proton structure contribution. This discrepancy is translated into an uncertainty that defines the search range needed to find the resonance.

Chapter 3 discusses the principles of the HFS experiment, highlighting the key processes necessary to achieve a successful resonance signal. It emphasizes the critical roles of laser excitation and μp collisions with H_2 molecules, summarizing findings from previous studies.

Chapter 4 integrates the results for the HFS transition probability, signal and background rates, and the estimated search range to determine the data points, measurement duration, and laser system requirements.

Chapter 5 builds on the laser system requirements outlined earlier to present the design of the down-conversion scheme, the core focus of this thesis. This scheme converts light from the 1030 nm thin-disk laser to the target wavelength of around $6.8 \mu\text{m}$ through multiple nonlinear optical stages. Simulations using the program SNLO define the input energies, gain, material properties, and beam sizes for each stage, starting with the final process and guiding the design of preceding stages. Based on these parameters, the complete layout of the down-conversion scheme is established.

Chapter 6 details the design and implementation of an optical parametric oscillator (OPO) and optical parametric amplifier (OPA) pumped at 1030 nm to generate pulses at 3142 nm. Utilizing a Periodically Poled Lithium Niobate (PPLN) crystal, the OPO, with a layout uniquely designed to optimize nonlinear optical conversion efficiency, produces tunable single longitudinal-mode pulses with energies up to 1.4 mJ. The output of the OPO is further amplified in an OPA up to 3.4 mJ with an excellent temporal and spatial mode characteristics. The OPO-OPA system demonstrated continuous tunability of approximately 20 GHz through pulsed absorption spectroscopy on methane near 3142 nm. The laser bandwidth was estimated to be below 100 MHz based on optical heterodyne measurements and methane absorption line spectroscopy.

Chapter 2

The hyperfine splitting theory

2.1 Introduction

In this chapter, we discuss the theoretical description of the origin of the hyperfine splitting in muonic hydrogen, and the detailed contribution of different corrections to the hyperfine splitting coming from the quantum electrodynamics, the recoil, and finite size effects. The goal is to predict the total energy splitting resulting from the hyperfine interaction and to determine a reliable value for its uncertainty. This will guide the search for the resonance and will define the performance of the experimental setup in terms of the laser system which increases with a larger search range.

2.2 The origin of the hyperfine splitting

The hyperfine splitting arises from the interaction of the magnetic moment of the proton with the magnetic field generated by the muon. The magnetic moment of the proton is defined by $\mu_p = g_p \left(\frac{Ze}{2m_p}\right) I$, where $g_p = 2(1 + \kappa)$, $I = 1/2$ is the proton spin, and κ is its anomalous magnetic moment. The nuclear magneton is $\mu_N = \frac{e}{2m_p}$. The charge number Z is included in the expression for generality, although $Z = 1$ here. In a non-relativistic picture, the magnetic field for S-states is generated by a magnetized sphere and, according to classical

electrodynamics, is given by:

$$\mathbf{B}_\mu(0) = \frac{2\pi}{3} \boldsymbol{\mu}_\mu |\psi_{ns}(0)|^2, \quad (2.1)$$

where $|\psi(0)|^2 = \frac{(Z\alpha)^3 m_\mu^3}{\pi}$ is the probability density of the wave function at the origin. The muon magnetic moment is $\boldsymbol{\mu}_\mu = g_\mu \left(\frac{e}{2m_\mu} \right) \vec{S}$, with $g_\mu = 2(1 + a_\mu)$, \vec{S} as the muon spin, and a_μ as the anomalous magnetic moment of the muon.

Expressed in terms of the Bohr magneton, $\mu_B = \frac{e}{2m_e}$, the magnetic moment of the muon is given by $\boldsymbol{\mu}_\mu = g_\mu \left(\mu_B \frac{m_e}{m_\mu} \right) \vec{S}$. The hyperfine interaction Hamiltonian and corresponding energy are expressed as:

$$\begin{aligned} H_{\text{HFS}} &= -\boldsymbol{\mu}_p \cdot \mathbf{B}_\mu, \\ E_{\text{HFS}} &= \langle ns | H_{\text{HFS}} | ns \rangle, \\ E_{\text{HFS}} &= \frac{2Z\pi}{3} g_p g_\mu \mu_N \left(\mu_B \frac{m_e}{m_\mu} \right) \langle ns | \delta(r)^3 | ns \rangle \langle I \cdot S \rangle. \end{aligned} \quad (2.2)$$

Rewriting the nuclear magneton in terms of the Bohr magneton, $\mu_N = \mu_B \frac{m_e}{m_p}$, and substituting g_p and g_μ , the expectation value of the Hamiltonian for the 1S state becomes

$$\begin{aligned} E_{\text{HFS}} &= \frac{2Z\pi}{3} g_p g_\mu \left(\mu_B^2 \frac{m_e^2}{m_\mu m_p} \right) |\psi(0)|^2 \langle I \cdot S \rangle \\ &= \frac{8Z\pi}{3} (1 + \kappa)(1 + a_\mu) \left(\mu_B^2 \frac{m_e^2}{m_\mu m_p} \right) |\psi(0)|^2 \langle I \cdot S \rangle. \end{aligned} \quad (2.3)$$

To evaluate $\langle I \cdot S \rangle$, the spin eigenstates are expressed in terms of the total spin $F = I + S$ and its projection m_F . The spin product is rewritten using the operators I^2 , S^2 , and F^2 as

$$I \cdot S = \frac{F^2 - I^2 - S^2}{2}. \quad (2.4)$$

Taking the expectation values between spin eigenstates and substituting the eigenvalues of \hat{I}^2 and \hat{S}^2 for spins of 1/2 for both I and S , we find

$$\begin{aligned} \langle m_F, F | \hat{I} \cdot \hat{S} | F, m_F \rangle &= \frac{1}{2} \langle m_F, F | \hat{F}^2 - \hat{I}^2 - \hat{S}^2 | F, m_F \rangle \\ &= \frac{F(F+1) - I(I+1) - S(S+1)}{2} = \frac{F(F+1)}{2} - \frac{3}{4}. \end{aligned} \quad (2.5)$$

Here $F = 1$ and $F = 0$ corresponds to the two hyperfine states shown in Figure 2.1. Substituting this into the energy expression of Eq. 2.3, along with $|\psi(0)|^2$, and dropping the

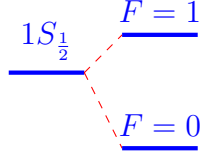


Figure 2.1: Hyperfine energy levels of the ground state in μp .

anomalous magnetic moment of the muon ($1 + a_\mu$), we obtain the total hyperfine splitting

$$E_{\text{HFS}}(F = 1) - E_{\text{HFS}}(F = 0) = \left[\frac{8Z\pi}{3}(1 + \kappa) \left(\frac{e^2}{4m_e^2} \right) \left(\frac{m_e^2}{m_\mu m_p} \right) \left(\frac{(Z\alpha)^3 m_\mu^3}{\pi} \right) \right] \left(\frac{1}{4} - \frac{-3}{4} \right),$$

$$E_{\text{HFS}}(1S) = \frac{8(Z\alpha)^4}{3}(1 + \kappa) \left(\frac{m_\mu^3}{m_\mu m_p} \right).$$
(2.6)

Replacing the muon mass with the reduced mass of the atom, $m_r = \frac{m_\mu m_p}{m_\mu + m_p}$, in the wave function $|\psi(0)|^2$, the hyperfine splitting becomes for the (1S) ground state

$$E_{\text{HFS}} = \frac{8}{3}(Z\alpha)^4(1 + \kappa) \left(\frac{m_\mu^2}{m_p} \right) \left(\frac{m_r}{m_\mu} \right)^3,$$
(2.7)

which simplifies to the well-known Fermi energy formula

$$E_F = \frac{8}{3}(Z\alpha)^4(1 + \kappa) \left(\frac{m_p}{m_p + m_\mu} \right)^3.$$
(2.8)

For numerical evaluations of the various terms discussed in this chapter, we use the values listed in Table. 2.1, which are derived from the most recent CODATA compilation [34].

Quantity	Symbol	Numerical Value	Unit
Fine structure constant	α	$7.2973525643(11) \times 10^{-3}$	
Proton magnetic moment to nuclear magneton ratio	$2(1 + \kappa)$	2.79284734463(82)	
Muon mass	m_μ	105.6583755(23)	MeV
Electron mass	m_e	0.51099895069(16)	MeV
Proton mass	m_p	938.27208943(29)	MeV

Table 2.1: Physical constants used in this thesis.

2.3 Definition of corrections and the framework for their calculation

We follow the formalism presented in [35] to structure the contributions to the hyperfine splitting as

$$\Delta E_{HFS} = E_F \left(1 + \delta_{\text{rel}} + \delta_{\text{QED}} + \delta_{\text{rad-recoil}} + \delta_{\text{struc}} \right), \quad (2.9)$$

where the electrodynamic corrections are expressed in terms of powers of the parameters, $\alpha, Z\alpha, \frac{m_\mu}{m_p}$.

The different corrections contributing to the hyperfine splitting are summarized below:

1. Relativistic corrections δ_{rel} : These corrections depend on the binding parameter $Z\alpha$, which arises due to the nature of the Coulomb problem.
2. Radiative non-recoil or loop corrections δ_{QED} : These corrections, also known as loop corrections, address the quantized field contributions. They depend on $\alpha, Z\alpha$, and $\ln(Z\alpha)$. Calculated within the framework of quantum electrodynamics (QED), they do not account for the two-body nature of the bound state problem and are independent of $\frac{m_\mu}{m_p}$.
3. Radiative recoil corrections $\delta_{\text{rad-recoil}}$: These arise from the interplay between the two-body relativistic system and radiative loops. They depend on $\frac{m_\mu}{m_p}, \ln(\alpha)$, and $Z\alpha$.
4. Proton structure contribution δ_{struc} : These corrections reflect the composite nature of the proton, accounting for its charge and magnetization distribution, as well as its polarizability.

The corrections are systematically calculated by sequentially applying specific limits where the expansions described above are valid:

- Nonrelativistic limit: Begin with the non-relativistic assumption, yielding Eq. 2.8.
- Point proton and infinite proton mass approximation: Assume $\lim r_p \rightarrow 0$ and $\lim m_p \rightarrow \infty$, which allows the calculation of δ_{QED} .
- Point proton approximation: Next, assume $\lim r_p \rightarrow 0$ to calculate $\delta_{\text{rad-recoil}}$.

- Finite size effects: Finally, incorporate the finite size of the proton to account for δ_{struc} .

2.3.1 Relativistic corrections

The Schrödinger equation is insufficient for calculating relativistic corrections. Instead, the Dirac-Coulomb wave function must be used for this purpose. To account for all binding corrections, including the Fermi energy, one considers the interaction Hamiltonian describing the muon's interaction with the external vector potential: $\mathbf{A} = \frac{\nabla \times \boldsymbol{\mu}_p}{(4\pi r)}$, which is created by the proton's magnetic moment, μ_p [36]. The matrix element for this interaction is then computed using the Dirac-Coulomb wave function as:

$$\langle nlf | \gamma_0 \boldsymbol{\gamma} \cdot \mathbf{A} | nlf \rangle, \quad (2.10)$$

where the Dirac wave function can be approximated as a product of the Schrödinger-Coulomb wave functions (dependent on the reduced mass m_r), and the free muon spinors (functions of the muon mass m_μ).

The relativistic corrections were first derived by Breit [37]. The result, as quoted in [36], is

$$\Delta E_{Br} = \left[1 + \frac{3}{2}(Z\alpha)^2 + \frac{17}{8}(Z\alpha)^4 + \dots \right] E_F. \quad (2.11)$$

It is important to note that the relativistic corrections calculated by Breit are not entirely accurate, as they neglect recoil effects. These recoil corrections will be addressed later in the discussion of radiative-recoil contributions.

2.4 Radiative non-recoil corrections

2.4.1 The muon anomalous magnetic moment

Radiative corrections cause the muon to develop form factors, deviating from the behavior of an ideal point-like Dirac particle. This deviation is evident in the anomalous magnetic moment, which has been observed experimentally [38]. The lowest-order correction arises from the second-order electromagnetic self-energy of the muon, represented by the diagram

in 2.6, as calculated by [39]. In this calculation, the muon behaves as a point dipole, resulting in a correction of $\frac{\alpha}{2\pi}E_F$.

The full corrections to the muon anomalous magnetic moment have been determined from the recent experimental average of the Fermilab and Brookhaven experiments [38]

$$a_\mu = 116592055(24) \times 10^{-11}. \quad (2.12)$$

This value contributes to the formula for the hyperfine splitting, expressed as

$$\Delta E_{a_\mu} = a_\mu E_F. \quad (2.13)$$

2.4.2 Vacuum polarization corrections

The electron-loop vacuum polarization gives rise to virtual electron-positron pairs at a characteristic momentum of approximately m_e . The spatial distribution where this polarization insertion occurs is of the order $\frac{1}{m_e}$, while the Bohr radius of muonic hydrogen is $\frac{1}{Z\alpha m_\mu} \approx \frac{137}{207m_e}$. Consequently, the external potential of the nucleus is distorted by the potential induced by vacuum polarization, which also modifies the wave function at the origin.

In comparison to normal hydrogen, the vacuum polarization correction to HFS in muonic hydrogen is significantly enhanced. While it appears on the order of $(\alpha Z\alpha)E_F$ in normal hydrogen, it is on the order of αE_F in muonic hydrogen. This enhancement, a factor of $Z\alpha$, can be qualitatively understood by considering the smaller length scale of muonic hydrogen compared to the Compton wavelength of the electron.

The contribution from the first-order vacuum polarization potential can be estimated by evaluating its expectation value, as expressed by Sternheim in [35]. This is done in terms of powers of the external potential (A_ν^e):

$$\langle A_\nu^{\text{vP}} \rangle \sim \alpha \frac{\eta^2}{m_e^2 + \eta^2} \langle A_\nu^e \rangle \sim \alpha \langle A_\nu^e \rangle, \quad (2.14)$$

where $\eta = Z\alpha\mu$. The enhancement factor, $(\frac{m_e}{Z\alpha\mu})$, clearly illustrates the scale of the correction.

2.4.2.1 Contributions of order $\frac{\alpha}{\pi}E_F$

The contributions of order $\frac{\alpha}{\pi}E_F$ arise primarily from the one-loop electron vacuum polarization (eVP), represented by the Uehling potential $V_U(\mathbf{r})$, which is detailed in Appendix 2.A. This correction is associated with the modified photon propagator shown in Fig. 2.A.1 and described by Eq. 2.91.

The first contribution, represented by the diagram in Fig. 2.2(a), originates from the insertion of the one-loop eVP into the exchanged photon in the hyperfine splitting, which modifies the magnetic interaction. Throughout the discussion of the eVP corrections of orders $\frac{\alpha}{\pi}, \frac{\alpha^2}{\pi^2}$, individual contributions are labeled using the subscript $C_{i,j}$, where i indicates the order of α , and j differentiates between contributions within the same order.

The energy shift due to this contribution, in coordinate space, is given by [35] and [40]

$$\begin{aligned} \Delta E_{C_{1.1}} = & -\frac{g_p}{4m_p m_r} \left(\frac{\alpha^2}{\pi} \right) \int_0^1 dv \frac{v^2 (1 - \frac{1}{3}v^2)}{(1 - v^2)} \\ & \times \int d^3r \phi_c^* [(\mathbf{S} \times \nabla \cdot \mathbf{I} \times \nabla) \\ & \times \frac{1}{r} \exp(-\lambda r)] \phi_c, \end{aligned} \quad (2.15)$$

where $\lambda = \frac{2m_e}{\sqrt{1-v^2}}$. The ∇ operator acts only upon the terms within the square bracket. The Coulomb wave function for the ground state is $\phi_c = (\beta^3/\pi)^{1/2} \exp(-\beta r)\chi$, where $\beta = Z\alpha m_r$ and χ is a normalised spinor. The analytical result derived in [41], can be expressed as

$$\Delta E_{C_{1.1}} = \frac{\alpha}{\pi} E_F R_{C_{1.1}}(nl), \quad (2.16)$$

where $R_{C_{1.1}}(1S)$ is given by

$$R_{C_{1.1}}(1S) = -\frac{\pi}{3\kappa_1^3} + \frac{\kappa_1^2 + 6}{9\kappa_1^2} + \frac{2\kappa_1^4 - \kappa_1^2 + 2 \arccos \kappa_1}{3\kappa_1^3 \sqrt{1 - \kappa_1^2}}, \quad (2.17)$$

and $\kappa_1 = \frac{Z\alpha m_r}{m_e}$.

The electronic vacuum polarization potential modifies the wave function at the origin due to the polarization insertion into the Coulomb photon, as shown in Fig. 2.2(b). This results in



Figure 2.2: Vacuum polarization corrections to the hyperfine splitting at first order. Diagram (a) illustrates the correction arising from the one-loop polarization insertion into the exchanged photon. Diagram (b) depicts the first-order correction to the wave function at the origin. The double line represents the non-relativistic reduced Green's function for a muon bound to a proton in a Coulomb field.

a correction of the order $\frac{\alpha}{\pi} E_F$. The correction is obtained using second-order nonrelativistic perturbation theory, where the general expression for the wave function correction is given by [42]

$$|\Delta\phi_{ns}\rangle = \sum_{n' \neq n} \frac{\langle \phi_{ns} | V_{VP} | \phi_{n's} \rangle}{E_n - E_{n'}} |\phi_{n's}\rangle, \quad (2.18)$$

where V_{VP} is the electronic vacuum polarization potential. At first order in α , only the one-loop Uehling potential V_U is included. This correction can be interpreted as a first-order adjustment in the contact term of the wave function due to the Uehling potential, represented as $\langle \delta\phi_U | A\delta(r) | \phi_C \rangle$, where ϕ_C is the Coulomb wave function.

The matrix element includes the one-loop Uehling potential and sums over intermediate states, which, for the Coulomb potential, are represented by the reduced Coulomb-Green's function $\bar{G}_{ns}(\mathbf{r}', \mathbf{r}; E_{ns})$. The energy correction is expressed as [43, 44]

$$\Delta E[\Delta\phi_{ns}(0)] = \left\langle \phi_{ns} \left| \delta(\mathbf{r}) \bar{G}_{ns}(\mathbf{r}', \mathbf{r}; E_{ns}) V_U \right| \phi_{ns} \right\rangle, \quad (2.19)$$

and it is calculated through the following integral

$$\frac{\Delta |\phi_{ns}(0)|^2}{|\phi_{ns}(0)|^2} = 2 \int d^3r \bar{G}_{ns}(0, \mathbf{r}; E_{ns}) V_U(\mathbf{r}) \phi_{ns}(\mathbf{r}), \quad (2.20)$$

where the reduced Coulomb-Green's function is given by [45]

$$\bar{G}_{ns}(0, \mathbf{r}; E_{ns}) = \sum_{n' \neq n} \frac{|\phi_{n's}\rangle \langle \phi_{n's}|}{E_{ns} - E_{n's}}. \quad (2.21)$$

The result is given by [41]

$$\Delta E_{\mathbf{C}_{1.2}} = \frac{\alpha}{\pi} E_F (R_{\mathbf{C}_{1.2}}(1S)), \quad (2.22)$$

where the analytical formula for $R_{\mathbf{C}_{1.2}}(1S)$ is provided in [41]

$$R_{\mathbf{C}_{1.2}}(1S) = \pi \frac{\kappa_1^2 - 2}{2\kappa_1^3} - \frac{5\kappa_1^4 - 8\kappa_1^2 + 6}{3\kappa_1^2(\kappa_1^2 - 1)} + \frac{2\kappa_1^6 - 3\kappa_1^4 + 4\kappa_1^2 - 2 \arccos \kappa_1}{\kappa_1^3(\kappa_1^2 - 1)} \frac{1}{\sqrt{1 - \kappa_1^2}} + J(\kappa_1), \quad (2.23)$$

and $J(\kappa_1) = -\frac{2\kappa_1^2}{3} \int_0^1 dy \frac{y\sqrt{1-y^2}(y^2+2)}{(1+\kappa_1 y)^2} \log \frac{\kappa_1 y}{1+\kappa_1 y}$.

The total first-order correction in $\frac{\alpha}{\pi} E_F$ is composed of the following contributions:

$$\begin{aligned} \Delta E_{\mathbf{C}_{1.1}} &= 0.883041 \frac{\alpha}{\pi} E_F = 374.217689(14) \mu eV, \\ \Delta E_{\mathbf{C}_{1.2}} &= 1.731152 \frac{\alpha}{\pi} E_F = 733.632641(27) \mu eV. \end{aligned} \quad (2.24)$$

The uncertainties come from the fine structure constant α . This agrees with Sternheim's value for the sum of the two contributions, $2.5376 \frac{\alpha}{\pi} E_F$ [35].

2.4.2.2 Contributions of order $\left(\frac{\alpha}{\pi}\right)^2 E_F$

The first type of corrections to the hyperfine splitting at the order $\left(\frac{\alpha}{\pi}\right)^2 E_F$ originates from two sources. These are the reducible two one-loop and the irreducible two-loop polarization insertions into the magnetic interaction between the muon and the proton. They are associated with the Uehling and Källén–Sabry potentials, described by the diagrams in Fig. 2.A.2(b) and Fig. 2.B.3 (Appendices. 2.B, 2.A).

The corresponding corrections are represented by the diagrams in Figs. 2.3(a) and 2.3(b). These are calculated similarly to Eq. 2.15, with $V_U(\mathbf{r})$ replaced by the potentials $V_U(\mathbf{r})_{1.1}, V_{KS}^{(2)}(\mathbf{r})$, as defined in Eqs. 2.93 and 2.94. The resulting integrals are evaluated numerically in [46], yielding

$$\begin{aligned} \Delta E_{\mathbf{C}_{2.1}} &= \left(\frac{\alpha}{\pi}\right)^2 E_F (1.28028) = 1.2602 \mu eV, \\ \Delta E_{\mathbf{C}_{2.2}} &= \left(\frac{\alpha}{\pi}\right)^2 E_F (1.68287) = 1.6565 \mu eV. \end{aligned} \quad (2.25)$$

Here, $\Delta E_{\mathbf{C}_{2.1}}, \Delta E_{\mathbf{C}_{2.2}}$ correspond to the corrections due to the diagrams in Fig. 2.3(a) and Fig. 2.3(b), respectively.

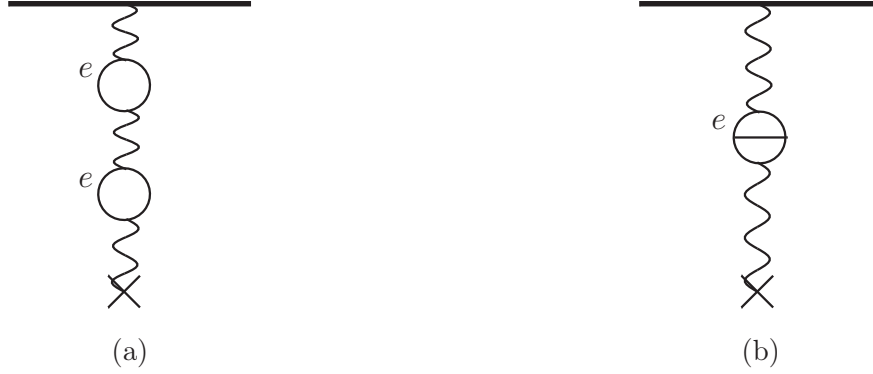


Figure 2.3: Second-order vacuum polarization corrections to the hyperfine interaction. (a) Reducible two one-loop polarization insertion (b) The one loop irreducible polarization insertion.

Corrections to the wave function at the origin at order $(\frac{\alpha}{\pi})^2 E_F$ are calculated as follow:

1. Second-order vacuum polarization contributions:

These corrections involve the potentials $V_U(\mathbf{r})_{1,1}, V_{KS}^{(2)}(\mathbf{r})$, encompassing both the reducible and irreducible second-order vacuum polarization, respectively. The corrections $\Delta E_{C_{2,3}}$ and $\Delta E_{C_{2,4}}$ are illustrated in Figs. 2.4(a), 2.4(b). They are computed by replacing the vacuum polarization potential $V_U(\mathbf{r})$ in Eq. 2.19 with $V_U(\mathbf{r})_{1,1}, V_{KS}^{(2)}(\mathbf{r})$, respectively. The numerical results from [46, 47] are

$$\begin{aligned} \Delta E_{C_{2,3}} &= 1.85512 \left(\frac{\alpha}{\pi}\right)^2 E_F = 1.8261 \mu eV, \\ \Delta E_{C_{2,4}} &= 3.79665 \left(\frac{\alpha}{\pi}\right)^2 E_F = 3.7373 \mu eV. \end{aligned} \quad (2.26)$$

2. Third-order perturbative contributions:

These terms involve quadratic corrections in the contact term $\delta(r)$, considering only the Uehling potential. The third-order corrections are computed as [48]

$$\begin{aligned} \Delta E_{\text{hfs}}^{(3,eVP)}(1S) &= \langle \Phi_{1S}(\mathbf{r}) | \delta V(\mathbf{r}) \tilde{G}(\mathbf{r}, \mathbf{r}') [\delta V(\mathbf{r}') - \delta E_{1S}^{(1)}] \\ &\quad \times \tilde{G}(\mathbf{r}', \mathbf{r}'') \delta V(\mathbf{r}'') | \Phi_{1S}(\mathbf{r}'') \rangle, \end{aligned} \quad (2.27)$$

where $\Delta E_{\text{hfs}}^{(3,eVP)}(1S)$ denotes third-order electronic vacuum polarization corrections. The term $\delta V(\mathbf{r})$ represents a combination of the Uehling potential and the contact

term. The factor $[\delta V(\mathbf{r}') - \delta E_{1S}^{(1)}]$ ensures proper renormalization of the wave function. The contributions are illustrated in Figs. 2.5(a) and 2.5(b). The numerical results, as calculated in [46, 47], are

$$\begin{aligned}\Delta E_{\mathbf{C}_{2.5}} &= 0.92294 \left(\frac{\alpha}{\pi}\right)^2 E_F = 0.9085 \mu\text{eV}, \\ \Delta E_{\mathbf{C}_{2.6}} &= 0.68104 \left(\frac{\alpha}{\pi}\right)^2 E_F = 0.6703 \mu\text{eV}.\end{aligned}\tag{2.28}$$

The final missing contribution in this order is represented by the diagram in Fig. 2.5(c) and is given by [46]

$$\Delta E_{\mathbf{C}_{2.7}} = 2.32694 \left(\frac{\alpha}{\pi}\right)^2 E_F = 2.2905 \mu\text{eV} .\tag{2.29}$$



Figure 2.4: Second-order vacuum polarization corrections to the wave function at the origin resulting from: (a) the reducible two one-loop polarization potential and (b) the irreducible two-loop Källén–Sabry potential.

The total contribution from electronic vacuum polarization at order $\left(\frac{\alpha^2}{\pi^2}\right)^2 E_F$ is given by

$$\Delta E_{\left(\frac{\alpha}{\pi}\right)^2}^{(eVP)}(1S) = \sum_n \left(\frac{\alpha^2}{\pi^2} \mathbf{C}_2(n)\right) (1 + a_\mu) E_{\text{hfs}}^{(0)}(1S).\tag{2.30}$$

The numerical evaluation of this expression yields a total value of $12.3641 \mu\text{eV}$.

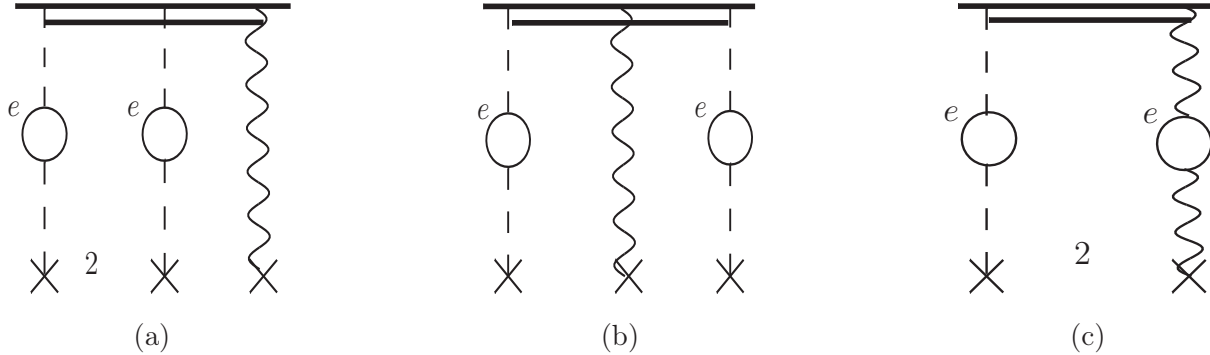


Figure 2.5: Second-order vacuum polarization corrections to the wave function at the origin, arising from the quadratic inclusion of the Uehling potential.

2.4.3 Radiative binding non-recoil corrections

Radiative binding corrections, calculated within the framework of QED, account for electromagnetic interaction in bound systems like muonic hydrogen. In the bound-state interaction picture, also known as the Furry picture, the nucleus is treated as an external potential that modifies the lepton (muon) field operator and the Green's function of the Dirac equation. The eigenstates in this formalism are those of the bound system [49]. These corrections arise from the interplay between the lepton field and the quantized electromagnetic field, involving processes such as the emission and absorption of real or virtual photons, as well as vacuum polarization effects.

Under the external field approximation, where the proton is assumed to have an infinitely large mass, recoil effects are negligible. In this approximation, the proton acts as a static external potential, and radiative corrections derived for hydrogen-like systems are applicable to muonic hydrogen. Contributions include radiative insertions in the muon line and the photon propagator exchanged between the muon and proton. They involve factors of $\frac{\alpha}{\pi}$, the binding parameter $Z\alpha$, and their first and second-order combinations along with logarithmic contributions at second order, which provide sufficient accuracy in the non-recoil limit.

Radiative corrections have been extensively studied using various approaches. The Bethe-Salpeter formalism was applied by Kroll et al. [50] and Brodsky [51], while Lepage's non-relativistic QED formulation for loosely bound systems was employed by Kinoshita et al. [52]. Pachucki introduced an alternative method in [53], which separates energy scales to compute different contributions at these scales.

2.4.3.1 Radiative binding corrections of order $\alpha(Z\alpha)$

The corrections in the order $\alpha(Z\alpha)$ arise from the second-order electromagnetic self-energy of a Dirac particle moving in a static external magnetic field. They are represented by the diagrams in Fig. 2.6 and 2.7 which include polarization insertions in the transverse photon of order $\alpha(Z\alpha)$. These corrections were fully calculated by Kroll and Pollock in [50], with extensions provided in [39]. The polarization potential consists of two components: the Coulomb part and the magnetic part. While the Coulomb part does not affect the nuclear moment, the magnetic part varies linearly with it. Since the magnetic part modifies the nuclear magnetic field, it directly influences the hyperfine splitting. Moreover, lower energy hyperfine states are more tightly bound and spend more time in regions where the Coulomb polarization potential is stronger, contributing to the overall correction. The contribution from the muonic vacuum polarization was first calculated in [50] to be

$$\Delta E_{\mu\text{VP}}^{\alpha(Z\alpha)} = \frac{3}{4}\alpha(Z\alpha)E_F. \quad (2.31)$$

Another component of the correction arises from the interaction of the Dirac propagator, both linearly and quadratically, with the external potential (proton potential in this case). This includes a mass renormalization contribution shown in Fig. 2.6(b), which is canceled by a mass-like term from Fig. 2.6(a). This cancellation results in a correction stemming from the anomalous magnetic moment at order α . At order $\alpha(Z\alpha)$, the correction from the muon self-energy is

$$\Delta E_{\mu\text{SE}}^{\alpha(Z\alpha)} = \left(\ln(2) - \frac{13}{4}\right)\alpha(Z\alpha)E_F. \quad (2.32)$$

The total corrections at this order are evaluated as: $(\ln(2) - \frac{5}{2})\alpha(Z\alpha)E_F$ [54].

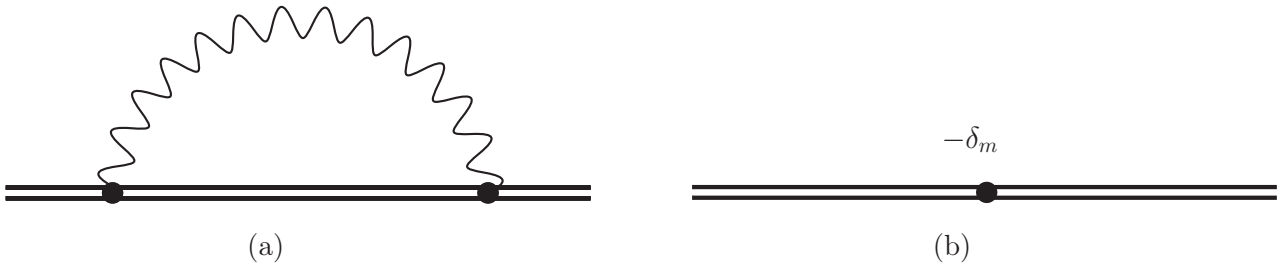


Figure 2.6: The muon self energy. (a) Radiative insertion into the muon line. (b) Mass renormalization term.

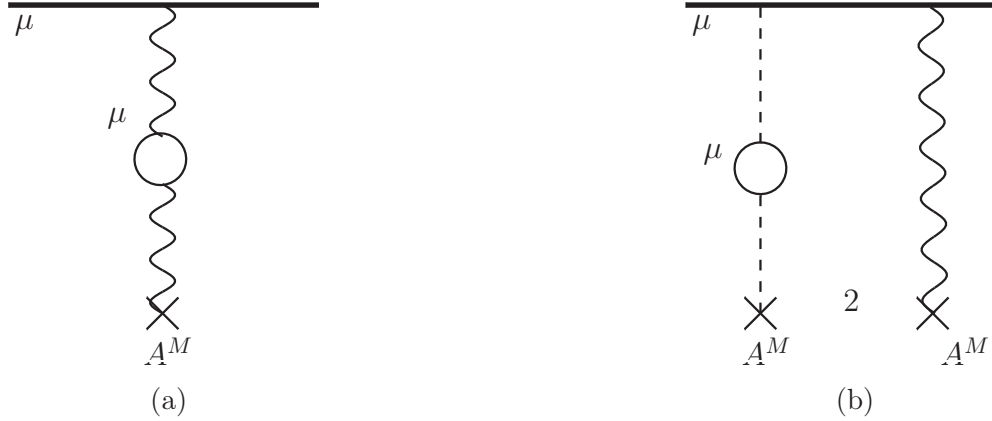


Figure 2.7: One-loop muonic vacuum polarization: (a) polarization insertion into the hyperfine interaction, and (b) one-loop polarization correction to the wave function. A^M represents the proton anomalous magnetic moment.

2.4.4 Next-to-leading order muon self-energy and muon vacuum polarization

Here, we list the two-loop non-recoil radiative corrections of order $\frac{\alpha^2}{\pi}(Z\alpha)$, shown in Fig. 2.8, which can be divided into six gauge invariant sets of diagrams:

(a) Two one-loop μ VP insertions [55, 56]:

$$\Delta E_{\mu\text{VP(a)}}^{\text{NLO}} = \frac{36}{35} \frac{\alpha^2(Z\alpha)}{\pi} E_F. \quad (2.33)$$

(b) One irreducible two-loop μ VP insertion [55, 56]:

$$\Delta E_{\mu\text{VP(b)}}^{\text{NLO}} = \left(\frac{224}{15} \ln 2 - \frac{38}{15} \pi - \frac{118}{225} \right) \frac{\alpha^2(Z\alpha)}{\pi} E_F. \quad (2.34)$$

(c) One-loop μ SE correction and μ VP insertion in the two photon skeleton diagram [36]:

$$\begin{aligned} \Delta E_{\mu\text{SE}+\mu\text{VP(c)}}^{\text{NLO}} = & \left(-\frac{4}{3} \ln^2 \frac{1+\sqrt{5}}{2} - \frac{64}{45} \ln 2 \right. \\ & - \frac{20}{9} \sqrt{5} \ln \frac{1+\sqrt{5}}{2} \\ & \left. + \frac{\pi^2}{9} + \frac{3}{8} + \frac{1043}{675} \right) \frac{\alpha^2(Z\alpha)}{\pi} E_F. \end{aligned} \quad (2.35)$$

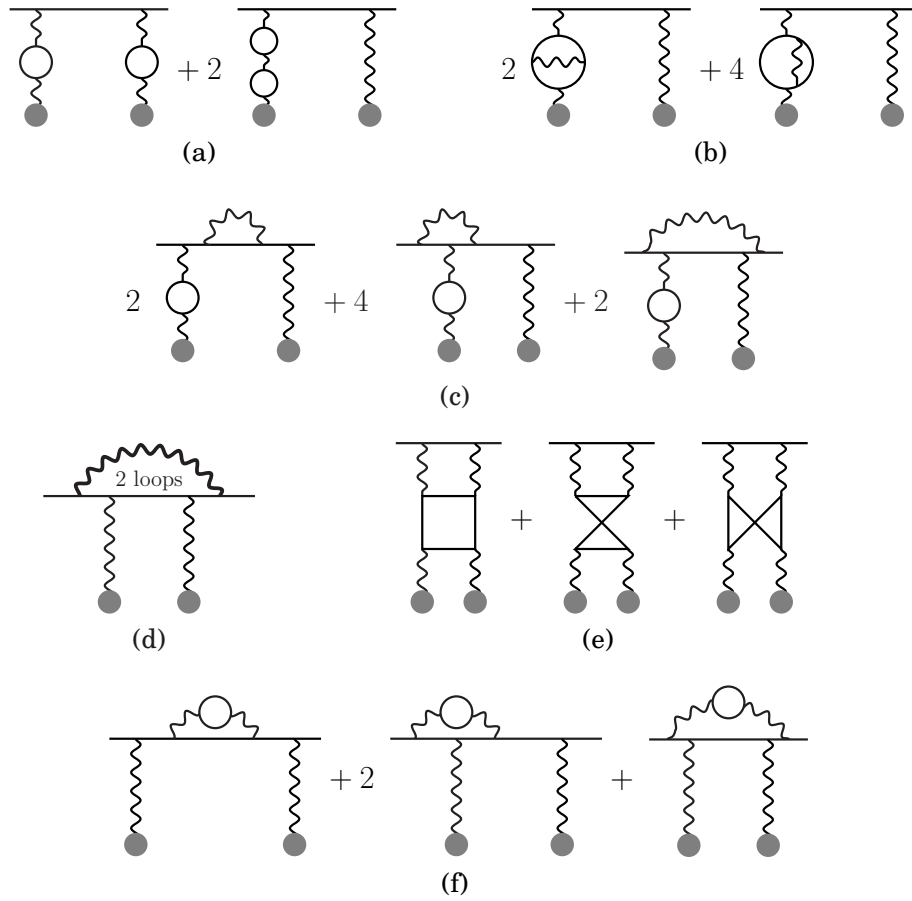


Figure 2.8: Six gauge invariant sets of diagrams for corrections of order $\frac{\alpha^2}{\pi}(Z\alpha)$.

(d) Two-loop μ SE correction [52]:

$$\Delta E_{\mu\text{SE(d)}}^{\text{NLO}} = 0.6764(79) \frac{\alpha^2(Z\alpha)}{\pi} E_F. \quad (2.36)$$

(e) Light-by-light μ VP [57]:

$$\Delta E_{\mu\text{VPLbL(e)}}^{\text{NLO}} = -0.472514(1) \frac{\alpha^2(Z\alpha)}{\pi} E_F. \quad (2.37)$$

(f) One-loop μ SE correction with internal μ VP insertion [58, 59]:

$$\Delta E_{\mu\text{SE with } \mu\text{VP(f)}}^{\text{NLO}} = -0.310742\dots \frac{\alpha^2(Z\alpha)}{\pi} E_F. \quad (2.38)$$

2.4.4.1 Non-logarithmic corrections of order $\alpha(Z\alpha)^2$

The first extended calculation of higher order $\alpha(Z\alpha)^2$ radiative corrections was conducted by Brodsky in [51]. However, later studies identified errors in the nonlogarithmic part of Brodsky's contributions. Schneider et.al. [60] revised the vacuum polarization contribution to order $\alpha(Z\alpha)^2$, finding it to be $-\frac{4}{5}\frac{\alpha}{\pi}(Z\alpha)^2$, which differs from Brodsky's earlier result of $-\frac{2}{3}\frac{\alpha}{\pi}(Z\alpha)^2$. This correction was subsequently confirmed numerically by Kinoshita [61]. The vacuum polarization contribution is quoted as:

$$\begin{aligned} & \frac{\alpha(Z\alpha)^2}{\pi} E_F \left[-\frac{8}{15} \ln 2 + \frac{214}{225} - \frac{4}{5} \right] \\ & \frac{\alpha(Z\alpha)^2}{\pi}, E_F(-0.218567\dots). \end{aligned} \quad (2.39)$$

Additional corrections arise from the radiative photon contribution. These were calculated as $[17.1227(11) \alpha(Z\alpha)^2 E_F]$ by [61] and as $[17.122 \alpha(Z\alpha)^2 E_F]$ by Pachucki [53].

2.4.4.2 Logarithmic contributions of order $\alpha(Z\alpha)^2$

The logarithmic contributions to order $\alpha(Z\alpha)^2$ were first calculated by Brodsky [51]. Their value is given as:

$$\begin{aligned} & E_F \frac{\alpha(Z\alpha)^2}{\pi} \left[-\frac{8}{3} \ln^2(Z\alpha)^{-1} \right. \\ & \left. + \left(-\frac{8}{3} \ln 4 + \frac{37}{36} + \frac{8}{15} \right) \ln(Z\alpha)^{-1} \right]. \end{aligned} \quad (2.40)$$

For the total contribution at this order, we adopt the value from [61]

$$\begin{aligned} \Delta E_{rad}^{\alpha(Z\alpha)^2} = E_F \frac{\alpha(Z\alpha)^2}{\pi} & \left[-\frac{8}{3} \ln^2(Z\alpha)^{-1} \right. \\ & \left. + \left(-\frac{8}{3} \ln 4 + \frac{37}{36} + \frac{8}{15} \right) \ln(Z\alpha)^{-1} + 16.9042(11) \right]. \end{aligned} \quad (2.41)$$

2.5 Electroweak corrections

The contribution from the t -channel Z -boson exchange depicted in Fig. 2.9, was first evaluated by Beg and Feinberg [62]. The correction to the hyperfine splitting is expressed as [63]

$$\Delta E_{\text{weak}} = \frac{g_A}{2I + \kappa} \frac{G_F}{\sqrt{2}} \frac{3m_\mu m_p}{4\pi Z\alpha} E_F, \quad (2.42)$$

where g_A is the axial charge, G_F is the Fermi constant.

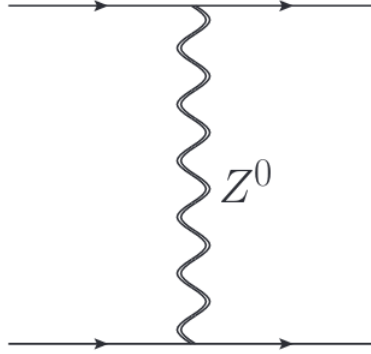


Figure 2.9: Weak interaction through the Z -boson exchange between the muon and the proton.

We evaluate this correction using g_A, G_F values from the Particle Data Group (PDG) [64]

$$\begin{aligned} g_A &= 1.2754(13), \\ G_F &= 1.1663788(6) \times 10^{-5} \text{GeV}^{-2}. \end{aligned} \quad (2.43)$$

The numerical result for the weak interaction contribution is

$$\Delta E_{\text{weak}} = 0.00223 \text{ meV}. \quad (2.44)$$

2.6 Hadronic vacuum polarization

The contribution from hadronic vacuum polarization (HVP) to the hyperfine splitting is given by [65]

$$\Delta E_{\text{HVP}}(1S) = 0.00356 \text{ meV}. \quad (2.45)$$

The uncertainty associated with this contribution is currently under investigation by Malaescu et.al.

2.7 Recoil corrections with proton anomalous magnetic moment

For recoil corrections including the proton anomalous magnetic moment, we use the expression from [66] (Eqs. 1.3 and 2.13), which are based on the earlier formulation in [67]

$$\begin{aligned} \Delta E_{\text{recoil}, \kappa}(1S) = & \left\{ \kappa \left(\frac{7}{4} \ln \frac{1}{2\alpha} - \ln 2 + \frac{31}{36} \right) \right. \\ & - \frac{\kappa}{1 + \kappa} \left(\frac{7}{4} \ln \frac{1}{2\alpha} - 4 \ln 2 + \frac{31}{8} \right) \\ & \left. + 2 \ln \frac{1}{2\alpha} - 6 \ln 2 + \frac{65}{18} \right\} \frac{m_\mu}{m_p} \alpha^2 E_F. \end{aligned} \quad (2.46)$$

2.8 Proton structure corrections

So far, we have treated the proton as a point-like nucleus with charge Ze . We now consider the effects arising from the internal structure of the proton. In muonic hydrogen, the muon exhibits an enhanced sensitivity to the proton structure and its short-range interactions. This is due to the overlap of the S-state wave function with the proton, which scales with the third power of the reduced mass of the system. Compared to regular hydrogen, muonic hydrogen exhibits an enhancement factor of approximately $(\frac{m_\mu}{m_e})^3 \approx 10^7$. For the hyperfine splitting, the structure contributions arise in the two-photon exchange at order $(Z\alpha) E_F$.

The forward two photon exchange diagram in Fig. 2.10 can be expressed in terms of

integrals over the spin dependent scalar amplitudes S_1, S_2 of the forward doubly-virtual Compton scattering (VVCS) on a nucleus [1, 68]

$$E_{nS^-}^{(2\gamma)} \text{HFS} = \frac{32\pi\alpha}{3m_p} \phi_{nS}^2(0) \int \frac{d^4q}{i(2\pi)^4} \frac{1}{Q^4 - 4m_\mu^2\nu^2} \left\{ \frac{(2Q^2 - \nu^2)}{Q^2} S_1(\nu, Q^2) + \frac{3\nu}{m_p} S_2(\nu, Q^2) \right\}, \quad (2.47)$$

where ν is the photon energy in the lab frame, and $q^2 = -Q^2$ is the photon virtuality. The amplitudes S_1, S_2 can be related to the empirical spin structure functions g_1 and g_2 through dispersion relations [1]

$$\left\{ \begin{array}{l} S_1(\nu, Q^2) \\ \frac{\nu}{m_p} S_2(\nu, Q^2) \end{array} \right\} = \frac{16\pi Z^2 \alpha m_p}{Q^2} \int_0^1 \frac{dx}{1 - x^2 (\nu/\nu_{\text{el}})^2 - i0^+} \left\{ \begin{array}{l} g_1(x, Q^2) \\ g_2(x, Q^2) \end{array} \right\}, \quad (2.48)$$

where $x = \frac{Q^2}{2m_p\nu}$ is the Bjorken variable, and $\nu_{\text{el}} = \frac{Q^2}{2m_p}$. The spin dependent structure functions $g_1(x, Q^2)$, $g_2(x, Q^2)$ can be obtained from scattering experiments of polarized electrons on polarized protons. These functions are expressed in terms of the virtual photon-absorption cross sections [69]

$$\begin{aligned} g_1(\nu, Q^2) &= \frac{m_p \cdot K}{8\pi^2\alpha (1 + Q^2/\nu^2)} \left[\sigma_{1/2}(\nu, Q^2) - \sigma_{3/2}(\nu, Q^2) + \frac{2\sqrt{Q^2}}{\nu} \sigma_{TL}(\nu, Q^2) \right], \\ g_2(\nu, Q^2) &= \frac{m_p \cdot K}{8\pi^2\alpha (1 + Q^2/\nu^2)} \left[-\sigma_{1/2}(\nu, Q^2) + \sigma_{3/2}(\nu, Q^2) + \frac{2\nu}{\sqrt{Q^2}} \sigma_{TL}(\nu, Q^2) \right], \end{aligned} \quad (2.49)$$

where $K = \frac{\nu - Q^2}{2m_p}$ is Hand kinematical flux factor for virtual photons. The terms $\sigma_{1/2}$, $\sigma_{3/2}$ represent the virtual photoabsorption cross sections corresponding to total helicities of $\frac{1}{2}$ and $\frac{3}{2}$, respectively, of the photon-nucleon system. The term σ_{TL} accounts for a cross section where the photon changes helicity and the nucleon undergoes a spin flip. For elastic scattering, the structure functions are given by [68]

$$\begin{aligned} g_1(\text{elastic}) &= \frac{1}{2} F_1 G_M \delta(1 - x), \\ g_2(\text{elastic}) &= -\frac{1}{2} \tau F_2 G_M \delta(1 - x), \end{aligned} \quad (2.50)$$

where $G_M(Q^2)$ and $G_E(Q^2)$ are the magnetic and the electric Sachs form factors, defined as:

$$\begin{aligned} G_M(Q^2) &= F_1(Q^2) + F_2(Q^2), \\ G_E(Q^2) &= F_1(Q^2) - \frac{Q^2}{4m_p^2} F_2(Q^2), \end{aligned} \quad (2.51)$$

and $F_1(Q^2), F_2(Q^2)$ are the Dirac and Pauli form factors, respectively, normalised as $F_1(0) = 1$ and $G_M(0) = 1 + \kappa$.

By combining Eq. 2.47, 2.48, and 2.49, then by substituting the elastic structure functions from Eq. 2.50 and then the inelastic structure functions from Eq. 2.49 separately, one can express the proton structure corrections to the hyperfine splitting as (see [1])

$$E_{1S\text{-HFS}}^{(2\gamma)} = E_F (\delta_Z + \delta_{\text{recoil}} + \delta_{\text{pol}}). \quad (2.52)$$

This result splits into three separate contributions. The Zemach term δ_Z and the recoil term δ_{recoil} arise when the nucleus in the intermediate state remains intact. These contributions are associated with the elastic two photon exchange diagrams shown in Figs. 2.10(a) and 2.10(b). The polarizability term δ_{pol} originates from the inelastic two photon exchange diagram shown in Fig. 2.10(c), where the nucleus in the intermediate state is excited. This contribution δ_{pol} can be expressed in terms of the inelastic spin-dependent structure functions $g_1(\nu, Q^2), g_2(\nu, Q^2)$, as well as the Pauli form factor $F_2(Q^2)$.

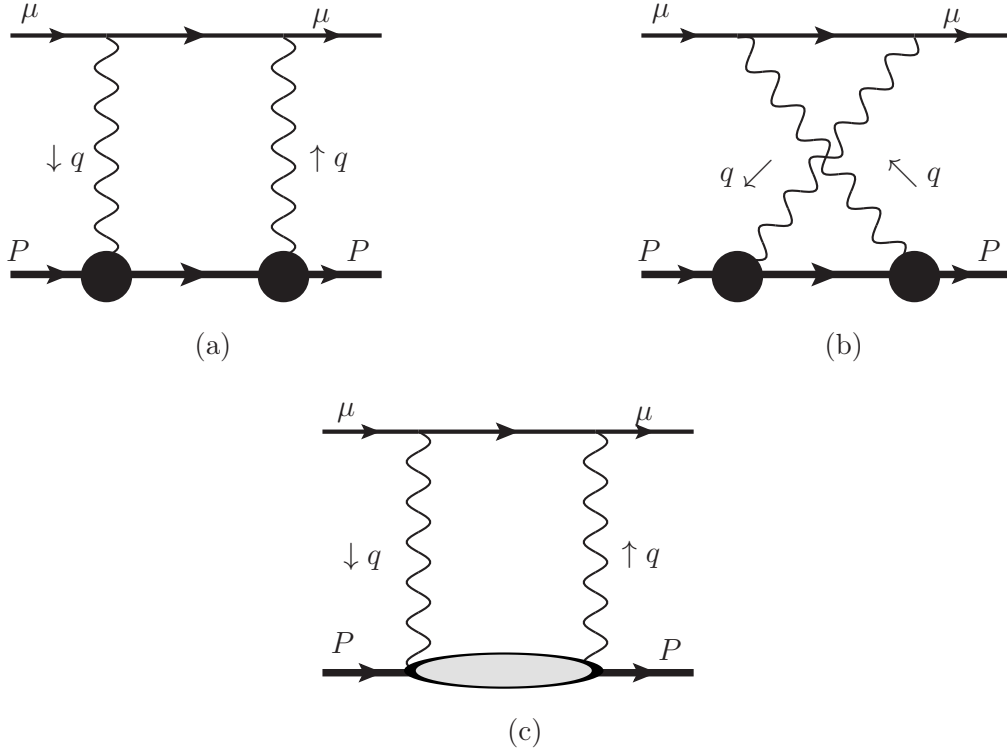


Figure 2.10: Two photon exchange diagrams: (a), (b) represent the elastic contributions to $2 - \gamma$ giving rise to $\delta_Z + \delta_{\text{recoil}}$. (c) represents the inelastic contribution to $2 - \gamma$, leading to the polarizability term δ_{pol} .

2.8.1 The finite size contribution

The finite-size contribution that is relevant for the HFS is a particular combination of electric and magnetic form factors, known as the Zemach contribution. This correction is expressed as [33]

$$\delta_Z = \frac{8(Z\alpha)m_r}{\pi} \int_0^\infty \frac{dQ}{Q^2} \left[\frac{G_E(Q^2) G_M(Q^2)}{1 + \kappa_N} - 1 \right] \equiv -2Z\alpha m_r r_Z, \quad (2.53)$$

where the (-1) term subtracts the lowest-order one-photon exchange contribution to avoid double counting. Here, r_Z is the Zemach radius, defined as [70]

$$r_Z = -\frac{4}{\pi} \int_0^\infty \frac{dQ}{Q^2} \left[\frac{G_E(Q^2) G_M(Q^2)}{1 + \kappa_N} - 1 \right]. \quad (2.54)$$

The Zemach radius can be determined using three different methods. The first method involves analyzing the electron-proton (e-p) scattering data to extract $G_E(Q^2)$, $G_M(Q^2)$ [71]. The second method compares the experimental and theoretical values of the hyperfine splitting in hydrogen, using the theoretical calculation of the polarizability contribution as an input [10, 11]. Similarly, the third method applies the same approach to the (2S) hyperfine splitting in muonic hydrogen, comparing experimental results with theoretical predictions [11].

The 2S-HFS measurement in muonic hydrogen was obtained from transitions between the 2S and 2P levels in μp with different hyperfine states. The limitation of this method arises eventually from the large 2P state lifetime [9]. Table 2.2 summarizes the values of the Zemach radius r_z extracted using the methods described above [11].

ep scattering		μp 2S HFS		H 1S HFS	
[33]	[71]	[9]	LOB χ PT [11]	[10]	LOB χ PT [11]
$1.054^{+0.003}_{-0.002}$	1.0227(107)	1.082(37)	1.040(33)	1.036(8)	1.010(9)

Table 2.2: Values of the Zemach radius r_Z in fm extracted using different methods. For μp and H, two r_Z values are given based on two values of δ_{pol} , one from the data-driven [9, 10] and the other is from chiral perturbation theory [11].

2.8.2 Recoil correction

The recoil correction is described using the electric and magnetic Sachs form factors, $G_E(Q^2)$, $G_M(Q^2)$, along with the Dirac and Pauli form factors, $F_1(Q^2)$, $F_2(Q^2)$ [72]. It is expressed as

$$\delta_{\text{recoil}} = \frac{Z\alpha}{\pi(1+\kappa)} \int_0^\infty \frac{dQ}{Q} \left\{ \frac{G_M(Q^2)}{Q^2} \frac{8mM}{\nu_l + \nu} \left(2F_1(Q^2) + \frac{F_1(Q^2) + 3F_2(Q^2)}{(\nu_l + 1)(\nu + 1)} \right) - \frac{8m_r G_M(Q^2) G_E(Q^2)}{Q} - \frac{mF_2^2(Q^2)}{M} \frac{5 + 4\nu_l}{(1 + \nu_l)^2} \right\}. \quad (2.55)$$

Specifically speaking, it is a recoil correction to the Zemach contribution. On the other hand, the polarizability contribution is calculated from the Compton scattering amplitude while considering the finite proton mass. Within this framework, recoil corrections to the polarizability contribution are unnecessary. A recent dispersive analysis of the world data of the nucleon form factors has provided a high precision evaluation of the recoil correction, given by [72]

$$\delta_{\text{recoil}} = (837.6_{-1.0}^{+2.8}) \text{ ppm}. \quad (2.56)$$

2.8.3 The polarizability contribution

The polarizability contribution arises from the diagram 2.10(c), which represents the excited intermediate nucleus states i.e (Δ – isobar, pion-nucleon, and others). There exist two methods to evaluate this contribution. The first is the data-driven approach utilizing measured structure functions from scattering experiments [68]. The second is the calculation of the VVCS amplitudes using chiral perturbation theory ($B\chi\text{PT}$) [11].

In the data-driven approach, a dispersive framework is employed to connect the scalar VVCS amplitudes S_1, S_2 with the proton spin-dependent structure functions $g_i(x, Q^2)$. The polarizability contribution in this framework is typically divided into two terms

$$\delta_{\text{pol}} = \Delta_1 + \Delta_2 = \frac{Z\alpha m_\mu}{2\pi(1+\kappa)m_p} [\delta_1 + \delta_2], \quad (2.57)$$

where δ_1, δ_2 are expressed as

$$\delta_1 = 2 \int_0^\infty \frac{dQ}{Q} \left(\frac{5 + 4\nu_l}{(\nu_l + 1)^2} \left[4I_1(Q^2) / Z^2 + F_2^2(Q^2) \right] - \frac{32m_p^4}{Q^4} \int_0^{x_0} dx x^2 g_1(x, Q^2) \right. \\ \left. \left\{ \frac{1}{(\nu_l + \nu_x)(1 + \nu_x)(1 + \nu_l)} \left[4 + \frac{1}{1 + \nu_x} + \frac{1}{\nu_l + 1} \right] \right\} \right), \quad (2.58)$$

$$\delta_2 = 96m_p^2 \int_0^\infty \frac{dQ}{Q^3} \int_0^{x_0} dx g_2(x, Q^2) \frac{1 - \nu_x}{(1 + \nu_l)(\nu_l + \nu_x)}.$$

This approach relies on experimental data for the spin-dependent structure functions g_1, g_2 obtained from $e - p$ scattering experiments. Several earlier evaluations of the polarizability contribution using this method were conducted by Carlson et al. [68] and Tomalak [73]. The most recent evaluation is provided by Ruth et.al. [10], yielding

$$\delta_{\text{pol}}(\text{dispersive}) = 200.6(52.4) \text{ ppm}. \quad (2.59)$$

The other approach to calculate the polarizability contribution is using baryon chiral perturbation theory (B χ PT). To discuss this approach we need to introduce the relation between the Born and the non-Born amplitudes of S_1 and S_2 . The non-Born amplitudes \bar{S}_1 and \bar{S}_2 are related to the VVCS scalar amplitudes S_1 and S_2 by

$$S_1(\nu, Q^2) = S_1^{\text{Born}}(\nu, Q^2) + \bar{S}_1(\nu, Q^2), \quad (2.60)$$

$$S_2(\nu, Q^2) = S_2^{\text{Born}}(\nu, Q^2) + \bar{S}_2(\nu, Q^2),$$

where $S_1^{\text{Born}}, S_2^{\text{Born}}$ correspond to the simple tree-level diagram that result into the elastic $2 - \gamma$ exchange. The non-Born amplitudes \bar{S}_1 and \bar{S}_2 account for all other contributions. Unlike the dispersive approach, B χ PT allows direct calculation of $\bar{S}_1(\nu, Q^2)$ and $\bar{S}_2(\nu, Q^2)$ without requiring a dispersive relation.

The most recent evaluation of the polarizability contribution using B χ PT is given by [11]

$$\delta_{\text{pol}}(\text{B}\chi\text{PT}) = 37(62) \text{ ppm}. \quad (2.61)$$

The total value of the two photon exchange contribution from [11] is:

$$\Delta E_{1S-\text{HFS}}^{(2\gamma)} = -1.1348(162) \text{ meV}. \quad (2.62)$$

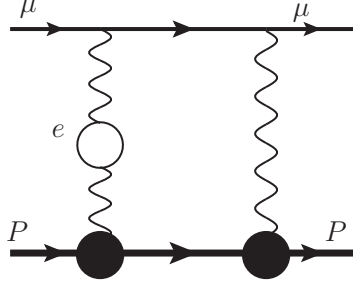


Figure 2.11: One loop electronic vacuum polarization insertion into the elastic two photon exchange.

2.8.4 Radiative corrections to the two photon exchange

Following [1], the radiative corrections to the elastic two photon exchange are expressed as

$$E_{1S\text{-HFS}}^{(\text{el})} = E_F \left[\left(1 + \frac{\alpha}{\pi} R_{\mathbf{C}_{1,2}} + \sum_i \Delta_Z^{\text{rad},i} \right) \delta_Z + \left(1 + \frac{\alpha}{\pi} R_{\mathbf{C}_{1,2}} + \sum_i \Delta_{\text{recoil}}^{\text{rad},i} \right) \delta_{\text{recoil}} \right]. \quad (2.63)$$

Here, $\frac{\alpha}{\pi} R_{\mathbf{C}_{1,2}} E_F$ represents the wave function correction at the origin, previously defined in Eq. 2.22. The terms $\Delta_Z^{\text{rad},i}$, $\Delta_{\text{recoil}}^{\text{rad},i}$ capture additional radiative corrections to the elastic two photon exchange.

The one loop electronic vacuum polarization insertion into the elastic two photon exchange depicted in Fig. 2.11 was calculated using empirical proton form factors [1], yielding

$$\begin{aligned} \Delta_Z^{\text{eVP}} &= 0.01846(13), \\ \Delta_{\text{recoil}}^{\text{eVP}} &= 0.01254(4). \end{aligned} \quad (2.64)$$

This result for Δ_Z^{eVP} agrees with the earlier result of Karshenboim [74], given as

$$\Delta_Z^{\text{eVP}} = \frac{\alpha}{3\pi} \left[2 \ln \frac{\Lambda^2}{m_e^2} - \frac{634}{315} \right] \sim 0.0182, \quad (2.65)$$

using the standard dipole form factor of the proton, $\Lambda^2 = 0.71 \text{ GeV}^2$.

Additional corrections from the muon self-energy and anomalous magnetic moment to the Zemach radius were also evaluated in [74]

$$\delta_Z^{\mu\text{-line}} = -\frac{5\alpha}{4\pi}. \quad (2.66)$$

The radiative corrections to the Zemach term, combining Eq. 2.64 and Eq. 2.66, amount to

$$\Delta E_Z^{\text{rad-tot}} = -0.0262(9) \text{ meV}. \quad (2.67)$$

The radiative corrections to the recoil term yield

$$\Delta E_{\text{recoil}}^{\text{rad-tot}} = 0.002531(9) \text{ meV}. \quad (2.68)$$

Additionally, corrections to the wave function at the origin due to the one-loop electronic vacuum polarization insertion into the inelastic two-photon exchange have been calculated as [11]

$$\Delta_{\text{Pol}}^{\text{eVP}} = 1 \text{ ppm}, \quad (2.69)$$

corresponding to an energy shift of

$$\Delta E_{\text{pol}}^{\text{eVP}} = 0.00003(5) \text{ meV}. \quad (2.70)$$

Combining all these contributions, the total radiative corrections to the two-photon exchange are

$$\Delta E_{1S\text{-HFS}}^{(2\gamma)\text{-rad, total}} = -0.02278(29) \text{ meV}. \quad (2.71)$$

2.9 Theory comparison

In this section, we compare the different theoretical compilations of the contributions to the 1S-HFS in muonic hydrogen from different authors. Our goal is to identify the main differences and the missing contributions between the different authors. At the end, we provide an updated prediction for the 1S-HFS value along with its associated uncertainty. The predicted HFS value, along with its associated uncertainty, defines the search range for our proposed measurement. This search range is a critical parameter that determines the central laser wavelength and its tunability. In turn, given the laser system performance, it establishes the projected time required to locate the resonance, as will be discussed in Chapter 4.

In addition to the theoretical compilation presented in this chapter, we include two key updates on proton structure contributions from the literature. Peset et.al. [66] provide a model-independent determination of the two-photon exchange using heavy baryon effective field theory, while Ruth et.al. [10] update the polarizability contribution using a data-driven

Eq.	Order [$\times E_F$]	Correction	Our choice	Ruth	Peset
2.8	1	1	182.443 329(7)	182.443 329(7)	182.656 037 9
2.12	α	a_μ	0.212 714		
2.11	$(Z\alpha)^2$	Δ_B	0.014 573		0.014 57
2.16	α	$\Delta E_{C_{1.1}}$	0.374 653		0.374 65
2.22	α	$\Delta E_{C_{1.2}}$	0.734 487		0.734 488
2.25	α^2	$\Delta E_{C_{2.1}+C_{2.2}}$	0.002 920		0.002 916 8
2.26	α^2	$\Delta E_{C_{2.3}+C_{2.4}}$	0.005 569		0.005 56
2.28	α^2	$\Delta E_{C_{2.5}+C_{2.6}}$	0.001 580		
2.29	α^2	$\Delta E_{C_{2.7}}$	0.002 293		
2.32	$\alpha(Z\alpha)$	$\Delta E_{\mu SE}^{\alpha(Z\alpha)}$	-0.024 869		-0.017 55
2.31	$\alpha(Z\alpha)$	$\Delta E_{\mu VP}^{\alpha(Z\alpha)}$	0.007 286		
2.33	$\alpha^2(Z\alpha)$	$\Delta E_{\mu VP(a)}^{NLO}$	0.000 07		
2.34	$\alpha^2(Z\alpha)$	$\Delta E_{\mu VP(b)}^{NLO}$	0.000 13		
2.35	$\alpha^2(Z\alpha)$	$\Delta E_{\mu SE+\mu VP(c)}^{NLO}$	-0.000 05		
2.36	$\alpha^2(Z\alpha)$	$\Delta E_{\mu SE(d)}^{NLO}$	-0.000 05		
2.37	$\alpha^2(Z\alpha)$	$\Delta E_{\mu VPLbL(e)}^{NLO}$	-0.000 03		
2.38	$\alpha^2(Z\alpha)$	$\Delta E_{\mu SE \text{ with } \mu VP(f)}^{NLO}$	-0.000 02		
2.41	$\alpha(Z\alpha)^2$	$\Delta E_{\text{rad}}^{\alpha(Z\alpha)^2}$	-0.001 312		
2.42	$g_A G_F (Z\alpha)^3$	ΔE_{weak}	0.002 23		
2.46	α^2	$\Delta E_{\text{recoil}, \kappa}$	0.017 52		0.017 52
2.45	α^2	ΔE_{HVP}	0.003 56		
2.62	$(Z\alpha)$	$E_{1S\text{-HFS}}^{(2\gamma)}$	-1.1348(162)	-1.139(14)	-1.161(20)
2.71	$\alpha(Z\alpha)$	$\Delta E_{1S\text{-HFS}}^{(2\gamma)\text{-rad, total}}$	-0.022 78(29)	-0.022 78(29)	-0.004 66
	Total sum	$E_{\text{HFS}}(1S)$	182.6389(163)	182.6345(140)	182.623(27)

Table 2.3: Comparison of the different theory update of the 1S μp HFS from various authors. All the numerical values are in meV. The final HFS value in the column labeled ‘Ruth’ combines their calculation for the 2PE with our selected values for all other corrections.

approach, incorporating it into the two-photon exchange corrections. We then incorporate our updated theoretical compilation to include the missing contributions (QED, weak interactions, and hadronic vacuum polarization), refining the total theoretical prediction presented in [10,66]. Table 2.3 compares the theoretical contributions to the 1S-HFS, highlighting the differences among our compilation, which is based on the B χ PT, Ruth results, and Peset calculations.

2.9.1 Comparison with heavy-baryon effective field theory

Table. 2.3 summarizes the different contributions to the 1S-HFS from the three sources indicated earlier. First, we examine the theoretical compilation provided by Peset et.al. [66], which employs heavy baryon effective field theory (HB EFT). This approach utilizes effective field theories techniques that exploit the hierarchy of various corrections scales. Contributions from the lepton mass scale, (in this case, the muon mass m_μ) and strong interactions are incorporated within the Wilson coefficient, naturally arising in the HB EFT calculation of the HFS. It is expressed as [66]

$$\delta E_{p\mu, \text{HFS}}^{c_4}(nS) = \frac{4m_r^3 Z^3 \alpha^5}{\pi m_p^2 n^3} c_4^{p\mu}, \quad (2.72)$$

$$c_4^{p\mu} \equiv c_{4, \text{TPE}}^{p\mu} + \alpha \delta c_4^{p\mu},$$

where $c_4^{p\mu}$ is the Wilson coefficient, and it has a one to one correspondence with the 2PE contribution. It can be determined by comparing experimental results with theoretical predictions for the lower-scale contributions, such as QED and recoil effects.

Since no high-precision determination of the HFS exists for muonic hydrogen, Ref. [66] extracts the Wilson coefficient through relating muonic hydrogen to normal hydrogen using the following equation

$$c_{4, \text{TPE}}^{p\mu} = c_{4, \text{TPE}}^{pe} + \left[c_{4, \text{TPE}}^{p\mu} - c_{4, \text{TPE}}^{pe} \right] + \mathcal{O}(\alpha). \quad (2.73)$$

Here, $c_{4, \text{TPE}}^{p\mu}, c_{4, \text{TPE}}^{pe}$ refer to the 2PE part of the Wilson coefficient of muonic hydrogen and normal hydrogen, respectively. $c_{4, \text{TPE}}^{pe}$ is determined from comparison of the precise experimental value of the 1S-HFS in hydrogen and its theoretical prediction. Using chiral perturbation theory, the difference term in Eq. 2.73 is computed. Ref. [66] reports the following values for the 2PE contribution and its radiative corrections

$$\Delta E_{1S-\text{HFS}}^{(2\gamma)}(\text{Peset}) = -1.161(20) \text{ meV}, \quad (2.74a)$$

$$\Delta E_{1S-\text{HFS}}^{(2\gamma-\text{rad})}(\text{Peset}) = -0.00466 \text{ meV}. \quad (2.74b)$$

The radiative correction $E_{1S-\text{HFS}}^{(2\gamma-\text{rad})}(\text{Peset})$ accounts solely for the wave function correction at the origin, as defined in Eq. 2.22. The additional radiative corrections to the 2PE contribution, missing from Ref. [66], amount to

$$\Delta E_{\text{Peset}}^{2\gamma-\text{missing-rad}} = -0.01812 \pm 0.00029 \text{ meV}. \quad (2.75)$$

Incorporating these missing contributions into the 2PE value from Ref. [66] would further increase the discrepancy with our chosen 2PE value given in Eq.2.71.

Additional missing contributions to the HFS value given in Ref. [66] are as follows:

- Corrections at order $\left(\frac{\alpha}{\pi}\right)^2 E_F$ arising from the two-loop electronic vacuum polarization insertion into the static Coulomb potential. They are corrections to the wave function at the origin, calculated in third order perturbation theory, corresponding to $\Delta E_{C_{2.5}+C_{2.6}}$ as well as $\Delta E_{C_{2.7}}$.
- Higher order radiative corrections at orders $\alpha(Z\alpha)^2 E_F$ and $\alpha^2(Z\alpha)E_F$.
- Weak interaction and hadronic vacuum polarization contributions, labeled as Δ_{weak} and Δ_{HVP} , respectively, in Table 2.3.

The above missing contributions together amount to:

$$\Delta E_{\text{missing}}^{\text{QED+weak+had}}(\text{Peset}) = 0.008401 \text{ meV}. \quad (2.76)$$

The contribution due to the anomalous magnetic moment is directly included in the evaluation of the Fermi energy in Ref. [66], which explains the difference from our value in Eq. 2.8.

The uncertainty associated with the two photon exchange extraction in Eq. 2.74a remains more than twice as large as the missing contributions outlined in Eq. 2.76. To refine the theoretical prediction, we add the missing contributions from Eq. 2.76 and remove the 0.007 meV uncertainty from $E_{1\text{S-HFS}}^{\text{Peset}}$, as it accounts for the previously unconsidered QED corrections now included. We also incorporate the missing radiative corrections to the 2PE from Eq. 2.75. After including these adjustments, the updated value from Ref. [66] is:

$$E_{1\text{S-HFS}}^{\text{Peset+add-corr}} = 182.613 \pm 0.020 \text{ meV}. \quad (2.77)$$

The resulting difference between our prediction and the revised value from Ref. [66] for the 1S hyperfine splitting in muonic hydrogen, expressed in both energy and frequency units, is:

$$\begin{aligned} \Delta E_{1\text{S-HFS}}^{\text{Diff-HBEFT}} &= 0.025706 \pm 0.025803 \text{ meV} \\ &= 6.216 \pm 6.242 \text{ GHz}. \end{aligned} \quad (2.78)$$

2.9.2 Comparison with the data driven approach

The second comparison is based on the data-driven dispersion evaluation of the 2PE contribution. As discussed earlier in Section. 2.8.3, the data-driven approach relies on independent experimental inputs, including inelastic spin structure functions and the elastic Pauli form factor. Historically, this approach has faced challenges due to the limited availability of data for the spin structure function g_1 and a complete lack of data for g_2 in the kinematic region relevant to the hyperfine splitting. Accurate parameterizations are crucial, as significant cancellations occur between σ_{LT} and σ_{TT} , as well as g_1 and F_2 , making uncertainty estimation critical for 2PE evaluations. Interpolation is required at low Q^2 due to insufficient data, but these approximations often lack precision, adding to the overall uncertainty. For a detailed discussion, we refer the reader to Section 4.2 of [11].

During the preparation of this thesis, Ruth et.al. [10] provided a new evaluation of the polarizability and the 2PE using the data-driven dispersion approach, incorporating recent data from the Jefferson Lab Spin Physics Program. The updated polarizability contribution is reported as

$$\Delta_{\text{pol}}^{\mu\text{P}} = 200.6 \pm 52.4 \text{ ppm}, \quad (2.79)$$

which reduces the discrepancy between the data-driven evaluation and χPT by a factor of two. However, this evaluation continues to suffer from a lack of data for the spin structure function g_2 .

Using this updated polarizability value, Ref. [10] extracted the Zemach radius by comparing the high-precision experimental data for the hydrogen hyperfine splitting with the latest theoretical compilation in [1]. The extracted Zemach radius is

$$r_z^{\text{Ruth}} = 1.036(8) \text{ fm}. \quad (2.80)$$

Including the recoil contribution from [72] and the radiative corrections to the 2PE as quoted in Subsec. 2.8.4, Ref. [10] reports

$$E_{1S\text{-HFS}}^{(2\gamma+\text{rad})}(\text{Ruth}) = -1.162(14) \text{ meV}. \quad (2.81)$$

Ref. [10] then relied on the theory update from [1] for the remaining contributions of $(\Delta_{\text{QED}}, \Delta_{\text{weak}}, \Delta_{\text{HVP}})$, which we replace here by the updated values listed in Table. 2.3. Based on this update, the total hyperfine splitting from Ref. [10] is

$$E_{1S\text{-HFS}}^{\text{Ruth}} = 182.634 \pm 0.014 \text{ meV}. \quad (2.82)$$

The discrepancy between our prediction and the value from the data-driven evaluation, expressed in meV is:

$$\Delta E_{1S-HFS}^{\text{Diff-Data}} = 0.004400 \pm 0.02149 \text{ meV}. \quad (2.83)$$

In GHz, this difference is

$$1.064 \pm 5.196 \text{ GHz}. \quad (2.84)$$

For completeness, we note the earlier evaluation of the 2PE by Tomalak. [73], which used the data-driven approach to calculate the polarizability and then combined it with precision hydrogen spectroscopy measurement of the 1S-HFS to extract r_z . However, we focus on comparing with Ruth et al. [10], as it provides the most up-to-date data-driven evaluation of the 2PE.

2.9.3 Theory prediction for the HFS measurement

Based on the comparisons in Subsec. 2.9.1, we present the total theoretical predictions and corresponding uncertainties for the 1S hyperfine splitting (HFS) in μp in Fig.2.12.

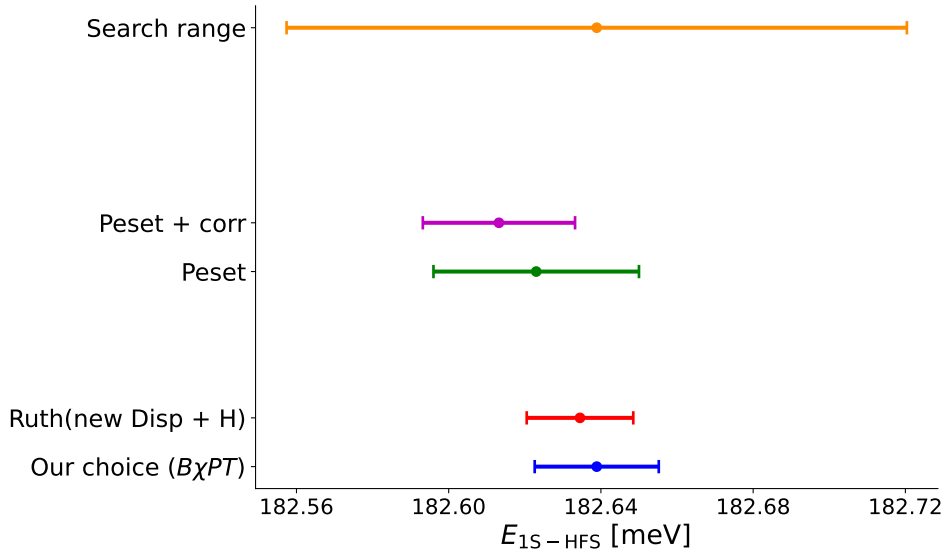


Figure 2.12: Theory predictions of the 1S hyperfine splitting in muonic hydrogen with uncertainties.

Our chosen value for the 1S-HFS in μp is:

$$E_{1\text{S-HFS}} = 182.6389(163) \text{ meV} \quad (2.85)$$

corresponding to a wavelength of:

$$E_{1\text{S-HFS}} = 6788.4847 \pm 0.6058 \text{ nm} \quad (2.86)$$

In Fig. 2.12, we indicate the search range corresponding to $\pm 5 \sigma$ of the theoretical uncertainty, which covers all other predictions and their uncertainties. Experimentally, to be on the conservative side, we chose a search range of 50 GHz.

We conclude this chapter by demonstrating the impact of incorporating high precision hydrogen HFS measurement to refine the theoretical predictions for HFS in μp . Figure 2.13 shows that incorporating high-precision hydrogen HFS measurement reduces the uncertainty of theoretical predictions by a factor of two. This underscores the potential impact of an HFS measurement in μp . Using the hydrogen HFS measurement to extract r_z , allows the μp HFS measurement to determine the polarizability contribution with a relative accuracy of $< 10\%$.

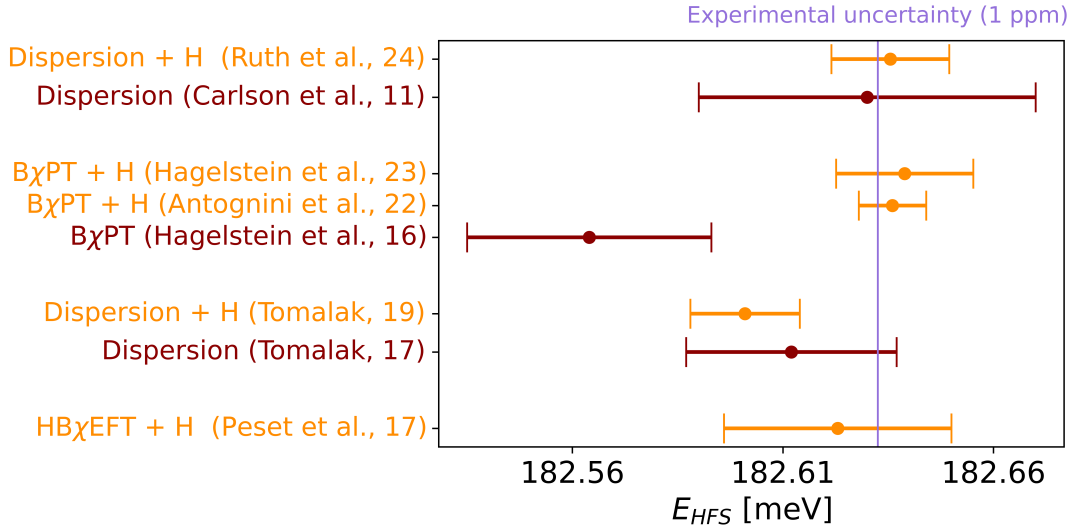


Figure 2.13: The 1S-HFS theory predictions with and without scaling from H hydrogen HFS measurements.

Appendices

2.A The Uehling potential

The Uehling potential arises from the leading-order correction to the photon propagator due to vacuum polarization. It modifies the Coulomb potential by accounting for the interaction of the photon with virtual electron-positron pairs, as illustrated in Fig. 2.A.1. The unmodified photon propagator is given by [75]

$$D_{\mu\nu}^{(0)}(q) = \frac{-ig_{\mu\nu}}{q^2 + i\epsilon}. \quad (2.87)$$



Figure 2.A.1: Vacuum polarization insertion in the photon propagator to first order in α .

To include vacuum polarization effects, the photon propagator is modified by inserting the vacuum polarization function $I_P(q^2)$ as [76]

$$\frac{1}{q^2 - i\epsilon} \rightarrow \frac{1}{q^2 - i\epsilon} I_P(q^2). \quad (2.88)$$

The modified propagator in the Landau gauge is represented as [75, 76]

$$D_+^-(q) = \frac{1}{q^2 - i\epsilon} + \frac{\alpha}{3\pi} \int_{(2m)^2}^{\infty} \frac{dM^2}{M^2} \left(1 + \frac{2m^2}{M^2}\right) \left(1 - \frac{4m^2}{M^2}\right)^{1/2} \frac{1}{q^2 + M^2 - i\epsilon}. \quad (2.89)$$

Here, q is the exchanged momentum, M^2 is an integration parameter for the spectral function starting at the threshold for pair production ($4m_e^2$ for electronic vacuum polarization), and

m_e is the electron mass. The first term in Eq. 2.89 represents the unmodified Coulomb interaction in momentum space, while the second term corresponds to the vacuum polarization correction.

In coordinate space, the vacuum polarization term is expressed as

$$\delta\mathcal{D}(\mathbf{r}) = \frac{\alpha}{\pi} \int_0^1 dv \frac{v^2 \left(1 - \frac{1}{3}v^2\right)}{1 - v^2} \exp\left(- (1 - v^2)^{-1/2} 2m_e r\right), \quad (2.90)$$

where $v = \left(1 - \frac{4m^2}{M^2}\right)^{1/2}$. The Uehling potential is represented by the diagram in Fig. 2.A.2(a), is then given by

$$\begin{aligned} V_U(\mathbf{r}) &= -\alpha \delta\mathcal{D}(r), \\ &= -\frac{\alpha}{\pi} \int_0^1 dv \frac{v^2 (1 - v^2/3)}{1 - v^2} \frac{\alpha e^{-\lambda r}}{r}, \end{aligned} \quad (2.91)$$

where $\lambda = \frac{2m_e}{\sqrt{1-v^2}}$



Figure 2.A.2: Vacuum polarization corrections to the electrostatic coulomb potential. (a) V_{VP}^1 One loop Uehling potential. (b) $V_{VP}^{1,1}$ reducible two-loop Uehling potential.

The reducible two one-loop Uehling potential is derived using the same procedure as for the one-loop potential. The key difference is the double insertion of the vacuum polarization function from Eq. 2.88 into the photon propagator. The resulting potential, corresponding to the diagram in Fig.2.A.2(b), is expressed in coordinate space as

$$\begin{aligned} V_U(\mathbf{r})_{1,1} &= -\frac{1}{9} \left(\frac{\alpha}{\pi}\right)^2 \int_0^1 dv \frac{v^2 (1 - v^2/3)}{1 - v^2} \\ &\times \left\{ 16 - 6v^2 + 3v (3 - v^2) \ln \left(\frac{1 - v}{1 + v}\right) \right\} \left(\frac{-\alpha e^{-\lambda r}}{\mathbf{r}}\right). \end{aligned} \quad (2.92)$$

For a more compact representation, the potential can be rewritten by isolating the spectral function $f(v)$, simplifying the integral form

$$V_U(\mathbf{r})_{1.1} = \int_0^1 dv f(v)_{1.1} \left(\frac{-\alpha e^{-\lambda r}}{\mathbf{r}} \right), \quad (2.93)$$

$$f(v)_{1.1} = -\frac{1}{9} \left(\frac{\alpha}{\pi} \right)^2 \frac{v^2 (1 - v^2/3)}{1 - v^2} \times \left\{ 16 - 6v^2 + 3v (3 - v^2) \ln \left(\frac{1 - v}{1 + v} \right) \right\}.$$

2.B The Källén-Sabry potential

The irreducible two-loop Källén-Sabry potential, represented by the diagram in Fig. 2.B.3, can be expressed in integral form following the formalism outlined in [48,56,77]. The potential is given by

$$V_{KS}^{(2)}(\mathbf{r}) = \left(\frac{\alpha}{\pi} \right)^2 \int_0^1 f(v) dv \frac{m_e^2}{(1 - v^2)^2} \left(\frac{-\alpha e^{-\lambda r}}{\mathbf{r}} \right), \quad (2.94)$$

where the function $f(v)$ is defined as

$$f(v)^{(2)} = \left(\frac{2v}{3} \right) \left\{ (3 - v^2)(1 + v^2) \left[\text{Li}_2 \left(-\frac{1 - v}{1 + v} \right) + 2\text{Li}_2 \left(\frac{1 - v}{1 + v} \right) \right. \right. \\ + \frac{3}{2} \ln \frac{1 + v}{1 - v} \ln \frac{1 + v}{2} - \ln \frac{1 + v}{1 - v} \ln v \\ + \left. \left. \left[\frac{11}{16} (3 - v^2) (1 + v^2) + \frac{v^2}{4} \right] \ln \frac{1 + v}{1 - v} \right. \right. \\ + \left. \left. \left[\frac{3}{2} v (3 - v^2) \ln \frac{1 - v^2}{4} - 2v (3 - v^2) \ln v \right] \right. \right. \\ \left. \left. + \frac{3}{8} v (5 - 3v^2) \right\}. \quad (2.95)$$

Here, $\text{Li}_2(z)$ represents the Euler dilogarithm.

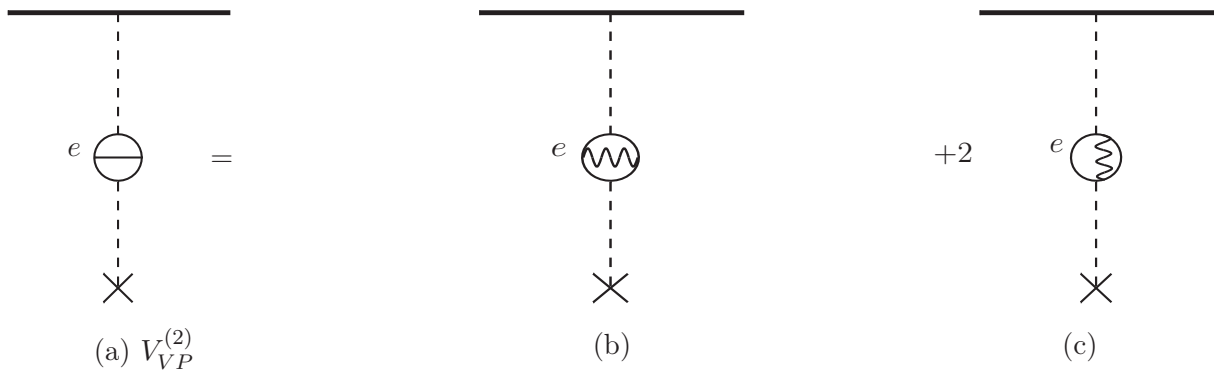


Figure 2.B.3: Irreducible two-loop potential (the Källen-Sabry potential).

Chapter 3

The experimental principle

In this chapter, we introduce the principles of the HFS experiment. We first provide a qualitative explanation of the different processes required and the scheme necessary to achieve a successful resonance signal. Together with the laser excitation, the collisions of μp with H_2 molecules are at the heart of the HFS experiment. In this chapter, we focus on these collisional processes which helps us understand the method that we use to expose a successful laser transition. As a result, this will enable us to define the events and the background rates, as well as the requirement for the laser system.

3.1 The experimental sequence

The experimental setup is depicted in Fig. 3.1, illustrating the subsequent sequence of events. A beam of negative muons with a momentum of $11 \frac{\text{MeV}}{c}$ at a rate of $1000 \frac{\mu}{s}$, delivered by the πE5 beamline is partially stopped in a cryogenic H_2 gas target. The H_2 gas target has a thickness of 1 mm and is kept at a cryogenic condition with a temperature of 22 K and a pressure of 0.5 bar. Before entering the target, the muons pass through an entrance detector, which defines the time $t = 0$ and triggers the laser system.

The muons are slowed down in the H_2 gas target until they bind to a proton from a hydrogen molecule forming a μp in a highly excited state. Subsequently, the μp atoms decay to the 1S ground state through various de-excitation mechanisms, including radiative,

Auger and Coulomb collisions. Because of collisions between the μp atoms in the ground state and the H_2 molecules, all the μp atoms will eventually be quenched to the lower lying hyperfine sublevel of $F = 0$ within few hundreds of nanoseconds. The quenched μp atoms will thermalise to the surrounding H_2 gas temperature in a $1 \mu s$.

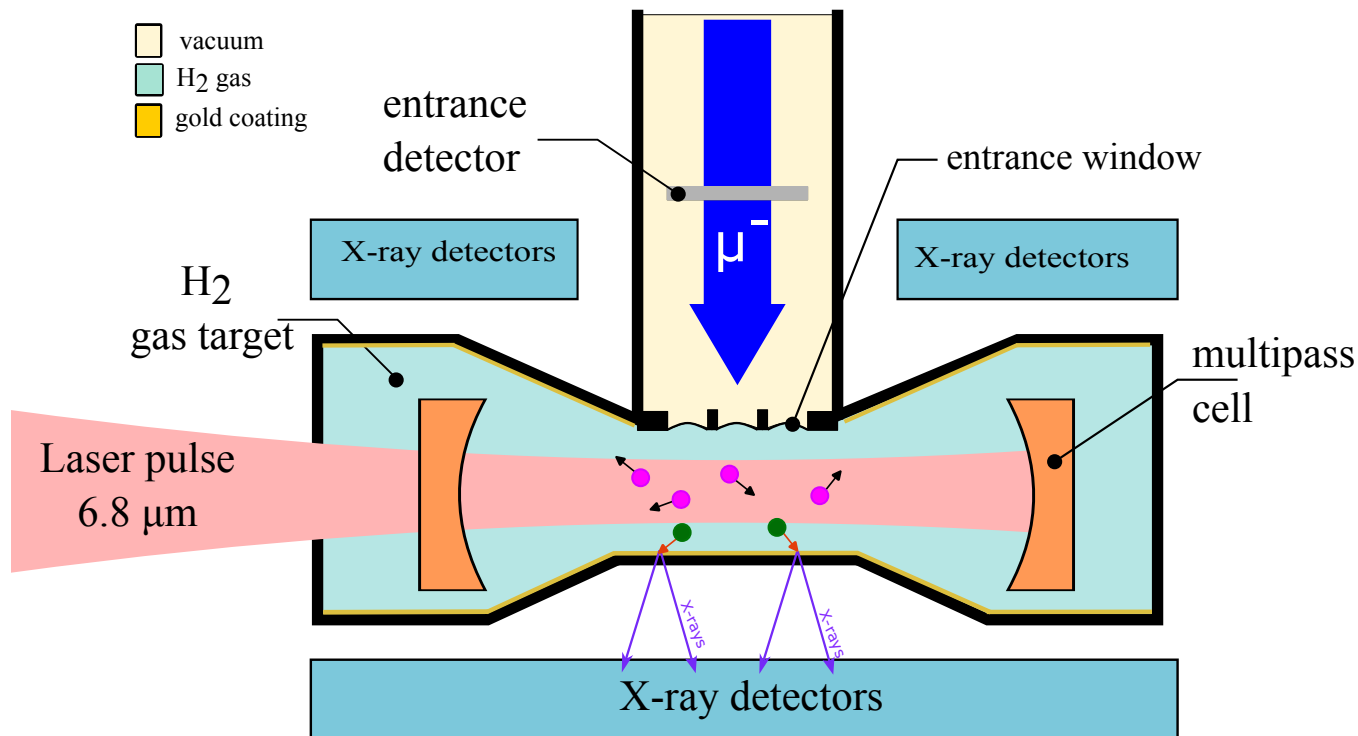


Figure 3.1: Schematic of the HFS experimental setup. A detailed description is given in the text.

After approximately $1 \mu s$, a laser pulse with an energy of few mJ and a pulse length of about 50 ns at a wavelength of $6.8 \mu m$ is coupled into a multi-pass cell. The multiple reflections within the multi-pass cell, gives rise to a disk shaped illumination volume and also yields an increase of the laser fluence at the position of the μp atoms. An on resonance laser pulse drives the transition from the singlet to the triplet state: $F = 0 \rightarrow F = 1$.

Upon a collision with the hydrogen molecules in the gas, the excited μp atom will de-excite from the triplet to the singlet state: $F = 1 \rightarrow F = 0$. As a result of this collisional de-excitation, the μp will gain on average a kinetic energy of 100 meV enabling it to travel through the target gas reaching the target walls with high probability. After reaching the gold coated target walls, the muon from the μp will be transferred to the gold nucleus creating a muonic gold (μAu) in a highly excited state. These highly excited μAu atoms

will decay to the ground state emitting several X-rays of MeV energy. The detection of these X-rays indicates a successful laser excitation. By counting the number of X-rays versus the laser wavelength, one can obtain a resonance.

3.1.1 Collisional processes

The μp atoms are created in a highly excited state with a principal quantum number n ranging from 7 to 40, with two peaks located around $n = 9$ and 13, and an average kinetic energy of about 1 eV [78]. Upon formation, the highly excited μp atoms quickly decay via a cascade of de-excitation to the $1S$ state through a number mechanisms, such as radiative, Auger and Coulomb collisions. We refer the reader to [79] as well as section 6.3 of [2] for details about the de-excitation processes. For a hydrogen density of $\varphi = 10^{-2}$, these de-excitation processes occur within $\sim 10^{-10}\text{s}$ [79, 80]. Here, the hydrogen density ρ is usually given as a fraction of the liquid hydrogen density (LHD): $\varphi = \frac{\rho}{(\rho_{\text{LHD}})}$ where the liquid hydrogen density is $\rho_{\text{LHD}} = 2.125 \times 10^{22}$ molecules / cm^3 .

To simulate the diffusion of the μp atoms through the H_2 molecules, four distinct scattering processes between the μp atoms and H_2 molecules need to be considered.



The superscript * in Eq. 3.1 indicates a change of the ro-vibrational state of H_2 resulting from the scattering with μp .

Collisional processes in which the total spin (F) of μp is conserved as in 3.1a and 3.1d, are called elastic collisions. The other collisional processes accounts for the spin flip events, wherein the muon is transferred to a proton in the H_2 molecule. These inelastic collisions can cause transitions between the two hyperfine levels, depending on the spin of the proton colliding with the muonic atom.

The calculation of differential cross sections for the scattering processes in Eq. 3.1 [81] relies on the cross sections for the corresponding "nuclear" scattering processes of μp on

single protons. Furthermore, these calculations account for the effects of molecular binding of protons in H_2 , electron screening, and spin correlations in specific rotational states of H_2 . In order to account for the thermal motion of the H_2 molecules in the simulation of the diffusion processes, we make use of collisional rates rather than cross sections [2].

The total collisional rates $\Gamma_{\text{if}}^{\text{CM}}$ in the center of mass frame are calculated

$$\Gamma_{\text{if}}^{\text{CM}} = \rho v_{\text{rel}} \sigma_{\text{if}}^{\text{CM}}, \quad (3.2)$$

where v_{rel} is the relative velocity of μp and H_2 , and $\sigma_{\text{if}}^{\text{CM}}$ [81] are the cross section in the center of mass frame. The "i" and "f" indices are the total spin of the initial and final hyperfine state, respectively. The total reaction rates Γ_{if} of the different scattering processes described in Eq. 3.1 are shown in Fig. 3.2 as a function of the μp kinetic energy for a temperature of 22 K and a liquid hydrogen density ($\varphi = 1$). In addition, the rates are shown for two different initial distributions of the H_2 rotational states. In red for thermal equilibrium (Boltzman distribution) at 22 K where all the H_2 molecules are in the rotational state $k = 0$. In blue is a 3:1 mixture of the states $k = 0, k = 1$ which corresponds to the degeneracy at room temperature. The 3:1 mixture is relevant because at the target conditions of the HFS experiment the relaxation of the rotational state $k = 1$ to $k = 0$ is very slow and will take weeks. From Fig. 3.2, we see that there is a threshold for the up-scattering rate Γ_{01} at a kinetic energy of ~ 0.3 eV. This means that a μp atom in the singlet state $F = 0$ with a kinetic energy < 0.3 eV can not be up-scattered to the triplet state ($F = 1$) in a collisional process. On the other hand, Γ_{10} is non zero even below this threshold, which means that all the μp atoms end up eventually in the $F = 0$ state.

3.1.2 Thermalization of the μp atoms

After analyzing the various collisional processes, we now examine the thermalization of μp atoms after they have de-excited to the ground state, and how do they quench to the $F = 0$ singlet sublevel. In Fig. 3.3 we present the time evolution of the μp average kinetic energy simulated for two temperatures (22 K and 50 K) and the densities ($\varphi = 0.005, 0.01$) of the H_2 gas target. An initial kinetic energy spreading from 1 to 100 eV was used in [5] which was based on the cascade model given by [82]. We observe that at the target conditions, within a 1 μs the μp are thermalized at the H_2 gas temperature. For times $t < 50$ ns, we observe a sharp decrease in the kinetic energy. This occurs because the μp atoms possess a kinetic

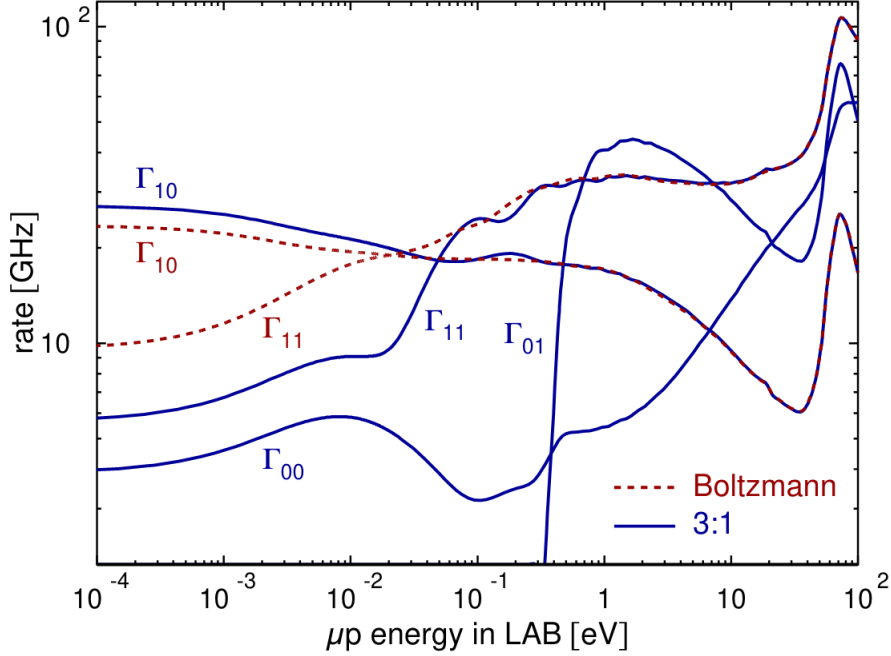


Figure 3.2: Collisional rates Γ_{if} of the different scattering processes of $\mu p - \text{H}_2$ for H_2 at temperature of 22 K and a liquid hydrogen density ($\varphi = 1$). The rates are calculated for two different distribution for rotational states of H_2 , the Boltzmann distribution and the 3:1 mixture of rotational states $k = 0, k = 1$. We see there is only a relevant difference in the total rates Γ_{11}, Γ_{10} below the kinetic energy of ~ 0.1 eV for different distributions of rotational states in the hydrogen gas. Figure is reprinted from [2].

energy above the up-scattering threshold, allowing all the collisional processes described in Eqs. 3.1 take place. However, for times $t > 50$ ns, the kinetic energies of the μp are below the up-scattering threshold. As soon as all the μp atoms have reached the singlet $F = 0$ state, the only collisional process that takes place is the elastic collision in the $F = 0$ state (Γ_{00}). Thus, the energy loss is slow.

While the μp atoms are thermalizing, they are diffusing in the H_2 gas and a fraction of them may reach the gold coated target wall where a muon transfer to the gold atoms takes place. Simulations in Ref. [5] shows that at our target conditions, about 50 – 80% of the μp atoms reach the target walls in the first microsecond after the μp atoms formation. In addition to the losses due to the muon decay, these atoms are not available for laser excitation. For more details, the reader is referred to Sec.7.2 in [5].

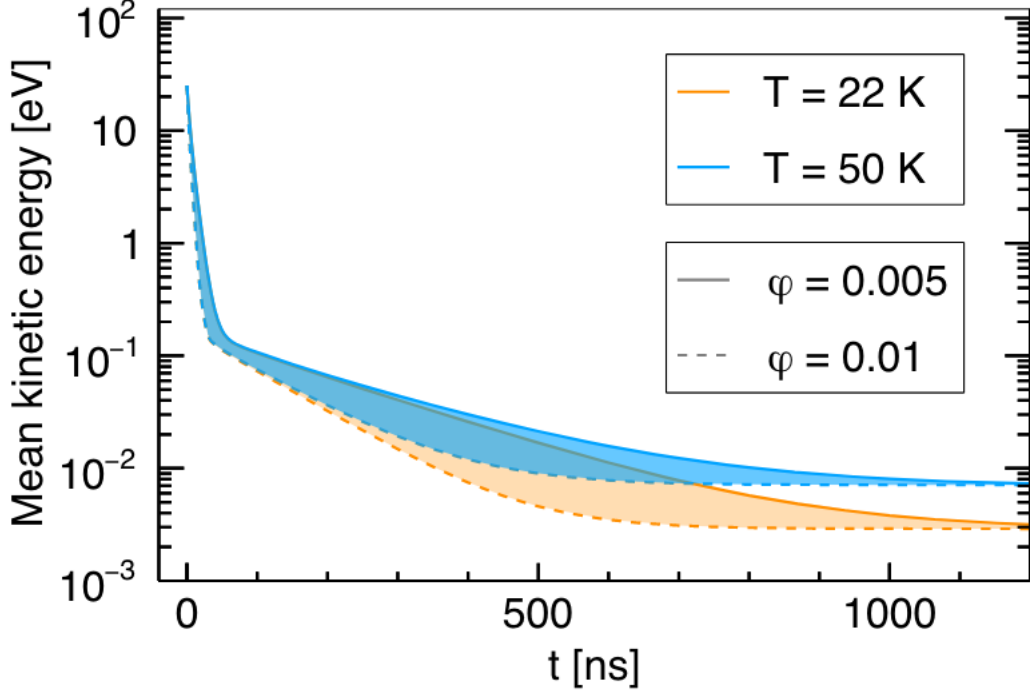


Figure 3.3: Time evolution of the average kinetic energy (in the LAB frame) of the μp atoms simulated for two different target conditions each of temperature and density. Figure is reprinted from [2].

3.1.3 Diffusion after laser excitation

The μp atoms in the singlet state ($F = 0$) within the central region of the target are excited by the laser pulse approximately $1 \mu s$ after the μp formation. The $1 \mu s$ time is to ensure that prior to the laser excitation, all the the μp are thermalized. A calculation of the excitation probability comprising a successful excitation from $F = 0$ to $F = 1$ followed by a collisional de-excitation to $F = 0$ was carried out in [4]. This calculation was performed accounting for de-coherence effects caused by collisions and laser bandwidth as well as the Doppler broadening. It was shown that the largest contribution to the linewidth comes from the Doppler broadening, and the linewidth of the laser pulse used to excite the μp atoms. Reducing the Doppler broadening necessitates the use of a cryogenic target. The minimum target temperature is 22 K, below which the H_2 gas liquifies. More details about the excitation probability and the enhancement of it using the multi-pass cell will be given in the next chapter.

After a successful laser excitation to the $F = 1$ state, the μp atom is quenched to the lower

singlet state $F = 0$ through an inelastic collision, see the rate Γ_{10} in Fig. 3.2. In this process, the transition energy of approximately 182 meV is shared between the quenched μp atom and the H_2 molecule. A simulation of the energy distribution of μp atoms right after de-excitation is shown by the orange curve in Fig. 3.4. This should be compared to the kinetic energy distribution of the μp atoms thermalised to the H_2 gas temperature prior to the laser excitation shown by the blue curve. On average, the μp atom kinetic energy increases by about 100 meV. The additional energy kick won by the μp atom after a successful laser excitation followed by a collisional quenching, allows them to efficiently diffuse in the H_2 gas. At these kinetic energy values, indeed the H_2 gas is more "transparent" for the μp atoms compared to the thermalized μp atoms. This can be evinced by the mean free path length versus the kinetic energy shown in Fig. 3.4.

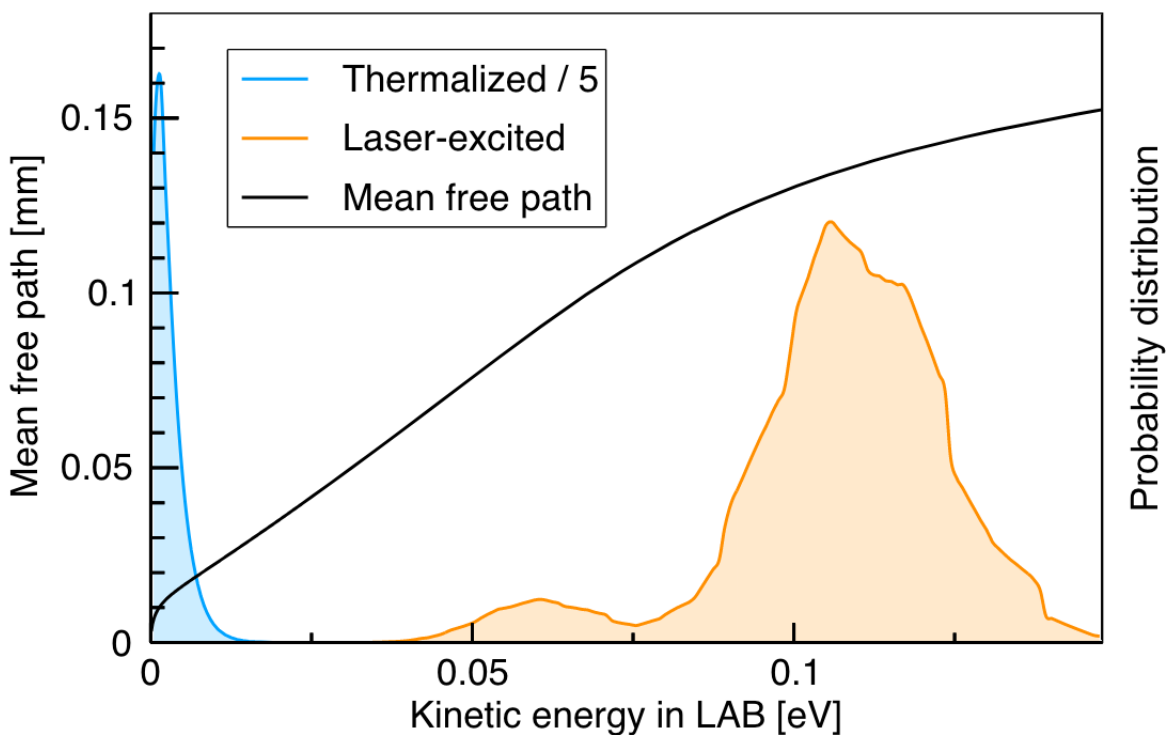


Figure 3.4: Kinetic energy distributions for thermalized μp atoms (blue), and for μp atoms immediately after a cycle of laser excitation and collisional quenching from the triplet to the singlet state (orange). The amplitude of the blue curve is scaled by a factor of 1/5. The black curve represents the mean free path of the μp atoms in H_2 versus the kinetic energy of μp atoms. Here the target conditions are a temperature of 22 K and a pressure of 0.6 bar. Figure is reprinted from [2].

The number of atoms reaching the target walls after laser excitation in the center of the target is shown by the orange curve in Fig. 3.5. In this simulation, the laser pulse enters the multi-pass cell at times $t = 1000$ ns, and the target has a thickness is of 1 mm. As shown by the simulation, the first μp atoms arrive at the target walls about 100 ns after the laser excitation. The majority of the atoms arrival at the walls happens within a time window of about 300 ns from $t = 1100$ to $t = 1400$ ns. That is why the laser induced events have to be counted within this time window. For larger target thickness this distribution would be broadened and the total number of μp atoms arriving at the target walls would decrease significantly. For this reason, the target thickness has to not exceed 1 mm significantly.

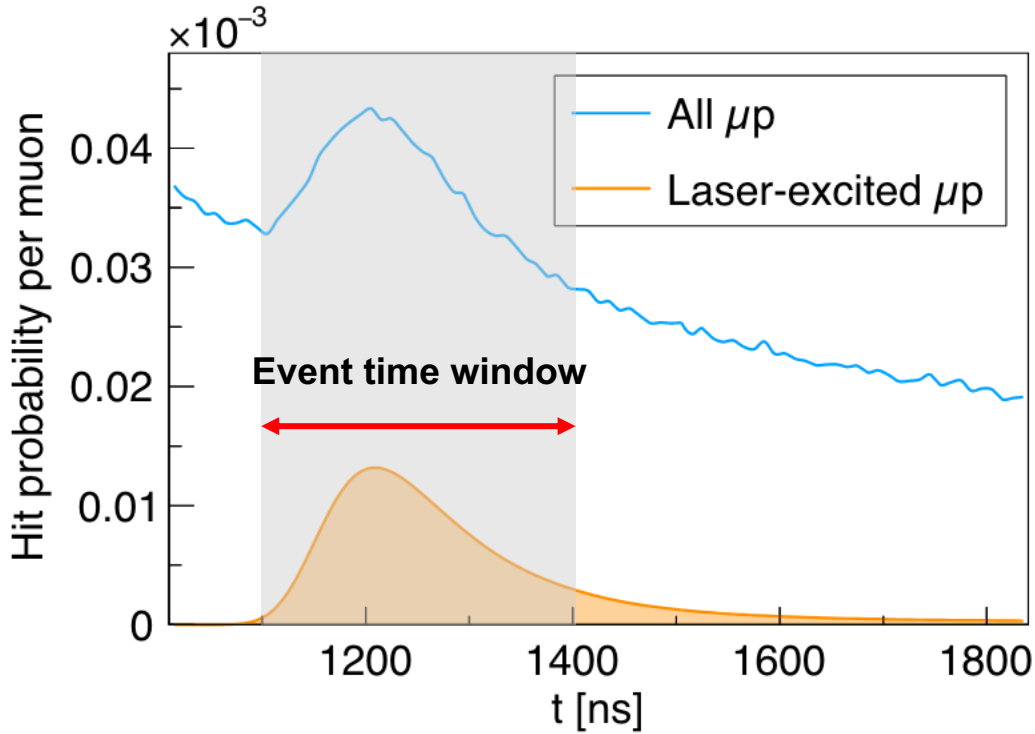


Figure 3.5: Time distribution of the laser excited μp atoms reaching one of the target walls (orange). The time distribution of all the μp atoms including those which did not undergo a laser excitation is shown in (blue). The event time window is highlighted by the grey band, and the horizontal line spanning times $t = 1100$ to $t = 1400$ ns. Here the target conditions are a temperature of 22 K and a pressure of 0.6 bar in addition to accounting for the muon lifetime. Figure is adapted from [2].

The blue curve represents the time distribution of all the μp atoms reaching the gold-coated target walls, independent on whether or not they have undergone a laser excitation. The thermalized and non laser excited μp atoms which are formed near the target walls at $t = 1000$ ns will diffuse to the gold-coated walls. By hitting the target walls, they create μAu

and give rise to X-ray events causing the diffusion background. This diffusion background can be mitigated by reducing the H_2 target temperature T , hence reducing the mobility of these thermalized and non laser-excited μp atoms.

The diffusion of the μp atoms through a cryogenic H_2 gas target is a determining process in the HFS experiment. The study of the collisional processes happening during the diffusion defines the optimal target conditions in terms of temperature and pressure. The optimal target condition taking into account the stopping probability, thermalization, laser excitation and diffusion have been found to be $d = 1$ mm thickness, temperature of 22 K, and a pressure of 0.5 bar. A larger temperature would increase the Doppler broadening and hence decrease the laser excitation probability, and would lead to larger diffusion background. A larger target pressure would mean an ineffective diffusion after the laser excitation, hence less laser excited atoms reaching the target walls.

3.2 The multi-pass cell

The diffusion process dictates that the target need to be 1 mm thick. While the muon beam has a diameter of 15 mm, the laser pulse should ideally illuminate a disk shaped volume of a 1 mm thickness and a 15 mm diameter. This is achieved by using a toroidal multi-pass cell. The multi-pass cell provide a large laser fluence at the position of the μp atoms in the order of few J/cm^2 which is needed to efficiently excite the μp atoms.

A sketch of the toroidal cavity under development is shown in Fig. 3.6(a). The laser pulse is coupled through a tiny slit into the multi-pass cell where it undergoes several hundreds of reflections before either coming out, being absorbed or scattered at the surface of the mirror. A ray tracing simulation was used to calculate the laser fluence distribution within the cell. In the z -direction (the muon beam direction), the light is coupled resonantly, meaning that the laser mode in the z -direction is matched to the cell resonant mode. The beam then propagates back and forth between the mirror surface while keeping the same resonant mode. This means that in the z -direction the cell design corresponds to a stable resonator. In the x - y plane, the cell design functions as an unstable resonator, causing the light to spread with each reflection, as shown in Fig. 3.6(a).

Figure 3.6(b) shows the fluence distribution in $x - y$ plane as obtained from the ray

tracing simulation carried out in [3], integrated over the thickness of the target. The minima in the center is related to the injection angle of the in-coupled beam. Using this fluence distribution, it is possible to compute the position dependence laser excitation probability which we will discuss next chapter. Additionally, using the fluence distribution, the average fluence in the multi-pass cell is calculated.

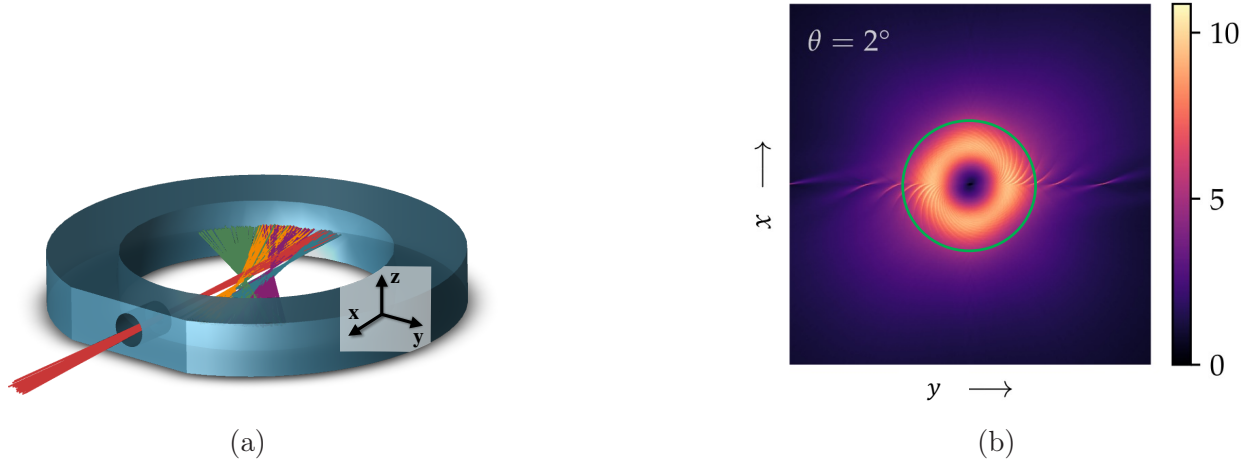


Figure 3.6: (a) Schematic of the toroidal multi-pass cell under development. The red rays represent the in-coupled beam. Upon each reflection, the colour of the rays is changed to illustrate the spreading of the light in the $x - y$ plane. (b) Simulation of the two dimensional fluence distribution inside the toroidal multi-pass cell in the transverse plan for an injection at an angle $\theta = 2^\circ$, a laser pulse energy of 1 mJ, and a reflectivity of 99.2 % of the multi-pass cell. The green circle represents the size of the muon beam with a diameter of 15 mm. Figure is adapted from [3].

3.3 Detection system and background

As previously mentioned, the X-rays emitted during the cascade in muonic gold serves as indicator of a successful laser transition. Figure 3.7 offers a schematic overview of a muonic gold event. Large high- Z scintillators are used to efficiently detect muonic gold events, as each event generates several detectable MeV X-rays, followed by neutrons (n) and gammas γ from the nuclear capture. The setup also include several thin plastic scintillators that are used to identify the MeV electrons produced by the muon decays.

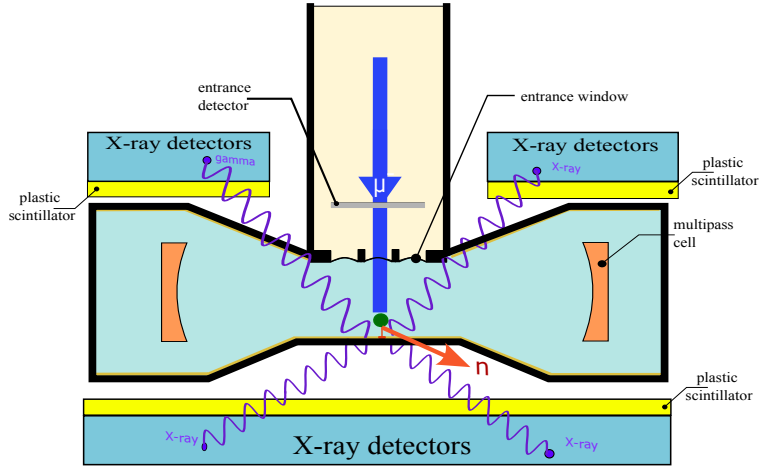


Figure 3.7: Schematic of a muonic gold event produced in the target region detected using a large high-Z scintillator (light blue).

Although high detection efficiency can be achieved, it is necessary to investigate potential background sources associated with this detection scheme. Overall, we need to consider three categories of events that produce background shown in Fig. 3.8:

- Diffusion background ($R_{\text{BG}}^{\text{diffusion}}$): This is caused by non-laser-excited μp atoms reaching the target walls in the anticipated event time window, $t \in [1100 - 1400]$ ns. This background can not be fundamentally distinguished from the signal events, but it can be mitigated by reducing the target temperature.
- Bremsstrahlung background ($R_{\text{BG}}^{\text{decay}}$): This arises from muon decays ($\mu \rightarrow e\nu\bar{\nu}$) occurring within the event time window, which are mistakenly identified as μAu cascade events. The primary source of this misidentification is Bremsstrahlung emitted by decay-electrons passing through the setup near the target region, as depicted in Fig. 3.8(a). The misidentification is taking place because the electron might not deposit energy in the plastic scintillator which is supposed to veto this event, while at the same time produces an Bremsstrahlung X-ray that deposits energy in the X-ray detector.
- Muon-uncorrelated background ($R_{\text{BG}}^{\text{uncorr}}$): This originates from energy depositions within the event time window uncorrelated with the muons from the beam. The source of this muon-uncorrelated energy deposition is natural radioactivity in the experimental area, electrons and neutrons from the beam line and in addition a smaller amount of cosmic-ray muons. An illustration of such an event is shown in Fig. 3.8(b)

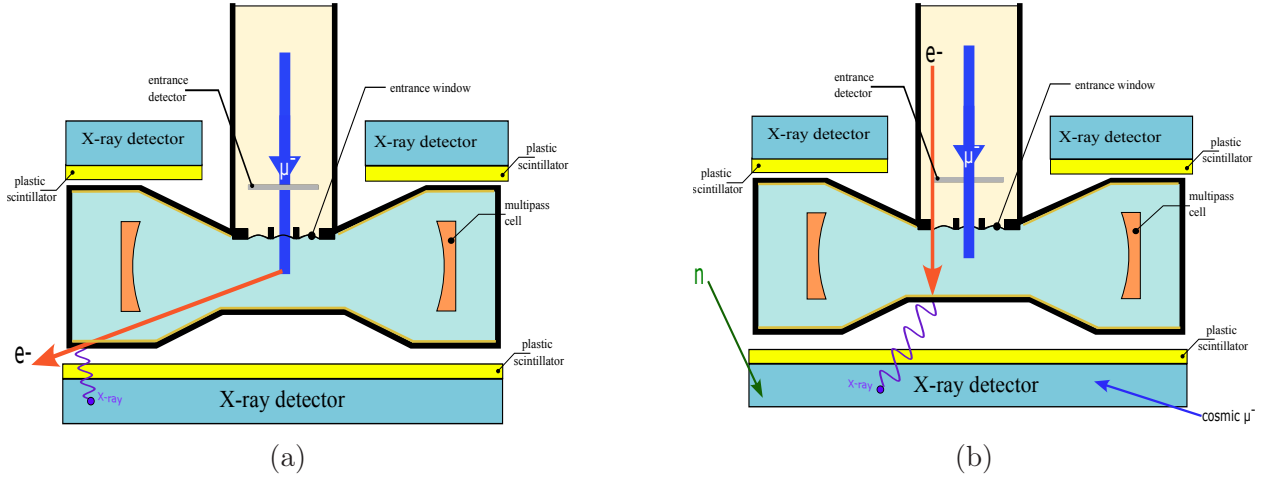


Figure 3.8: (a) Schematic of a Bremsstrahlung process where the decay-electron is falsely identified as an X-ray (muonic gold cascade event). The Bremsstrahlung photon deposit energy in the X-ray detector but none in the plastic scintillator (yellow colour) which are used to identify these false X-ray events. (b) Examples of uncorrelated background events due to electrons coming with the muon beam, cosmic particles and neutrons produced at the radiation zone. These events as well deposit energy in the X-ray detector and are rejected through non correlation with events timed by the muon entrance detector.

The total sum of the background rate is thus

$$R_{BG} = R_{BG}^{\text{diffusion}} + R_{BG}^{\text{decay}} + R_{BG}^{\text{uncorr}}. \quad (3.3)$$

The rate of the diffusion background for a target temperature of 22 K and a pressure of 0.5 a bar is given by [5, 83]

$$\begin{aligned} R_{BG}^{\text{diffusion}} &= P_{\text{Diff}} \cdot R_{\mu} \cdot \varepsilon_{\text{Au}} \\ &= 8.3 \times 10^{-4} \cdot 500 \cdot 0.7 = 0.39 \text{ 1/s}, \end{aligned} \quad (3.4)$$

Here, P_{Diff} is the probability that a muon passes through entrance detector creating a μP which will diffuse without undergoing a laser excitation reaching the walls and creating a μAu atom. R_{μ} is the muon triggering rate, and ε_{Au} is the detection efficiency of a μAu event. The rate of the Bremsstrahlung background is given by

$$\begin{aligned} R_{BG}^{\text{decay}} &= P_{\text{decay}} \cdot R_{\mu} \cdot \varepsilon_{\text{e-X}} \\ &= 42.5 \times 10^{-4} \cdot 500 \cdot 0.1 = 0.30 \text{ 1/s}, \end{aligned} \quad (3.5)$$

where P_{decay} is the probability that a muon passes through entrance detector then decaying during the event time window, leading to misidentification of the decay electron as a muonic

gold X-ray event. ε_{e-X} is the detection efficiency of an electron from a muon decay event. The rate of the uncorrelated background is given by [5, 83]

$$\begin{aligned}
 R_{\text{BG}}^{\text{uncorr}} &\approx R_{\text{Uncorr}} \cdot \Delta t_{\text{events}} \cdot R_{\mu} \cdot \varepsilon_{\text{non-terminated}} \\
 &\approx 4000 \cdot 300 \times 10^{-9} \cdot 500 \cdot 0.2 \\
 &\approx 1.2 \times 10^{-1} \text{ 1/s},
 \end{aligned}
 \tag{3.6}$$

where R_{Uncorr} is the measured non-correlated background rate. The additional factor $\Delta t_{\text{events}} \cdot R_{\mu} \cdot \varepsilon_{\text{non-terminated}}$ accounts for the μAu events as well as decay electrons that have not been recorded in the detection system. This factor is given because any detection of energy deposition from μAu events or decay electrons prior to the event time window $t = 1100$ to $t = 1400$ will terminate the event gate that started with a muon crossing the entrance detector. $\varepsilon_{\text{non-terminated}}$ is estimated to be 0.2. A more detailed description of the background and detection scheme can be found in the PhD thesis of Laura Sinkunaite [83].

Chapter 4

Spectroscopy aspects of the HFS experiment

4.1 The transition probability

An accurate calculation of the transition probability from $F = 0$ to $F = 1$ is a key factor in determining the experimental requirements. We carried out a calculation of the transition probability [4] in which the decoherence effects due to the laser bandwidth and collisional effects were taken into account in the optical Bloch equations (density matrix formalism). This calculation, under variable experimental conditions, was used alongside the diffusion simulation to determine the required laser fluence, the performance of the multi-pass cell, and the total energy of the laser pulse. In addition, this calculation allows the quantification of the effect of the laser bandwidth and of the target parameters (pressure and temperature) on the transition probability which is essential in optimising the experimental setup. The combined probability of a laser excitation $F = 0$ to $F = 1$ followed by collisional de-excitations where the μp atoms gain a kinetic energy of 100 meV was computed. This computation was done by applying the optical Bloch equations to the three level system shown in Fig. 4.1. ρ_{11} and ρ_{22} are the population of the thermalised singlet and triplet states respectively. ρ_{33} describes the population of the state where μp atoms have a kinetic energy of around 100 meV. ρ_{33} is the relevant quantity for the experiment, and we refer to it for simplicity in this thesis as the "transition probability". The μp atoms in the ρ_{33} are far detuned from the resonance frequency and, therefore, cannot go through another cycle of the laser excitation.

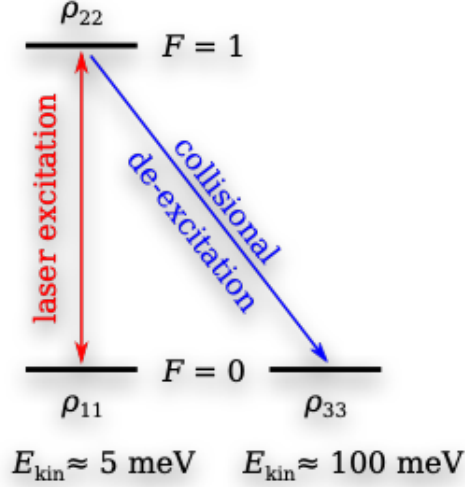


Figure 4.1: Three-level system described by the Bloch equations. The thermalised singlet and triplet states are described by ρ_{11}, ρ_{22} , respectively. ρ_{33} describes the level where the μp atom goes through a laser excitation followed by a collisional de-excitation, acquiring an average kinetic energy of 100 meV. Figure is reprinted from [4].

The Bloch equations describing the three level system is given by [4]

$$\begin{aligned}
 \frac{d\rho_{11}}{dt}(t) &= -\text{Im}\left(\Omega\rho_{12}e^{i\Delta t}\right) + \Gamma_{\text{sp}}\rho_{22}, \\
 \frac{d\rho_{22}}{dt}(t) &= \text{Im}\left(\Omega\rho_{12}e^{i\Delta t}\right) - (\Gamma_i + \Gamma_{\text{sp}})\rho_{22}, \\
 \frac{d\rho_{12}}{dt}(t) &= \frac{i\Omega^*}{2}(\rho_{11} - \rho_{22})e^{-i\Delta t} - \frac{\Gamma_c}{2}\rho_{12}, \\
 \frac{d\rho_{33}}{dt}(t) &= \Gamma_i\rho_{22},
 \end{aligned} \tag{4.1}$$

where ρ_{12} describes the coherence between ρ_{11} and ρ_{22} . $\Delta = \omega - \omega_r$ represents the laser detuning from the resonance frequency ω_r . Γ_i is the inelastic collision rate from ρ_{22} to ρ_{33} . Γ_{sp} is the spontaneous radiative decay from the triplet state $F = 1$. The decoherence rate is given by

$$\Gamma_c = 2\pi\Delta_l + \Gamma_e^{00} + \Gamma_e^{11} + \Gamma_i + \Gamma_{\text{sp}}, \tag{4.2}$$

where Δ_l is laser bandwidth, $\Gamma_e^{00}, \Gamma_e^{11}$ are the elastic collisional rates defined in Eq.3.1a and 3.1d. Ω is the Rabi frequency defining the coupling strength between the laser intensity \mathcal{I}

and the transition matrix element \mathcal{M} , where

$$\Omega = \sqrt{\frac{8\pi\alpha\mathcal{I}}{\hbar}}\mathcal{M}. \quad (4.3)$$

The Doppler effect is accounted for by convoluting the population ρ_{33} , with a Gaussian distribution representing the Doppler profile, where the Doppler standard deviation is given by

$$\sigma_D \simeq 12.7\sqrt{T} \text{ [MHz]}, \quad (4.4)$$

and T is the temperature. Through the numerical integration of the Bloch equations, the excitation probability $\bar{\rho}_{33}$ at different experimental conditions was calculated in [4]. The bar in $\bar{\rho}_{33}$ indicates it accounted for the Doppler effect. By calculating $\bar{\rho}_{33}$ for different values of the laser frequency detuning, the line-shapes of Fig. 4.2 were obtained. The four panels show how the transition probabilities and the line-shapes are affected by the laser bandwidth and fluence. Each panel shows the dependence on the target parameters through the collisional effects and the Doppler broadening.

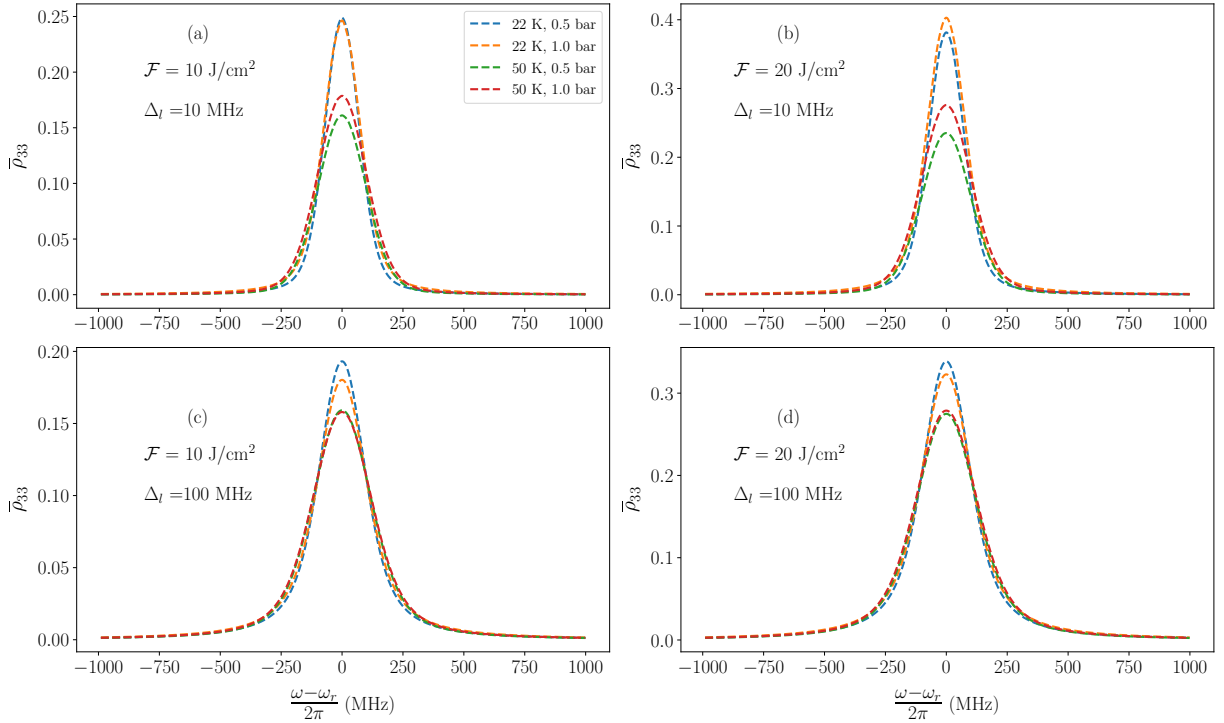


Figure 4.2: Line-shapes of the excitation probability around the resonance for two laser fluence (\mathcal{F}) values, each at two laser bandwidths Δ_l . Courtesy of Miguel Ferro.

Table 4.1 compares the value of the excitation probability $\bar{\rho}_{33}$ and linewidth for different laser bandwidth, laser fluence and target conditions

					$\mathcal{F} = 10 \text{ J/cm}^2$		$\mathcal{F} = 20 \text{ J/cm}^2$	
					$(\Omega = 8\text{MHz})$		$(\Omega = 11\text{MHz})$	
p [bar]	T [K]	Δ_l [MHz]	Γ_c [MHz]	σ_D [MHz]	Γ [MHz]	$\bar{\rho}_{33}$	Γ [MHz]	$\bar{\rho}_{33}$
0.5	22	100	770	60	228	0.19	232	0.33
1	22	100	913	60	242	0.18	256	0.32
0.5	22	10	205	60	167	0.25	176	0.38
1	22	10	348	60	183	0.25	187	0.40

Table 4.1: A comparison of the different values of the excitation probability obtained through numerical integration of the Bloch equations $\bar{\rho}_{33}$. The table shows the experimental conditions at different sets of temperature (T), pressure (p), laser bandwidth (Δ_l) and fluence (\mathcal{F}). Γ is the full width at half maximum (FWHM) of $\bar{\rho}_{33}$ which estimates the line-shape around the resonance frequency ω_r . The table values were adapted from [4].

At a fluence of 10 J/cm^2 , and a laser bandwidth of 10 MHz , we obtain an excitation probability $\bar{\rho}_{33} \approx 25\%$ and a linewidth FWHM of 167 MHz for $T = 22 \text{ K}, p = 0.5 \text{ bar}$. As we will see in Sec. 4.2, our experiment is strongly limited by statistics. This calls for maximising $\bar{\rho}_{33}$ which is achieved through increasing the laser fluence and minimising the laser bandwidth. Our goal in the experiment is to have a bandwidth $< 20 \text{ MHz}$. If this is achieved, the FWHM of $\bar{\rho}_{33}$ line-shape is not basically affected by the laser bandwidth. If only a 100 MHz laser bandwidth will be obtained, the transition probability is decreased by a factor $\bar{\rho}_{33}(\Delta_l=100\text{MHz})/\bar{\rho}_{33}(\Delta_l=10\text{MHz}) = 0.76$ at our optimal experimental conditions. The impact of $\bar{\rho}_{33}$ and linewidth on the signal rate and consequently on the precision of the measurement as well as the time needed to search for the resonance will be discussed in Sec. 4.2.

4.1.1 Excitation probability from the fluence distribution

The study of the fluence distribution reveals its impact on the average laser-induced excitation probability and the saturation effects on the excitation probability. Different fluence distributions, even with equal average fluence, can lead to variations in average excitation probability. For this reason, fluence distributions should have minimum local hot spots with

fluence values close to saturation values. The fluence distribution and the corresponding transition probability are shown in Fig. 4.3(a),4.3(b), respectively, for the toroidal copper cell with reflectivity of 99.2%. The saturation effects are visible for fluence values above 10 J/cm². The results in Fig. 4.3(a),4.3(b) are obtained assuming a laser pulse energy $E = 1\text{mJ}$ and a laser bandwidth of 100 MHz at the target temperature of 22 K and a pressure of 0.5 bar. An average fluence of 1.4 J/cm² is obtained from the toroidal cell with a 99.2% reflectivity assuming a laser pulse energy of 1 mJ where the volume of interest is of 1 mm thickness and a diameter of 10 mm. Figure 4.4 illustrates the relationship between average fluence (\bar{F}) and excitation probability ($\bar{\rho}_{33}$), showing a linear trend for fluence values below $\bar{F} = 20\text{J/cm}^2$. This highlights the significant impact of high laser pulse energy on excitation efficiency.

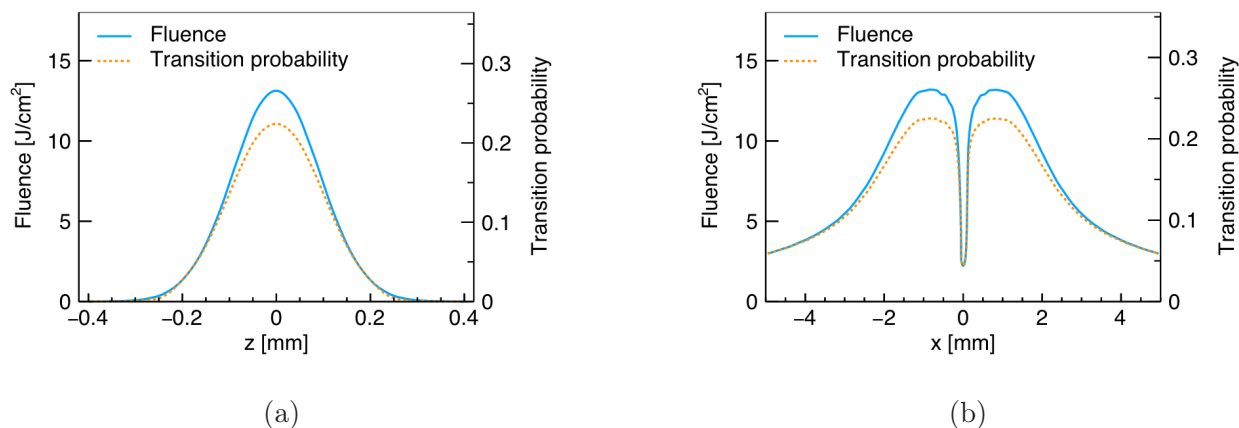


Figure 4.3: (a) Representation of the fluence distribution along the thickness of the target volume (z direction) in blue. The dotted curve represents the transition probability corresponding to the fluence. (b) Same as (a) but showing the fluence distribution and corresponding transition probability for the transverse x-direction. The simulation presented in (b) and (c) are for a laser pulse energy of 1 mJ, reflectivity of 99.2% of the multi-pass cell, target pressure of 0.5 bar and temperature of 22 K. Figure is reprinted from [5] and [3].

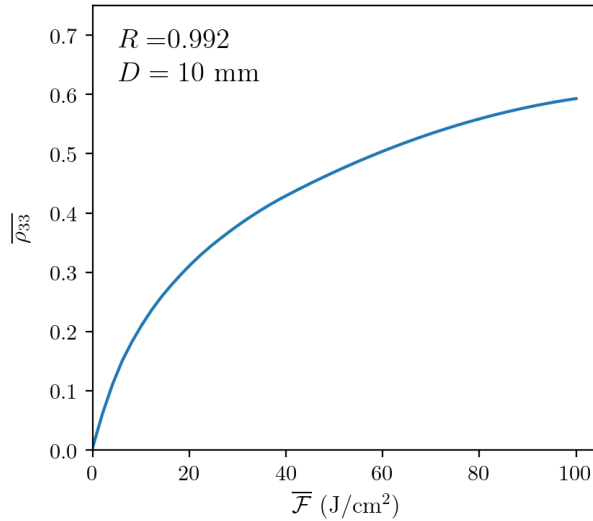


Figure 4.4: Combined laser excitation probability followed by collisional de-excitation against the average fluence for a volume diameter of 10 mm, cell reflectivity of 99.2%, laser bandwidth of 10 MHz and a 50 ns pulse length. Courtesy of Miguel Ferro.

4.2 Rates of signal and background

To predict the signal and background rates, it is necessary to fully consider the diffusion processes of the μp atoms in the target, the fluence distribution within the target volume, the excitation probability calculation, and the detection efficiency. The rate of signal events is given by

$$\begin{aligned}
 R_{\text{signal}} &= P_{\text{signal}} \cdot R_{\mu} \cdot \varepsilon_{\text{Au}} \\
 &= 2.5 \times 10^{-4} \cdot 500[1/\text{s}] \cdot 0.7 = 0.088 \text{ 1/s},
 \end{aligned}
 \tag{4.5}$$

where P_{signal} is the probability that a muon passes the entrance detector, creates a μp atom which will undergo a laser excitation then eventually creating a μAu atom. P_{signal} has been calculated by combining the diffusion calculation with the laser excitation. The value P_{signal} of 2.5×10^{-4} quoted here is extracted from the orange curve in Fig. 3.4 for the event time window. For more details on this, we refer the reader to Sec. 7.3 in [5]. R_{μ} is the muon rate, and ε_{Au} is the detection efficiency of a μAu event.

To achieve sufficient signal statistics over the background, the signal-to-noise ratio ($R_{\text{signal}}/\sqrt{R_{\text{BG}}}$) must be maximized by selecting optimal target and experimental conditions. The time needed to expose a statistical significance of 4σ to background is defined

by

$$t_{4\sigma} = 16 \frac{R_{\text{BG}}}{R_{\text{signal}}^2}. \quad (4.6)$$

The optimum experimental conditions are those for which the time $t_{4\sigma}$ is minimised. A comparison of the different experimental conditions are shown in Tab.4.2 which was adapted from the full study of the different experimental conditions in [5].

Δ_l [MHz]	d [mm]	p [bar]	R_{Signal} [1/s]	R_{BG} [1/s]	$R_{\text{Signal}} / R_{\text{BG}}$	$t_{4\sigma}$ [min]
100	1.0	0.5	$7.7 \cdot 10^{-3}$	0.74	$1.0 \cdot 10^{-2}$	34
100	1.0	0.6	$8.8 \cdot 10^{-3}$	0.89	$9.8 \cdot 10^{-3}$	31
100	1.2	0.5	$7.0 \cdot 10^{-3}$	0.86	$8.0 \cdot 10^{-3}$	48
100	1.2	0.6	$7.4 \cdot 10^{-3}$	1.20	$7.3 \cdot 10^{-3}$	50
10	1.0	0.5	$1.2 \cdot 10^{-2}$	0.74	$1.6 \cdot 10^{-2}$	15
10	1.0	0.6	$1.3 \cdot 10^{-2}$	0.89	$1.5 \cdot 10^{-2}$	14
10	1.2	0.5	$1.1 \cdot 10^{-2}$	0.86	$1.2 \cdot 10^{-2}$	21

Table 4.2: Time needed to expose a 4σ statistical significance of signal over background ($t_{4\sigma}$) at various experimental conditions. A target thickness d below 1 mm can lead to smaller $t_{4\sigma}$ but can not be realized practically due to diffraction losses. These numbers were obtained assuming a laser pulse of a 1 mJ energy and 50 ns length coupled into the multi-pass cell which has a reflectivity of 99.2%. The table is adapted from [5].

Looking at the numbers in Tab.4.2, we see that the laser bandwidth (Δ_l) decreases the time needed for the sufficient statistics by a factor of 2 at the same target conditions of thickness and pressure. Moreover, the signal rate R_{signal} is linearly proportional to the laser fluence in the muon stopping volume hence the laser energy, if we avoid the saturation effects.

4.3 Time needed to search for the resonance

The search range is determined by the uncertainty in the theoretical prediction. To adopt a conservative approach, we define a search range corresponding to 50 GHz. Since the linewidth of the HFS transition is approximately 230 MHz, as shown in Fig .4.2 [4], the resonance has to be searched for in steps of about 100 MHz. The total time required to search for the resonance across this range is given by:

$$\begin{aligned} t_{\text{search}} &= N_{\text{steps}} \times (1.4t_{4\sigma} + t_{\lambda\text{-change}}) \frac{1}{\varepsilon_{\text{uptime}}} \\ &= 500 \times (1.4 \times 60(\text{mins}) + 60(\text{min})) \frac{1}{0.7} \approx 10 \text{ weeks}, \end{aligned} \quad (4.7)$$

where N_{steps} is the number of frequency points required to search for the resonance, $t_{\lambda\text{-change}} = 60$ min is the time needed to change the laser frequency, $t_{4\sigma} = 60$ min is the time required for sufficient statistical significance at each step, and $\varepsilon_{\text{uptime}}$ represents the accelerator uptime of 70%. The factor of 1.4 multiplying $t_{4\sigma}$ accounts for the possibility that the resonance may lie between two points separated by less than 100 MHz [2]. This calculation demonstrates that, even under the most conservative assumptions regarding the laser system, detection scheme, and diffusion process, the resonance can be identified within approximately 10 weeks of beam time.

Once the resonance is located, a more precise determination of the centroid position can be achieved by accumulating additional statistics in the range $v_0 - 150 \text{ MHz} \leq v \leq v_0 + 150 \text{ MHz}$, where v_0 is the resonance frequency. Figure 4.5(a) shows a simulation of 10^5 pseudo-measurements for a laser pulse energy of 1 mJ and a bandwidth of 100 MHz. From these plots, the resonance centroid is determined, and the associated statistical uncertainty is extracted. The results indicate that even under conservative assumptions, an accuracy of a few MHz, corresponding to 0.1 ppm, can be achieved, which is an order of magnitude better than the anticipated experimental accuracy.

Figure 4.5(b) highlights the impact of laser bandwidth on statistical uncertainty. Reducing the bandwidth from 100 MHz to 10 MHz halves the resonance position uncertainty, a much larger effect compared to increasing the laser pulse energy by a factor of 1.5. While both enhancements improve the experiment's precision, a narrower bandwidth has a more substantial impact. To meet experimental requirements, the laser system should deliver around 4 mJ of pulse energy, accounting for 50% transmission losses before coupling into the multi-pass cell, and maintain a bandwidth of less than 100 MHz.

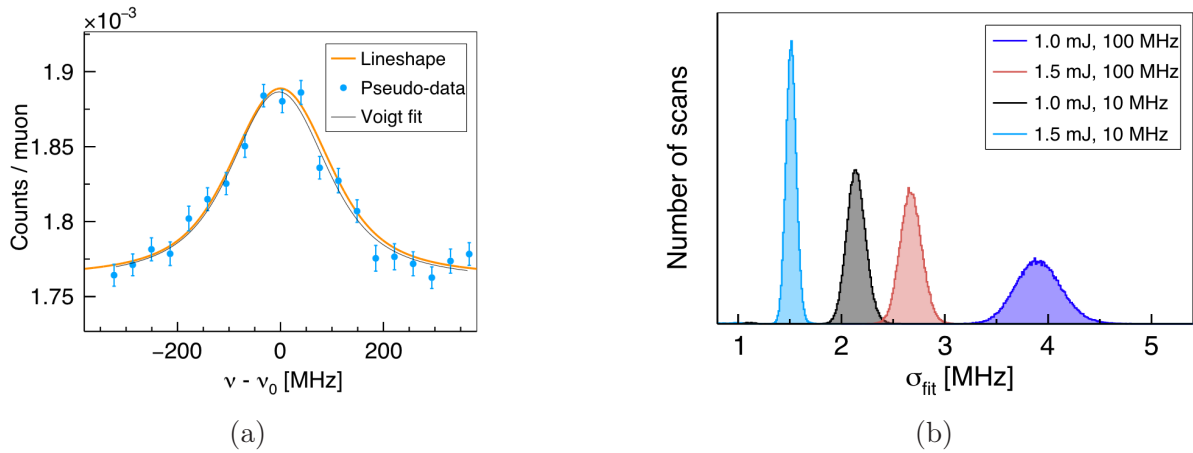


Figure 4.5: Monte Carlo simulation of resonance measurements assuming two weeks of data collection. (a) Line shape for a laser pulse energy of 1 mJ and bandwidth of 100 MHz. (b) Statistical uncertainty of the resonance position for various laser system energies and bandwidths. Figure is reprinted from [5].

Chapter 5

The HyperMu laser system

In the previous chapters, we have established the processes that determine the the laser system requirements. The transition probability requires a high laser pulse energy up to 4 mJ and a bandwidth of less than 100 MHz. The theoretical prediction for the HFS transition requires a wavelength of approximately $6.8 \mu\text{m}$ while theoretical uncertainty requires a tunability of the laser by around 50 GHz. The laser is triggered on each muon entering the H_2 target at stochastic times. Once triggered, the laser pulse need to be delivered within $1 \mu\text{s}$, due to the muon lifetime.

5.1 The general scheme

No laser exists at $6.8 \mu\text{m}$ that is capable of delivering few mJ pulse energy at fast triggers, which is the reason why we based our laser system on the well established thin-disk laser operating at a wavelength of 1030 nm with a short delay ($< 1 \mu\text{s}$) [84]. The pulses generated at 1030 nm are then frequency shifted to $6.8 \mu\text{m}$ through a series of down conversion stages.

The laser system we are developing is shown in Fig. 5.1. It starts with an injection-seeded Q-switched thin-disk oscillator at 1030 nm, which produces pulses with energy of 50 mJ and a pulse length of about 50 ns. The oscillator is followed by a multi-pass amplifier that boosts the energy up to 330 mJ. The thin-disk oscillator-amplifier system is followed by two branches of parametric down-conversion stages in forms of Optical-Parametric-Oscillators

(OPO), optical-parametric-amplifiers (OPA) followed by a difference frequency generation (DFG) stage. The output of the DFG stage is then coupled into the multi-pass cell in which the pulses go through hundreds of reflection to enhance the excitation probability. The first OPO branch (OPO1) is injection seeded at 1532 nm by a CW-laser and pumped at 1030 nm by the single-frequency pulse of the thin-disk laser to produce pulses with 50 ns pulse length at 1532 nm (signal) and 3142 nm (idler). The pulses at the idler wavelength (3142 nm) is sent into an OPA that is pumped again with 1030 nm pulses to amplify them up to 3.4 mJ. The second OPO (OPO2) which is injection seeded by a CW-laser at 1979 nm, is pumped by 1030 nm pulses to produce signal and idler pulses at 1979 nm and 2148 nm, respectively. OPO2 is also followed by an OPA that is pumped by pulses at 1030 nm to amplify the idler pulses at 2148 nm. At the end, the outputs of both branches at 3142 nm and 2148 nm are mixed in what is called difference frequency generation to produce pulses at a wavelength tunable around $6.8 \mu\text{m}$.

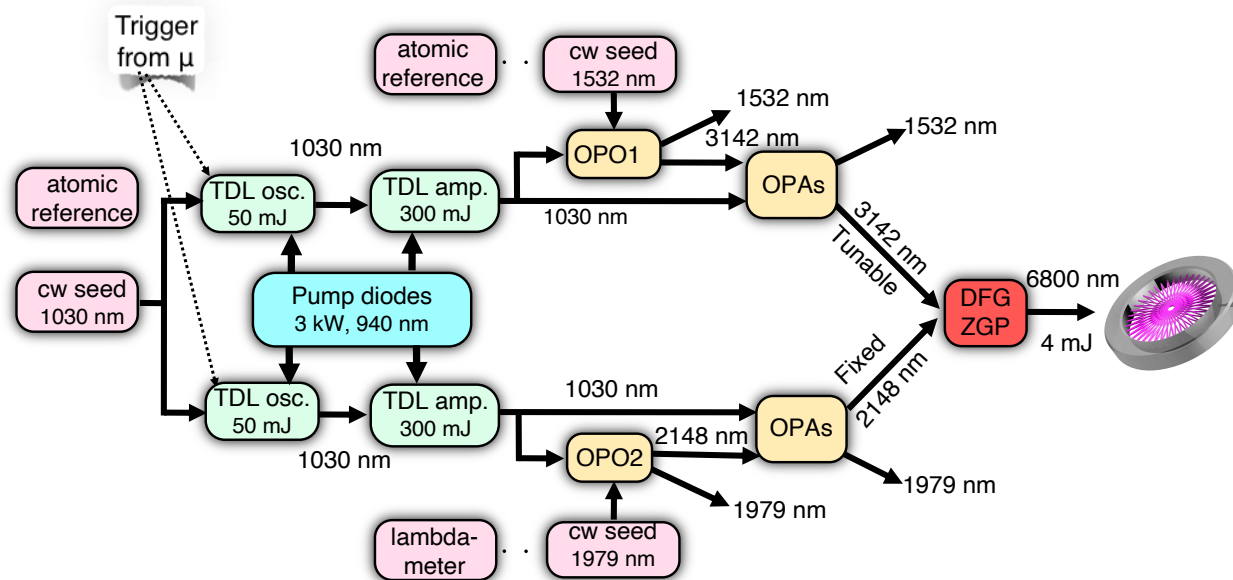


Figure 5.1: The HyperMu laser system. A detailed description is given in the text.

5.1.1 Tunability and frequency control

The frequency control of the laser system is achieved through stabilizing the frequencies of the three seed lasers. The frequency of the spectroscopy at $6.8 \mu\text{m}$ is then tuned by shifting the frequency of the OPO1 seed laser while keeping the seed laser frequency of OPO2 fixed.

To ensure a single frequency operation, the thin-disk oscillator length is stabilised via Pound-Drever-Hall lock technique [84] to the frequency of its seed laser. The seed laser in turn has its frequency stabilised to a wave meter. The same technique is used to stabilize the OPOs cavities to their corresponding seed lasers. In order to cover the theoretical uncertainty of the HFS, we need to scan our final laser frequency by a 50 GHz. This corresponds to changing our laser wavelength from 6783 nm to 6793 nm. To produce this wavelength range, the seed laser of OPO1 need to be tuned from 1532.58 nm to 1532.0 nm resulting in an idler wavelength range from 3140.9 nm to 3143.3 nm.

5.2 Down-conversion scheme

This section discusses the down-conversion scheme in the laser system, which uses nonlinear optical processes to convert 1030 nm to 6788 nm. This process depends on factors such as the properties of the nonlinear materials and the input laser beam parameters. Using the SNLO program [85], simulations begin with the DFG stage, targeting 4 mJ at 6788 nm. From this requirement, we calculate the input energies needed from the preceding branches. These inputs guide simulations of the earlier OPA stages, enabling us to determine the required gain, crystal properties (e.g. length), input energy, and beam size for each stage.

Key concepts and formulas related to nonlinear optical processes are introduced, focusing on DFG, with many principles also applicable to parametric amplification, discussed later in the OPA and the OPO context in this chapter and the next capter. These principles are used to analyze the simulation parameters and results. We also provide a brief overview of laser beam properties, which are essential for understanding the beam parameter results obtained from the simulations.

5.2.1 Difference frequency generation (DFG)

In optical materials, the polarization induced by an electric field can typically be described by a linear relationship, where the polarization \vec{P}^L is directly proportional to the applied electric field \vec{E} through the linear susceptibility $\chi^{(1)}$. This linear response governs most everyday optical phenomena, such as refraction and diffraction, where the material responds

predictably without generating new frequencies.

However, in materials with nonlinear properties, the induced polarization \vec{P} becomes a nonlinear function of the electric field, expressed as a series expansion [6]:

$$\vec{P} = \epsilon_0 \left[\chi^{(1)} \cdot \vec{E} + \chi^{(2)} \cdot \vec{E} \cdot \vec{E} + \chi^{(3)} \cdot \vec{E} \cdot \vec{E} \cdot \vec{E} + \dots \right] = \vec{P}^L + \vec{P}^{NL}, \quad (5.1)$$

where ϵ_0 is the permittivity of vacuum, $\chi^{(1)}$ is the linear electric susceptibility defined by $\chi^{(1)} = n^2 - 1$, where n is the refractive index of the material, and $\chi^{(2)}, \chi^{(3)}$ are the second and the third order electric susceptibilities. \vec{P}^L, \vec{P}^{NL} describe the linear and nonlinear induced polarization density. These nonlinear effects become significant under strong electric fields, enabling interactions between light waves, such as frequency mixing and generation of new optical frequencies.

We focus on $\chi^{(2)}$, the second-order susceptibility, to describe the nonlinear processes in a down-conversion scheme. Consider the optical field consisting of two distinct frequency components incident upon a nonlinear optical medium:

$$\begin{aligned} \vec{E}(t) &= \vec{E}_1 \cos(\omega_1 t) + \vec{E}_2 \cos(\omega_2 t) = \text{Re} \left\{ \vec{E}_1 e^{i\omega_1 t} + \vec{E}_2 e^{i\omega_2 t} \right\} \\ &= \frac{1}{2} \left(\vec{E}_1 e^{i\omega_1 t} + \vec{E}_2 e^{i\omega_2 t} + \vec{E}_1^* e^{-i\omega_1 t} + \vec{E}_2^* e^{-i\omega_2 t} \right) \\ &= \frac{1}{2} \vec{E}_1 e^{i\omega_1 t} + \frac{1}{2} \vec{E}_2 e^{i\omega_2 t} + c.c., \end{aligned} \quad (5.2)$$

where $c.c.$ is the complex conjugate. The second-order nonlinear polarization is $P^{(2)}(t) = \epsilon_0 \chi^{(2)} E(t)^2$ leads to:

$$\begin{aligned} \vec{P}^{(2)}(t) &= \epsilon_0 \chi^{(2)} \frac{1}{4} \left(\vec{E}_1 e^{i\omega_1 t} + \vec{E}_2 e^{i\omega_2 t} + \vec{E}_1^* e^{-i\omega_1 t} + \vec{E}_2^* e^{-i\omega_2 t} \right)^2 \\ &= \epsilon_0 \chi^{(2)} \frac{1}{4} \left[\vec{E}_1^2 e^{2i\omega_1 t} + \vec{E}_2^2 e^{2i\omega_2 t} + 2\vec{E}_1 \vec{E}_2 e^{i(\omega_1 + \omega_2)t} + 2\vec{E}_1 \vec{E}_2^* e^{i(\omega_1 - \omega_2)t} + c.c. \right] \\ &+ \epsilon_0 \chi^{(2)} \frac{1}{2} \left(\vec{E}_1 \vec{E}_1^* + \vec{E}_2 \vec{E}_2^* \right). \end{aligned} \quad (5.3)$$

This expression includes various frequency-mixed terms resulting from the interaction of the electric field components with themselves and with the polarization densities.

Of particular interest here is the difference frequency generation component, represented as:

$$\vec{P}(\omega_1 - \omega_2) = \epsilon_0 \chi^{(2)} \vec{E}_1 \vec{E}_2^*, \quad (5.4)$$

which describes a nonlinear optical process where two photons of different frequencies ω_1 (pump) and ω_2 (signal) interact within a nonlinear medium, such as a Zinc Germanium

Phosphide (ZGP) crystal, to generate a new photon with a frequency equal to the difference between the original frequencies. This process is governed by the principles of energy and momentum conservation shown in Fig. 5.2, often referred to as phase matching given by:

$$\omega_i = \omega_p - \omega_s. \quad (5.5)$$

$$\Delta k = k_s + k_i - k_p = 0. \quad (5.6)$$

Here, ω_p and \vec{k}_p are the frequency and wave vector of the pump beam, ω_s and \vec{k}_s are the frequency and wave vector of the signal beam, ω_i and \vec{k}_i are the frequency and wave vector of the idler beam.

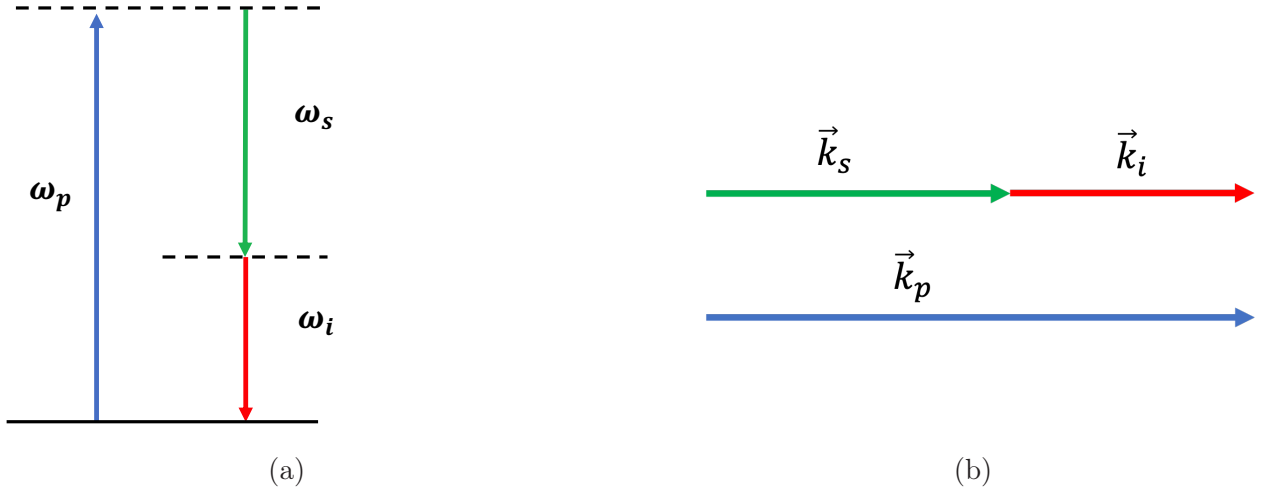


Figure 5.2: Conservation principles in the DFG process [6]: (a) Energy conservation. (b) Momentum conservation: collinear phase matching.

In our notation, the pump is the photon with the highest frequency (lowest wavelength), the one with the lowest frequency is called the idler (longest wavelength), and the signal refers to the photon with frequency in between the pump and the idler.

5.2.2 Phase matching and nonlinear coefficient

For collinear beams, Eq. 5.6 can be written in terms of frequencies and the refractive indices as:

$$n_i\omega_i + n_s\omega_s = n_p\omega_p. \quad (5.7)$$

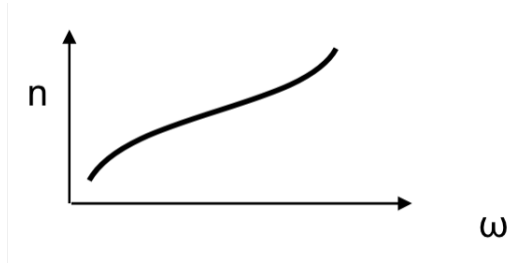


Figure 5.3: An example of the monotonic relation between the refractive index (n) and the frequency (ω) in lossless materials. Figure is reprinted from [7].

This relation can not be satisfied in lossless materials, because the refractive index has a monotonic relation with the frequency [7], shown in Fig. 5.3.

The common way to achieve phase matching is by using birefringence. Birefringence is the dependence of the refractive index on the direction of polarization of the optical radiation. A uniaxial crystal, the type used in our DFG stage, has two independent refractive indices, called ordinary index (n_o) and the extraordinary index (n_e), as shown in Fig. 5.4(a). Such a crystal has a symmetry axis (optical axis) named the c-axis and is usually aligned towards the z-axis in a rectangular coordinate system. Light polarized perpendicular to the plane defined by the propagation vector \vec{k} and the optical axis is called ordinarily polarized and experiences n_o . Light polarized within the plane containing \vec{k} and the optical axis (x-z plane) is extraordinarily polarized and experiences n_e . For light propagating at an angle θ relative to the z-axis in the x-z plane (Fig. 5.4(b)), one field polarization lies in x-y plane and experiences n_o , while the orthogonal polarization lies in the x-z plane and experiences a refractive index dependent on θ

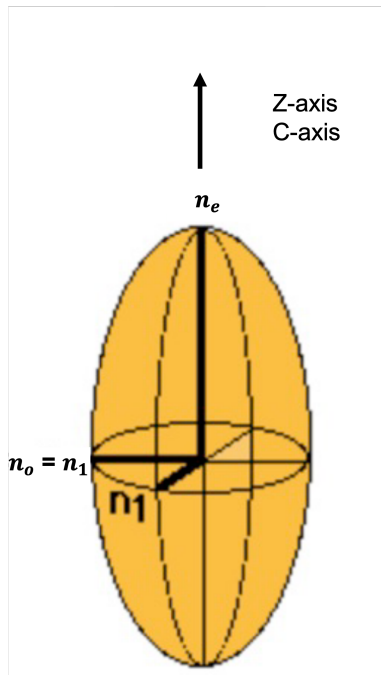
$$n_e(\theta) = \frac{n_o n_e}{[n_e^2 \cos^2(\theta) + n_o^2 \sin^2(\theta)]^{1/2}}. \quad (5.8)$$

Birefringent phase matching can be categorised into three types. In type *I* phase matching, the signal and idler waves have the same polarization, which differs from the pump polarization. This can be described using the notation $p \rightarrow s + i$ as

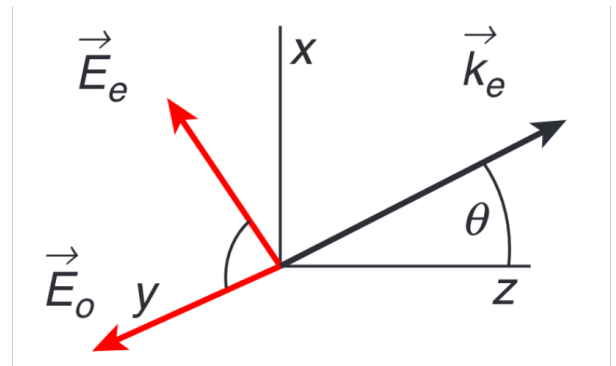
$$o \rightarrow e + e \quad \text{or} \quad e \rightarrow o + o.$$

In contrast, type II and type III phase matching involve the signal and idler waves having orthogonal polarizations. These cases can be expressed as

$$o \rightarrow e + o, \quad o \rightarrow o + e,$$



(a)



(b)

Figure 5.4: (a) The index ellipsoid of a uniaxial crystal, illustrating the optical axis and the two principal refractive indices. (b) Angle tuning by varying the angle θ relative between \vec{k}_e and the optical axis. \vec{E}_e and \vec{E}_o correspond to the light polarized in the extraordinary and the ordinary direction. The figure in (b) is reprinted from [7].

or

$$e \rightarrow e + o, \quad e \rightarrow o + e.$$

By Combining Eq. 5.7 and Eq. 5.8, one can obtain the condition of type *I* phase matching for the DFG process using a positive uniaxial crystal ($n_e > n_o$) [86]:

$$n_o(\omega_p)\omega_p - n_e(\omega_s, \theta)\omega_s = \omega_i \sqrt{\left(\frac{\sin^2 \theta_{pm}}{[n_e(\omega_i)]^2} + \frac{1 - \sin^2 \theta_{pm}}{[n_o(\omega_i)]^2}\right)^{-1}}, \quad (5.9)$$

where θ_{pm} is the phase matching angle. This phase matching through angle tuning is realized by either rotating the angle of the optical axis of the crystal relative to the incident laser, or by inducing a cut in the crystal so that the incident light and the optical axis are at an angle θ .

The nonlinear susceptibility experienced by light within the crystal is influenced by its propagation direction relative to the optical axis. This is characterised by the dielectric constant which is proportional to the non-linear susceptibility $d_{ijk} = \chi_{ijk}^{(2)}/2$. Since the dielectric constant is a tensor, it is typically represented by d_{eff} called usually the nonlinear coefficient, which depends on the phase-matching type and the angle θ mentioned above.

5.2.3 Conversion efficiency

The conversion efficiency of the DFG is defined as the ratio of the output intensity at the idler wavelength to the incident pump intensity, expressed as $\eta_p = I_{\text{out}}/I_p$. For the DFG, the conversion efficiency and idler intensity are given by [86,87]

$$\eta_p = 2 \frac{\omega_i^2 d_{\text{eff}}^2 L^2 I_s}{c^3 \varepsilon_0 n_p n_s n_i} \text{sinc}^2 \left(\frac{\Delta k L}{2} \right), \quad (5.10)$$

$$I_{\text{DFG}} = \eta_p I_p,$$

where I_s is the intensity of the input beam at the signal wavelength, ω_i is the frequency of the generated light (idler), L is the length of the interaction path of the input beams within the crystal, Δk is the phase mismatch, c is the speed of light, n_p, n_s, n_i are the refractive indices of pump, signal, and idler, respectively. While the conversion efficiency can also be defined relative to I_s , we adhere to the pump intensity-based definition. For pulsed lasers, the beam intensity I is related to the pulse energy E by $I = \frac{E}{\tau A}$, where τ is the pulse duration, and A is the beam area.

Equation 5.10 shows that the conversion efficiency scales with the square of d_{eff} which in turn depends on the nonlinear material chosen, the type of phase matching and the angle of the incident light at the crystal. It also shows that the conversion efficiency scales with the crystal length. The output intensity of the DFG scales with the pump intensity. However, high pump intensities can trigger competing nonlinear effects, such as optical parametric generation or amplification, limiting efficiency. Similarly, increasing L may introduce walk-off in birefringent materials, where interacting beams diverge due to phase mismatch. Maximum efficiency is achieved under perfect phase matching $\Delta k = 0$, assuming no losses or beam focusing effects.

Beam focusing impacts efficiency and is captured by the function $h(\mu, \xi_s, \rho)$, modifying Eq. 5.10 to [88, 89]:

$$\eta_p = 2 \frac{\omega_i^2 d_{\text{eff}}^2 L^2 I_s}{n_p n_s n_i c^3 \varepsilon_0} h(\mu, \xi_s, \rho), \quad (5.11)$$

where $\mu = k_s/k_p$, ρ is the walk-off angle, and $\xi_{s,p} = L/(k_{s,p} w_{s,p}^2)$ relates to beam waist w_s, w_p of the signal and the idler, respectively. For optimal focusing $h(\mu, \xi, \rho) \sim 1$ [90] and minimal walk-off, the efficiency approaches the maximum theoretical value. However, $h(\mu, \xi, \rho) \leq 1$ generally reduces efficiency compared to ideal conditions.

5.2.4 Laser beam quality

An ideal laser beam in the transverse TEM₀₀ mode has a Gaussian intensity profile, (shown in Fig. 5.5) and is described by

$$I(r) = I_0 \exp\left(\frac{-2r^2}{w(z)^2}\right), \quad (5.12)$$

where I_0 is the peak intensity, r is the radial distance, and $w(z)$ is the beam radius at $1/e^2$ (13.5%) of I_0 . The minimum value of $w(z)$ is called the beam waist denoted by w_0 . The beam waist w_0 evolves with the propagation as

$$w^2(z) = w_0^2 \left(1 + \frac{z^2}{z_R^2}\right), \quad (5.13)$$

with the Rayleigh length $z_R = \frac{\pi w_0^2}{\lambda}$ where λ is the wavelength. z_R refers to the position at which $w(z_R) = \sqrt{2}w_0$. Key beam radius metrics include the full width at half maximum (FWHM), related to $w(z)$ by a factor of 1.18, and $D_{4\sigma}$, which accounts for deviations from

the ideal Gaussian shape to the elliptical shape. Beam quality is evaluated using the M^2 factor, which quantifies deviations from ideal Gaussian behavior ($M^2 = 1$ for perfect beams). Using the definition of $D_{4\sigma}$, the beam radius evolution in the different transverse directions is given by [91].

$$w_i^2(z) = w_{0i}^2 + \left(M_i^2\right)^2 \left(\frac{\lambda}{\pi w_{0i}}\right)^2 (z - z_{0i})^2, \quad (5.14)$$

where i refers to the transverse direction, w_{0i} is the beam waist radius in that direction, and z_{0i} is the beam waist position.

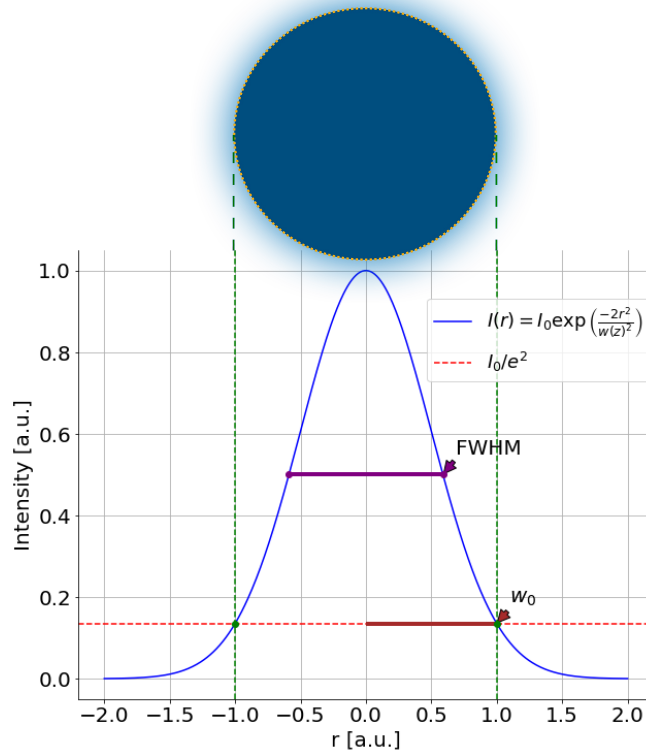


Figure 5.5: The Gaussian beam intensity profile. Beam waist (w_0) and the FWHM beam diameter are indicated.

5.2.5 The ZGP crystal

The Zinc Germanium Phosphide $ZnGeP_2$ (ZGP) crystal is an ideal gain medium for generating high-energy pulses around 6800 nm. It has a high nonlinear coefficient (75 pm/V), as well as a high damage threshold (up to 5 J/cm²), making it well-suited for high-energy

applications. ZGP offers excellent transparency in the mid-infrared range, with low absorption between 2000 nm and 8000 nm. The ZGP nonlinear figure of merit d_{eff}^2/n^3 establishes it as the most advanced nonlinear crystal for mid-IR applications [8, 92–94]. Figure 5.6 shows the transparency range and the nonlinear figure of merit of the most common nonlinear crystals for the mid-infrared region. While cadmium silicon phosphide (CSP) and orientation-patterned GaAs (OP-GaAs) crystals exhibit higher nonlinear figures of merit, CSP is challenging to grow in large sizes, and OP-GaAs is limited by sample thickness for high-energy generation. For ZGP, its transparency at 6800 nm ensures efficient light transmission and amplification without significant absorption. However, its absorption characteristics restrict the pump wavelength to above 2000 nm, necessitating a 2148 nm pump source. This, in turn, requires a signal wavelength of 3142 nm to generate pulses at 6788 nm, explaining the need for two OPO branches to produce the required wavelengths for the DFG stage.

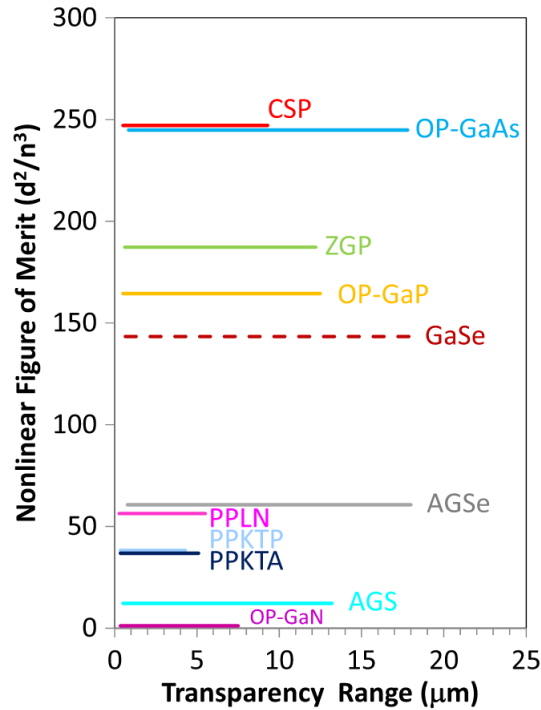


Figure 5.6: Nonlinear figure of merit d_{eff}^2/n^3 plotted against the transparency range of various mid-infrared nonlinear crystals. Figure is reprinted from [8].

5.2.6 Simulation of the DFG in the ZGP crystal

This section presents simulation results for the DFG stage using the software SNLO [85] with a ZGP crystal provided by BAE Systems. The crystal, of dimension 12 x 12 x 10 mm, is angle-cut at 50.8° relative to the z-axis for Type I phase matching. The pump beam (2148 nm) is S-polarized (ordinary), while the signal beam (3142 nm) is P-polarized (extraordinary). Within the crystal, these beams interact to generate an idler wave at around 6788 nm, which is also P-polarized. Here, S-polarization refers to light polarized perpendicular to the plane of incidence, and P-polarization refers to light polarized parallel to it.

The phase-matching conditions are obtained from the SNLO software, which provides the nonlinear coefficient d_{eff} and the refractive indices for the pump and signal wavelengths at the specified phase-matching angle. These parameters for the ZGP crystal are essential for the simulation, and their values are provided in Appendix. 5.A.

The simulation results shown in Fig. 5.7 explore the idler pulse energy as a function of the FWHM beam diameter for pump energies of 15 mJ, 20 mJ, and 25 mJ, with a constant signal pulse energy of 2.5 mJ. As expected from Eq. 5.10, the idler energy increases with pump energy. Beam size significantly affects conversion efficiency, with variations of up to 20% of the maximum obtainable output energy. For pump energies of 15 mJ and 20 mJ, smaller beam waists generally result in higher idler energies due to increased intensity within the crystal. However, beyond an optimal beam waist range, the idler energy may decrease due to factors like diffraction or walk-off, as described by Eq. 5.11.

At a pump energy of 25 mJ, the optimal FWHM beam diameter lies between 950 and 1000 μm . To verify that no back-conversion occurs, Fig. 5.8 plots the energy evolution and spatial characteristics of the output and input beams. For signal and pump beam diameters of 1000 μm , the output beam maintains excellent quality, as indicated by M^2 values close to 1.

To investigate the effect of signal energy (E_s) on DFG conversion efficiency, simulations were conducted for E_s ranging from 1 mJ to 3 mJ, paired with the three pump energy (E_p) values mentioned earlier. For $E_s = 1$ mJ and a beam size of 1000 μm , achieving idler energy above 4.5 mJ requires E_p up to 30 mJ, increasing the demands on the 2.1 μm OPO/OPA branch. Maintaining E_p between 20–25 mJ while achieving similar idler energy necessitates

a 25% reduction in beam size, raising the risk of crystal damage.

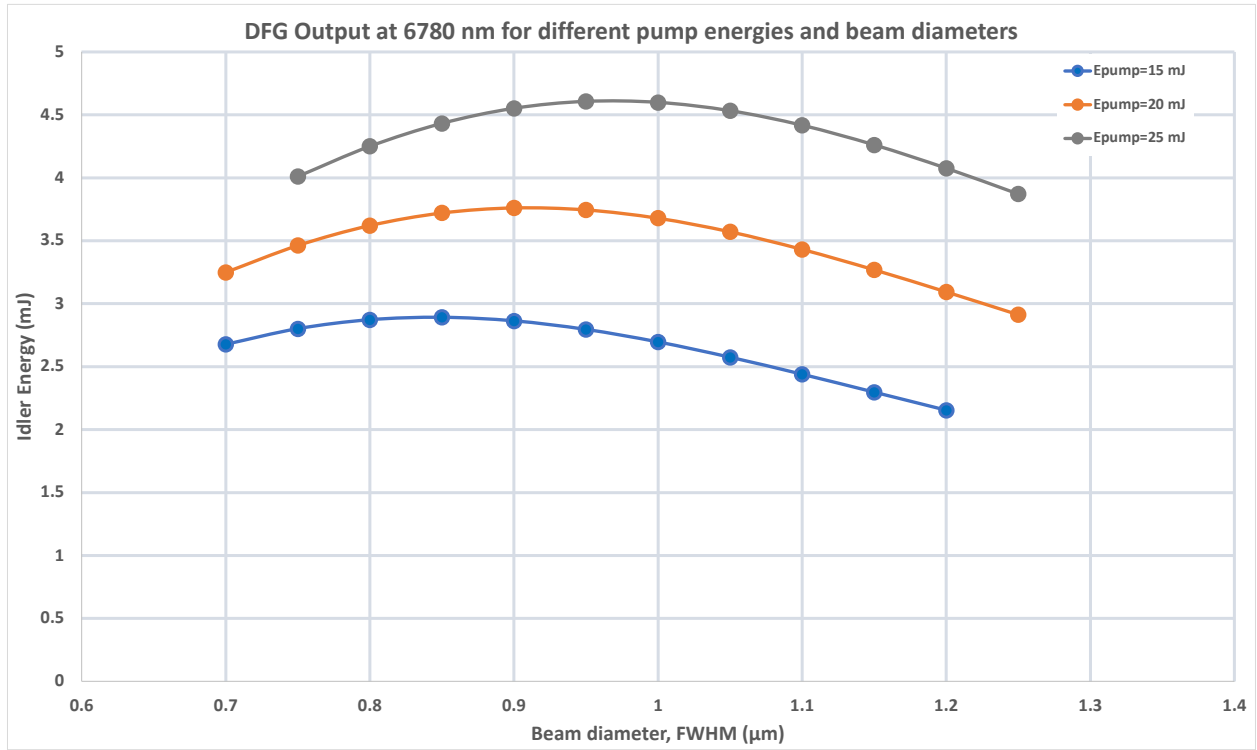
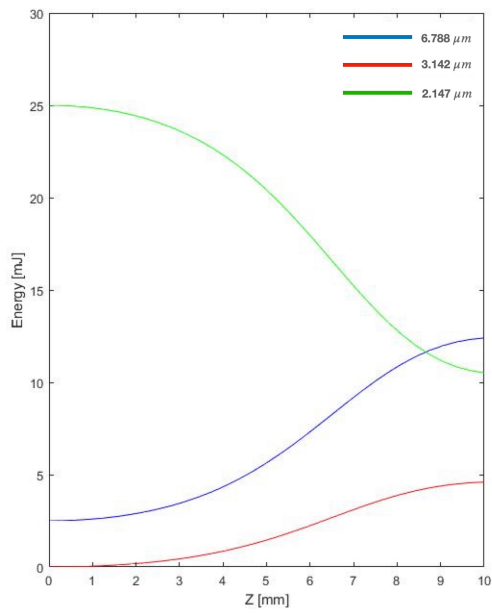


Figure 5.7: Simulated idler energy at 6788 nm from the DFG simulation in a ZGP crystal, plotted against FWHM beam diameter for pump energies of 15 mJ, 20 mJ, and 25 mJ, with a fixed input signal energy of 2.5 mJ.

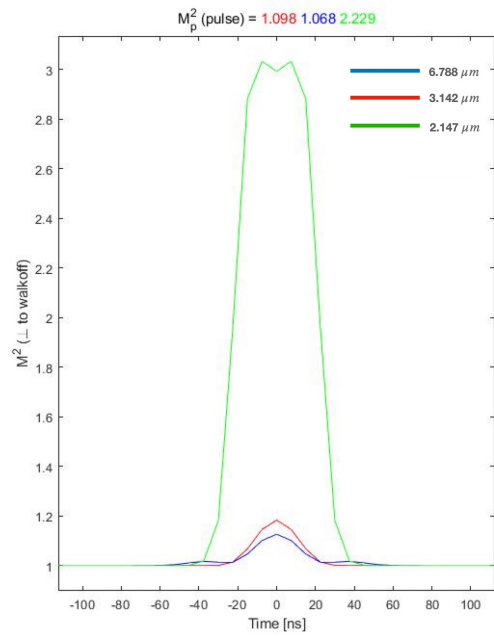
In contrast, for $E_s = 3$ mJ and $E_p = 25$ mJ, the idler energy increases by less than $100 \mu\text{J}$ compared to $E_s = 2.5$ mJ, indicating stable performance. The optimal configuration, with $E_p = 25$ mJ at 2148 nm and $E_s = 2.5$ mJ at 3142 nm, produces approximately 4.6 mJ at 6788 nm. These results set the required output energies for the preceding OPA stages.

5.2.7 Optical parametric amplification

In the previous section, we established the output energy requirements for the 3142 nm and 2148 nm branches. While the OPO/OPA branch at 3142 nm is successfully realized as will



(a)



(b)

Figure 5.8: (a) Simulation of the energy evolution of the 3 different wavelengths for the DFG process along the propagation length inside the ZGP crystal. (b) The corresponding beam quality given by M^2 for the 3 different wavelengths is shown.

be demonstrated in Chapter 6, here we investigate the feasibility of achieving such high energy from the 2148 nm branch.

Optical parametric amplification operates similarly to the DFG. In the OPA process, a pump beam and a signal beam interact in a nonlinear crystal, generating an idler beam at the frequency $\omega_i = \omega_p - \omega_s$, as illustrated in Fig. 5.9. Note that for the OPA, the signal and idler notation here are reversed. The nonlinear mixing process is described by Eqs.5.4 and 5.3. The presence of photons at ω_i stimulates additional photon generation at ω_s , which further regenerates photons at ω_i , resulting in amplification of the signal field as shown in Figs. 5.9(b) and 5.9(c). This amplification, referred to as single-pass gain, is described by the growth of signal intensity from its initial value $I_s(0)$ to $I_s(L)$, assuming no pump depletion [95]:

$$\frac{I_s(L)}{I_s(0)} = 1 + (gL)^2 \frac{\sinh^2 \left(\sqrt{(gL)^2 - (\Delta k_{\text{tot}} L/2)^2} \right)}{(gL)^2 - (\Delta k_{\text{tot}} L/2)^2}, \quad (5.15)$$

where L is the interaction length, Δk_{tot} is the phase mismatch, and

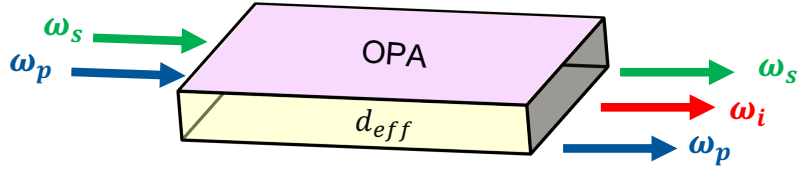
$$g^2 = \frac{2\omega_s \omega_i d_{\text{eff}}^2 I_p}{\varepsilon_0 c^3 n_p n_s n_i}, \quad (5.16)$$

with I_p being the pump intensity. The efficiency of the process depends on the nonlinear coefficient d_{eff} of the nonlinear material used and achieving phase-matching conditions.

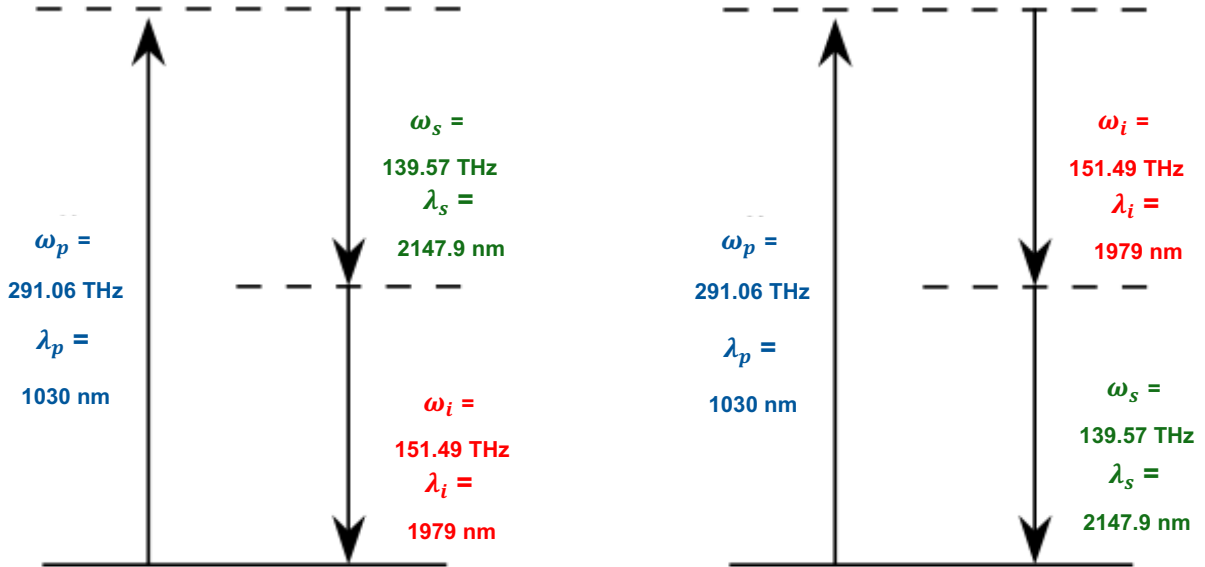
5.2.8 The PPKTP crystal

For the 2148 nm branch, a periodically poled potassium titanyl phosphate (PPKTP) crystal is used for OPA2. Periodic poling involves inverting the ferroelectric domains of KTP along its z -axis, creating a periodic modulation in the effective nonlinear coupling coefficient, d_{eff} . This modulation counteracts wave vector mismatch Δk and enables efficient nonlinear optical processes through quasi-phase matching (QPM) [6].

As shown in the previous section, the energy required at 2148 nm is 10 times greater than that at 3142 nm, necessitating a nonlinear medium with a high nonlinear coefficient and high damage threshold. The PPKTP crystal meets these criteria, with reported light-induced damage thresholds (LIDT) of 10 J/cm² at 2 μm and 12 J/cm² at 1030 nm for 8



(a)



(b)

(c)

Figure 5.9: Schematic of the optical parametric amplification (OPA) process. (a) Illustration of the nonlinear medium showing input photons (signal and pump) and output photons (signal, pump, and idler) with their respective frequencies. (b) and (c) Energy diagrams demonstrating the regeneration of the signal photon, highlighting the parametric amplification mechanism at the required frequencies and corresponding wavelengths for OPA2.

ns long pulses [96]. After scaling these values for 50 ns pulses, the LIDT is estimated to be around 25 J/cm². For a conservative design, we adopt an LIDT value of 12 J/cm².

5.2.9 Simulation of the OPA at 2148 nm

We simulate the extractable output energies from the OPA using a PPKTP crystal provided by SFN (Svenska LaserFabriken). The crystal measures 4 × 4 × 12, mm, has an effective nonlinear coefficient of $d_{\text{eff}} = 9$ pm/V, and a poling period of 37.85 μm for quasi-phase matching. The refractive indices for the signal (2148 nm), idler (1979 nm), and pump (1030 nm) are 1.723, 1.726, and 1.745, respectively. Assuming a conservative output of 1 mJ from OPO2 based on the performance of OPO1, which achieves up to 1.4 mJ and will be discussed in the next chapter. we set the input to OPA2 at 700 μJ at 2148 nm, accounting for 30% transmission losses between OPO2 and OPA2

Equation. 5.15 shows that the gain scales with crystal length, and for strong gain ($g \gg \Delta k_{\text{tot}}/2$), the signal field is exponentially amplified, simplifying Eq. 5.15 to:

$$I_s(L) = I_s(0) \cosh^2(gL). \quad (5.17)$$

Selecting an optimal crystal length is crucial to achieve maximum gain. Simulations were conducted to estimate the amplified signal energy at 2148 nm for various crystal lengths, given a signal energy input of 700 μJ and pump energies at 1030 nm of 75 mJ and 95 mJ, as shown in Fig. 5.10. The plot reveals exponential gain up to 9 mm, followed by saturation around 12 mm, likely due to pump depletion. Thus, a crystal length of 12 mm is identified as optimal.

Next, we analyze the effect of three different beam waists of the two input beams at the signal and pump wavelengths on crystal gain through simulations. Fig. 5.11 shows the output signal energy at 2148 nm as a function of pump energy at 1030 nm. For the orange curve, the beam waist at both signal and pump wavelengths is set to $w_0 = 1$ mm, the maximum size allowed (half the crystal width) to avoid spherical aberration. This large beam waist enables higher pump energies without optical damage and ensures better overlap between the signal and pump beams. The orange curve reaches 41.6 mJ at a pump energy of 200 mJ, with no full saturation, suggesting potential for further energy extraction.

The blue curve represents a variable beam waist constrained by a fixed damage threshold

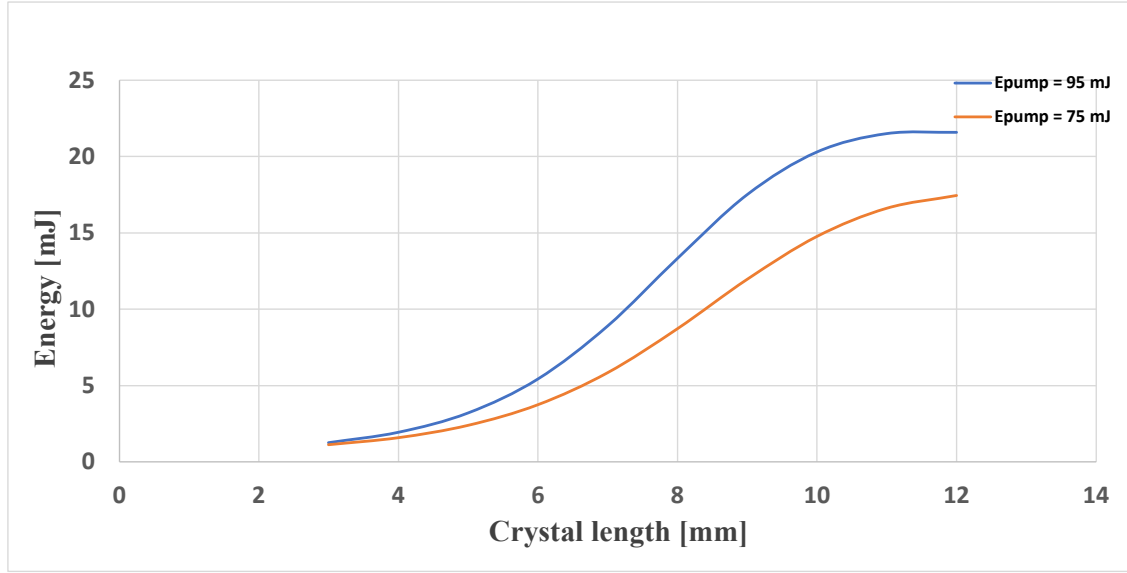


Figure 5.10: Amplified signal energy at 2148 nm as a function of crystal length for two different pump energies at 1030 nm. The input signal energy was $700 \mu\text{J}$, with a pulse length of 50 ns and a beam waist of 0.84 mm for both the signal and pump.

of 12 J/cm^2 . Above 60 mJ, the 1 mm beam waist outperforms smaller waists for the pump energies of interest. In the gray curve, the beam waist from the blue curve is scaled by $\sqrt{2}$, improving performance below 100 mJ compared to the orange curve. However, to achieve the required 35 mJ output from the OPA (to deliver 25 mJ to the DFG after accounting for 30% transmission loss), the OPA must be pumped at 160 mJ. Re-adjusting the beam size for each pump energy is impractical, so a 1 mm beam waist is chosen for optimal performance.

In addition to energy, we examined the spatial properties of the OPA output, represented by the M^2 beam quality, for two beam waist values at a fixed input pump energy of 120 mJ at 1030 nm. Fig. 5.12 shows the M^2 values for the signal pulses at 2148 nm with beam waists of $564 \mu\text{m}$ and 1 mm. The simulations reveal that smaller beam waists degrade beam quality, with M^2 exceeding 2.2, indicating a non-Gaussian spatial mode. Additionally, energy evolution along the crystal shows back conversion from the signal and idler to the pump. In contrast, a 1 mm beam waist produces a Gaussian mode with an M^2 around 1.04 and no back conversion, with energies saturating at the end of the crystal. Based on energy output, beam quality, and back conversion, the optimal performance for a single OPA for an input signal energy of $700 \mu\text{J}$ is achieved with a 1 mm beam waist.

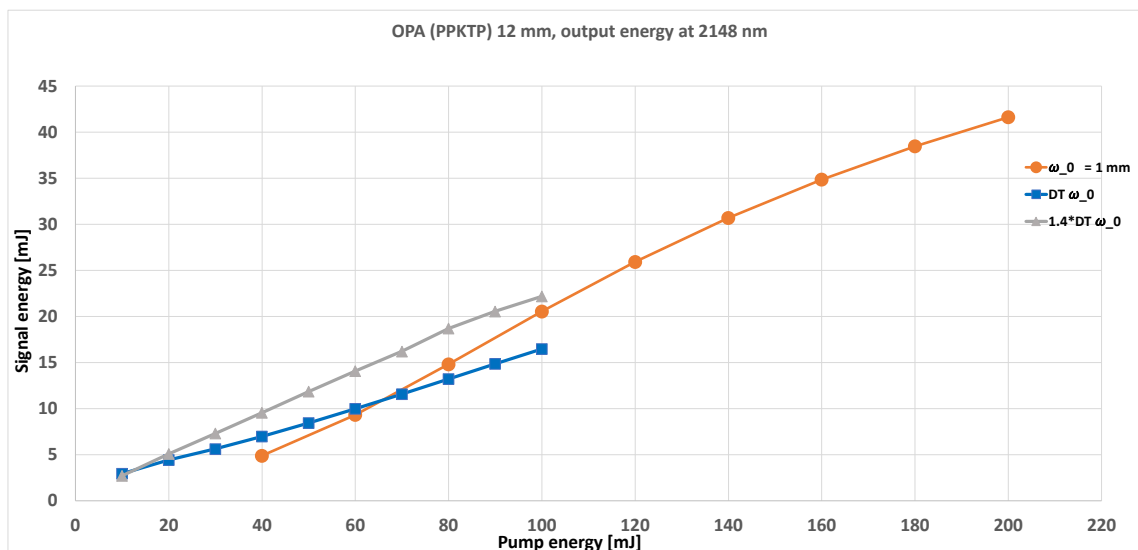
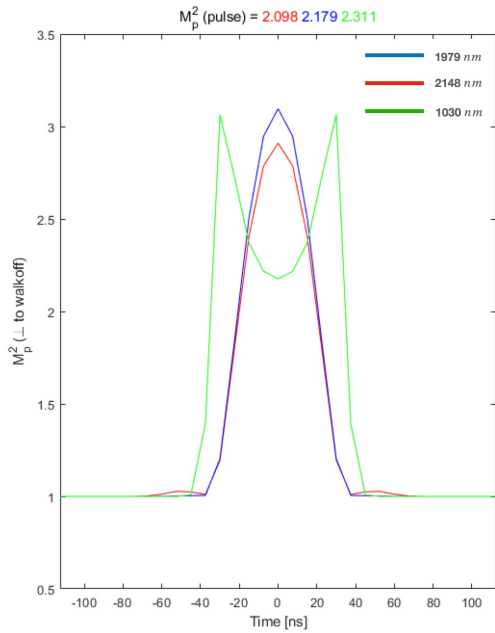


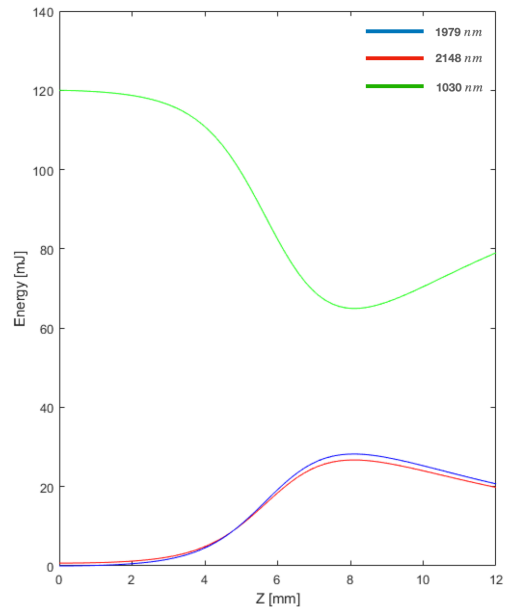
Figure 5.11: Simulation results of the output signal energy at 2148 nm as a function of input pump energy for a single OPA stage using a 12 mm PPKTP crystal. The simulation assumes an input signal pulse energy of 0.7 mJ with a 50 ns duration. Results are shown for three beam waist configurations: the orange line represents a fixed beam waist of 1 mm, the blue line adjusts the beam waist at each pump energy to reach the damage threshold intensity, and the gray line uses a beam waist 1.4 times larger than the corresponding values of the blue line.

We next examine the effect of higher signal input energy at 2148 nm on the performance of a two-stage OPA system. The first stage, OPA2.1, serves as a preamplifier for the second stage, OPA2.2. The beam waist is set to $w_0 = 0.84$ mm, slightly smaller than 1 mm, to increase the fluence and reduce the total pump energy required. Figure 5.13 shows the simulation results for both stages, with a fixed total pump energy of 160 mJ, equally distributed between the two OPAs (80 mJ per stage).

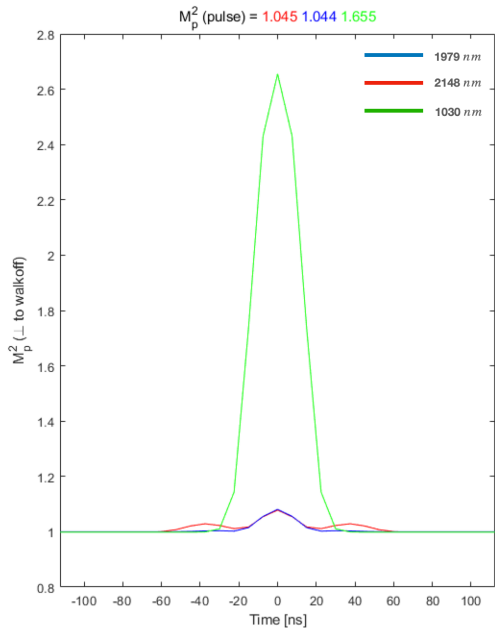
For OPA2.2, the output signal energies as a function of input pump energy are plotted for two different input signal energies at 2148 nm, represented by the orange and blue lines. These input signal energies are approximately an order of magnitude higher than the input signal energy used in the single-stage OPA. However, the maximum output signal energy from OPA2.2 reaches only 30 mJ, about 5 mJ lower than the single-stage OPA result at the same total pump energy (Fig. 5.11). This highlights the importance of higher pump energy over increasing input signal energy for OPA performance. Therefore, a single-stage OPA is chosen for the 2148 nm branch.



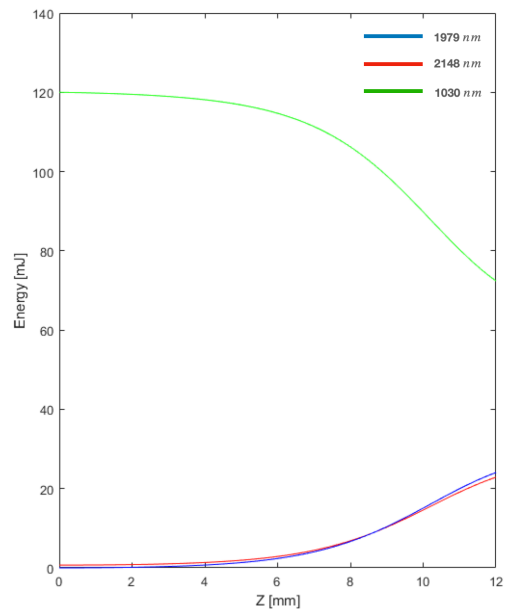
(a)



(b)

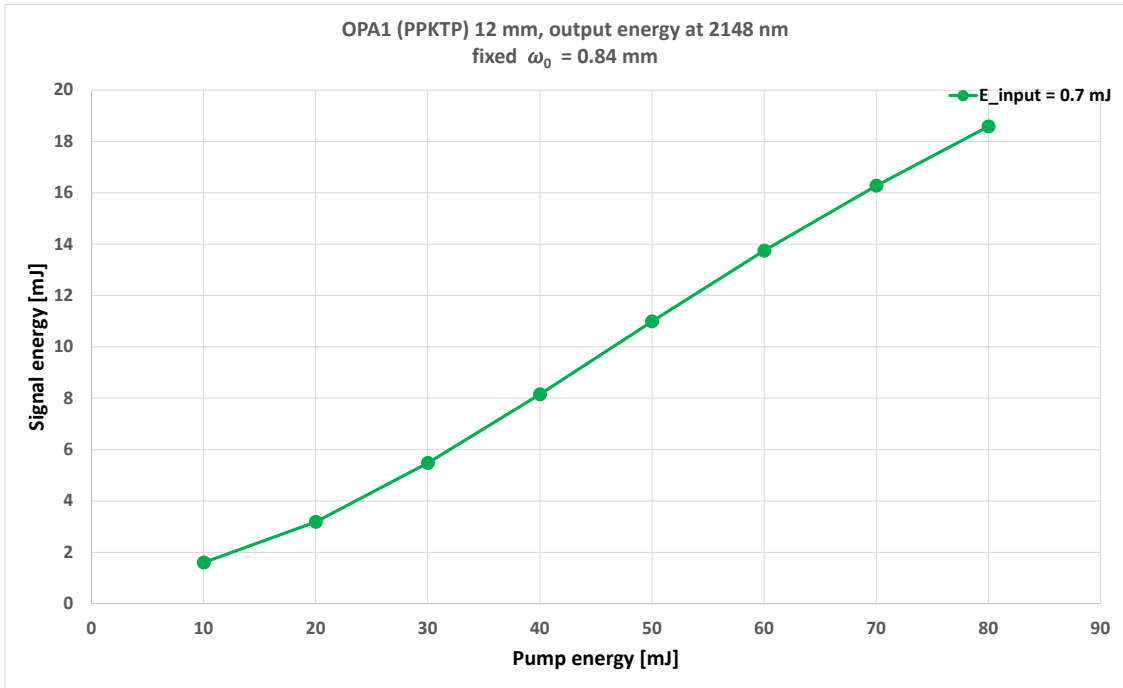


(c)

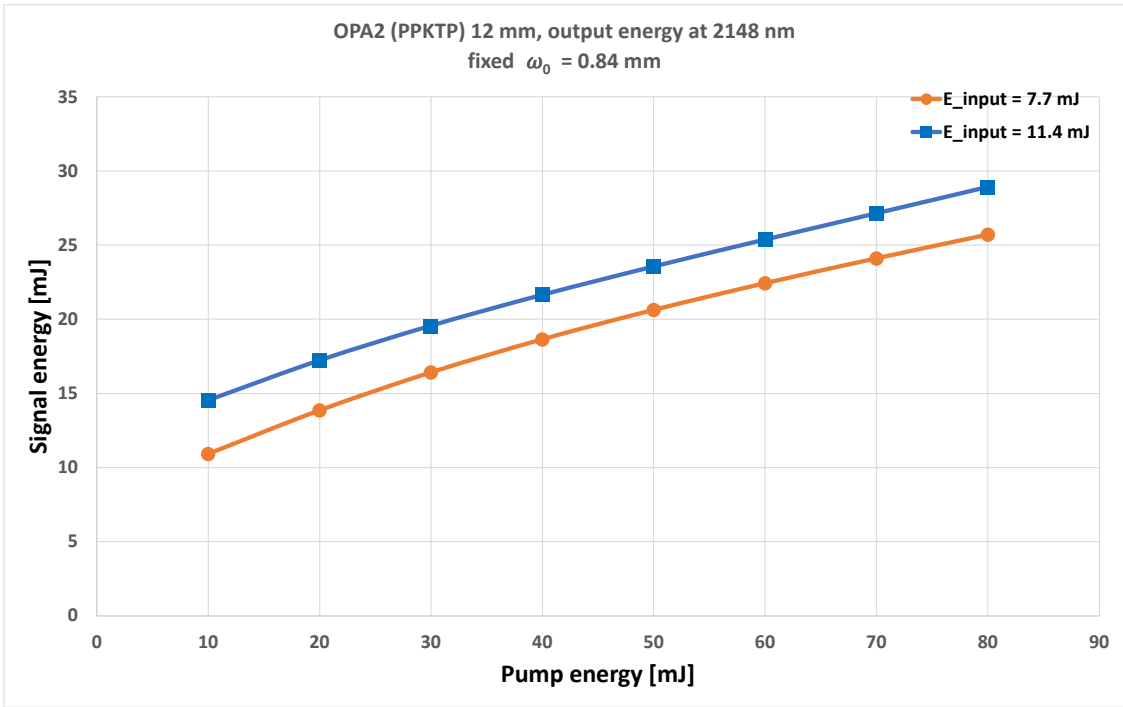


(d)

Figure 5.12: Simulation results of the beam quality, expressed as M^2 , and the pulse energy evolution along the crystal length for OPA2. Plots (a) and (b) correspond to an input pump energy of 120 mJ with a beam waist w_0 of $564 \mu\text{m}$ for both the signal and pump input beams. Plots (c) and (d) present similar results for the same input pump energy but with a larger beam waist of 1 mm for the input signal and pump beams. For both simulations, the input signal pulse energy was $700 \mu\text{J}$ with a pulse duration of 50 ns.



(a)



(b)

Figure 5.13: Simulation results for two consecutive OPAs, each using a 12 mm long PPKTP crystal. (a) shows the output signal energy of the preamplifier, OPA2.1, as a function of pump energy, with an input signal energy of 0.7 mJ at 2148 nm. (b) displays the output signal energy of OPA2.2 for two different seed energies at 2148 nm, 7.7 mJ and 11.4 mJ. The simulations were performed for a pulse length of 50 ns, with w_0 representing the beam waist of both the signal and pump beams.

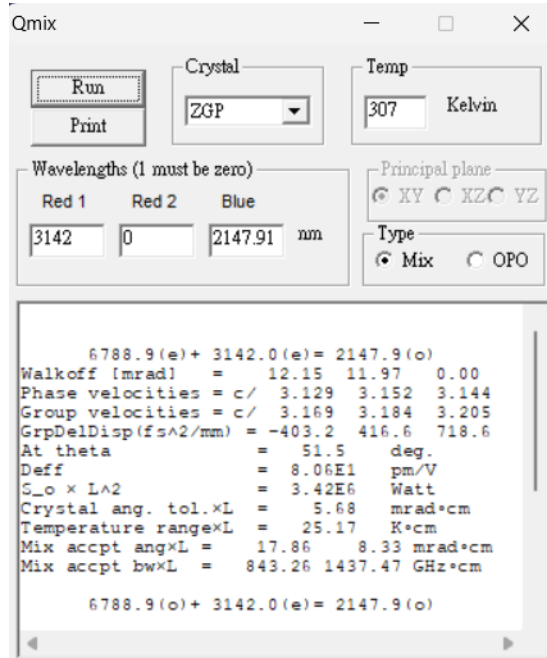
In conclusion, simulations demonstrate that the OPO2/OPA2 branch can achieve pulse energies up to 35 mJ by pumping a single-stage OPA with a PPKTP crystal at intensities near its damage threshold. Details on the optical layout of the down-conversion scheme and its implementation is provided in Appendix 5.B.

Appendices

5.A DFG simulation

The phase-matching parameters for the ZGP crystal, with an input signal at 3142 nm and a pump at 2148 nm, are shown in Fig.5.A.1(a). The SNLO program calculates a phase-matching angle of 51.5° . Under these conditions, the effective nonlinear coefficient (d_{eff}) experienced by both the signal and the pump is 80.6 pm/V. The refractive indices, as determined from the phase-matching conditions (see Fig.5.A.1(b) and Fig. 5.A.1(c)), are 3.144 for the pump (2148 nm) and 3.151 for the signal (3142 nm).

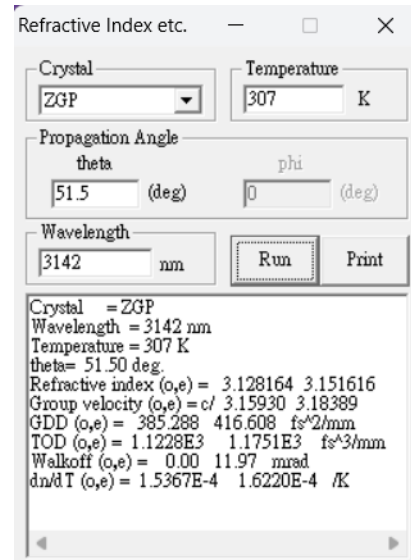
Table 5.A.1 and Table 5.A.2 present the detailed numerical results of the DFG simulation for input pulse energies of 2.5 mJ and 1 mJ, respectively, at the signal wavelength of 3142 nm. Each table includes five sets of pump pulse energies at 2148 nm, with the beam diameter (FWHM) of both the signal and the pump varied from 0.7 mm to 1.2 mm for each set.



(a)



(b)



(c)

Figure 5.A.1: Phase-matching parameters for the ZGP crystal extracted using the SNLO program. (a) displays the effective nonlinear coefficient $d_{\text{eff}} = 80.6 \frac{\text{pm}}{\text{V}}$ and phase-matching angle of 51.5° . (b) shows the refractive index for the pump wavelength (2148 nm), and (c) provides the refractive index for the signal wavelength (3142 nm) under the same phase-matching conditions.

Signal Energy (mJ)	Beam FWHM (mm)	Pump Energy (mJ)	Idler Energy (mJ)
2.5	0.7	15	2.68
2.5	0.75	15	2.80
2.5	0.8	15	2.87
2.5	0.85	15	2.89
2.5	0.9	15	2.86
2.5	0.95	15	2.80
2.5	1.0	15	2.70
2.5	1.05	15	2.57
2.5	1.1	15	2.44
2.5	1.15	15	2.30
2.5	1.2	15	2.15
2.5	0.7	18	3.03
2.5	0.75	18	3.21
2.5	0.8	18	3.33
2.5	0.85	18	3.40
2.5	0.9	18	3.41
2.5	0.95	18	3.38
2.5	1.0	18	3.29
2.5	1.05	18	3.18
2.5	1.1	18	3.04
2.5	1.15	18	2.88
2.5	1.2	18	2.72
2.5	0.7	20	3.25
2.5	0.75	20	3.46
2.5	0.8	20	3.62
2.5	0.85	20	3.72
2.5	0.9	20	3.76
2.5	0.95	20	3.75
2.5	1.0	20	3.68
2.5	1.05	20	3.57
2.5	1.1	20	3.43
2.5	1.15	20	3.27
2.5	1.2	20	3.09
2.5	1.25	20	2.91
2.5	0.7	23	3.53
2.5	0.75	23	3.79
2.5	0.8	23	4.00
2.5	0.85	23	4.16
2.5	0.9	23	4.24
2.5	0.95	23	4.27
2.5	1.0	23	4.24
2.5	1.05	23	4.16
2.5	1.1	23	4.03
2.5	1.15	23	3.87
2.5	1.2	23	3.69
2.5	1.25	23	3.49
2.5	0.75	25	4.01
2.5	0.8	25	4.25
2.5	0.85	25	4.43
2.5	0.9	25	4.55
2.5	0.95	25	4.61
2.5	1.0	25	4.60
2.5	1.05	25	4.53
2.5	1.1	25	4.42
2.5	1.15	25	4.26
2.5	1.2	25	4.08
2.5	1.25	25	3.87

Table 5.A.1: Simulation results for DFG output idler energy at $6.8 \mu\text{m}$ as a function of the FWHM beam diameter and pump energy, for a fixed signal input energy of 2.5 mJ at 3142 nm.

Signal Energy (mJ)	Beam FWHM (mm)	Pump Energy (mJ)	Idler Energy (mJ)
1	0.7	15	2.66
1	0.75	15	2.61
1	0.8	15	2.51
1	0.85	15	2.35
1	0.9	15	2.18
1	0.95	15	1.99
1	1.0	15	1.80
1	0.7	18	3.12
1	0.75	18	3.13
1	0.8	18	3.07
1	0.85	18	2.94
1	0.9	18	2.76
1	0.95	18	2.56
1	1.0	18	2.34
1	1.05	18	2.12
1	1.1	18	1.92
1	1.15	18	1.73
1	0.7	20	3.40
1	0.75	20	3.45
1	0.8	20	3.42
1	0.85	20	3.32
1	0.9	20	3.15
1	0.95	20	2.95
1	1.0	20	2.72
1	1.05	20	2.48
1	1.1	20	2.25
1	1.15	20	2.03
1	1.2	20	1.83
1	1.25	20	1.65
1	0.7	23	3.76
1	0.75	23	3.88
1	0.8	23	3.91
1	0.85	23	3.86
1	0.9	23	3.72
1	0.95	23	3.53
1	1.0	23	3.30
1	1.05	23	3.04
1	1.1	23	2.78
1	1.15	23	2.52
1	1.2	23	2.28
1	1.25	23	2.06
1	0.75	25	4.14
1	0.8	25	4.22
1	0.85	25	4.19
1	0.9	25	4.09
1	0.95	25	3.91
1	1.0	25	3.68
1	1.05	25	3.42
1	1.1	25	3.14
1	1.15	25	2.87
1	1.2	25	2.60
1	1.25	25	2.35

Table 5.A.2: Simulation results for the DFG output idler energy at $6.8 \mu\text{m}$ as a function of the FWHM beam diameter and pump energy, with a fixed input signal energy of 1 mJ at 3142 nm.

5.B Down conversion optical layout

In the previous sections, we determined the required input pulse energies from the thin disk oscillator and amplifier at 1030 nm, as well as the optimal beam sizes at different stages of the down-conversion scheme. Using this information, we now present an optical layout illustrating the physical implementation of these stages. Figure 5.B.2 shows the complete optical layout of the laser system up to the DFG stage. The layout allows switching between the TDL oscillator for lower pulse energies (up to 50 mJ) and the full operation with pulses from the TDL amplifier. The former is used for optimizing and operating the OPOs, while the latter pumps both OPO and OPA stages. The switch between the TDL oscillator and amplifier is controlled by adjusting the polarization of the beam as follows:

- Pulses from the TDL oscillator: The half-wave plate (HWP) $\lambda/2(0)$ rotates the polarization from P to S, causing the beam to reflect off the thin-film polarizer (TFP) labeled as (TFP AMP/OPO) in the layout. The beam is then directed to the OPO/OPA branches via the mirror M_{OPO} .
- Pulses from the TDL amplifier: The HWP $\lambda/2(0)$ keeps the pulses P-polarized, allowing them to pass through the TFP to the TDL amplifier. After amplification, the beam reflects off $M1_{\text{amp}}$ at a different height. The amplified beam is then redirected by a periscope $M1_{\text{height}}$ to reach the required height of 75 mm above the optical table, where it is directed to TFP1. The HWP $\lambda/2(\text{ampl})$ adjusts the polarization so the beam is either reflected to the OPO/OPA branches or blocked by the beam dump behind TFP1.

After reaching the OPO/OPA branches, the beams are distributed between them using polarization control. The HWP $\lambda/2(2)$ adjusts the polarization so that 80% of the beam is S-polarized and reflected by TFP2 to the OPA branches, while the remaining 20% is P-polarized and transmitted to the OPO branches.

When switching to the TDL amplifier, a beam size adjustment unit consisting of a convex lens ($f = 200$ mm) and a concave lens ($f = -150$ mm), ensures consistent beam collimation and avoids realigning the lens telescopes in the layout. The TDL amplifier has a beam waist of $w_0 = 3$ mm, while the TDL oscillator has $w_0 = 2.25$ mm. The beam size adjustment unit rescales the amplifier beam waist to match the oscillator one. This ensures the mode

matching of pump beams into the OPO/OPA branches remains unaffected when switching between the oscillator and amplifier.

The pulses at 1030 nm are distributed to the two OPOs via TFP3. The input beam waists at 1030 nm are collimated to match the OPO cavity beam waists at the center of the nonlinear crystals. However, the pump beam waist at 1030 nm is set to be 5% larger than the signal (seed) beam waist for both OPOs to facilitate alignment and improve beam overlap within the nonlinear crystals. Details about mode matching will be discussed in the next chapter for the 3.1 μm branch of the OPO and OPA.

To control the pump pulse energy incident on each OPO, an “energy distribution” unit consisting of two HWPs and one TFP is placed before each OPO, as shown in Fig. 5.B.2. The first HWP adjusts the pulse energy transmitted through the TFP, while the second HWP sets the polarization of the light entering the OPO crystal. Adjusting the pump beam polarization is crucial for achieving phase matching in the PPLN crystals of the OPO, which uses the QPM method described earlier.

The output pulses from each OPO at the idler wavelength are separated from the pump and signal wavelengths using separator mirrors. The beams at 3142 nm and 2148 nm are then collimated to the required beam waist and aligned to seed their respective OPAs for further amplification. In addition to spatial overlap and mode matching of the beams, temporal overlap between the 1030 nm pump pulses and the signal (seed) pulses for the OPAs must also be ensured. For this purpose, a delay line, symbolized by the mirror (M delay), is installed after the 1030 nm beam reflected from TFP2 toward the OPA branches. This delay adds a few nanoseconds to the pump pulse path, matching the time taken by the pump beam to the OPO and the path propagated from the OPO to the OPA by the generated pulses. Further details about this delay line will be discussed in the description of the 3.1 μm OPA.

The pump beam waist at 1030 nm is adjusted from 3 mm to 2.25 mm, as in the OPO setup when using the TDL amplifier, and collimated to match the signal input beam waist to the OPAs. Both pump and signal beams must be mode-matched and spatially overlapped at the center of the OPA crystal. Control of the pulse energies at 1030 nm is managed similarly to the OPO setup, using a unit of two HWPs and one TFP. The generated pulses at 2148 nm and 3142 nm are then separated from other wavelengths and prepared for the DFG stage.

Pulses at 2148 nm, S-polarized after OPA2, are collimated to a beam waist of 849 μm and

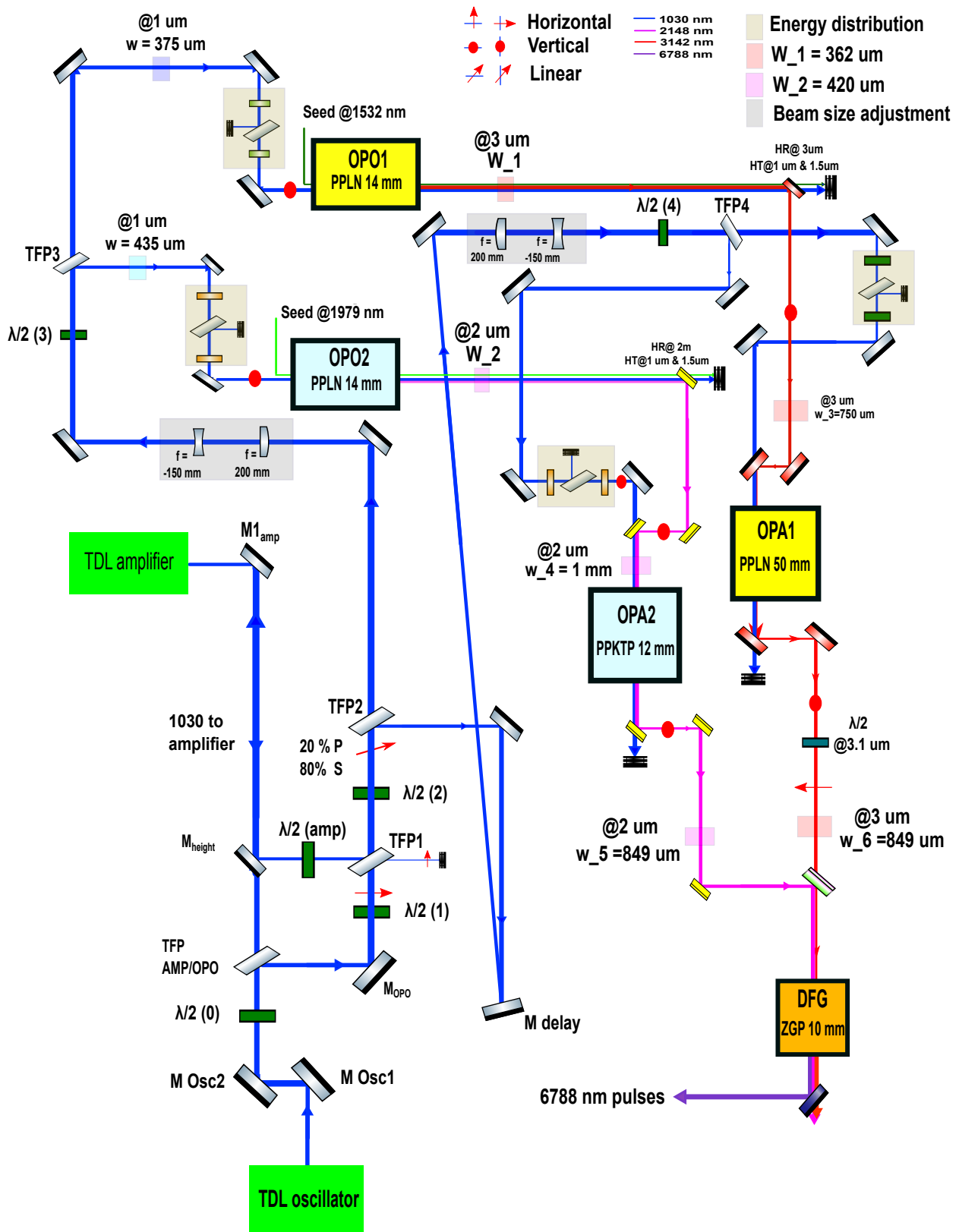


Figure 5.B.2: Scheme of the complete optical layout of the laser system. Detailed description is given in the text.

serve as the pump input for the DFG stage. Pulses at 3142 nm are also collimated to the same beam waist, but their polarization is adjusted to P-polarized using a $\lambda/2$ wave plate, representing the seed (signal) input to the DFG. Both beams are spatially overlapped within the DFG crystal to generate idler pulses at approximately 6788 nm. The generated 6788 nm light is then separated from the other wavelengths and directed to the experimental area.

Chapter 6

OPO and OPA at 3142 nm

In this chapter we describe the design and implementation of the optical parametric oscillator and optical parametric amplifier pumped by the 1030 nm to produce pulses at 3142 nm. We first describe the optical parametric oscillator based on a Periodically Poled Lithium Niobate crystal (PPLN) seeded at 1532 nm and pumped by 50 ns long pulses at 1030 nm provided by the TDL. This OPO produces continuously tunable single-longitudinal mode pulses at an idler wavelength of 3142 nm and energies up to 1.4 mJ. We implemented a novel optical layout of the OPO cavity that enables a tunable outcoupling leading to a cheap and efficient way of optimizing the nonlinear conversion efficiency. We reached a total conversion efficiency of up to 44 %. Single-frequency operation was implemented by locking the OPO cavity length to a continuous wave (CW) tunable diode laser at 1532 nm through the Pound-Drever-Hall (PDH) method. The injection seeding and the cavity layout of the OPO ensured a TEM₀₀ transverse mode. We demonstrated a beam quality of $M^2 \sim 1$ for the idler pulses. The injection seeding ensured also a single-frequency operation as demonstrated by the optical-heterodyne measurement.

The second part of this chapter describes the further amplification of output pulses at 3142 nm within an optical parametric amplifier based on a PPLN crystal pumped by 1030 nm pulses and producing output pulse energies up to 3.4 mJ. A beam quality of $M^2 \approx 1.3$ at 3142 nm was achieved. A pulse-to-pulse RMS stability of about 1.5% was observed thanks to the stability of the TDL pulses and the OPO cavity. Continuous tunability of ≈ 20 GHz of the OPO-OPA system was shown through pulsed absorption spectroscopy on methane by scanning over the absorption lines around the central wavelength of 3142 nm. An estimation

of the OPO laser bandwidth < 10 MHz from optical heterodyne measurement was obtained. Spectroscopy of the methane absorption lines provided an upper bound of 100 MHz.

6.1 Optical parametric oscillator at 3142 nm

A scheme of the OPO setup is shown in Fig. 6.1. The OPO cavity has an L shaped layout with two end-mirrors (CM1 and CM2), a 14 mm long PPLN crystal with an aperture of 3×4 mm and a poling period of $30.2 \mu\text{m}$. The cavity is single-resonant to the signal wavelength at 1532 nm. The combination of the TFP and the quarter wave plate ($\lambda/4$ - plate) controls the amount of 1532 nm light circulating within the cavity through polarization adjustment. The TFP and the ($\lambda/4$ - plate) constitute together with the mirror CM1 a mirror with a variable effective reflectivity adjusted via the angle of the quarter wave plate. Pulses of up to 11 mJ at 1030 nm are coupled into the cavity through the TFP. The beam waist of the pump beam is adjusted through a Galilean type telescope to match the beam size of the transverse mode at 1532 nm resonant within the cavity. The end mirrors are highly reflective (HR) for the seed (signal) wavelength at 1532 nm while they are highly transmissive (HT) for the pump at 1030 nm and the idler at 3142 nm. The PPLN crystal is anti-reflective (AR)-coated for all the three wavelengths. The idler pulses at 3142 nm are coupled out through the mirror CM2 and is separated from the signal and the pump pulses by a separator mirror, which reflects only the pulses at 3142 nm while transmitting the other wavelengths.

A tunable diode laser at the central wavelength of 1532 nm with a narrow bandwidth of ~ 10 kHz is used for injection seeding the OPO cavity. The light from the seed laser passes through a fiber isolator, which protects the laser diode from back-reflections. It is then phase-modulated by an electro-optical modulator (EOM). The EOM is an integral component of the PDH locking scheme, which will be elaborated upon later. The output is then collimated and passes the polarization-dependent elements TFP₁, $\lambda/2_2$ and a faraday rotator (FR) which ensures that the light coupled into the OPO cavity is P-polarized, while the P-polarized light reflected back from the cavity is turned into an S-polarised then reflected by the TFP₁. This system has two functionalities, the first is to act as an isolator against the light back-reflected into the laser diode and the EOM. The second is to use the light reflected from the cavity to generate an error signal for the PDH locking as well as measuring the output pulse energies at the signal wavelength.

The single frequency operation of the OPO cavity is achieved by locking the cavity to the seed laser. This is achieved by adjusting the cavity length through a Piezo actuator acting on the mirror CM1 using a PDH locking technique. The schematic of this PDH locking is shown on the lower left corner of Fig. 6.1.

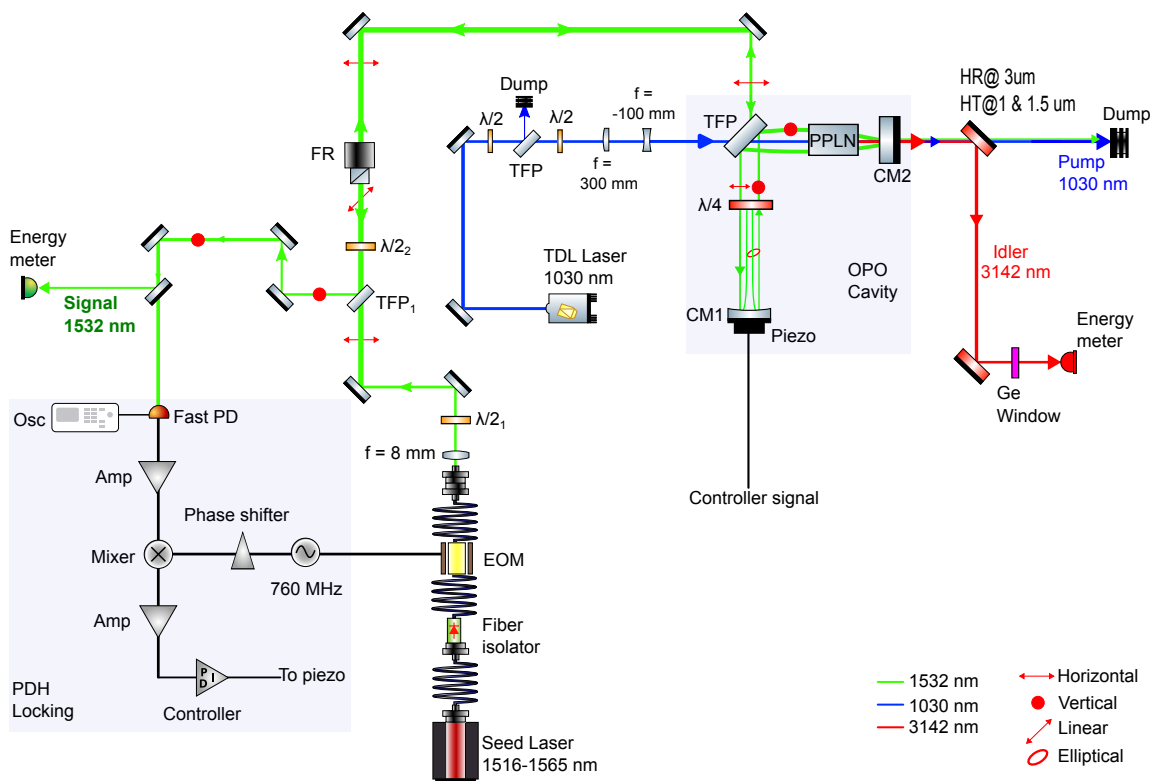


Figure 6.1: Scheme of the pulsed optical parametric oscillator CW seeded at the signal wavelength. Detailed description is given in the text.

6.2 OPO cavity optical layout

This section provides details on the optical layout designed to allow for a large transverse mode size within the OPO cavity with minimal collimation optics and high stability. In the following we provide a brief overview of the notation commonly used to model laser beam propagation under the paraxial approximation, allowing the Gaussian beam formalism to be applied. This applies well to our case as we are aiming at a TEM_{00} mode operation at both the signal and idler wavelengths at 1532 nm and 3142 nm, respectively.

6.2.1 Gaussian beam propagation using ABCD-matrices

For a beam propagating along the z -axis, the primary parameters of interest are the transverse beam size $w(z)$ in the $x - y$ plane and the phase front curvature $R(z)$ along the propagation axis. The transverse beam size $w(z)$ is defined as the radial distance from the axis at which the intensity of the beam drops to $1/e^2$ of its maximum value on axis as shown in Fig. 6.2.

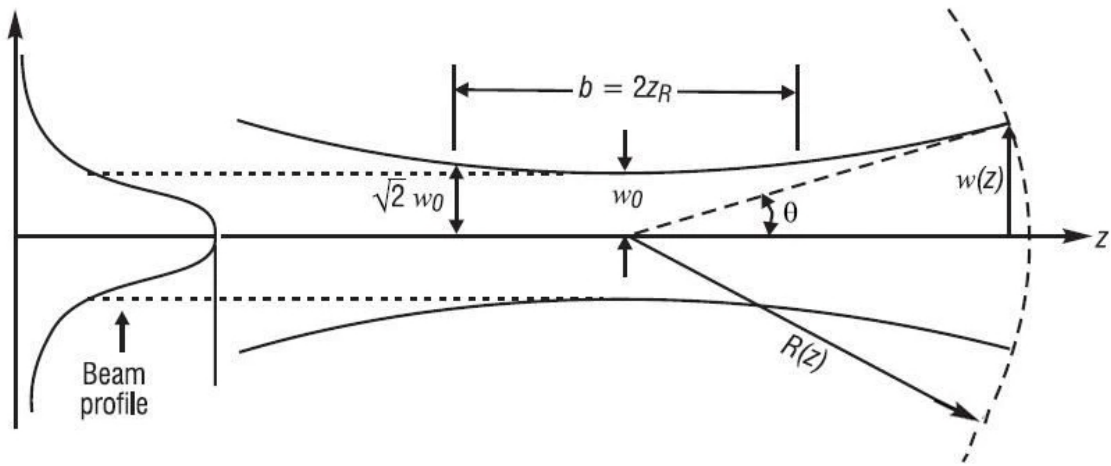


Figure 6.2: Gaussian beam propagation parameters. Z_R is the rayleigh length.

A Gaussian beam can be described by the complex beam parameter q [97], which is related to both the curvature of the beam wavefront $R(z)$ and the beam spot size $w(z)$. The complex beam parameter is defined as

$$\frac{1}{q(z)} = \frac{1}{R(z)} - i \frac{\lambda}{\pi w^2(z)}, \quad (6.1)$$

where λ is the wavelength of the light, and i is the imaginary unit.

The propagation of a Gaussian beam through an optical system is conveniently described by the ABCD-matrix formalism. Here, an optical system is represented by an ABCD matrix of the form

$$M = \begin{pmatrix} A & B \\ C & D \end{pmatrix}. \quad (6.2)$$

For free-space propagation over a distance d , the corresponding ABCD matrix is

$$M_d = \begin{pmatrix} 1 & d \\ 0 & 1 \end{pmatrix}. \quad (6.3)$$

For a thin lens with focal length f , the ABCD-matrix is

$$M_f = \begin{pmatrix} 1 & 0 \\ -\frac{1}{f} & 1 \end{pmatrix}. \quad (6.4)$$

When a Gaussian beam passes through an optical system described by an ABCD-matrix, its complex beam parameter from the input to the output planes transforms as:

$$q_{\text{out}} = \frac{Aq_{\text{in}} + B}{Cq_{\text{in}} + D}, \quad (6.5)$$

where q_{out} is the complex beam parameter after propagation through the system.

When a Gaussian beam propagates through multiple successive optical components, the overall transformation of the system can be described by combining the ABCD-matrices of each individual element. For a system with N components, each described by a matrix M_i , the overall matrix becomes

$$M_{\text{total}} = M_N \cdot M_{N-1} \cdots \cdots M_2 \cdot M_1, \quad (6.6)$$

where M_1 represents the first optical component along the propagation and M_N represents the last optical component encountered along the propagation. By multiplying the matrices of individual components, we can describe the entire system. This total matrix can then be applied to the initial complex beam parameter q to analyze the beam properties after it has propagated through the system.

6.2.2 OPO cavity mode

One can apply the ABCD-matrix formalism to the OPO cavity to calculate the OPO cavity mode. Such a cavity mode is characterized by a field distribution that reproduces itself after completing a round trip. Figure 6.3(a) shows a round trip propagation of the light inside the cavity starting from the reference point represented by the dashed red line at the surface of the flat mirror CM2. The light propagates a distance L_2 before being reflected by the TFP.

It then passes through a $\lambda/4$ – plate, which does not alter the field distribution. Afterwards, the light travels an additional distance L_1 from the TFP to reach the mirror CM1. The mirror CM1 is a plano concave mirror with a radius of curvature $R = 1000$ mm back reflects the light towards the reference plane at which it has completed the round trip propagating a total distance of $2L_1 + 2L_2$.

This round trip propagation can be described through the following three steps, a free space propagation of $L = L_2 + L_1$ where L is the cavity length, a focusing by the concave mirror CM1 by a focal length $f = R/2$, then another free space propagation of $L_2 + L_1$. These three steps are described through the product

$$\mathbf{M}_{\text{cavity}} = \begin{bmatrix} 1 & L \\ 0 & 1 \end{bmatrix} \cdot \begin{bmatrix} 1 & 0 \\ -\frac{1}{f} & 1 \end{bmatrix} \cdot \begin{bmatrix} 1 & L \\ 0 & 1 \end{bmatrix}. \quad (6.7)$$

We obtain the cavity mode by forcing the complex beam parameter at the reference plane to reproduce itself after a round trip $q_{(0+2L)} = q_0$. At the flat mirror CM2 the phase front curvature $R = \infty$ which means this is the position of the beam waist w_0 . Solving for Eq. 6.5 using the matrix elements in Eq. 6.7, we have

$$\frac{1}{q_0} = -\frac{A - D}{2B} - i \frac{\left[1 - \left(\frac{A+D}{2}\right)^2\right]^{1/2}}{B}. \quad (6.8)$$

Using the above equation, the spot size at the reference plane (end mirror CM2) can be calculated. The square of the spot size is given by

$$\begin{aligned} w_0^2 &= \frac{\lambda_0}{\pi n} \frac{B}{\left[1 - \left(\frac{A+D}{2}\right)^2\right]^{1/2}} \\ &= (LR)^{1/2} \left(1 - \frac{L}{R}\right)^{1/2}, \end{aligned} \quad (6.9)$$

where n is the refractive index and for air it is 1. Substituting $L = 78$ mm and $R = 1000$ mm in Eq. 6.9, we get a beam waist $w_0 = 362 \mu\text{m}$. To couple the seed laser into the OPO cavity, the seed laser mode has to be matched to that of the OPO cavity. Figure 6.3(b) shows the collimation of the seed laser beam to match the mode of the OPO cavity at the surface of the flat mirror CM1. This is achieved through a fiber collimator with an aspheric lens of $f = 8$ mm focal length, and by adjusting the distance $d_2 = 511$ mm from the fiber collimator to get a collimated beam at the required position. Instead of measuring the beam

parameters at the CM1 mirror, we opted to reproduce a waist w_0 and $R = \infty$ at a plane a distance L_2 away from the TFP (see Fig. 6.3(b)). Indeed the two planes are from the mode matching point of view equivalent.

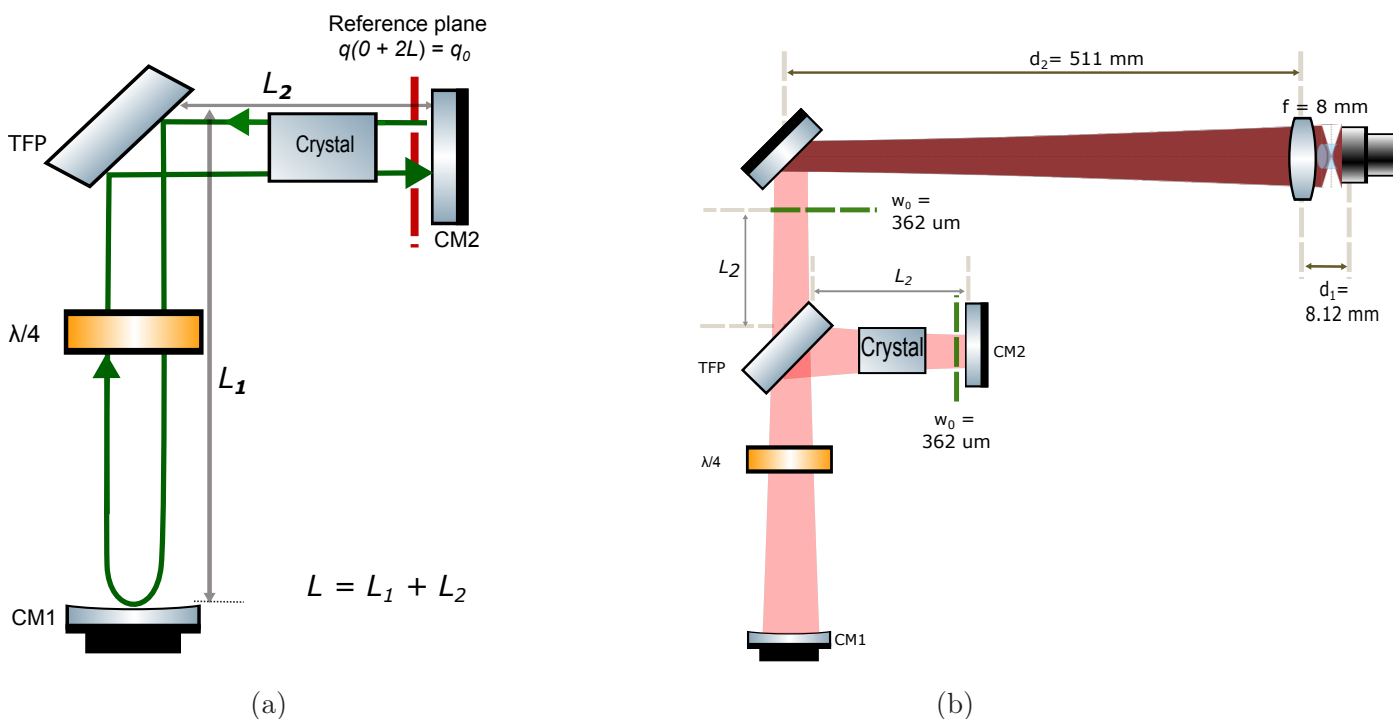


Figure 6.3: (a) The L shaped cavity layout with a $\lambda/4$, TFP and the nonlinear crystal indicated. CM1 is the flat end mirror and CM2 is the plano concave mirror with $R = 1000$ mm. The reference plane used to calculate the laser mode is indicated by the red line. (b) Mode matching between the fiber coupled seed laser and the OPO cavity. d_1 represents the distance between the output of the fiber and the aspheric lens of the collimator. d_2 represents the distance from the aspheric lens to the position at which the beam waist should be collimated to the value of $w_0 = 362 \mu\text{m}$.

6.3 Realization of a variable outcoupling cavity

A resonant optical cavity is a structure that confines light between two or more mirrors arranged in a specific configuration. The mirrors reflect the light back and forth, allowing certain wavelengths λ (or frequencies f) to build up resonantly in the cavity. Figure 6.4(a) shows an optical cavity composed of two mirrors with intensity reflectivity R_1 and R_2 , respectively, excited by a laser light with an amplitude E_{inc} . The field amplitudes after each round trip is multiplied by a factor of $(r_1 r_2) e^{-i2kL}$ where $r_1 = \sqrt{R_2}$ and $r_2 = \sqrt{R_1}$ are the

field reflectivities. The factor $2kL$ is the phase delay acquired in a round trip propagation where L is the length of the optical cavity and $k = \frac{2\pi}{\lambda}$ is the wave number. In order for the field amplitudes to build up constructive interference, the phase acquired after each round trip should satisfy $\Delta\phi = 2kL = 2n\pi$ where n is an integer number. In other words, for a cavity to be resonant to a certain wavelength, the cavity length has to be an integer multiple of half wavelength $L = n(\lambda_n/2)$ or frequency $L = \frac{2f_n}{n}$. The separation between two adjacent resonant frequencies is called the free spectral range FSR and is given by:

$$FSR = f_{n+1} - f_n = \frac{c}{2L}, \quad (6.10)$$

where c is the speed of light.

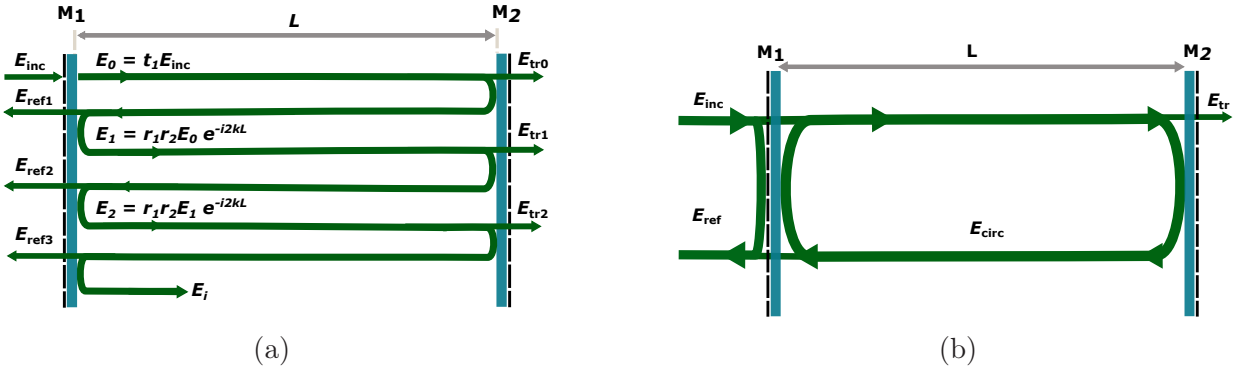


Figure 6.4: Schematic of an optical cavity consisting of two mirrors M1, M2, with a cavity length L . (a) shows the field amplitudes circulating within the cavity. (b) The cavity response to the input field is shown. E_{inc} , E_{ref} , E_{tr} and E_{circ} are the incident, reflected, transmitted and circulating fields, respectively.

The response of a two mirror optical resonator to the excitation of a laser radiation can be described through the total field amplitudes circulating E_{circ} between the two mirrors which is given by

$$E_{circ} = E_0 \left[1 + (r_1 r_2)^{1/2} e^{-i2kL} + ((r_1 r_2)^{1/2} e^{-i2kL})^2 + \dots \right]. \quad (6.11)$$

The backreflected E_{ref} and the transmitted E_{tr} field amplitudes depicted in Fig. 6.4 can be expressed in terms of the circulating light. The circulating fields are related to the incident field through the following relation [98]

$$\begin{aligned} E_{circ} &= t_1 E_{inc} + r_1 r_2 \exp^{-i2kL} E_{circ}, \\ \frac{E_{circ}}{E_{inc}} &= \frac{t_1}{1 - r_1 r_2 \exp^{-i2kL}}, \end{aligned} \quad (6.12)$$

where $t_1 = \sqrt{T_1}$ is the field transmission coefficient of the front mirror M_1 . T is the power transmission coefficient related to the power reflection coefficient through $T = 1 - R$. At resonance assuming a symmetrical cavity with equal reflectivity R for $R_1 = R_2$, the ratio of the circulating to the incident intensity then becomes

$$\begin{aligned} \left| \frac{E_{\text{circ}}}{E_{\text{inc}}} \right|^2 &= \left| \frac{t}{1 - r^2} \right|^2, \\ \frac{I_{\text{circ}}}{I_{\text{inc}}} &\approx \left| \frac{1}{t} \right|^2 = \frac{1}{T}. \end{aligned} \quad (6.13)$$

For a mirror reflectivity of $R = 99\%$, Eq. 6.13 gives a factor of 100 enhancement for the circulating intensity as opposed to the incident intensity $\frac{I_{\text{circ}}}{I_{\text{inc}}} = 100$. Such an amplification of the light within the optical cavity is used in our OPO to amplify the CW light at the seed wavelength injected into the cavity.

The field reflected from the cavity is given by [98]

$$\frac{E_{\text{ref}}}{E_{\text{inc}}} = \frac{r_1 - r_2 e^{-i2kL}}{1 - r_1 r_2 e^{-i2kL}} = \frac{1}{r_1} \times \frac{r_1^2 - r_1 r_2 e^{-i2kL}}{1 - r_1 r_2 \exp^{-i2kL}}. \quad (6.14)$$

The reflected intensity enhancement factor is given by

$$\frac{I_{\text{ref}}}{I_{\text{inc}}} = \frac{r_1^2 + r_2^2 - 2r_1 r_2 \sin(2kL)}{1 + (r_1 r_2)^2 - 2r_1 r_2 \sin(2kL)}. \quad (6.15)$$

We will use this information to compare the performance of our OPO cavity to the usual two mirror cavity referred to as Fabry-Perot interferometer.

6.3.1 The principle of operation of the variable outcoupling OPO cavity

To elucidate the working principle of our OPO cavity, we first introduce the Jones matrix formalism, which describes the influence of polarization elements on light. This formalism is then utilized to derive the effective reflectivity of the OPO cavity.

6.3.1.1 The Jones matrix formalism

We treat the laser field circulating in the OPO cavity as uniform plane-waves which has the general formula

$$E(\vec{z}, t) = \text{Re} \left\{ \left(a_x \hat{e}_x e^{i\phi_x} + a_y e^{i\phi_y} \hat{e}_y \right) \right\} E_0 e^{-i(\vec{k} \cdot \vec{z} - \omega t)}, \quad (6.16)$$

where $a_x = \frac{E_x}{E_0}$, $a_y = \frac{E_y}{E_0}$, z is the distance along which the wave travels, ω is the frequency of the propagating wave, and \vec{k} is the wave vector indicating the propagation direction with $|k| = \frac{\omega}{c} = 2\pi/\lambda$. The polarization is defined by the complex vector $\hat{e} = a_x e^{i\phi_x} \hat{e}_x + a_y e^{i\phi_y} \hat{e}_y$ in the plane \vec{k}^\perp as shown in Fig. 6.5. Equation 6.16, in general describes an ellipse in the \vec{k}^\perp plane for a fixed value of z , $(\phi_y - \phi_x) \neq 0$ and $t \in \mathbb{R}$.

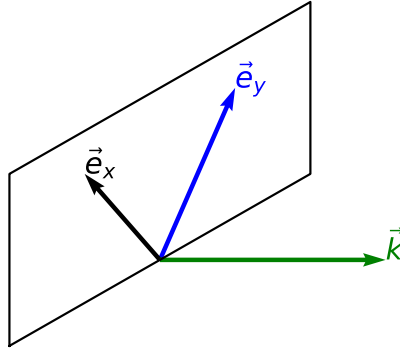


Figure 6.5: Sketch of polarization plane \vec{k}^\perp perpendicular to the propagation direction.

The complex envelope can be represented as a column matrix, referred to as the Jones vector [99, 100]

$$\mathbf{J} = \begin{bmatrix} a_x e^{i\phi_x} \\ a_y e^{i\phi_y} \end{bmatrix} = \begin{bmatrix} A_x \\ A_y \end{bmatrix}. \quad (6.17)$$

The intensity of the Jones vectors is normalized such that $|A_x|^2 + |A_y|^2 = 1$, and the phase of the x -component is set to $\phi_x = 0$. The Jones vectors provide a compact notation for representing the polarization state of the field. Specific polarization states are shown in Fig. 6.6. A common convention is to define \hat{x} as horizontal and \hat{y} as vertical. Since the direction of the beam (\vec{k}) is typically parallel to the table on which the laser setup is mounted, "horizontal" noted by (P or H) refers to being parallel to the table plane, while "vertical" noted by (S or V) refers to being perpendicular to it.

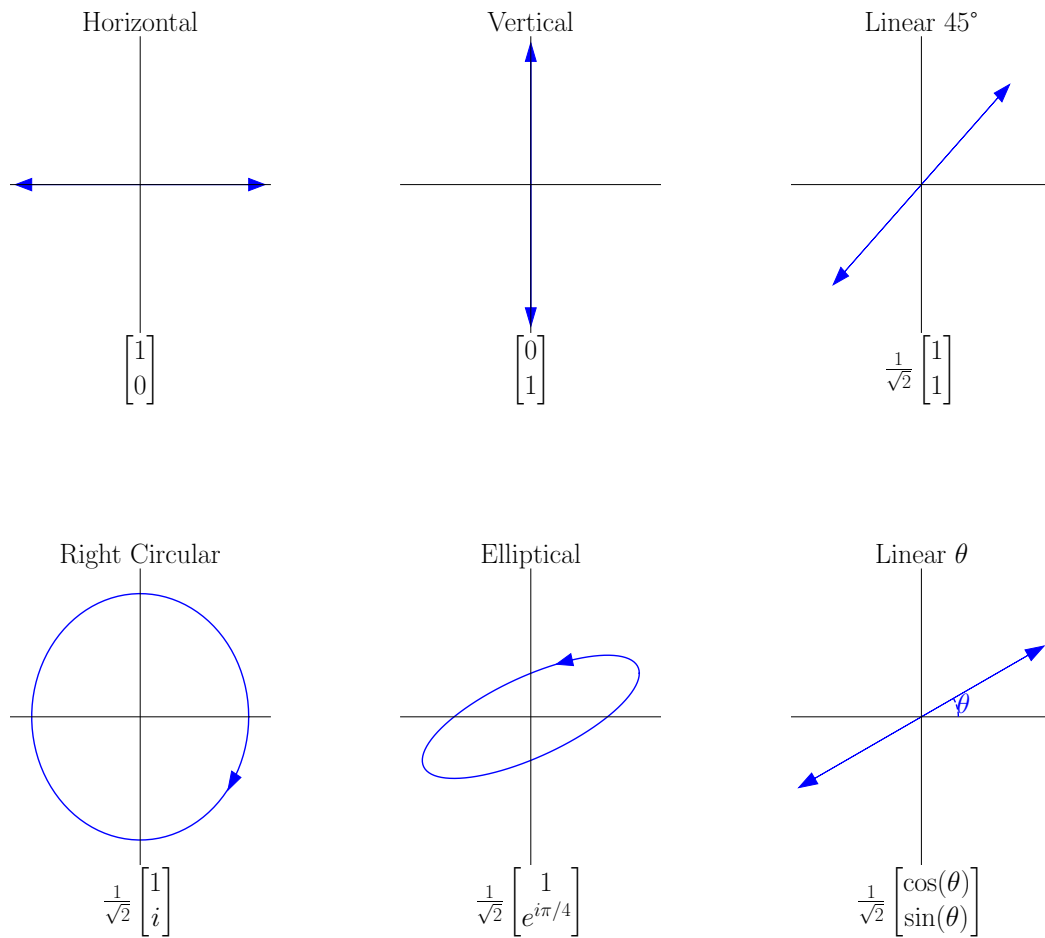


Figure 6.6: Jones vectors and representations for specific polarization states. θ is the angle w.r.t the horizontal direction. The propagation vector direction is out of the page.

Polarization devices can be described by the Jones matrices. The transmission of the optical wave through an optical element described by a 2×2 matrix M_1 is given by the relation $\vec{J}_2 = M_1 \vec{J}_1$, where \vec{J}_2 and \vec{J}_1 are the Jones vectors of output and the input wave, respectively. The structure of the Jones matrix will determine its effect on the polarization and the intensity of the wave. A polarizer in the horizontal direction will transform the incoming light with arbitrary polarization into a P-polarized light as shown in Fig. 6.7. This polarizer is described by the following Jones matrix

$$\mathbf{M}_{\text{LP}} = \begin{bmatrix} 1 & 0 \\ 0 & 0 \end{bmatrix}. \quad (6.18)$$

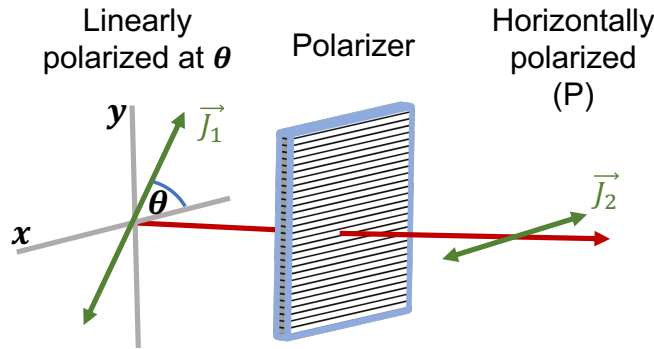


Figure 6.7: Linear polarizer: The lines on the polarizer indicate the permitted field direction for the transmitted light.

A thin film polarizer (TFP) transmits the light polarized parallel to its transmission axis (P-polarization) while reflecting the component perpendicular to it (S-polarization).

A wave retarder, or wave plate, transforms the field components (A_{1x}, A_{1y}) into $(A_{1x}, e^{-i\alpha} A_{1y})$. This introduces a phase delay α to the y-component while leaving the x-component unaffected. Retardance is achieved using birefringent materials, which were introduced in Chapter 5. The axis with the lower refractive index (n_f) is called the fast axis, as the wave exhibit a higher phase velocity, while the axis with the higher refractive index (n_s) is known as the slow axis. An example of such a wave plate is shown in Fig. 6.8.

The Jones matrix describing a waveplate is given by

$$\mathbf{M}_{\text{WP}} = e^{-i\frac{\pi}{2}} \begin{bmatrix} 1 & 0 \\ 0 & e^{i\alpha} \end{bmatrix}, \quad (6.19)$$

with $\alpha = k(n_s - n_f)\Delta z$, Δz is the thickness of the waveplate, and $e^{-i\frac{\pi}{2}}$ is a general phase shift. Here, the fast axis has been aligned to the x-direction while the slow axis has been aligned to the y-direction. A representation of such a wave plate is given in Fig. 6.8. For $\alpha = \frac{\pi}{2}$, we obtain the matrix of a quarter waveplate

$$\mathbf{M}_{\lambda/4} = e^{-i\frac{\pi}{2}} \begin{bmatrix} 1 & 0 \\ 0 & i \end{bmatrix}. \quad (6.20)$$

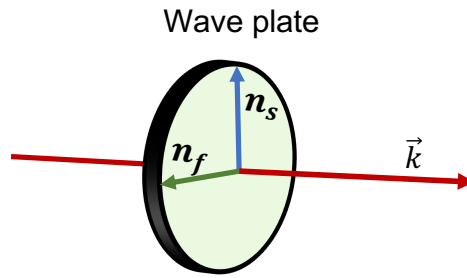


Figure 6.8: A wave plate with its fast axis aligned to the x-direction, and its slow axis aligned to the y-direction.

When the wave plate is rotated by an angle θ around the propagation direction \vec{k} , the corresponding Jones matrix, M'_{WP} , is given by $M'_{WP} = R_{\theta} M_{WP} R_{-\theta}$, where R_{θ} represents the rotation matrix defined as

$$R_{\theta} = \begin{bmatrix} \cos \theta & -\sin \theta \\ \sin \theta & \cos \theta \end{bmatrix}. \quad (6.21)$$

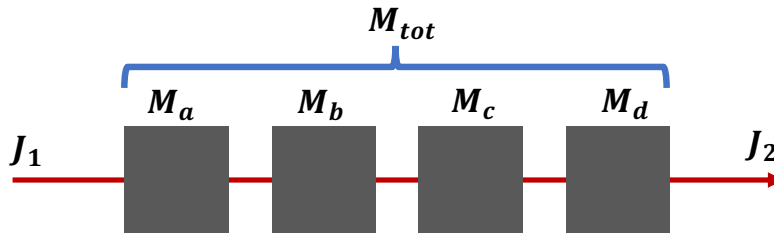


Figure 6.9: Transmission of light through several polarizing optical elements. J_1, J_2 represent the Jones vector of the input and output wave, respectively. The output vector is related to the input vector by the matrices product given in Eq. 6.22.

Finally, the transmission of a wave through cascaded optical elements as shown in Fig. 6.9 can be described by the matrix product

$$M_{\text{tot}} = M_d \cdot M_c \cdot M_b \cdot M_a. \quad (6.22)$$

In this product, the matrix of the optical element through which the light is first transmitted stands at the right end of the product.

6.3.1.2 OPO cavity reflection and transmission

We now apply the Jones matrix formalism to describe the propagation of the laser light within the OPO cavity. Our OPO cavity contains polarization-dependent elements: quarter wave plate ($\lambda/4$ – plate) and a thin film polarizer (TFP) as shown in Fig. 6.10. In such a cavity, the circulating intensity depends on the angle θ of the $\lambda/4$ – plate. This is the angle between the fast axis of the wave plate and the horizontal direction. To illustrate how the light propagation inside the cavity changes with the angle θ of the $\lambda/4$ – plate, we consider two special cases of $\theta = 0^\circ$ and 45° as depicted in Fig. 6.10(a) and 6.10(b), respectively. Here, a $\lambda/4$ – plate with an angle $\theta = 0$ refers to the slow axis aligned to the (vertical) y-direction while the fast axis is aligned to the (horizontal) x-direction as shown earlier in Fig. 6.8.

- $\lambda/4$ – plate at an angle $\theta = 0^\circ$:

The polarization evolution of the light transmitted through TFP, point ①, $\lambda/4$ –plate then reflected by the CM1 mirror back to point ② is described by the product of the Jones matrices:

$$\vec{E}_2 = M_{\lambda/4}(0^\circ) \cdot M_{\lambda/4}(0^\circ) \cdot M_{\text{TFP}}(P) \cdot \vec{E}_{\text{inc}} e^{-2ikL_1}, \quad (6.23)$$

where \vec{E}_2 is the field amplitude at point ②. The TFP is described by the matrix of a linear polarizer $M_{\text{TFP}}(P)$ in the horizontal direction. The field of the incident beam \vec{E}_{inc} is assumed to be linearly polarized at an arbitrary angle β described by

$\vec{E}_{\text{inc}} = \frac{|E_{\text{inc}}|}{\sqrt{2}} \begin{bmatrix} \cos(\beta) \\ \sin(\beta) \end{bmatrix}$. The beam experience a phase delay e^{-2ikL_1} after propagating a

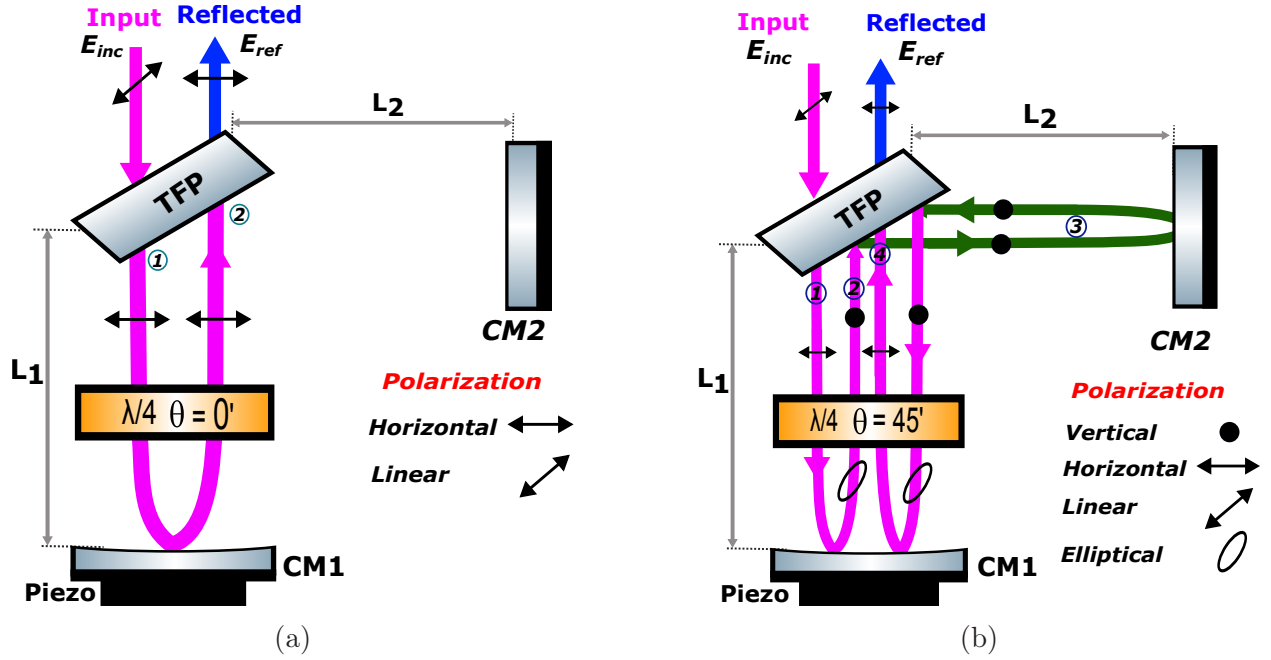


Figure 6.10: Beam incoupling and propagation within the OPO cavity for two special angles of the $\lambda/4$ – plate. (a) $\theta = 0^\circ$, (b) $\theta = 45^\circ$ shown in (b).

distance of $2L_1$. The matrix product relating the field amplitudes \vec{E}_2, \vec{E}_{inc} is given by:

$$\begin{aligned} \vec{E}_2 &= \frac{|E_{inc}|}{\sqrt{2}} e^{-i\frac{\pi}{2}} e^{-i\frac{\pi}{2}} e^{-2ikL_1} \begin{bmatrix} 1 & 0 \\ 0 & i \end{bmatrix} \begin{bmatrix} 1 & 0 \\ 0 & i \end{bmatrix} \begin{bmatrix} 1 & 0 \\ 0 & 0 \end{bmatrix} \begin{bmatrix} \cos(\beta) \\ \sin(\beta) \end{bmatrix} \\ &= \frac{|E_{inc}| \cos(\beta)}{\sqrt{2}} e^{-i\pi} e^{-2ikL_1} \begin{bmatrix} 1 \\ 0 \end{bmatrix}. \end{aligned} \quad (6.24)$$

We see in this case that the light returns completely P-polarised, and the factor $e^{-i\pi} e^{-2ikL_1}$ only represents a phase shift that does not affect the polarization. The beam will be completely transmitted back through the TFP since it is horizontally polarized.

- $\lambda/4$ – plate at $\theta = 45^\circ$:

The polarization evolution of the light transmitted through TFP, point (1), $\lambda/4$ –plate then reflected back by CM1 to point (2) is described by the product of the Jones

matrices:

$$\begin{aligned}
\vec{E}_2 &= e^{-i\frac{\pi}{2}} e^{-i\frac{\pi}{2}} e^{-2ikL_1} \cdot M_{\lambda/4}(45^\circ) \cdot M_{\lambda/4}(45^\circ) \cdot M_{\text{TFP}}(P) \cdot \vec{E}_{\text{inc}} \\
&= \frac{|E_{\text{inc}}| e^{-i\pi} e^{-2ikL_1}}{4\sqrt{2}} \begin{bmatrix} 1-i & 1+i \\ 1+i & 1-i \end{bmatrix} \begin{bmatrix} 1-i & 1+i \\ 1+i & 1-i \end{bmatrix} \begin{bmatrix} 1 & 0 \\ 0 & 0 \end{bmatrix} \begin{bmatrix} \cos(\beta) \\ \sin(\beta) \end{bmatrix} \\
&= \frac{|E_{\text{inc}}| \cos(\beta)}{4\sqrt{2}} e^{-i\pi} e^{-2ikL_1} \begin{bmatrix} (1-i)^2 + (1+i)^2 \\ 2+2 \end{bmatrix} = \frac{|E_{\text{inc}}| \cos(\beta)}{\sqrt{2}} e^{-i\pi} e^{-2ikL_1} \begin{bmatrix} 0 \\ 1 \end{bmatrix}.
\end{aligned} \tag{6.25}$$

The result is that the beam at point ② is completely S-polarized and the action of the TFP on that beam is to totally reflect it towards point ③ (see Fig. 6.10(b)). The beam reflection from the TFP, going through point ③, reflected back by the TFP to pass through the $\lambda/4$ – plate, reflecting from the mirror CM1 then crossing the $\lambda/4$ – plate to point ④ is described by

$$\begin{aligned}
\vec{E}_4 &= e^{-i\frac{\pi}{2}} e^{-i\frac{\pi}{2}} e^{-2ik(L_1+L_2)} \cdot M_{\lambda/4}(45^\circ) \cdot M_{\lambda/4}(45^\circ) \cdot M_{\text{TFP}}^2(S) \cdot \vec{E}_2 \\
&= \frac{|E_2| e^{-i\pi} e^{-2ik(L_1+L_2)}}{4} \begin{bmatrix} 1-i & 1+i \\ 1+i & 1-i \end{bmatrix} \begin{bmatrix} 1-i & 1+i \\ 1+i & 1-i \end{bmatrix} \begin{bmatrix} 0 & 0 \\ 0 & 1 \end{bmatrix} \begin{bmatrix} 0 \\ 1 \end{bmatrix} \\
&= \frac{|E_2| e^{-i\pi} e^{-2ik(L_1+L_2)}}{4} \begin{bmatrix} 2(1-i)(1+i) \\ (1+i)^2 + (1-i)^2 \end{bmatrix} = |E_2| e^{-i\pi} e^{-2ik(L_2+L_1)} \begin{bmatrix} 1 \\ 0 \end{bmatrix}.
\end{aligned} \tag{6.26}$$

Here, the resultant field is P-polarized and it would be totally transmitted back by the TFP.

If the $\lambda/4$ – plate is turned to an arbitrary angle θ , the combination of the TFP, $\lambda/4$ – plate, and the mirror CM1 is equivalent to a mirror or an (outcoupler for the seed light) with a variable effective reflectivity (R_{eff}). This R_{eff} depends on the orientation of the axis of the $\lambda/4$ – plate as we will show below. The OPO cavity layout is equivalent to a polarizing Gires-Tournois interferometer (PGTI) but with a variable partial reflector [101]. That is a linear two mirror optical cavity with a front mirror which has a variable partial reflectivity (PR) and an end mirror which is highly reflecting (HR) as shown in Fig. 6.11(b).

In order for us to describe the effective reflectivity of the front mirror, we will derive the relation between reflected intensity and relate it to the incident intensity. We then compare the formulas to a simple two mirror cavity and derive the effective reflectivity of

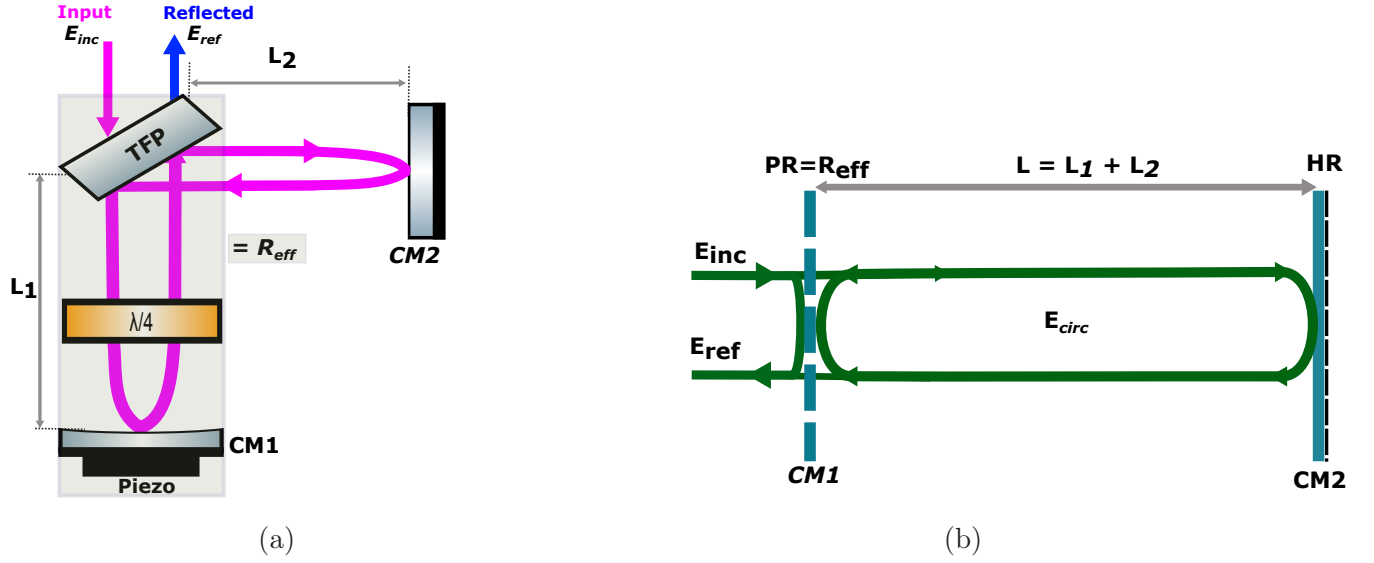


Figure 6.11: (a) Layout of the OPO optical cavity with the polarization elements. $\lambda/4$ refer to the quarter wave plate, TFP is the thin film polarizer. CM1 and CM2 are the end mirrors of the cavity. L_1 and L_2 correspond to the distance from the TFP to CM1 and CM2, respectively. (b) An equivalent representation in terms of a linear two mirror cavity.

the outcoupler. The incoming beam has a field amplitude of E_{inc} , the reflected beam has a field amplitude of E_{ref} and the intra-cavity field amplitude is E_{circ} . A full derivation of the expression for E_{circ} and E_{ref} is given in Appendix 6.A.1. The total field amplitude reflected E_{ref} back through the TFP is given by:

$$E_{ref} = \frac{(r_1 e^{-2iL_1 k} t_{\lambda}^2 t_{TFP}^2) e^{-i\pi/2}}{1 + r_1 r_2 e^{-2i(L_1+L_2)k} \rho e^{-i\pi/2} \cos(2\theta)} \left(\cos(2\theta) + r_1 r_2 e^{-2i(L_1+L_2)k} \rho e^{-i\pi/2} \right) E_{inc}. \quad (6.27)$$

Hence, the reflected intensity enhancement factor is given by:

$$\frac{I_{ref}}{I_{inc}} = \frac{(r_1 t_{\lambda}^2 t_{TFP}^2)^2 [\cos^2(2\theta) + (r_1 r_2 \rho)^2 - 2r_1 r_2 \rho \cos(2\theta) \sin(2kL)]}{1 + (r_1 r_2 \rho)^2 \cos^2(2\theta) - 2r_1 r_2 \rho \cos(2\theta) \sin(2kL)}. \quad (6.28)$$

Here, we remind the reader that L is the total cavity length.

Comparing Eq. 6.28 to the one of a two mirror cavity given in Eq. 6.15, shows that our cavity can be described as a two mirror cavity with $r_{eff} = \sqrt{R_{eff}} = \cos(2\theta)$, and another highly reflective mirror of $r = \sqrt{R} = r_1 r_2 \rho$, where $\rho = t_{\lambda}^2 r_{TFP}^2$ is the field round trip loss factor.

Figure 6.12 shows the intra-cavity resonances measured at different angles of the $\lambda/4$ – plate, and they are proportional to the intensity enhancement factor. The linewidths of the resonances increase, while the amplitudes decrease when increasing the angle of wave plate

or when reducing the effective reflectivity $r_{\text{eff}} = \sqrt{R_{\text{eff}}} = \cos(2\theta)$. The sharpness of the resonances or the selectivity of the cavity is measured in terms of the finesse \mathcal{F} , which is a ratio of the free spectral range to the linewidth (full width at half maximum $\delta\nu_{1/2}$). The finesse can be expressed in terms of the cavity losses (L_{loss}) and the two mirrors reflectivity R_{eff}, R given by [102]

$$\mathcal{F} = \frac{FSR}{\delta\nu_{1/2}} = \frac{2\pi}{-\ln[(\cos 2\theta R)^2(1 - L_{\text{loss}})]}. \quad (6.29)$$

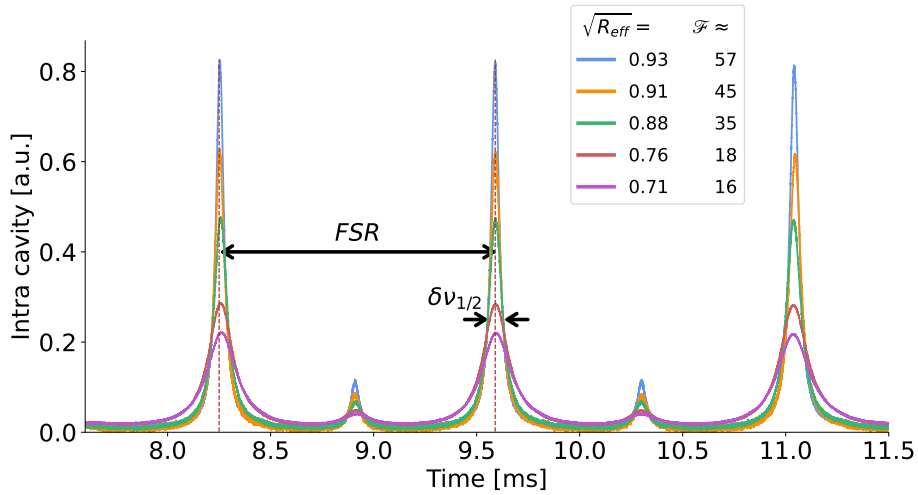


Figure 6.12: Measured intra-cavity resonances for various effective reflectivities $\sqrt{R_{\text{eff}}}$ and its corresponding finesse \mathcal{F} values. The free spectral range FSR as well as the linewidth $\delta\nu$ of the resonances are indicated.

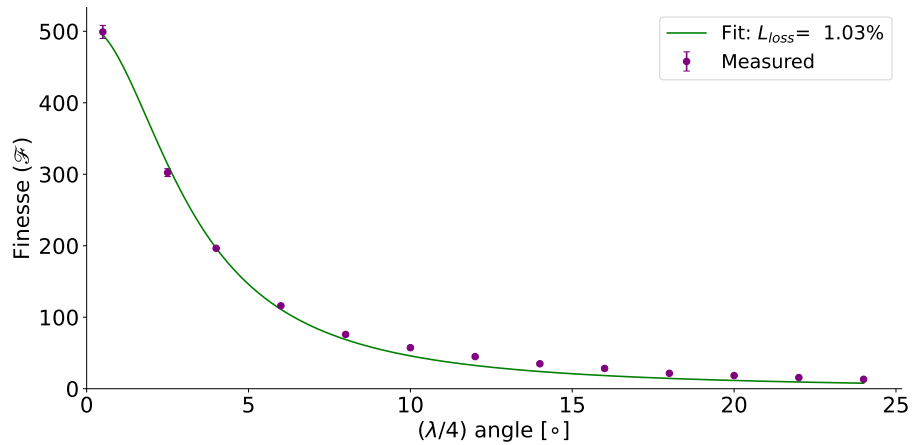


Figure 6.13: The finesse \mathcal{F} versus angle of $\lambda/4$ – plate extracted from the measured intra-cavity resonances. A fit of the data using Eq. 6.29 was carried out, where the uncertainty comes from the cavity losses L_{loss} , for details see text.

Figure 6.13 shows the finesse for various R_{eff} , for this we measured the the intra-cavity resonances against the rotation angle of the $\lambda/4$ – plate. The finesse was deduced from the linewidths and the FSR of the measured intra-cavity resonances. Fitting Eq. 6.29 to the deduced finesse, yielded a cavity round trip loss factor of $L_{\text{loss}} \approx 1\%$ as indicated in Fig. 6.13. This shows that we can adjust the finesse, hence the intra-cavity enhancement factor of the OPO cavity through the rotation angle of the $\lambda/4$ – plate.

6.4 PDH locking of the OPO cavity

We use the Pound-Drever-Hall (PDH) technique to lock the OPO cavity to the seed laser by stabilizing the cavity length to the seed laser frequency [103]. In this method, a phase modulation is applied to the laser light using an EOM, generating sidebands around the carrier frequency. When the modulated light enters the cavity, only the carrier resonates if the cavity length matches the laser frequency, while the sidebands are reflected. The reflected signal is detected using a photodetector and demodulated at the modulation frequency to produce an error signal. This error signal, proportional to the cavity-laser detuning, is fed back to control the cavity length [104]. A detailed theoretical description of the PDH error signal is provided in [105].

The setup used to implement this technique is depicted in Fig. 6.14. The laser light is sent through an EOM driven by a local oscillator to modulate the phase of the laser field at a frequency f_{mod} . This modulation generates frequency sidebands separated from the carrier at the central frequency, which is resonant with the cavity. A fiber isolator is placed to protect both the seed laser and the EOM from back reflections, particularly during pulsed operation.

The combination of the three elements—TFP, half-waveplate ($\lambda/2$ – plate), and Faraday rotator (FR)—functions as follows. It rotates the linearly polarized light coming out of the fiber isolator into P-polarized light, which is coupled into the cavity. The P-polarized light reflected from the cavity, however, is rotated by $\frac{\pi}{2}$ and becomes S-polarized due to the non-reciprocal action of the FR and the $\lambda/2$ – plate on the polarization of waves propagating in opposite directions.

The frequency of the sidebands is off-resonant with the cavity; therefore, they are reflected

with a phase shift different from that of the resonant central frequency. The light at the resonant frequency, reflected from the cavity, acquires a phase shift proportional to the deviation of the cavity resonance from the laser frequency. The S-polarized light reflected by the TFP is directed onto a fast photodiode (2 GHz PD), which produces a beat signal at f_{mod} .

The beat signal is high-pass filtered and amplified before being combined with a frequency-doubled local oscillator signal at $2f_{\text{mod}}$ in an active mixer to produce the error signal. This error signal is a DC signal with a phase proportional to the phase of the PD signal and is thus proportional to the cavity-laser detuning. The error signal is low-pass filtered, amplified, and sent to a PID controller, which generates the feedback signal. The feedback signal, further amplified by a high-voltage amplifier, acts on the piezoelectric element of the cavity end mirror to compensate for frequency changes δf through length changes $\delta l = \frac{\delta f}{FSR} \frac{\lambda_{\text{seed}}}{2}$, where λ_{seed} is the laser wavelength resonant with the cavity.

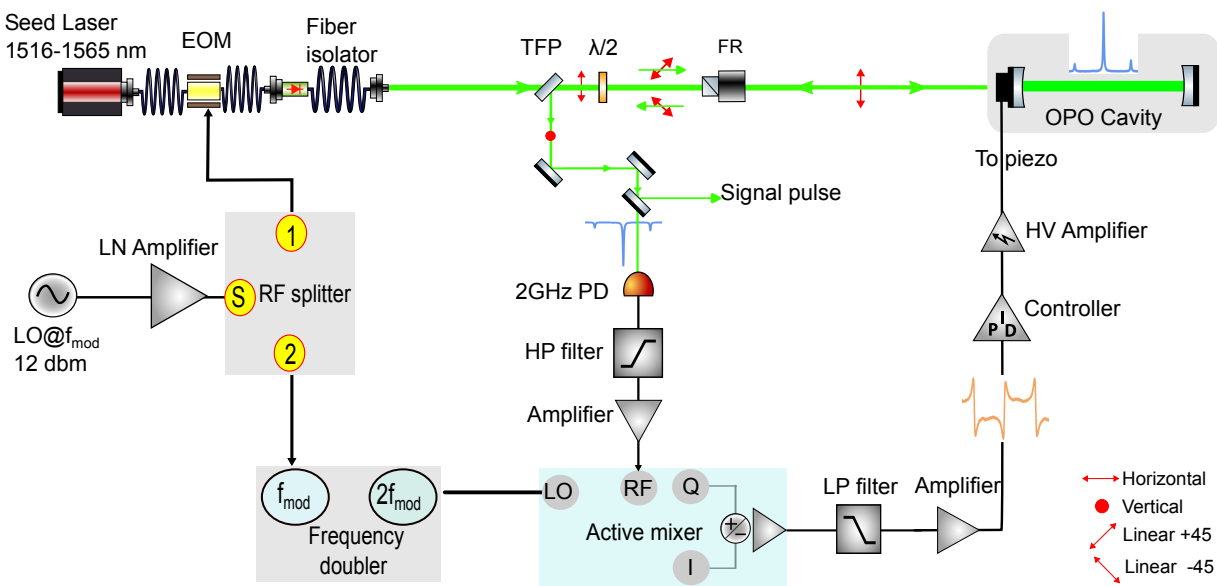


Figure 6.14: Schematic of the PDH locking. Detailed description is given in the text.

An error signal obtained for a modulation frequency of $f_{\text{mod}} = 300$ MHz is shown in Fig. 6.15. The sign of the error signal determines the direction in which the cavity length is corrected to achieve resonance, as indicated by the black arrows on the error signal annotated as ‘Lock’. The compensation range, however, is limited by the factor $\delta l = \frac{f_{\text{mod}}}{FSR} \frac{\lambda_{\text{seed}}}{2}$. If the laser-cavity frequency detuning exceeds $\delta f > f_{\text{mod}}$, the sign of the error signal reverses, and the cavity is pulled into an off-resonant state, as indicated by the green arrows on the error signal annotated as "Anti Lock".

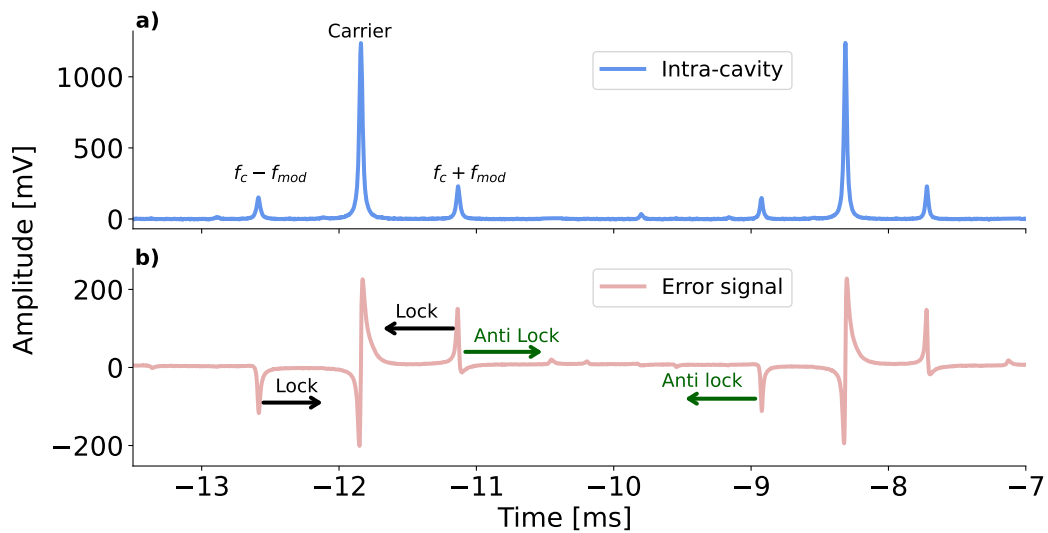


Figure 6.15: a) The modulated intra-cavity intensity is shown. The carrier corresponds to the central frequency of the longitudinal mode resonant with the cavity. The frequencies $f_c + f_{mod}$ and $f_c - f_{mod}$ represent the two sidebands generated by the phase modulation and are made visible by scanning the cavity length. b) The PDH error signal obtained for $f_{mod} = 300$ MHz. The black arrows indicate the direction in which the cavity is pulled to lock on resonance. The green arrows indicate the direction in which locking occurs between resonances, referred to as "Anti-locking".

6.4.1 Realization of a PDH lock with infinite capture range

For the OPO, long-term stable operation over 10 weeks is required as part of the overall laser system. Additionally, this OPO branch will be used to tune the final laser system wavelength during the search for the HFS resonance. Achieving such a wide tunability range of approximately 50 GHz necessitates stable operation under varying conditions, such as changes in temperature and seed wavelength.

To meet these requirements, we have modified the PDH locking technique to operate with a modulation frequency of $f_{\text{mod}} = FSR/2$ [106]. This modification ensures that stable locking points align with the cavity resonances. Consequently, the feedback loop consistently re-locks to the nearest resonance, regardless of the laser-cavity detuning magnitude. This method was initially implemented in the thin-disk oscillator at $f_{\text{mod}} = 40$ MHz and has been adapted to accommodate the 20 times larger FSR of the OPO cavity.

6.4.1.1 Experimental setup

For an OPO cavity with a length of $d = 78.12$ mm, the free spectral range (FSR) is 1918 MHz. Installing the non-linear crystal within the cavity decreases the FSR to 1520 MHz. This reduction occurs due to the longer effective optical path length within the crystal, which has a higher refractive index.

We use a modulation frequency of $f_{\text{mod}} = \frac{FSR}{2} = 760$ MHz (see the setup in Fig. 6.14), generated by an RF synthesizer (SG03-840001-S5S5) and amplified by a low-noise amplifier (ZX60-P103LN+). After amplification, the RF signal is split equally and fed into the EOM (MPZ-LN-01), which modulates the phase of the laser light field. The reflected signal from the OPO cavity is detected on a fast photodiode (ET-3000A), high-pass filtered, and amplified by a high-gain amplifier (ZFL-1000VH2+) before being fed into the active mixer.

A copy of the RF signal sent to the EOM is frequency-doubled by a multiplier (MK-5BR) and then combined with the output of the fast photodiode in the active mixer. The active mixer, which is a custom-built unit based on the quadrature demodulator board (EVAL-ADL5387), dynamically adjusts the phase shift between the photodiode signal and the modulation signal. A detailed description of the active mixer is provided in Appendix 6.B.

After generating the error signal, it is fed into a PID controller (PID 110), which includes an internal HV amplifier providing an input signal from 0 to 150 volts to actuate the piezoelectric element attached to the mirror CM1. The mirror itself is mounted on a heavy copper piece and is secured to a highly stable mount (POLARIS-K1VS2) to enhance stability, as shown in Fig. 6.16. The piezoelectric element (HPCh150/15-8/3) has a maximum displacement range of $3 \mu\text{m}$ at a maximum applied voltage of 150 volts. In the non-locked state, we scan over three resonance modes, requiring a cavity length change of $\lambda = 1.54 \mu\text{m}$.

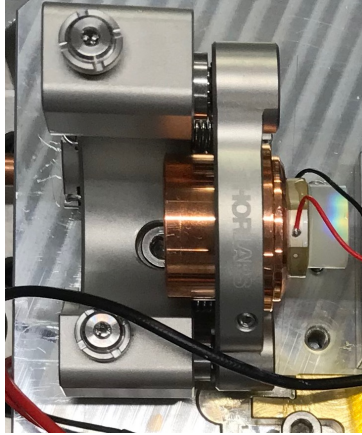


Figure 6.16: The high-stability mirror mount designed for the combination of the piezoelectric element and the mirror CM1. The mirror has a diameter of 0.5 " and a thickness of 6 mm.

Figure 6.17 shows the intra-cavity resonances and the corresponding error signal obtained for $f_{\text{mod}} = \frac{FSR}{2} = 760 \text{ MHz}$ during cavity scanning and locking. The short-term response of the PDH lock during pulse generation is shown in Fig. 6.18. The intra-cavity intensity, shown in blue, returns to its pre-pulse level in less than 100 ns. Within approximately $0.75 \mu\text{s}$, the error signal, shown in green, also returns to its pre-pulse level. This recovery time is much shorter than the pulse-to-pulse interval, which occurs on the millisecond scale, as will be discussed in the next section. The long-term stability of the locking will be demonstrated by showcasing the tunability of the OPO in Sec. 6.5.3.

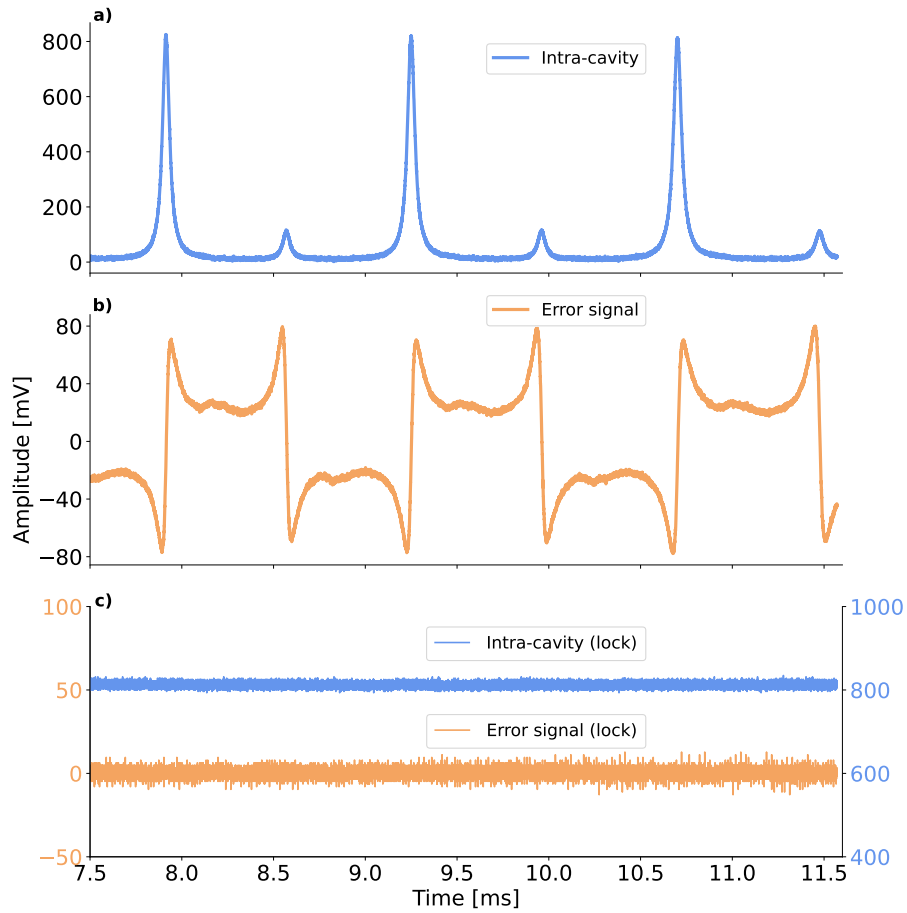


Figure 6.17: a) Modulated intra-cavity resonances, with the sidebands at 760 MHz visible when scanning the cavity length. b) The PDH error signal generated at a modulation frequency of $FSR/2$. c) The intra-cavity intensity and error signal when the cavity is locked to the laser frequency.

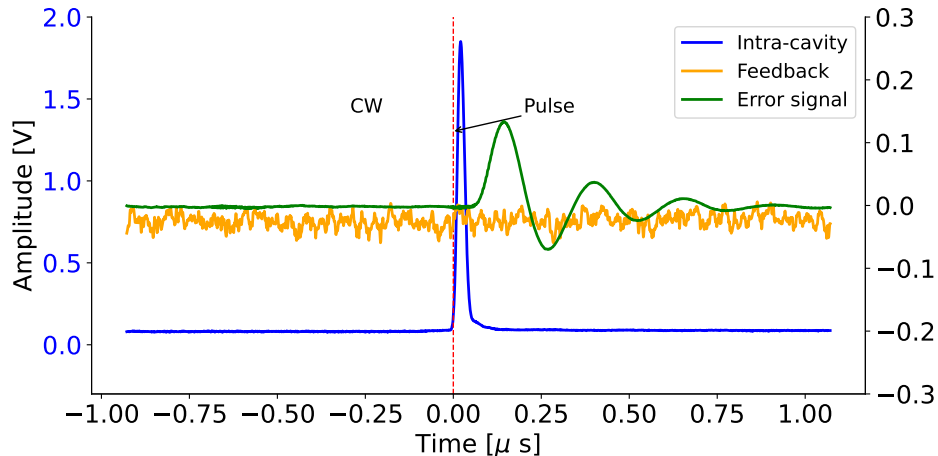


Figure 6.18: The stabilized error signal, intra-cavity power, and piezo feedback voltage (which controls the cavity length) are shown as functions of time during pulse generation. In this case, a pulse energy of $500 \mu\text{J}$ at 3142 nm was extracted.

6.5 Optical parametric oscillator with variable conversion efficiency

An optical parametric oscillator (OPO) is a device in which the field at one or two frequencies generated during the DFG process is made resonant with an optical cavity. This is achieved by placing the nonlinear crystal inside the optical cavity and coating the cavity mirrors to have specific transmission and reflectivity properties for ω_p , ω_s , and ω_i , as shown in Fig. 6.19. When the amplification due to the parametric gain of the resonant waves meets or exceeds the resonator losses, a significant growth of the signal and idler waves occurs (oscillation). The primary sources of loss include mirror transmission, as well as crystal and coating absorption.

In our case, the OPO cavity is made resonant only to ω_s or, equivalently, the wavelength λ_s , which is referred to as a singly resonant oscillator (SRO). We remind the reader that, in the context of the OPO, ω_i corresponds to the lowest frequency, or equivalently, the longest wavelength λ_i . Conversely, the pump frequency ω_p refers to the highest frequency or the shortest wavelength λ_p .

The growth of the signal intensity from the initial value $I_s(0)$ is described by the same parametric gain given in Eq. 5.15. In the case of the OPO, both the signal and pump fields are focused into the nonlinear crystal and exhibit a transverse Gaussian distribution.

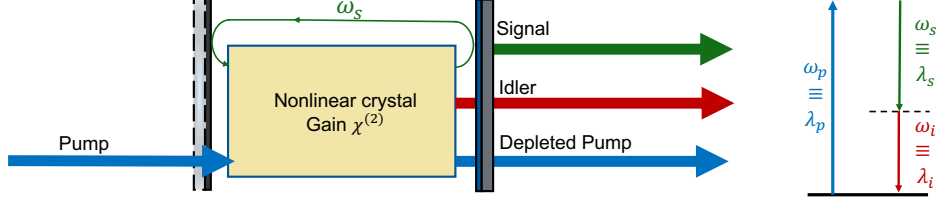


Figure 6.19: Sketch of the singly resonant OPO and the corresponding energy level diagram for the parametric down-conversion process.

Efficient nonlinear conversion is achieved when the three fields share a common confocal parameter [107], described by

$$b_0 = b_j = \frac{2\pi n_j w_{0j}^2}{\lambda_{0j}}, \quad (6.30)$$

where $j = p, s$ or i . The confocal parameter represents the distance around the focal point where the beam radius remains less than $\sqrt{2}w_0$, equivalent to twice the Rayleigh length. The gain factor g for interacting gaussian beams is modified by the following function [95]

$$g^2 = \frac{4\omega_s\omega_i d_{eff}^2 P_p}{\varepsilon_0 c^3 n_s n_i \lambda_p L} \bar{h}_m(B, \xi), \quad (6.31)$$

$$\xi = L/b_0,$$

where L is the interaction length, and P_p is the power of the pump radiation. B is approximately the ratio of the walk-off angle to the far-field diffraction angle of the Gaussian beam. In our case, we use a PPLN crystal with quasi-phase matching, for which no angle tuning is required, and hence there is no walk-off.

For the case of no walk-off angle and weak focusing ($\xi < 1$), which applies to our setup with $\xi = 0.01$, the result follows the asymptotic behavior $\bar{h}_m(B, \xi) \rightarrow \xi$. Substituting this result into Eq. 6.31 restores the gain formula for the plane-wave case, as given in Eq. 5.15 [108].

The conversion efficiency, defined as I_s/I_p , depends on several parameters: the pump intensity above the threshold value $I_{p,thr}$, the cavity reflectivity R_{cav} , and the losses L_{loss} inside the cavity. For a pulsed OPO with Gaussian beams, the maximum achievable conversion efficiency is $0.63 \eta_{max}$, which is reached when pumping at approximately $10.3 I_{p,thr}$. Here, η_{max} is the maximum conversion efficiency expressed in terms of the cavity reflectivity and losses as [109]

$$\eta_{max} = \frac{1 - R_{cav}}{1 - R_{cav}(1 - L_{loss})}, \quad (6.32)$$

where $R_{cav} = \sqrt{RR_{eff}}$.

The threshold pump intensity at which oscillations start is not a fixed value but varies depending on several cavity parameters, as described by the following equation [110, 111]

$$I_{p,\text{thr}} = \frac{1.8}{\kappa g_s L_{\text{eff}}^2} \left(\frac{25L_{\text{cav}}}{c\tau} + 2\alpha L_{\text{eff}} + \ln \frac{1}{\sqrt{R_{\text{tot}}}} + \ln 2 \right)^2. \quad (6.33)$$

Here, $L_{\text{eff}} = L_{\text{crystal}}$ represents the crystal length, which is also the effective interaction length, and L_{cav} is the cavity length. R_{tot} is the product of the input-coupling, outcoupling, and cavity losses, given by $R_{\text{tot}} = R_{\text{cav}}(1 - L_{\text{loss}})$. g_s is the mode coupling coefficient between the pump and signal Gaussian beams, τ is the FWHM of the pump pulse length, and α represents the absorption loss. The coupling constant is defined as:

$$\kappa = \frac{2\omega_s \omega_i d_{\text{eff}}^2}{n_s n_i n_p \epsilon_0 c^3}. \quad (6.34)$$

The physical interpretation of the terms in Eq. 6.33 is as follows: the first term represents the loss due to the cavity buildup time, which increases with L_{cav} . Therefore, we opted for the shortest realizable cavity length, considering the size of the optical components and the space required for alignment and diagnostics. The second term corresponds to absorption losses throughout the cavity. The third term relates to cavity outcoupling and transmission losses. Finally, the last term pertains to the nature of the singly resonant OPO.

To achieve optimal output pulse energies, the gain must be finely balanced to generate laser pulses without damaging the OPO. From Eq. 5.15, the gain of the nonlinear crystal depends on the intensity of the pump radiation. The simplest way to operate an OPO is to use an outcoupling mirror with very high reflectivity ($R = 97\text{--}99\%$). At high reflectivity, $I_{p,\text{thr}}$ is low, making it easy to achieve oscillation; however, this configuration becomes inefficient for extracting output energy. Even a small nonlinear gain would suffice to enable laser operation, but it would also result in a significant enhancement of signal radiation within the cavity. Consequently, small pump pulse energies could lead to intra-cavity intensity high enough to cause optical damage, thereby limiting the laser output power.

At high pump intensity, the gain per pass is sufficiently large, necessitating lower reflectivity to achieve higher output energies. While it is possible to use a set of outcoupling mirrors with different reflectivities, this approach would be expensive and would require realigning the cavity after each change. Therefore, we opted for a design where the amount of signal field outcoupled from the cavity can be varied continuously without misaligning the OPO cavity. High reflectivity allows for initial optimization of alignment and crystal parameters, such as length and phase matching. Once these parameters are optimized, R_{eff} can be

adjusted to maximize efficiency for a given pump energy, constrained by the light-induced damage threshold.

6.5.1 Experimental setup

We realized an OPO using a periodically poled lithium niobate (LiNbO_3) crystal as the nonlinear medium. The crystal, an MgO:PPLN (5 mol%) from HCP, has a length of 14 mm, a thickness of 3 mm, and a width of 4 mm. It has a period of $30.2 \mu\text{m}$ and is anti-reflective coated for three different wavelengths. Figure 6.20 shows an image of the realized OPO, based on the variable outcoupling cavity discussed in previous sections.

S-polarized 50 ns-long pulses at a pump wavelength of 1030 nm and at a repetition rate of 30 Hz are coupled through the TFP and focused onto the center of the nonlinear crystal. The pump beam has a TEM_{00} mode with a beam waist of approximately $370 \mu\text{m}$, matched to the cavity transverse mode at the signal wavelength of $362 \mu\text{m}$. The crystal is mounted on a Peltier element inside a home-built oven, which controls the temperature to achieve phase matching, producing an idler at a wavelength of approximately 3142 nm. For this configuration, the phase matching temperature was 31°C .

The cavity is locked to operate at the single longitudinal mode defined by the seed laser. The input pump energy is varied using a set of $\lambda/2$ – plates and a TFP, as shown in Fig. 6.1, and the pulse energies at the idler wavelength is measured for different outcoupling reflectivities. The outcoupling variation is achieved by adjusting the angle of the $\lambda/4$ – plate, thereby changing R_{eff} . A separator mirror, anti-reflective coated for the pump and signal wavelengths but highly reflective (95%) for the idler wavelength, is used to reflect only the idler light. A thermoelectric energy meter detects and records the pulse energies.

The total output energy, $E_{\text{total}} = E_s + E_i$, and the corresponding conversion efficiency as a function of the input pump energy are shown in Fig. 6.21, measured at different R_{eff} . The conversion efficiency is defined as:

$$\eta_p = \frac{E_s + E_i}{E_p}. \quad (6.35)$$

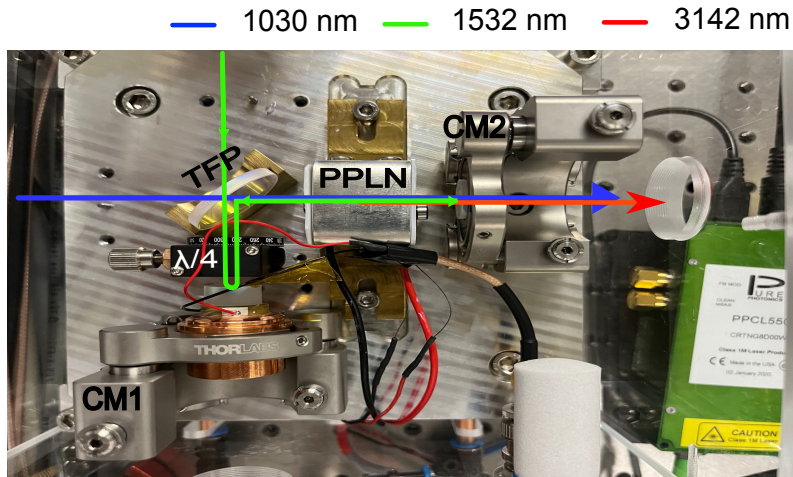


Figure 6.20: Picture of the OPO setup we built. The pump beam, shown in blue, is coupled through the TFP, which is HT for the pump wavelength. The signal light, shown in green, is resonant within the cavity. The (PPLN) text refers to the nonlinear crystal inside the home-built oven used to control the crystal temperature. The generated pulses at the idler wavelength are coupled through the mirror (CM2), which is HT for this wavelength.

The lowest pump threshold is achieved at $r_{\text{eff}} = 94\%$, but the conversion efficiency declines at pump energies around three times the threshold value. The highest extractable energy is achieved for $r_{\text{eff}} = 71\%$, with values of $E_i = 1.41$ mJ and $E_{\text{total}} = 4.25$ mJ at $E_p = 10.36$ mJ, corresponding to $\eta = 41\%$. In principle, higher extractable energy values could be achieved, but we are limited by the damage threshold observed at higher pump energies. A 50% increase in the maximum value of E_{total} at $r_{\text{eff}} = 71\%$ is achieved compared to the highest reflectivity, and the maximum achievable pump energy is increased by approximately 30%.

The relationship between the output energy and the pump energy is linear as long as backconversion does not occur, as shown by Terry et al. [112]. This linear behavior is observed in Fig. 6.21 for pump energies below a certain threshold, after which the slope changes due to backconversion. Backconversion is a process in which the signal and idler interact to produce photons at the pump wavelength. A detailed study by Smith et al. [113] highlights the effects of backconversion on various aspects of OPO performance. Backconversion is inherent to nanosecond OPOs due to the high single-pass gain required to reach the threshold within a single pulse. Once the threshold is exceeded, the intense gain depletes the pump beam center, enabling backconversion of the signal and idler. Our OPO cavity design allows optimization of the cavity outcoupling to minimize backconversion while maximizing the output energy.

The effect of injection seeding on the output pulse energy is demonstrated by measuring

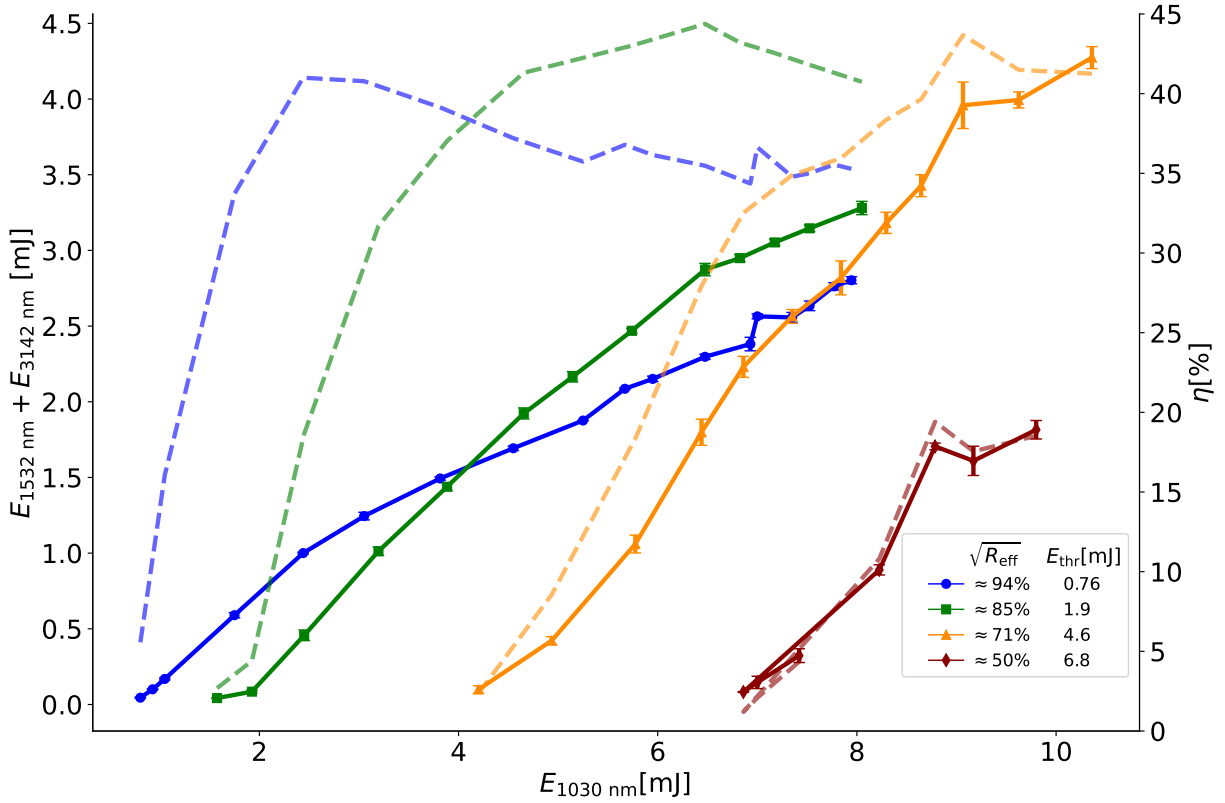


Figure 6.21: Total output pulse energies (solid lines, left axis) at the signal and idler wavelengths, along with their corresponding conversion efficiencies (dashed lines, right axis), are plotted as functions of the input pump energy at a wavelength of 1030 nm. The data is presented for four different outcoupling values, represented by $r_{\text{eff}} = \sqrt{R_{\text{eff}}}$. E_{thr} refers to the threshold pump energy. The signal and idler wavelengths are 1532 nm and 3142 nm, respectively.

the signal pulse shape for the injection-seeded and unseeded (free-running) OPO cavity, as shown in Fig. 6.22. In the case of the free-running OPO, oscillation starts from quantum noise, which requires a higher threshold and, consequently, more round trips in the cavity. This is evident from the time delay between the pulses for the seeded and unseeded OPO. The signal pulse of the free-running OPO starts 6 ns later than the pulse in the seeded case.

Moreover, the ratio of the pulse energy in the seeded to the unseeded case, calculated from the area under the pulse, shows a factor of 2 difference. The reduction in pulse energy and pulse length in the unseeded case is attributed to the reduced gain, as only the falling edge of the pump pulse contributes to the gain.

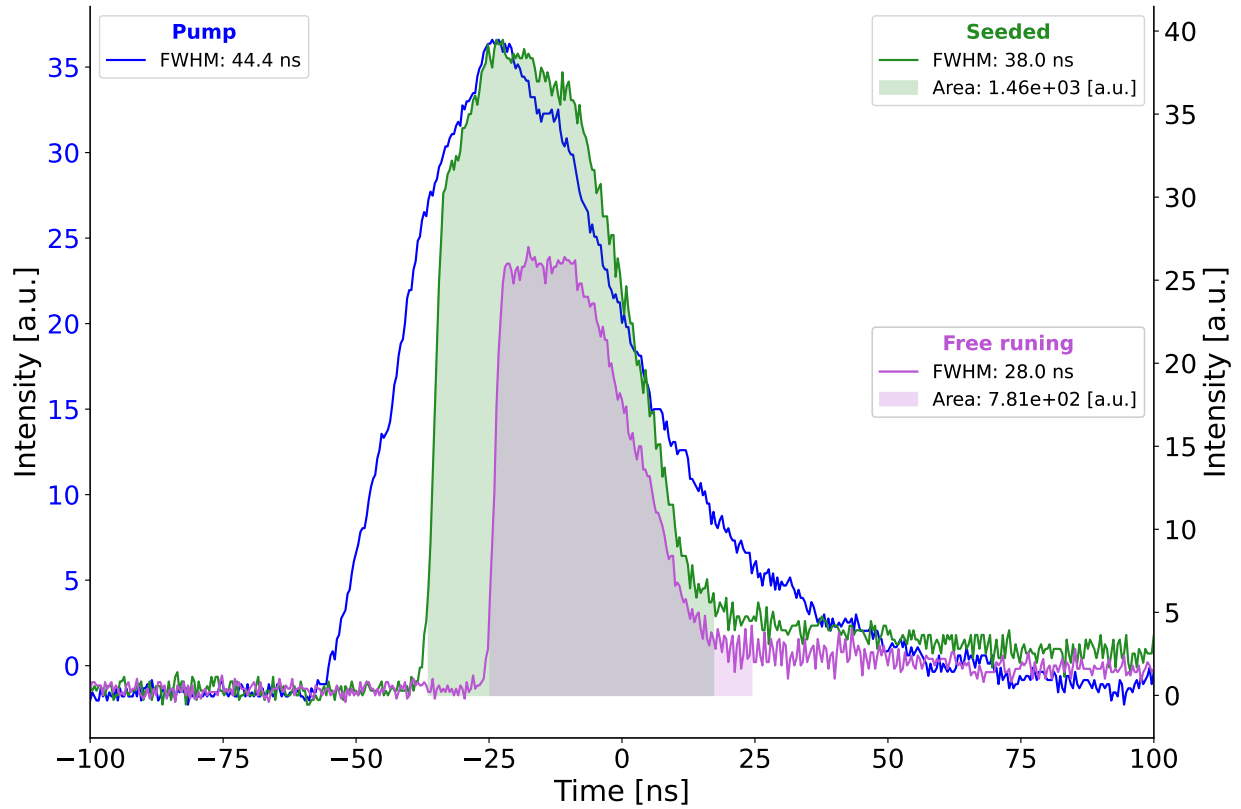


Figure 6.22: Measured pulse shapes at the signal wavelength for the seeded and free-running OPO cavity. The area under the pulses is calculated between 15% of the maximum pulse amplitude on both the rising and falling edges. This measurement was performed at $r_{\text{eff}} = 71\%$ and $E_p = 8$ mJ.

6.5.2 Beam quality measurement

For beam quality measurements, 1% of the total idler energy (1 mJ) was reflected using a prism and focused onto a camera with a CaF₂ focusing lens ($f = 200$ mm), anti-reflection (AR) coated for the 3-5 μm wavelength range. The beam profile was captured using an infrared pyroelectric array sensor (MKS Ophir Pyrocam IV Beam Profiling Camera) in accordance with the test method for laser beam parameters, including beam widths, divergence angle, and beam propagation factor.

Beam diameters were measured using the $D_{4\sigma}$ formalism [91] over a distance centered at the beam waist. The variation of the beam radius (W) as a function of distance (z), centered around the minimum waist, was fitted using Eq. 5.14. The camera, with a resolution of 320×320 pixels and an 80 μm pixel pitch, operated in triggered mode (30 Hz) for all beam images. Figure 6.23 shows the measurement and fitting results. We obtained values of $M_y^2 = 1.003(3)$ and $M_x^2 = 1.023(2)$.

6.5.3 OPO wavelength tuning

To achieve tunability in the OPO across several nanometers, the phase-matching temperature (T_{pm}) was determined for different wavelengths over a 10 nm range. This process involved scanning the crystal temperature while monitoring the output power at the signal wavelength. The procedure begins by adjusting the central wavelength of the seed laser and locking the cavity to the seeding wavelength. A temperature scan is then conducted, and the signal pulse energy is measured using a thermal power meter. The temperature corresponding to the maximum recorded power is identified as T_{pm} .

Figure 6.24 illustrates temperature scans performed at three distinct wavelengths (1529 nm, 1534 nm, and 1539 nm) in the top panel, while the corresponding extracted T_{pm} values are presented in the lower panel. These results allow for the extrapolation of T_{pm} values for other wavelengths within the 10 nm range. The observed fluctuations in recorded power are attributed to variations in pump beam energy and the slow response time of the thermal power meter.

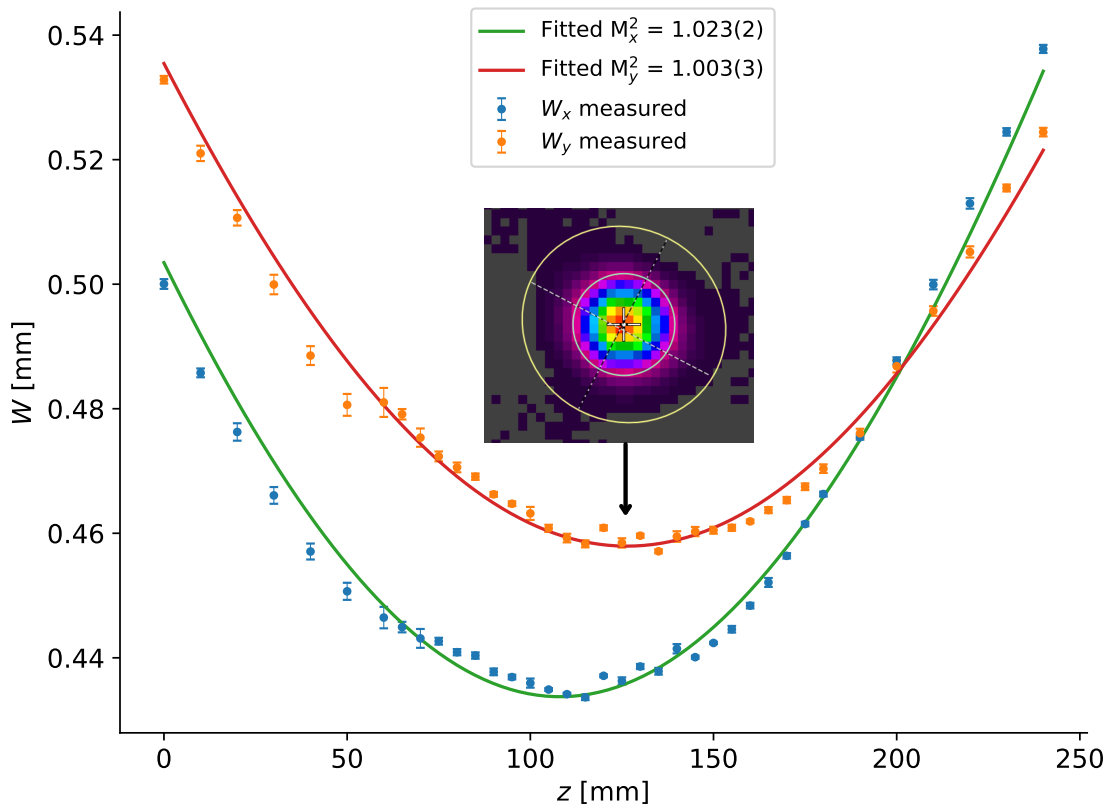


Figure 6.23: Measurement of the OPO beam radius W along the distance z . The extracted M^2 values in both the x and y directions are shown. The measurement was carried out for $r_{\text{eff}} = 71\%$ at an idler energy of $E_i = 1$ mJ. A sample beam profile image at the waist position is included.

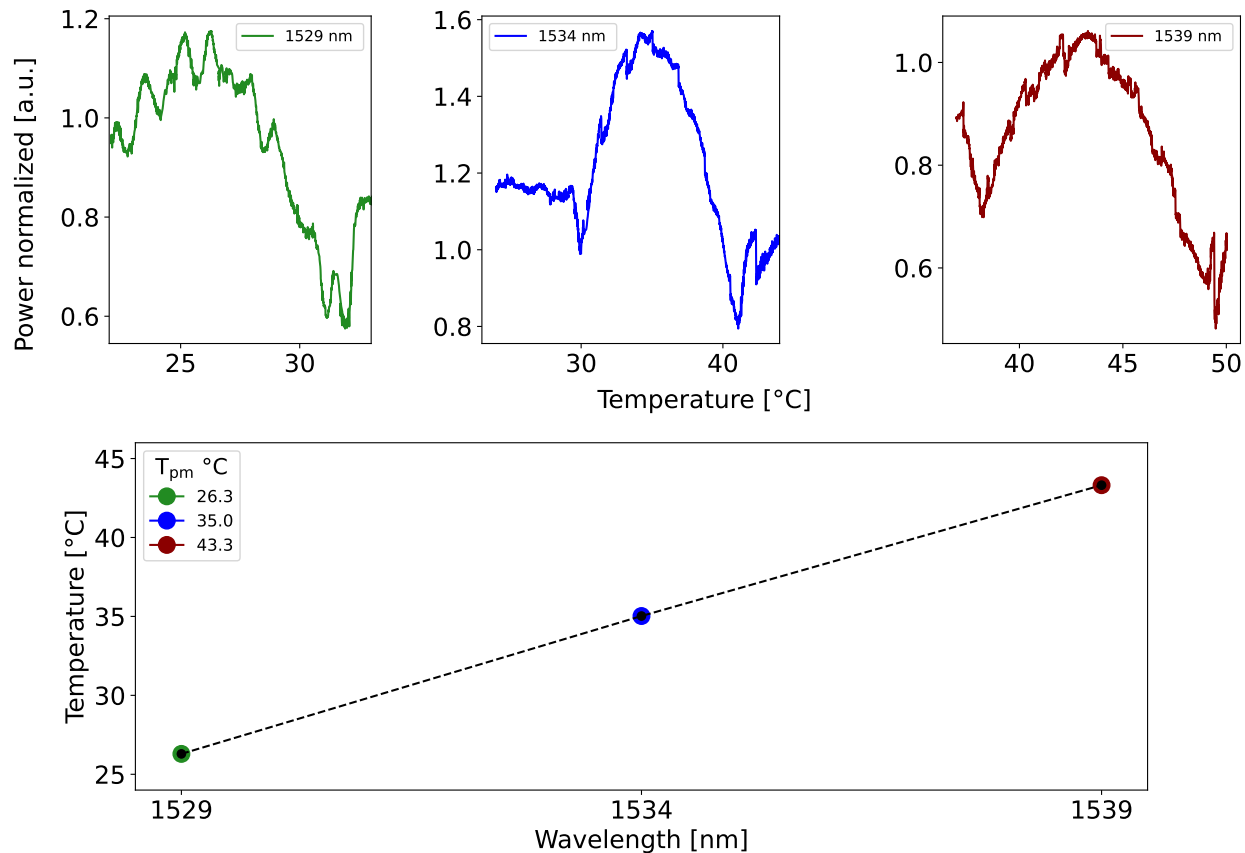


Figure 6.24: The top panel displays temperature scans conducted at three distinct wavelengths, while the bottom panel presents the corresponding extracted phase-matching temperature values. The temperature scan was performed with a resolution of 0.01°C , and the measured power was normalized relative to the baseline value recorded by the power meter. Measurements were carried out at $r_{\text{eff}} = 71\%$ with an idler energy of approximately $E_i = 900 \mu\text{J}$.

6.6 Heterodyne measurement of the frequency chirp

Heterodyning techniques can be used to test the injection seeding [114]. The electric field of the pulsed radiation is assumed to be described as linearly polarized plane waves

$$E_p(t) = A_p(t) \exp[i\langle\omega\rangle t + i\phi(t)] + \text{c.c.} , \quad (6.36)$$

where $A_p(t)$ represents the amplitude envelope of the electric field, and $\langle\omega\rangle$ represents the central frequency which is time independent. Any variation of the angular frequency is attributed to the time dependent phase $\phi(t)$. If this perturbation in the pulse phase is linear in time, it is referred to usually as a "chirp". The instantaneous frequency is

$$f_{\text{inst}}(t) = (2\pi)^{-1} d\phi(t)/dt. \quad (6.37)$$

Figure 6.25 shows an example of the electric field envelope of the pulse radiation with and without frequency chirp.

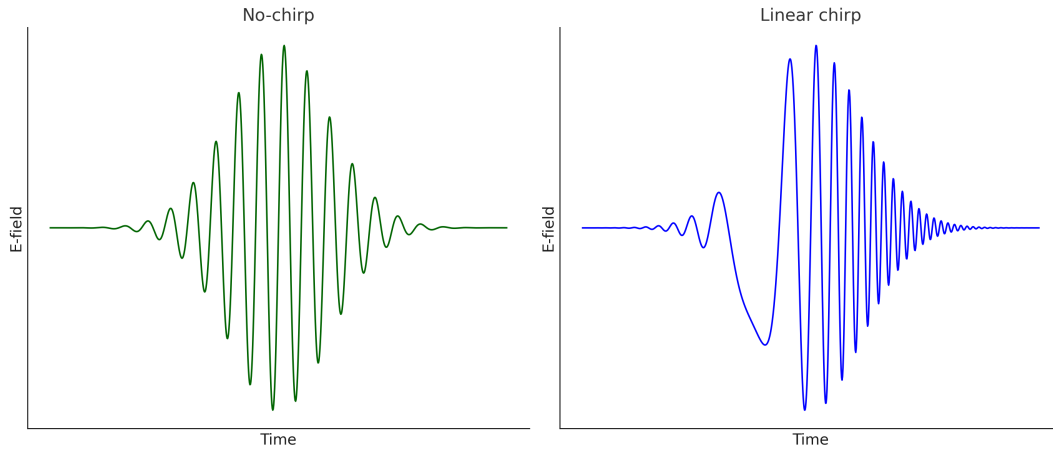


Figure 6.25: An example of the electric field envelope of the pulse radiation without and with a chirp.

We performed an optical heterodyne (OH) measurement to extract the instantaneous frequency of the OPO pulses, $f_{\text{inst}}(t)$, at the signal wavelength and compare it with the seed laser frequency. This was achieved by beating the CW light from the seed laser with the pulses at the signal wavelength on a fast photodiode. The instantaneous frequency was extracted from the heterodyne signal using two methods, Fourier transform and quadrature demodulation of the heterodyne signal [114–116].

The setup for the optical heterodyne measurement is shown in Fig. 6.26. Signal pulses generated by the OPO were combined co-linearly on a photodiode (fast PD) with a portion of the CW seed laser, which was frequency-shifted to $f_{\text{seed}} + f_{\text{mod}}$. At the photodiode, a beat waveform was generated at frequencies near f_{mod} .

The CW light at a frequency of $f_{\text{seed}} + f_{\text{mod}}$ was produced by modulating the seed laser light using the same EOM employed for the PDH lock. This modulation generated sidebands at $f_{\text{seed}} \pm f_{\text{mod}}$. The light was then filtered through a Fabry-Perot (FP) cavity, which was locked to the sideband at $f_{\text{seed}} + f_{\text{mod}}$. The resulting electric field is described by

$$E_{\text{SB}+}(t) = A_{\text{SB}+} \cos((\omega_{\text{seed}} + \omega_{\text{mod}})t), \quad (6.38)$$

where $A_{\text{SB}+} = \frac{A_s \beta}{2}$, and β represents the modulation depth. Here, $\omega_{\text{mod}} = 2\pi f_{\text{mod}}$, with $f_{\text{mod}} = 760$ MHz. This modulation frequency is identical to $f_{\text{mod}} = \text{FSR}/2$, which is used for PDH locking of the OPO cavity to the seed laser.

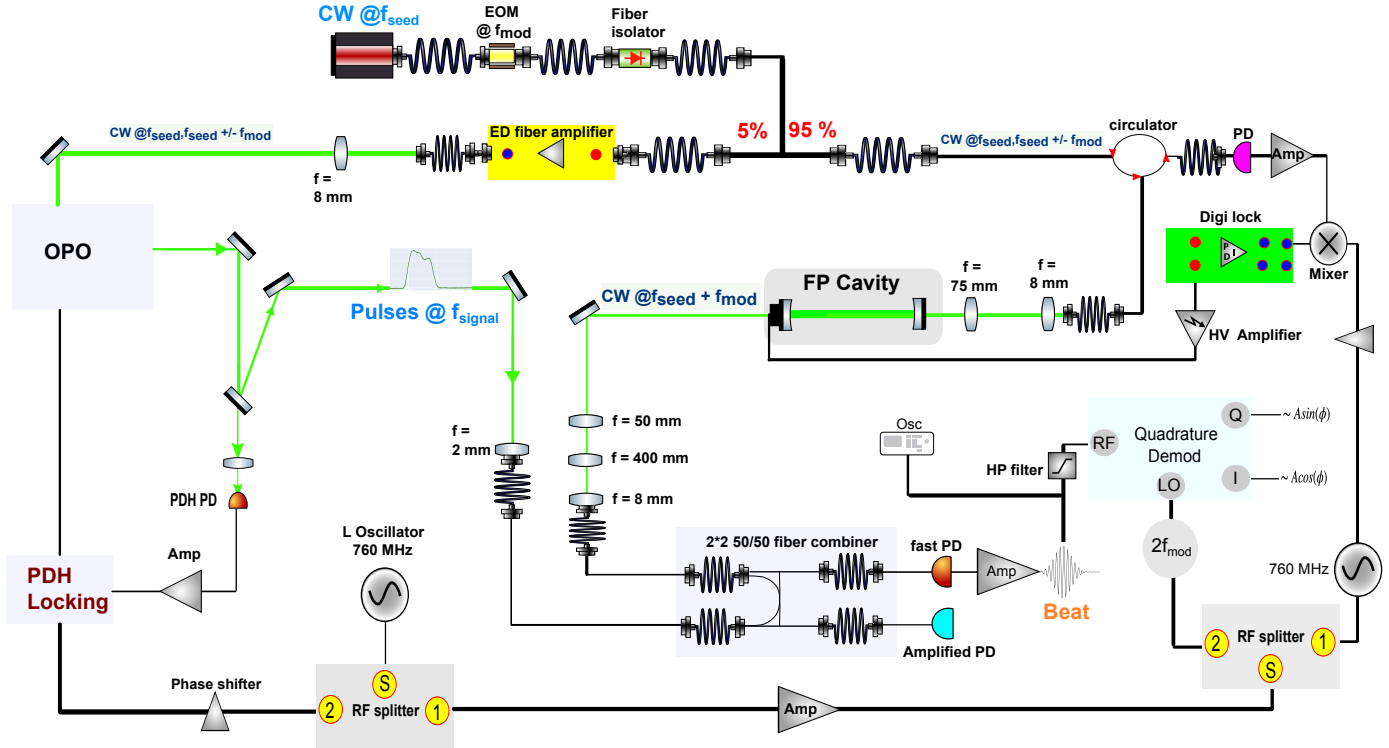


Figure 6.26: Scheme of the optical heterodyne measurement from which we extract the instantaneous frequency of the OPO pulses. Detailed description is given in the text.

The light transmitted from the FP cavity and the OPO pulses are coupled through a fiber coupler into the input of a two-port 50 : 50 fiber combiner. The combined signals are

then directed to a fast photodiode via one port, where the beat waveform is generated. The second port is used to monitor the CW signal level, ensuring a balanced combination of the CW and pulse amplitudes.

The beat waveform generated at the fast photodiode is amplified and split into two paths. The first path directs the signal to an oscilloscope with a 6.25 GHz sampling rate for recording. The second path passes the beat waveform through a high-pass filter to isolate frequency components above f_{mod} . This filtered signal is then sent to a quadrature demodulator. These two paths correspond to the two methods for measuring the chirp in the instantaneous frequency, as described earlier.

6.6.1 Fourier transform method

The voltage corresponding to the intensity profile of the beat waveform generated by the fast photodiode can be described by

$$V_{\text{PD}} \propto |A_{\text{SB}+}(t) + A_p(t)|^2 = |A_{\text{SB}+}|^2 + |A_p(t)|^2 + A_{\text{SB}+}A_p(t) \left\{ \exp \left[i \left(\langle \omega \rangle - \omega_{\text{seed}} + \omega_{\text{mod}} \right) t + i\phi(t) \right] + \text{c.c.} \right\}, \quad (6.39)$$

where the first and second terms correspond to the CW intensity and the intensity envelope of the OPO pulse, respectively. The third term represents the optical heterodyne (OH) interference, which is the component of interest. By isolating this third term, the time-dependent phase $\phi(t)$ can be extracted, given that $\langle \omega \rangle - \omega_{\text{seed}} \approx 0$.

To isolate the third term in Eq. 6.39, the Fourier transform of the equation is taken to obtain the power spectrum. A band-pass filter centered around ω_{mod} is then applied to extract the positive-frequency interference term [117]. The filtered signal is subsequently transformed back into the time domain using an inverse Fourier transform, resulting in

$$I(t)^{\text{filtered}} = A_{\text{SB}+}A_p(t) \exp \left(i \left(2\pi f_{\text{mod}} t - \phi(t) \right) \right), \quad (6.40)$$

from which the phase information $\phi(t)$ is extracted by calculating its derivative. The instantaneous frequency is then determined by subtracting the modulation frequency f_{mod} from

$$f(t) = f_{\text{mod}} - \frac{1}{2\pi} \frac{d\phi}{dt}. \quad (6.41)$$

To test the Fourier transform method and assess its precision, we applied the described steps to optical heterodyne beat waveforms generated from synthesized Gaussian pulses using Eq. 6.39. The synthesized pulses were designed to have a similar amplitude and full width at half maximum (FWHM) as the measured OPO pulses.

To evaluate the effect of noise on the extraction of instantaneous frequency, noise with an amplitude equivalent to 1% RMS of the peak amplitude of the synthesized pulse envelope was added. This noise level was chosen to match the noise observed in the experimental OPO pulses. Figures 6.27 and 6.28 show the extraction of the instantaneous frequency from synthesized OH beat waveforms for two cases: one without chirp and the other with an induced positive linear chirp of 30 MHz.

The extracted $f(t)$ exhibits a variation of approximately ± 2 MHz within the region corresponding to the FWHM of the pulse intensity, which is the region of interest. This result demonstrates that the Fourier transform method has an uncertainty of about ± 2 MHz. A modulation behavior was observed at the start of the pulse, between 465 ns and 480 ns, corresponding to the fast-rising edge of the pulse. However, this modulation does not contribute to the frequency chirp [114]. The oscillations observed during the time interval corresponding to the FWHM of the pulse are attributed to the edge effects of the band-pass filter.

We measured 1000 pulses and their corresponding OH beat waveforms at three different values of r_{eff} for the OPO cavity and at varying signal pulse energies, including pulses in the saturation regime. The extraction of the instantaneous frequency was performed using the Fourier transform (FT) method under these different conditions. Figure 6.29 illustrates an optical pulse (in red) and its corresponding beat waveform (in blue), measured at $r_{\text{eff}} = 96\%$ and $E_{\text{signal}} = 700 \mu\text{J}$. The data was recorded at a sampling rate of 6.25 GSa/s, exceeding twice the Nyquist critical frequency, which is determined by the detection frequency of 2 GHz for the photodiode used to record the OH beat waveform.

The power spectral density (PSD) of the beat waveform, obtained via the Fourier transform, is shown in Fig. 6.30 on a logarithmic scale. Higher-order sidebands are suppressed by at least 35 dB (approximately three orders of magnitude) relative to the peak at f_{mod} . Therefore, these sidebands do not significantly affect the desired frequency component. A Butterworth filter, with a full width at half maximum (FWHM) of 600 MHz, was applied to isolate the interference term at the frequency $f_{\text{seed}} + f_{\text{mod}}$. The filter's lower and upper

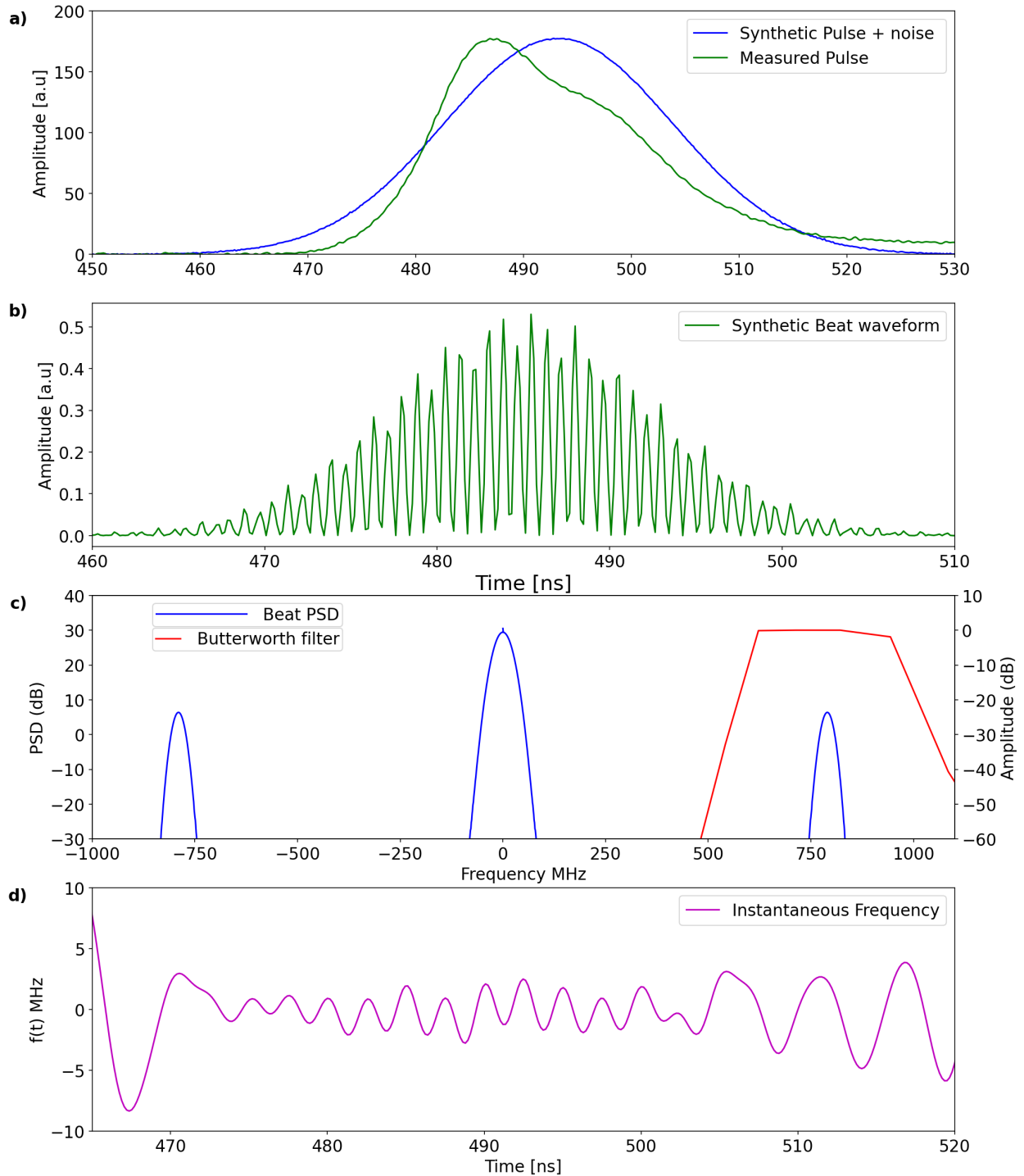


Figure 6.27: (a) A synthesized pulse with a Gaussian envelope is compared to a measured output pulse at $r_{\text{eff}} = 71\%$ and a pulse energy of $E_{\text{signal}} = 1$ mJ. (b) The synthesized OH waveform generated by beating the synthesized pulse with CW light at $f_{\text{seed}} + f_{\text{mod}}$, where $f_{\text{seed}} = 1532$ nm and $f_{\text{mod}} = 760$ MHz. (c) The power spectrum of the OH beat waveform (left scale), with a Butterworth filter (right scale) applied to isolate the interference term at the frequency $f_{\text{seed}} + f_{\text{mod}}$. (d) The extracted instantaneous frequency of the synthesized pulse.

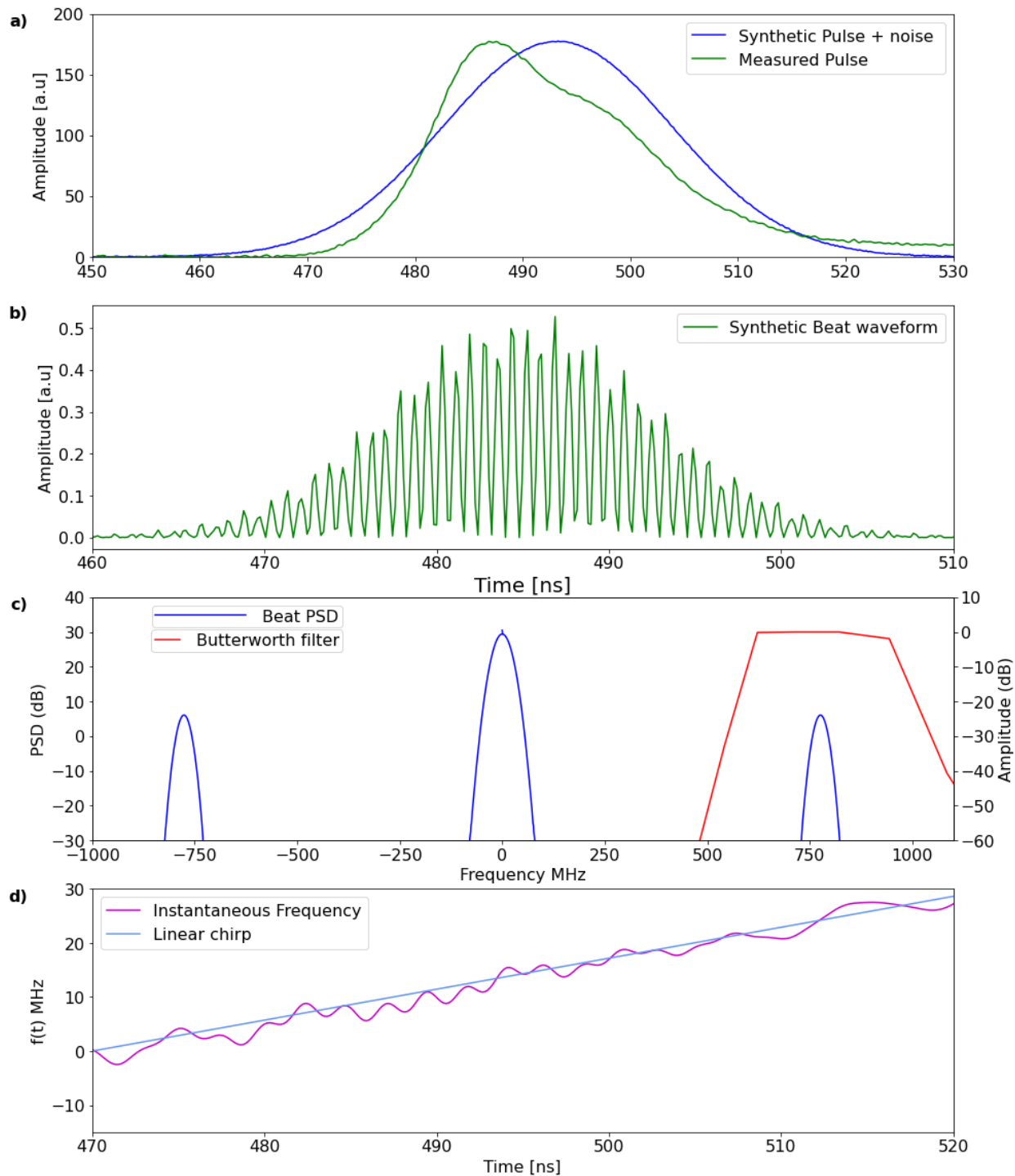


Figure 6.28: (a), (b), and (c) correspond to their counterparts in Fig. 6.27, but with an induced linear chirp added to the phase of the synthesized pulse. (d) The extracted instantaneous frequency of the synthesized pulse is shown, demonstrating a frequency variation consistent with the induced linear chirp of approximately 30 MHz.

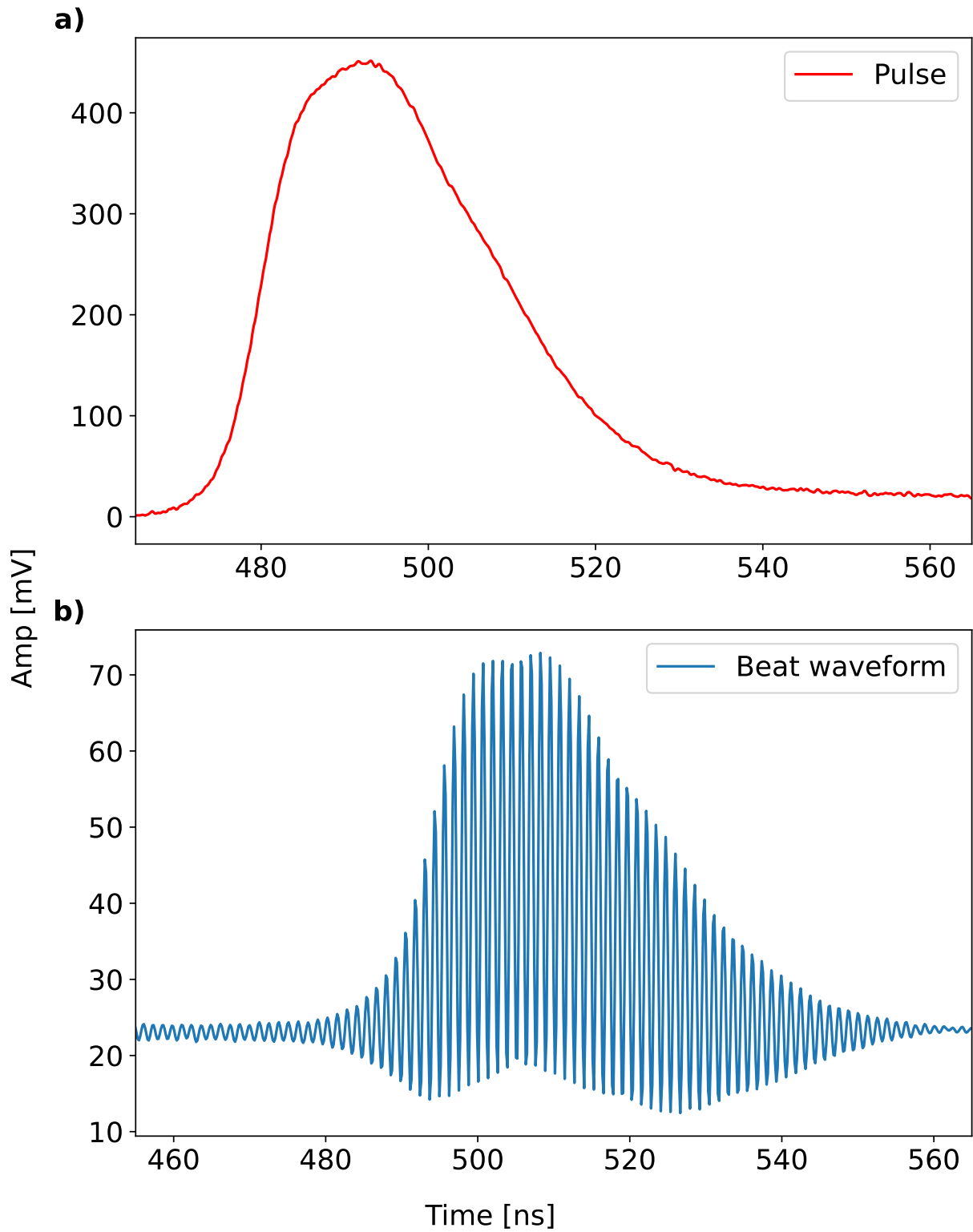


Figure 6.29: (a) The amplitude envelope of the optical output pulse measured at $r_{\text{eff}} = 96\%$ and $E_{\text{signal}} = 700 \mu\text{J}$. (b) The OH beat waveform generated by combining the pulse in (a) with the CW light output of the FP cavity at a frequency $f_{\text{seed}} + f_{\text{mod}}$.

cutoff frequencies were 500 MHz and 1100 MHz, respectively. The filtered beat waveform is displayed in Fig. 6.31, where the corresponding power spectrum is also shown.

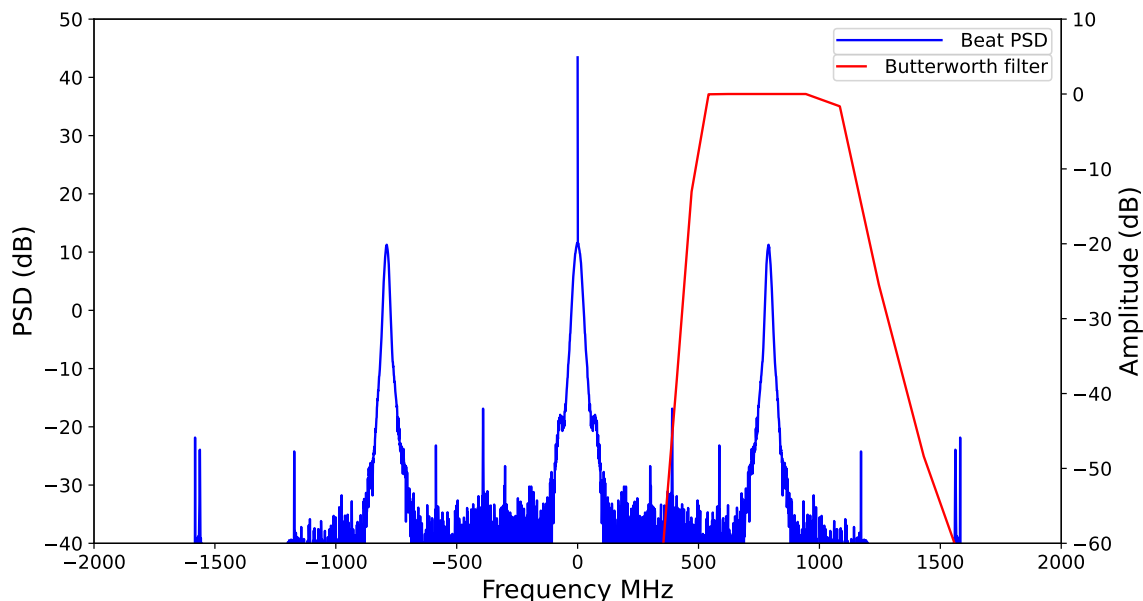


Figure 6.30: The power spectral density (PSD) of the beat waveform, obtained via Fourier transform, is shown in blue (left scale). A Butterworth filter, applied to isolate the positive-frequency interference term, is shown in red (right scale).

Figure 6.32 presents the instantaneous frequency extracted via the inverse Fourier transform of the filtered signal shown in Fig. 6.31, which corresponds to the beat waveform in Fig. 6.29. The extracted $f(t)$ exhibits a variation limited to approximately ± 2 MHz around zero within the time interval from 505 to 525 ns, corresponding to the peak region of the OH beat waveform. The modulation behavior observed between 490 ns and 500 ns corresponds to the fast rising edge of the pulse and does not contribute to a frequency chirp, as previously noted. The main result is that the chirp in the region corresponding to the FWHM of the pulse is only around 2 MHz and is therefore negligible.

In addition to the result obtained at $r_{\text{eff}} = 96\%$, we analyzed the instantaneous frequency extracted via the FT method from beat waveforms and pulse envelopes measured at $r_{\text{eff}} = 84\%$ and $r_{\text{eff}} = 71\%$, shown in Fig.6.33 and Fig.6.34, respectively. In both cases, the

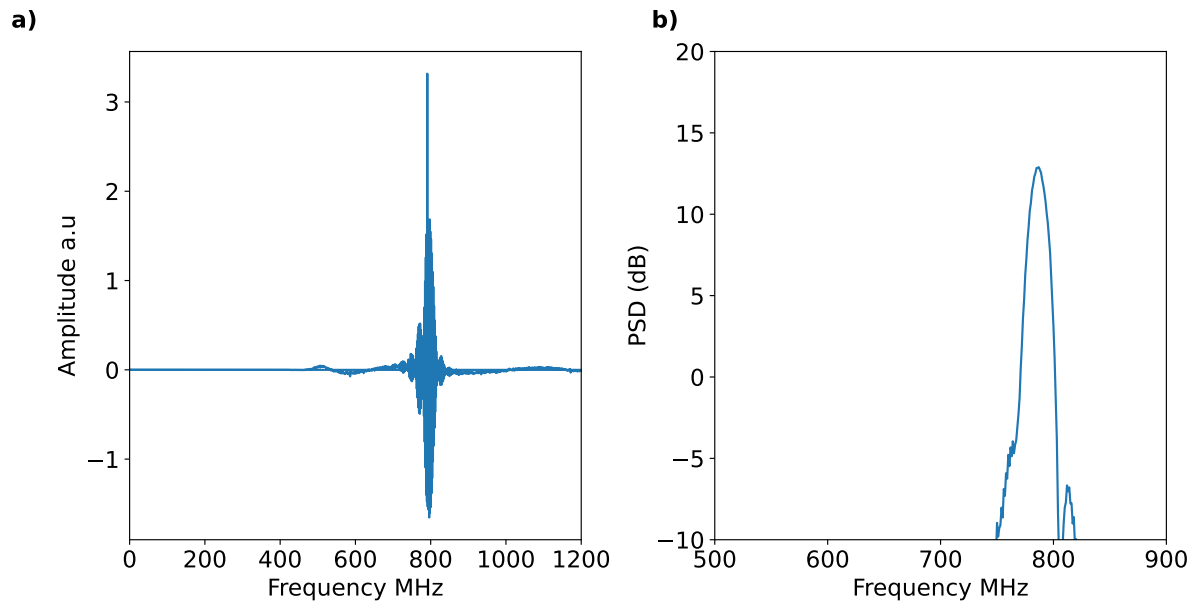


Figure 6.31: a) The amplitude of the positive-frequency interference term as a function of frequency. b) The power spectral density (PSD) of the positive-frequency interference term, corresponding to a), shown in dB.

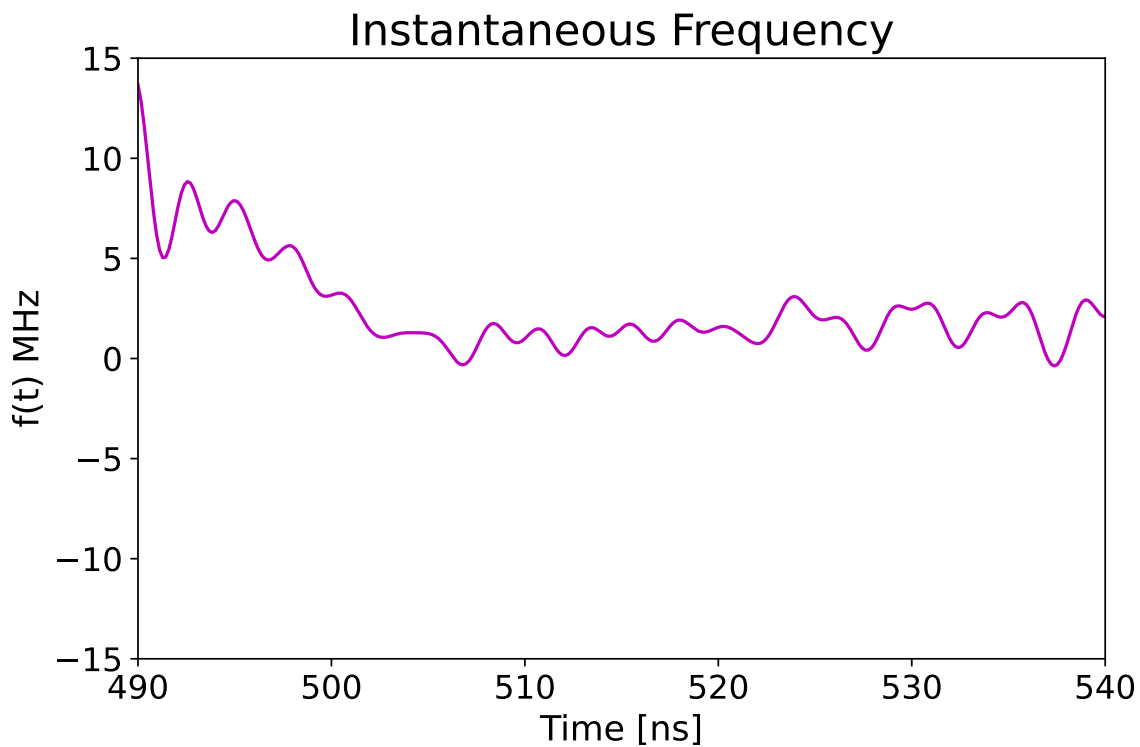


Figure 6.32: The extracted instantaneous frequency of the beat waveform, shown in MHz, corresponds to the beat waveform presented in Fig. 6.29.

modulation observed in the early time region of $f(t)$ is attributed to the fast rising edge of the pulses, as mentioned earlier. Within the FWHM region of the pulses, the instantaneous frequency remains within a range of ± 2 MHz.

A global shift of approximately -5 MHz is observed in the central region of the pulse in Fig. 6.34. This shift is likely due to an unaccounted change in the modulation frequency. However, no frequency chirp is observed in any of the pulses.

Furthermore, we investigated whether misalignment between the OPO cavity and the input pump could generate frequency shift. In this case only the pump beam was misaligned while the cavity and the seed laser was optimally aligned. We show the f_{inst} extracted from the beat waveform measured at $E_{\text{signal}} = 2.1$ mJ and $r_{\text{eff}} = 71\%$ in Fig. 6.35. The induced misalignment resulted into a clear deviation of the instantaneous frequency from the seed frequency by around 20 MHz. Hence attention has to be paid during the data taking to operating the laser at optimal alignment.

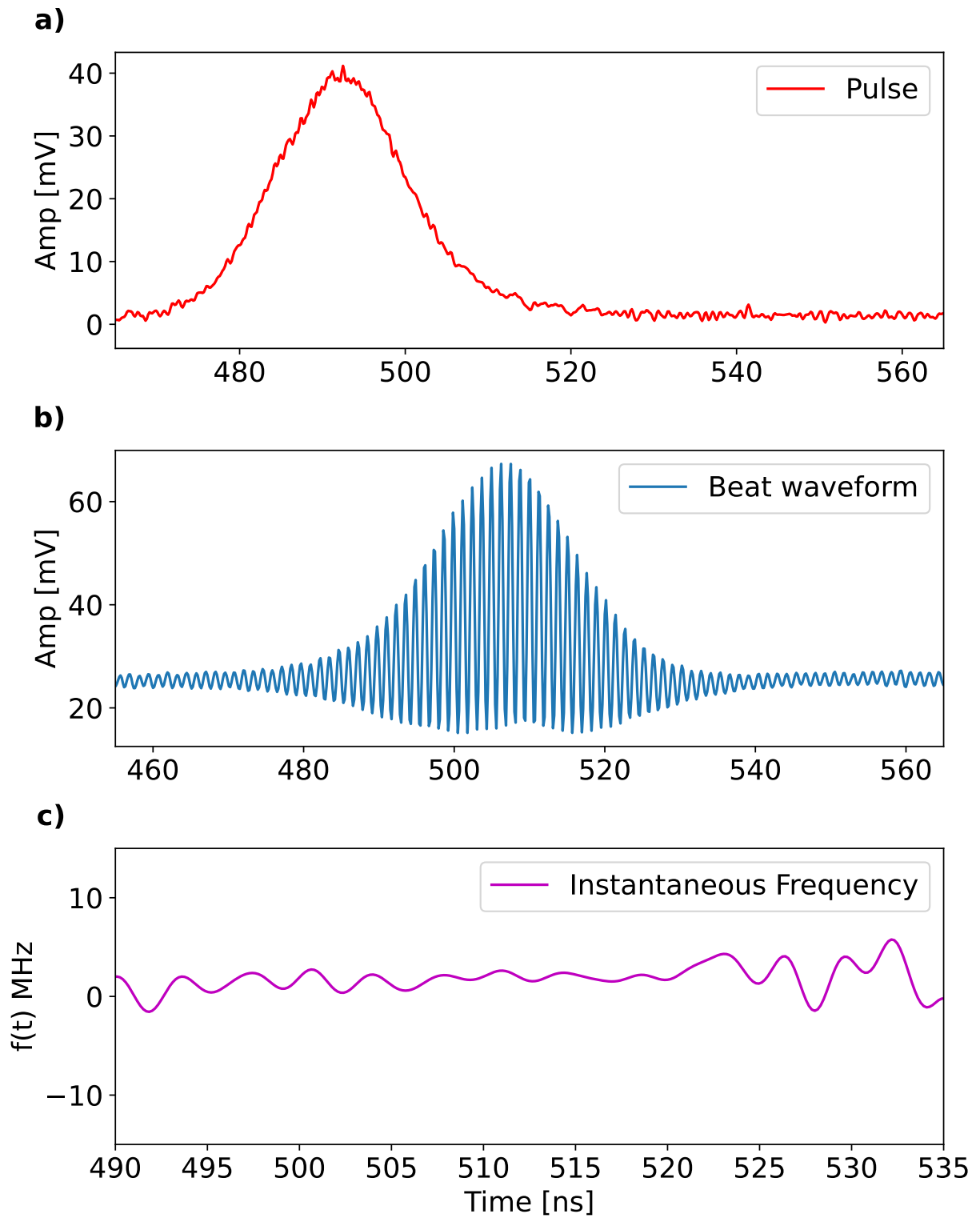


Figure 6.33: a, b) The pulse envelope and corresponding beat waveform recorded at a signal energy of $E_{\text{signal}} = 800 \mu\text{J}$ and reflectivity $r_{\text{eff}} = 84\%$. c) The extracted instantaneous frequency corresponding to the beat waveform is shown.

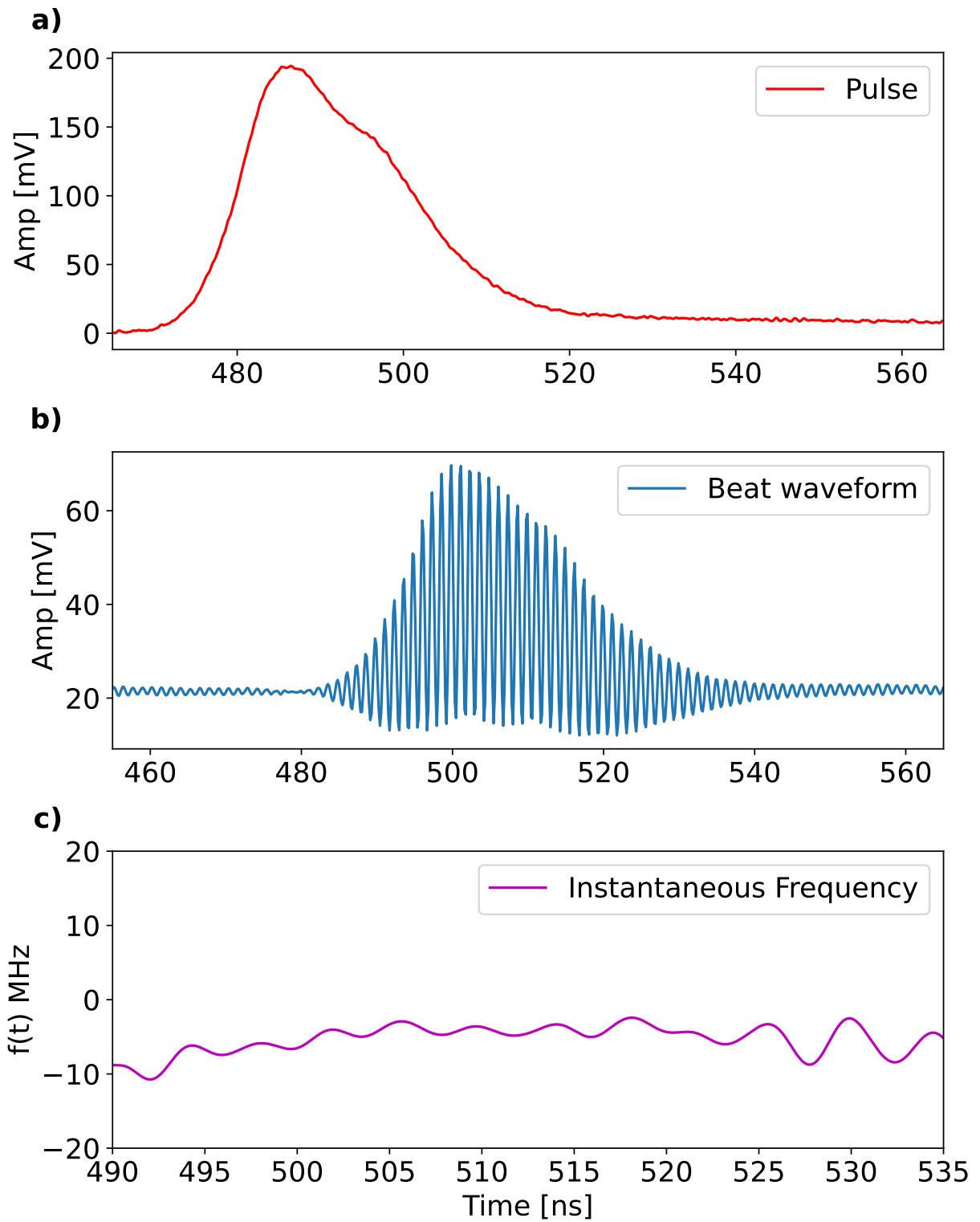


Figure 6.34: a, b) The pulse envelope and corresponding beat waveform recorded at a signal energy of $E_{\text{signal}} = 1$ mJ and reflectivity $r_{\text{eff}} = 71\%$. (c) The extracted instantaneous frequency corresponding to the beat waveform is displayed.

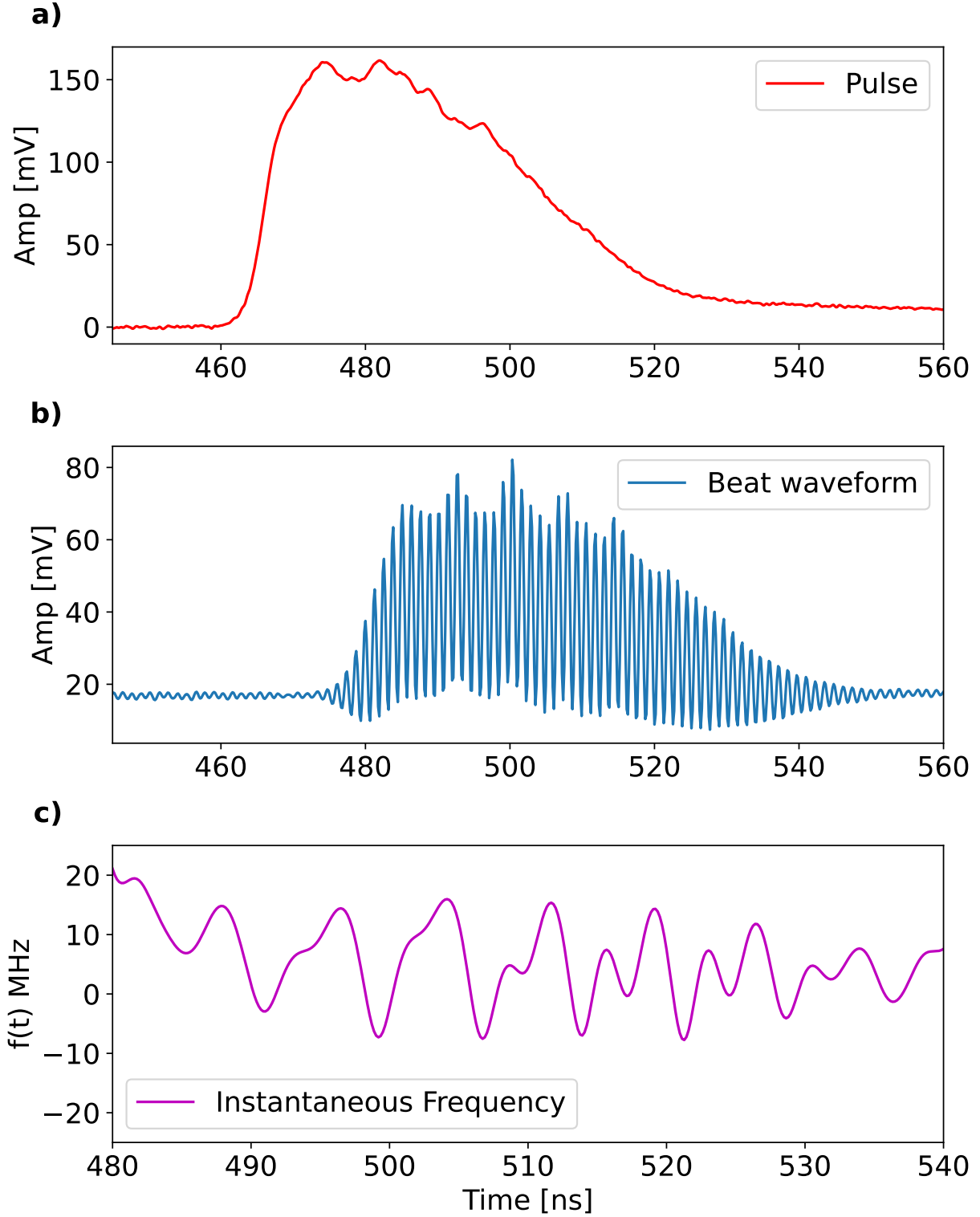


Figure 6.35: a) The pulse envelope recorded from the misaligned OPO. (b) The corresponding beat waveform generated by combining the pulse with the CW light. (c) The extracted instantaneous frequency showing frequency deviation, attributed to the misalignment between the seed and pump beams in the OPO cavity.

6.6.2 Quadrature demodulation

The second method employed for extracting the instantaneous frequency involves quadrature demodulation of the OH beat signal, isolating only the frequency chirp components. The layout of the quadrature demodulator is illustrated in Fig. 6.36. In this approach, the OH beat waveform recorded at the fast photodiode, as described in Eq. 6.39, is passed through a high-pass filter (HPF) to eliminate frequency components below f_{mod} .

The filtered signal is then equally split into two channels. In one channel, the signal is electronically mixed with a reference radio frequency (RF) signal (LO) at $f = f_{\text{mod}}$, while in the second channel, it is mixed with an LO signal delayed by 90° (or $\pi/2$ phase shift). The output from the mixers corresponds to the intermodulation product voltage, given by $V_I \propto V_{\text{PDH}} V_{\text{LO}}$, where V_{PDH} represents the filtered OH beat waveform.

The quadrature outputs of the two channels are described by

$$\begin{aligned} V_I^I &= A_{\text{SB}+} A_p(t) \left(\cos \left[\phi(t) + (\omega_{\text{seed}} t - \langle \omega t \rangle) \right] + \cos \left[2\omega_{\text{mod}} t - \phi(t) \right] \right), \\ V_I^Q &= A_{\text{SB}+} A_p(t) \left(\sin \left[\phi(t) + (\omega_{\text{seed}} t - \langle \omega t \rangle) \right] + \sin \left[2\omega_{\text{mod}} t - \phi(t) \right] \right). \end{aligned} \quad (6.42)$$

Subsequent application of a low-pass filter (LPF) removes the high-frequency components at $2\omega_{\text{mod}}$, simplifying the above equations to

$$\begin{aligned} I(t) &= A_{\text{SB}+} A_p(t) \cos(\phi(t)), \\ Q(t) &= A_{\text{SB}+} A_p(t) \sin(\phi(t)), \end{aligned} \quad (6.43)$$

where $I(t)$ and $Q(t)$ represent the components in phase and in quadrature with the LO RF signal, respectively.

The pulse envelope $A_p(t)$ and the instantaneous phase $\phi(t)$ are extracted from the quadrature components using the following relationships:

$$\phi(t) = \arctan \frac{Q(t)}{I(t)}. \quad (6.44)$$

$$|A_p(t)|^2 \propto I^2 + Q^2. \quad (6.45)$$

Finally, the instantaneous frequency $f(t)$ is derived by computing the time derivative of the instantaneous phase

$$f(t) = \frac{1}{2\pi} \frac{d\phi(t)}{dt}. \quad (6.46)$$

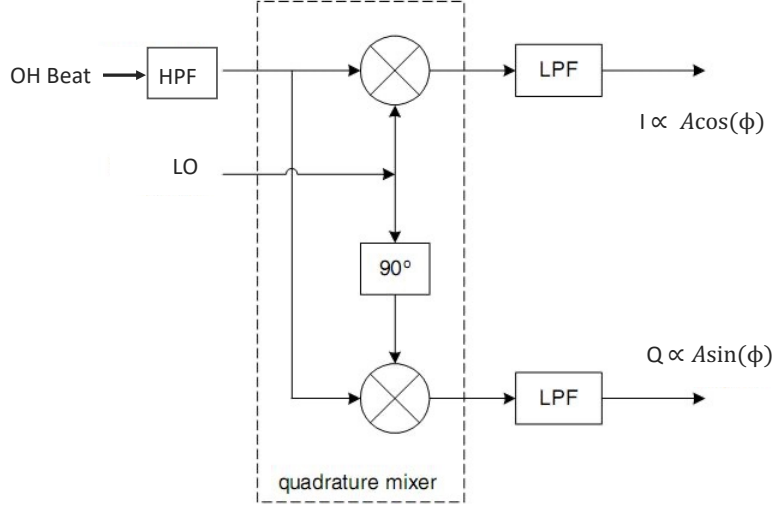


Figure 6.36: Diagram of the quadrature demodulator. The LO corresponds to the RF signal driving the electro-optic modulator (EOM), which generates the $f_{\text{mod}} = 760$ MHz modulation frequency. The cross symbols represent electronic mixers, while the LPF blocks indicate low-pass filters used to remove high-frequency components. The HPF eliminates low-frequency signals below f_{mod} , enabling the extraction of the in-phase ($I \propto A \cos(\phi)$) and quadrature ($Q \propto A \sin(\phi)$) components of the optical heterodyne (OH) beat signal.

To implement the quadrature demodulation method, the OH beat waveform obtained using the setup in Fig. 6.26 was passed through a HPF and fed into a commercial quadrature demodulator (ADL5387) from Analog Devices. A low-pass filter (LPF) with a 250 MHz cutoff frequency was applied to the resulting I and Q signals, which were recorded on an oscilloscope. The I and Q components were then used to reconstruct the pulse envelope via Eq. 6.44 and compared to the pulse measured directly on a photodiode. Measurements were conducted for pulses and their corresponding OH beat waveforms at three values of r_{eff} , as discussed earlier.

Figure 6.37 displays the results for the OH beat waveform and quadrature signals for a signal pulse energy of $700 \mu\text{J}$ at $r_{\text{eff}} = 96\%$. The I and Q signals obtained from the quadrature demodulator are shown in (b), while (c) presents the reconstructed pulse envelope, shifted by 26 ns to temporally overlap with the directly measured pulse. The reconstructed pulse closely matches the directly measured pulse, except for discrepancies on the falling edge caused by differences in the fall times of the photodiodes used for each measurement. The instantaneous frequency, extracted by applying $\arctan(Q/I)$ followed by differentiation and scaling by $1/(2\pi)$, is shown in (d). Within the time region corresponding to 50% of the pulse intensity, the extracted instantaneous frequency $f(t)$ fluctuates by approximately ± 5 MHz

around a central value of zero.

The fluctuations in $f(t)$ result from the noise level on the pulses, with the quadrature demodulation method. Across all examined conditions, including different E_{signal} , r_{eff} , and induced chirp from OPO misalignment, the extracted $f(t)$ values and trends are consistent with those obtained using the Fourier transform method. Figures 6.37, 6.38, 6.39, and 6.40 compare the results of the quadrature demodulation method with the corresponding OH beat waveforms shown in Fig. 6.29, Fig. 6.33, Fig. 6.34, and Fig. 6.35, respectively.

In conclusion, the results demonstrate that the instantaneous frequency variation of the OPO remains well below the 10 MHz limit. The heterodyne measurements further indicate that the instantaneous frequency of the OPO is insensitive to variations in pump energy. These findings fulfill the experimental requirement of maintaining a laser bandwidth below 100 MHz, ensuring optimal conditions for the resonance search. To validate the central frequency of the generated pulses, a secondary frequency calibration method is required and will be presented in Sec. 6.8.

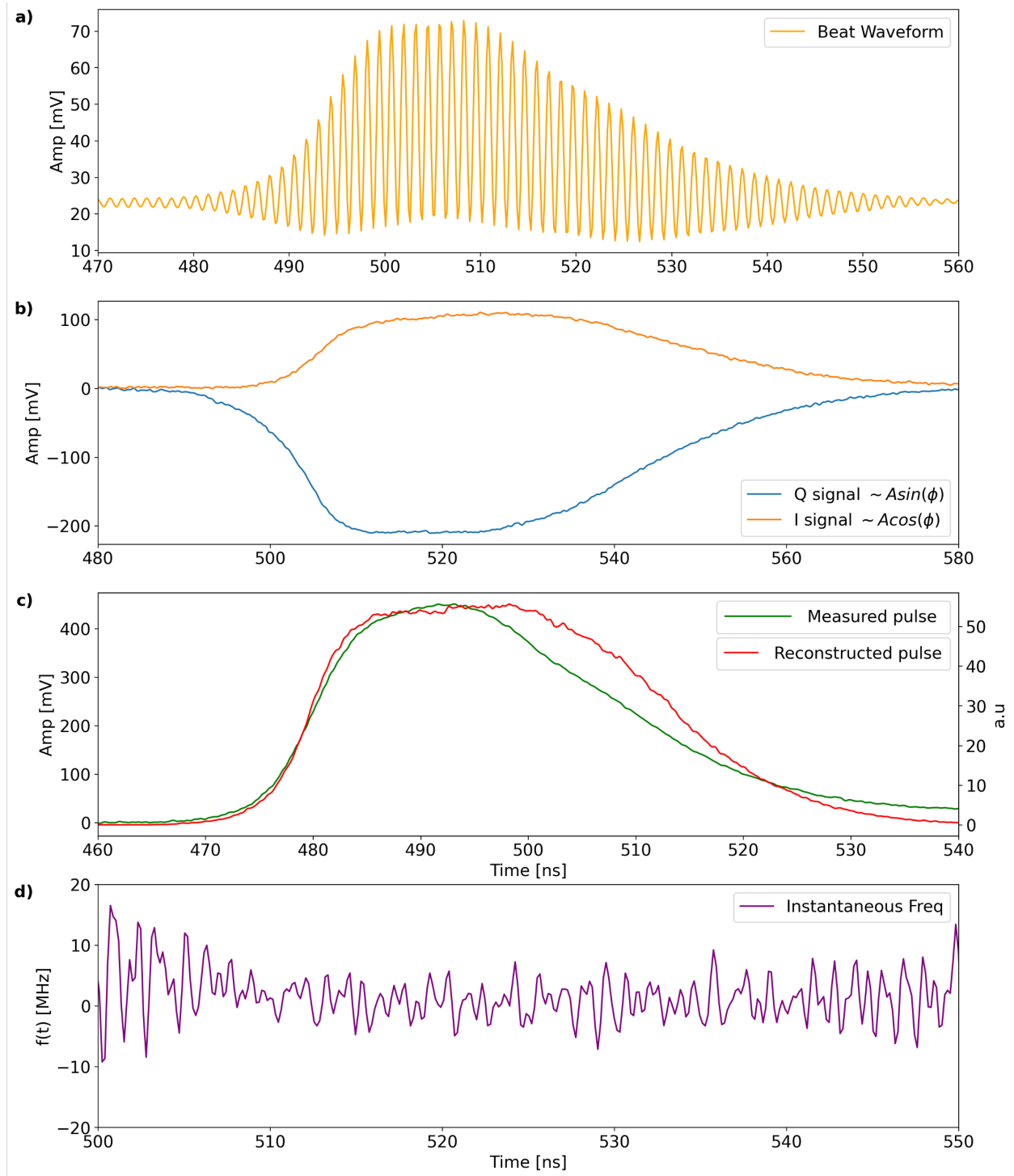


Figure 6.37: The OH beat waveform measured at a signal energy of $E_{\text{signal}} = 700 \mu\text{J}$ and $r_{\text{eff}} = 96\%$ is shown in a). Panel b) presents the resulting I and Q components extracted from the quadrature demodulator, representing the in-phase and quadrature signals of the beat waveform. In c), the directly measured output pulse is compared with the reconstructed pulse derived from the I and Q components, shifted by 26 ns to ensure temporal alignment. Panel d) illustrates the extracted instantaneous frequency, where the time domain coincides with the pulse duration derived from the quadrature demodulator components.

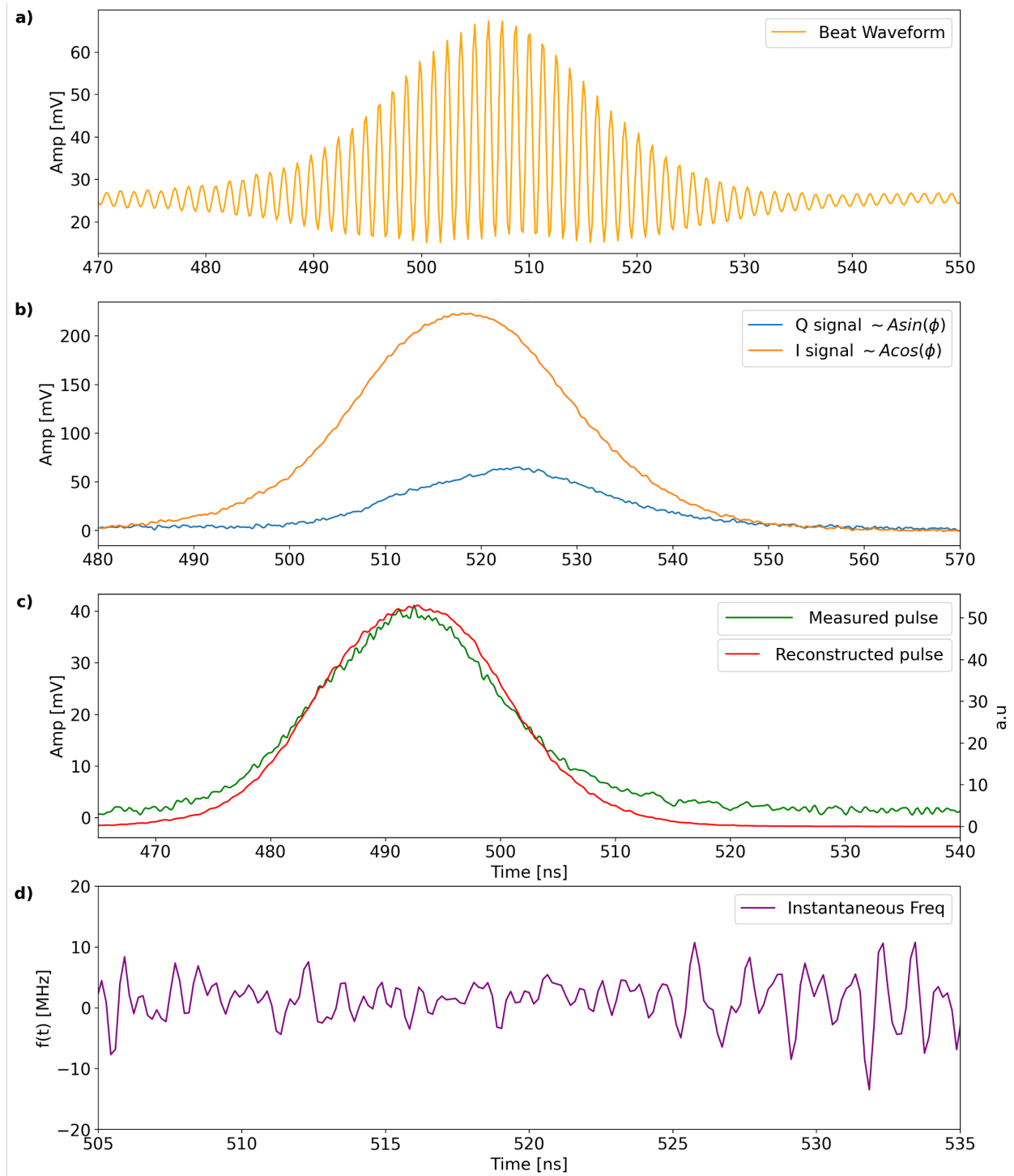


Figure 6.38: a) The OH beat waveform measured at a seed energy of $E_{\text{signal}} = 800 \mu\text{J}$ and $r_{\text{eff}} = 84\%$. b), c), and d) share the same explanation as provided in Fig. 6.37, illustrating the quadrature demodulator components, reconstructed pulse compared to the measured pulse, and the extracted instantaneous frequency, respectively.

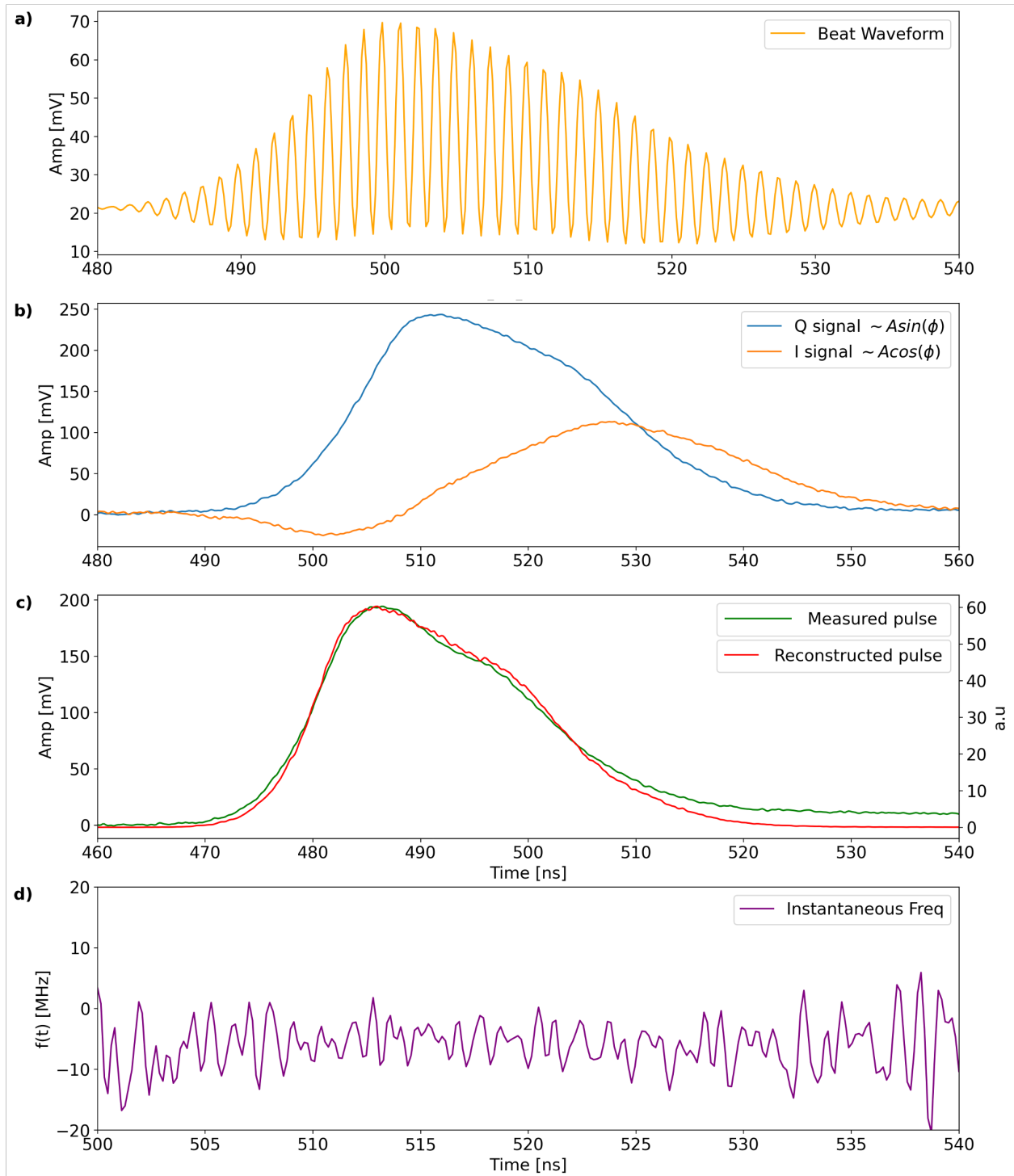


Figure 6.39: a) The optical output pulse and (b) the corresponding OH beat waveform recorded at a seed energy of $E_{\text{signal}} = 1$ mJ and $r_{\text{eff}} = 71\%$. c) and d) share the same explanation as provided in Fig. 6.37, illustrating the reconstructed pulse compared to the measured pulse, and the extracted instantaneous frequency, respectively.

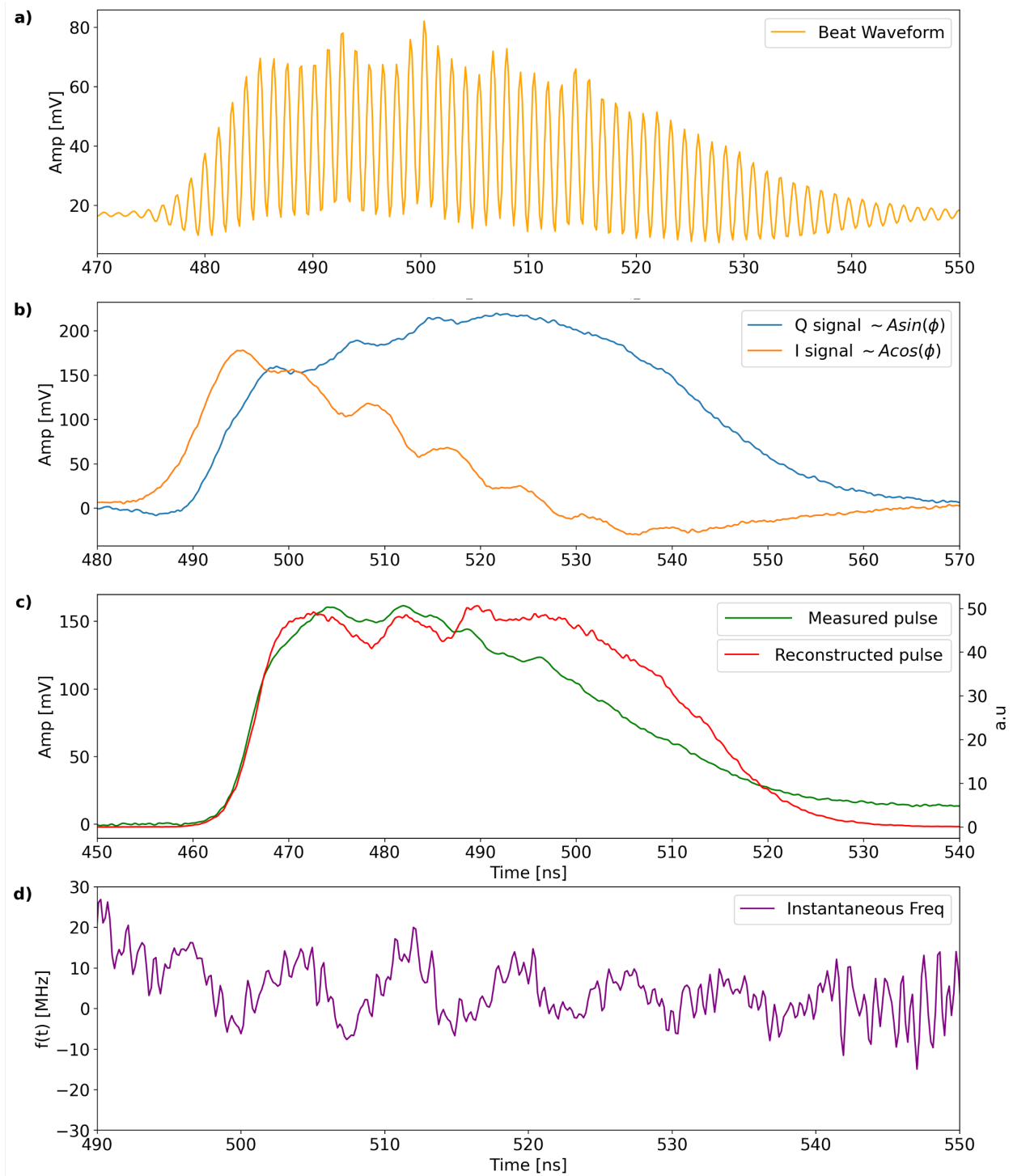


Figure 6.40: a) The OH beat waveform recorded for the misaligned OPO. (b) The I and Q components extracted from the quadrature demodulator, showing the in-phase ($\cos(\phi)$) and quadrature-phase ($\sin(\phi)$) signals. (c) The directly measured pulse and the reconstructed pulse obtained from the I and Q components, with a time shift applied for temporal alignment. (d) The extracted instantaneous frequency, showing an induced frequency deviation due to the misalignment between the seed and pump beams.

6.7 Optical parametric amplifier at 3142 nm

To amplify the energy at $3.1 \mu\text{m}$, the generated pulses were boosted using an optical parametric amplifier based on a periodically poled lithium niobate (PPLN) crystal with a poling period of $30.3 \mu\text{m}$. Two PPLN crystals, with lengths of 50 mm and 25 mm, and dimensions of 4 mm in width and 3 mm in thickness, were tested. The principles and theory underlying the optical parametric amplification process are detailed in Sec. 5.2.7.

Figure 6.41 illustrates the input and output wavelengths of the OPA along with the crystal used. In the OPA, the input near 3142 nm, designated as the signal (seed), undergoes amplification, while the shorter wavelength generated at approximately 1532 nm is termed the idler.

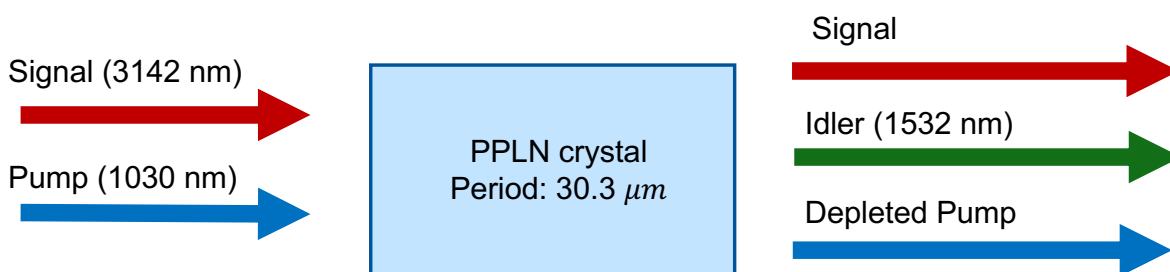


Figure 6.41: Sketch of the optical parametric amplification process. A PPLN crystal with a period of $30.3 \mu\text{m}$ is used as the gain medium.

The setup of the implemented OPA is depicted in Figure 6.43. Pulses at a wavelength of 3142 nm, generated by the OPO, are separated from other wavelengths using mirrors MA and MB, which are (HR, 95%) around $3.1 \mu\text{m}$ and AR coated at 1030 nm and 1532 nm. The pulses are collimated to a beam waist of approximately $740 \mu\text{m}$, about quarter the crystal thickness, representing the maximum allowable waist to avoid spherical aberration [118].

The pump beam, originating from the oscillator, is routed through a delay unit to synchronize the arrival of the pump pulse with the $3.1 \mu\text{m}$ pulse. Figure 6.42 shows the temporal overlap of the input pulse at $3.1 \mu\text{m}$ and the pump pulse at 1030 nm. Two movable retroreflectors, each with a 30 cm range, allow adjustment of the delay time by up to 4 ns. The pump beam is then focused using a Galilean telescope consisting of lenses with focal lengths of 300 mm and -100 mm, achieving a beam waist of approximately $750 \mu\text{m}$ at the center of

the crystal.

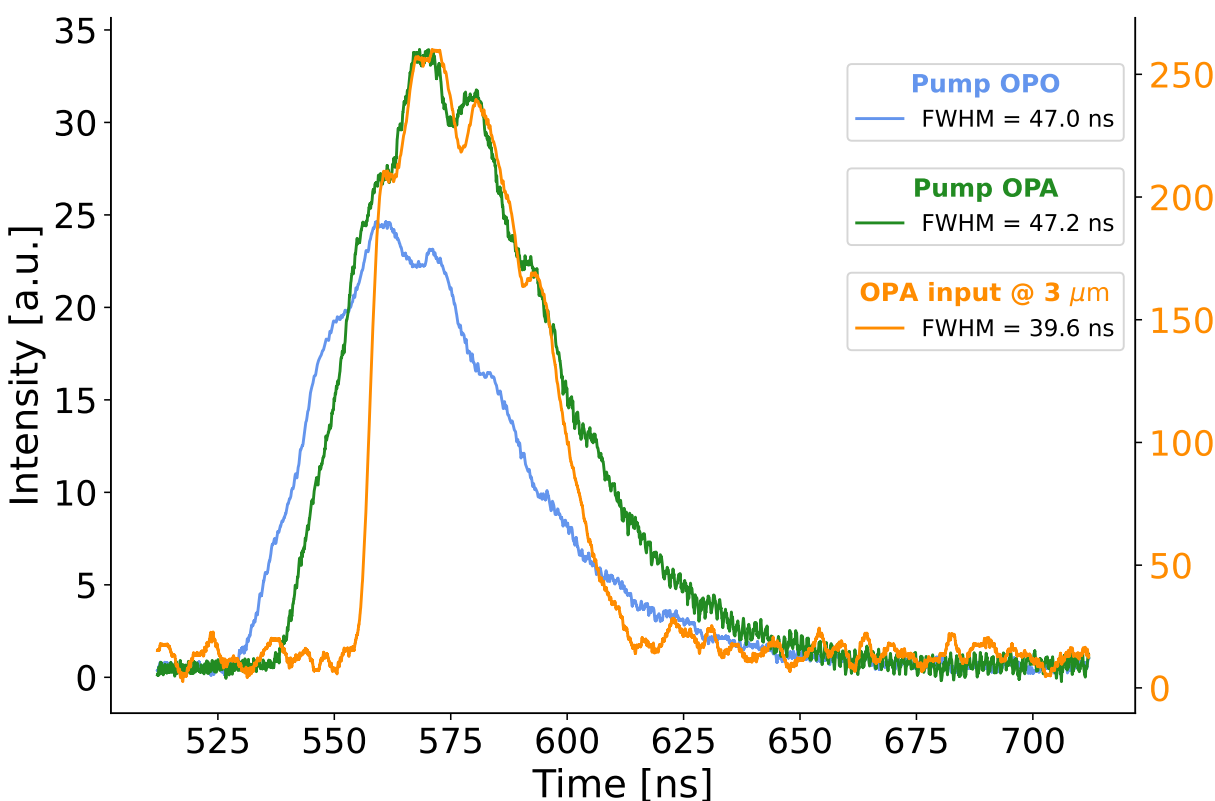


Figure 6.42: The temporal overlap of the OPA pump pulse and the input pulse at 3142 nm. The left scale refers to the OPO, OPA pump pulses while the right scale refers to the OPA input pulse.

Polarization control is achieved using $\lambda/2(1)$ and TFP(1) to regulate the pump energy entering the OPA, and $\lambda/2(2)$ to rotate the pump polarization to the S-polarization required for phase matching. The signal and pump beams are combined via mirror ME and directed into the crystal, which is mounted on a Peltier element within a custom-built housing. Phase matching is achieved by maintaining the crystal at a temperature of 11.7°C.

To isolate the amplified signal pulses at 3142 nm, separator mirrors MF and MG, which are (HR, 95%) at 3.1 μm and AR-coated for other wavelengths, are used. The amplified signal pulses are directed through a germanium window into a pyroelectric energy meter for pulse energy measurements.

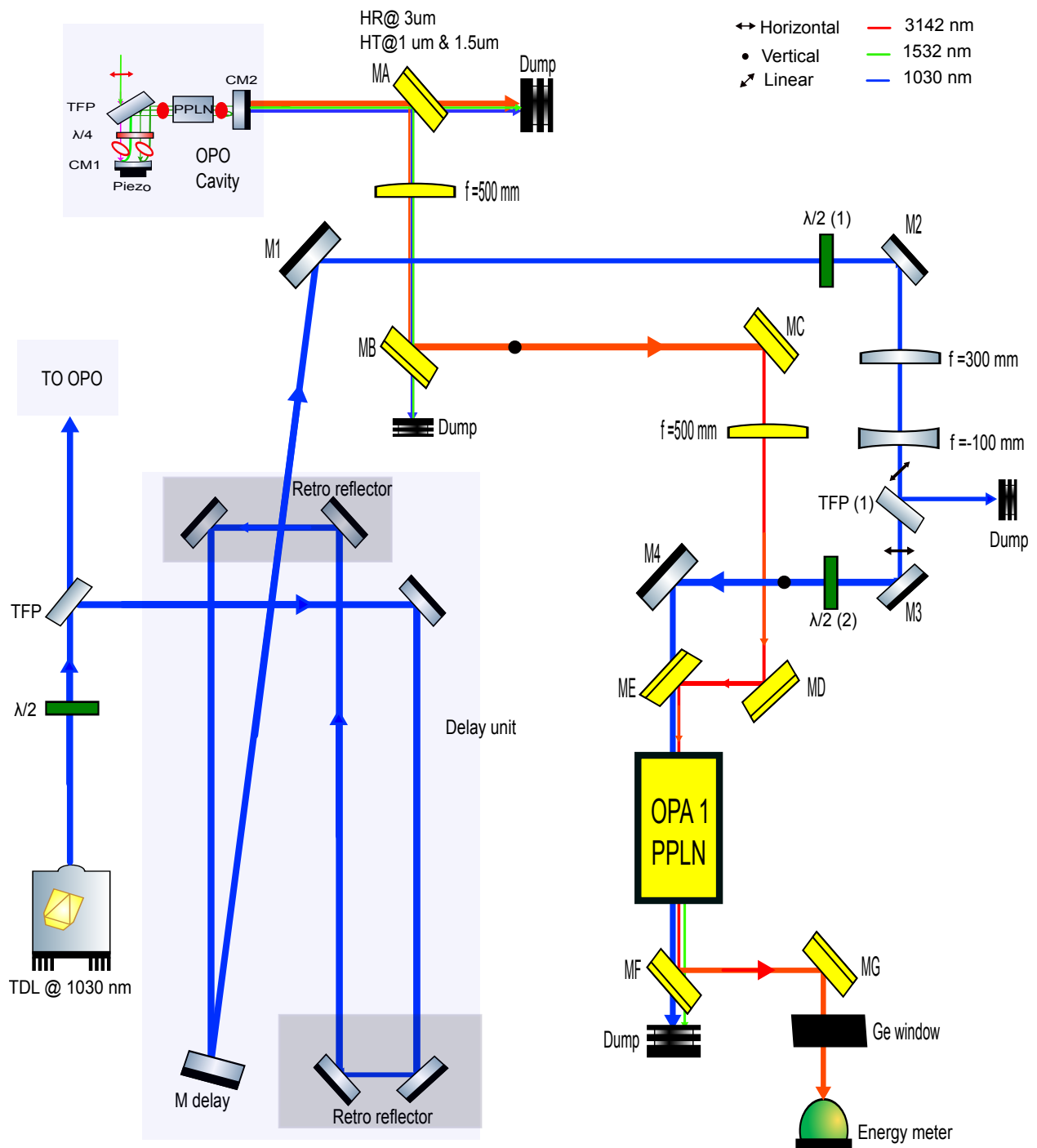


Figure 6.43: Scheme of the implemented OPA for amplifying the $3.1 \mu\text{m}$ Pulses. Detailed description is given in the text.

6.7.1 Energy, stability and beam quality of the OPA

The measured pulse energies at 3142 nm as a function of the input pump energy at 1030 nm are shown in Fig. 6.44 for two different crystals with lengths of 50 mm and 25 mm, respectively. An output pulse energy of up to 3.4 mJ at 3142 nm was reached using the 50 mm long crystal. The gain, defined as $E_s(\text{output})/E_s(\text{input})$, is also shown in the same plot for both crystals. The 25 mm-long crystal exhibited a higher gain at the same pump energies, with an increase of up to 30% around 23 mJ compared to the 50 mm-long crystal. Additionally, the gain for the 25 mm crystal demonstrated a nearly linear behavior with respect to pump energy, unlike the saturation behavior observed in the 50 mm crystal.

According to Eqs. 5.16 and 5.15, the small-signal gain of parametric amplification is linearly proportional to the pump energy. Moreover, a longer crystal length generally results in higher gain. However, longer crystals and higher pump intensities increase pump depletion, which, in turn, increase backconversion, thereby reducing the gain [119–121]. This may explain the higher gain observed in the shorter crystal. Pump energies exceeding 23 mJ were avoided to prevent potential induced optical damage, although the damage threshold was approximately 29 mJ for the pump beam radius.

The 50 mm-long crystal was seeded with 770 μJ compared to 500 μJ for the 25 mm-long crystal. The seed energy primarily affects the total output energy and has minimal impact on the gain of the OPA [119]. However, high seed energies, combined with high pump intensities, can also contribute to backconversion [121].

To investigate the stability of the OPA pulse energies, we recorded the output pulse energies at 3142 nm and compared them with the pump pulses at 1030 nm. The energy fluctuation was quantified in terms of the RMS stability, calculated as:

$$\text{RMS Stability (\%)} = \left(\frac{\text{STD}}{\text{Mean Energy}} \right) \times 100, \quad (6.47)$$

where STD represents the standard deviation. The resultant RMS stability over 90 minutes was approximately 1.5%, which was nearly identical to that of the input pump energy. This demonstrates stable output pulse energies over the 60-minute data acquisition period assigned for each frequency point, as discussed in Chapter 4.

The beam quality measurement of the OPA follows the same formalism and procedures

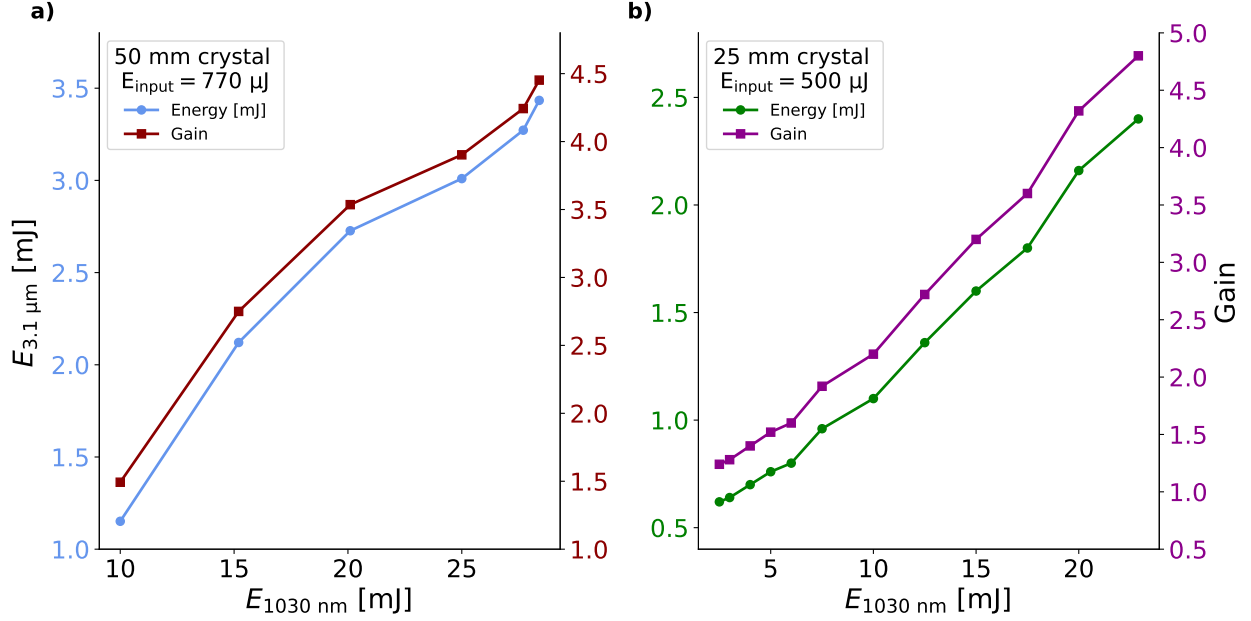


Figure 6.44: Gain of the OPA and output pulse energy for two different crystal lengths: 50 mm and 25 mm, shown in (a) and (b), respectively. The input signal pulse energy was $770 \mu\text{J}$ and $500 \mu\text{J}$ for the 50 mm long and the 25 mm long crystals, respectively. For details, see the text.

described earlier for the OPO in Sec.6.5.2. The beam diameters were measured according to the ISO standard [122]. The ISO standard specifies that measurements should be taken at a minimum of 10 different positions, with roughly half within one Rayleigh length of the beam waist and the other half beyond two Rayleigh lengths. The variation of the beam radius (W) as a function of distance (z), centered around the minimum waist, was fitted using Eq. 5.14. Figure 6.46 shows the measurement and fitting results. We obtained values of $M_y^2 = 1.163(1)$ and $M_x^2 = 1.348(2)$.

The pulse energy generated from the combined system of OPO1/OPA1 with a 50 mm-long crystal in the OPA achieves the pulse energy at 3142 nm required for the DFG stage, as specified in Chapter 5. At this pulse energy, a single transverse mode with good beam quality, as indicated by the extracted M^2 values for the full system, is obtained.

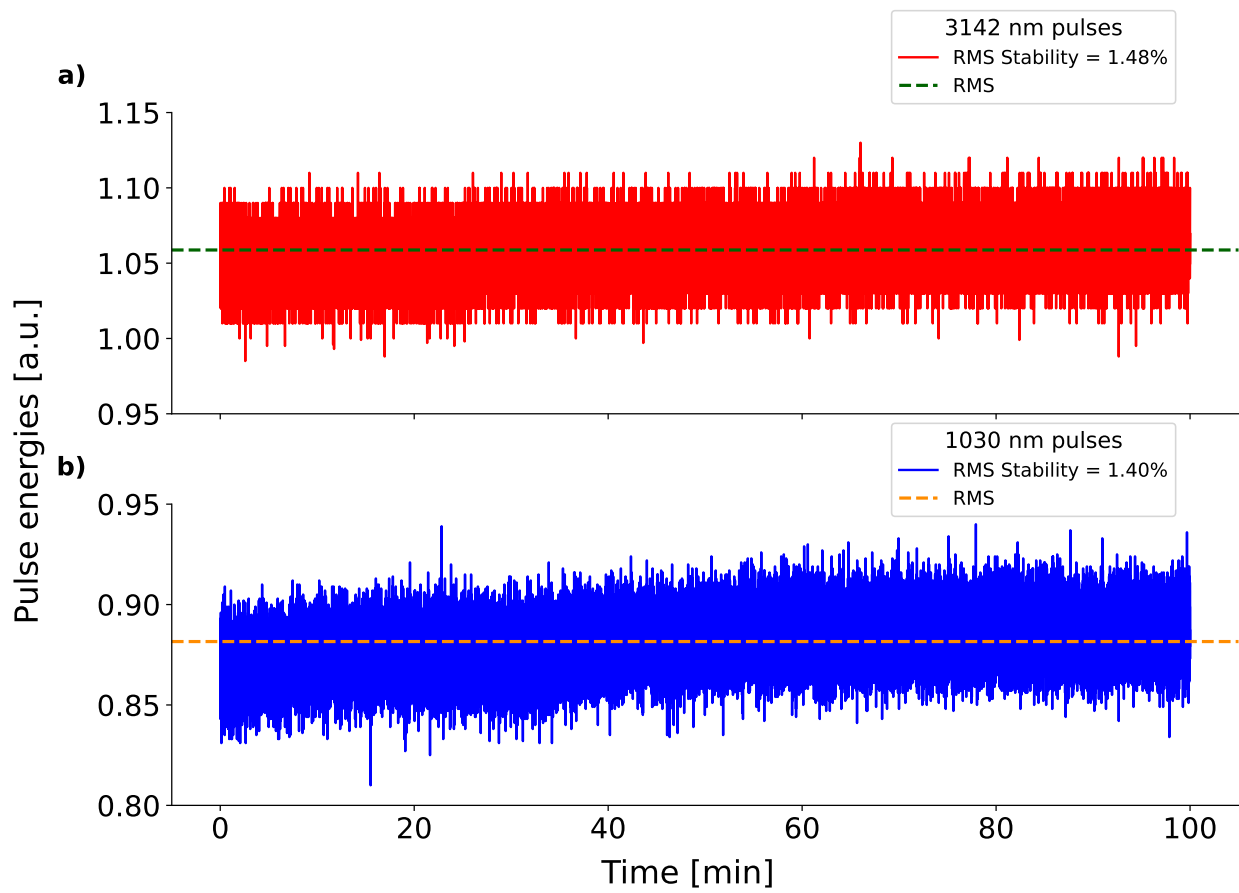


Figure 6.45: RMS stability of the OPA pulse energies at 3142 nm (red) compared to the input pump pulse energies (blue). For details, see text.

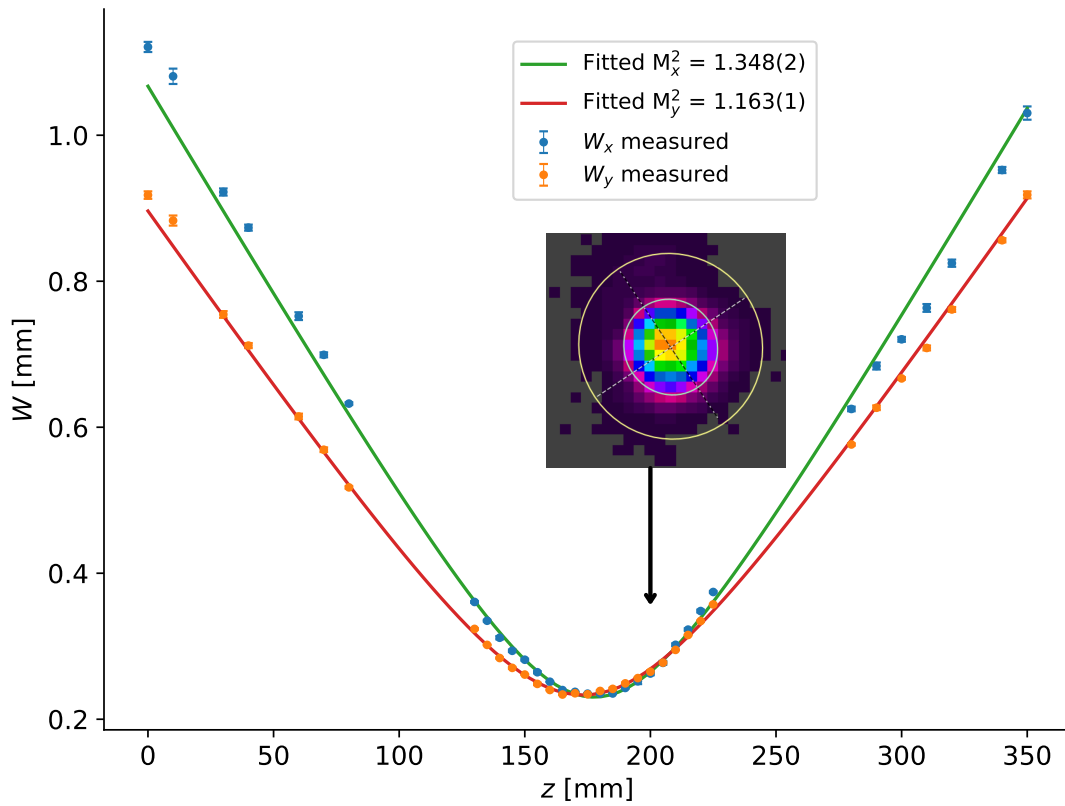


Figure 6.46: Measurement of the OPA beam radius W along the distance z . The extracted M^2 values for both x and y directions are given. The measurement was carried out at an output pulse energy of 2 mJ for a 25 mm-long crystal. A sample of the beam profile image near the waist position is also shown.

6.8 Tunability and frequency calibration

As indicated in the previous chapters, to search for the resonance around $6.8 \mu\text{m}$, the laser wavelength must be tunable by approximately 50 GHz. This tunability will be achieved by adjusting the seed laser wavelength of OPO1 around the central value of 1532 nm (signal). Consequently, the output wavelength (idler) will vary around 3142 nm, while the pump wavelength remains stabilized at the maximal gain of the disk laser, near 1030 nm. Throughout this process, the laser system must maintain single-frequency operation.

Single-frequency operation was demonstrated using the heterodyne technique presented in Sec.6.6. Here, we investigate the laser system ability to scan the frequency. Demonstrating continuous tunability around $3.1 \mu\text{m}$ is a critical prerequisite for the rapid wavelength adjustments required in the HFS experiment. This capability addresses the large search range needed to locate the resonance. To verify the tunability of the laser system, we performed a preliminary pulsed laser spectroscopy on methane (CH_4) using the $3.1 \mu\text{m}$ pulses generated by the OPO1/OPA1 system.

A schematic of the spectroscopy setup is shown in Fig. 6.47. The wavelengths of both the pump laser at 1030 nm and the OPO seed laser at 1532 nm were stabilized using the high-finesse WS-8 wavemeter. The wavemeter was referenced to a narrow-bandwidth laser at 1532 nm (SLR-1532), ensuring fixed central frequencies. The OPO seed laser frequency was varied in 10 MHz steps, with a waiting time of 30 seconds between steps. Approximately 5% of the seed laser power was sent to the wavemeter via an optical fiber, enabling precise frequency/wavelength measurements for each seed laser.

The OPO idler frequency was calculated as the difference $f_{\text{pump}} - f_{\text{signal}}$. The $3.1 \mu\text{m}$ output pulses from the OPA were split using a beam splitter (BSW505). One path directed the pulses to an energy meter (Energy meter 2) to monitor energy fluctuations, while the other path sent the pulses into a CH_4 gas cell. Within the cell, the pulses underwent multiple reflections, achieving a total path length of 2 m. The transmitted energy at the output of the cell was measured by an energy meter and recorded for each frequency point.

The transmitted energy was normalized to the calibrated pulse energy measured by Energy meter 2. By plotting this normalized energy against the output pulse frequency scanned around 95.184 THz (equivalent to 3142 nm), the absorption lines of CH_4 were measured.

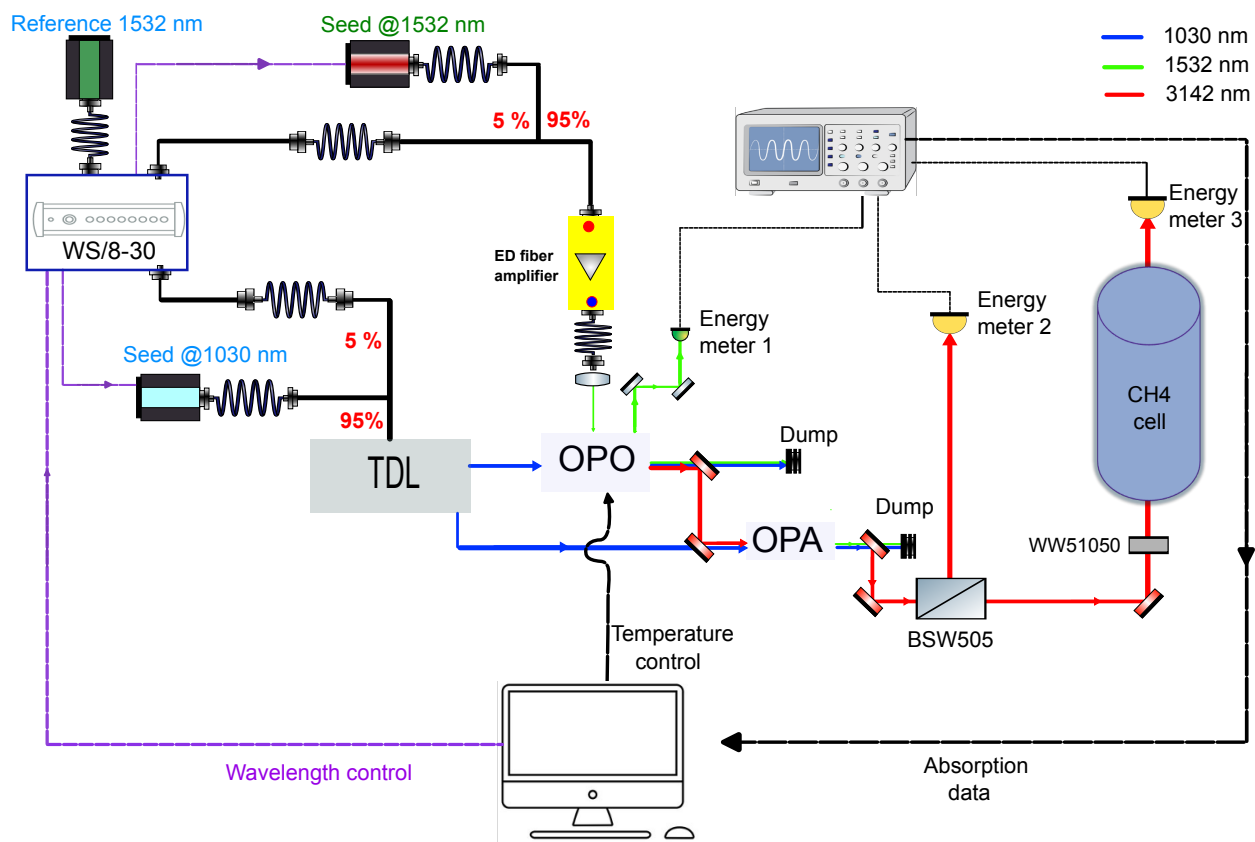


Figure 6.47: Schematic of the frequency calibration and tunability measurement. For detailed description, see text.

Plots of the measured absorption lines at pressures of 1.2 mbar and 17 mbar are shown in Fig. 6.48. A fit was performed for both lines to determine their central frequencies and widths, which were then compared to the HITRAN data. The absorption signal showed saturation at a pressure of 17 mbar. To investigate whether the observed absorption is intrinsic, the absorption lines were simulated under the same pressure and path length conditions in CH₄. A plot of the absorption lines from the HITRAN database is shown in Fig. 6.49 [123]. Peaks A and B in the plot correspond to frequencies of 95.1796 THz and 95.1789 THz, respectively.

The absorption lines were fitted using a Voigt profile, which is the convolution of a Gaussian and a Lorentzian profile. The convolution is expressed as

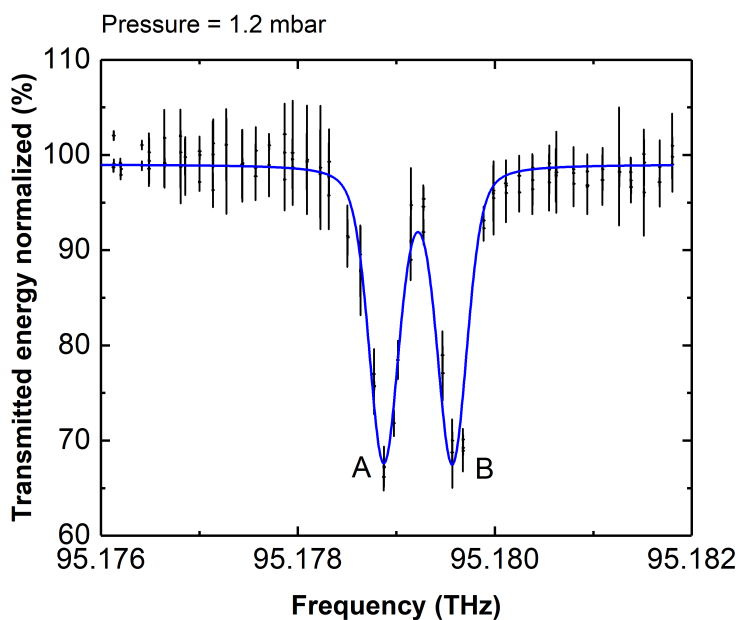
$$\begin{aligned}
y &= y_0 + \int_{-\infty}^{\infty} (f_1 * f_2)(x) \\
&= y_0 + A \frac{2 \ln 2}{\pi^{3/2}} \frac{W_L}{W_G^2} \int_{-\infty}^{\infty} \frac{e^{-t^2}}{\left(\sqrt{\ln 2} \frac{W_L}{W_G}\right)^2 + \left(\sqrt{4 \ln 2} \frac{x-x_c}{W_G} - t\right)^2} dt, \\
\text{where } f_1(x) &= \frac{2A}{\pi} \frac{W_L}{4(x-x_c)^2 + W_L^2}, \\
\text{and } f_2(x) &= \sqrt{\frac{4 \ln 2}{\pi}} \frac{e^{-\frac{4 \ln 2}{W_G^2} x^2}}{W_G}.
\end{aligned} \tag{6.48}$$

Here, y_0 represents the offset, x_c is the central value of the peak, and A is the area. W_G and W_L correspond to the FWHM of the Gaussian and Lorentzian profiles, respectively.

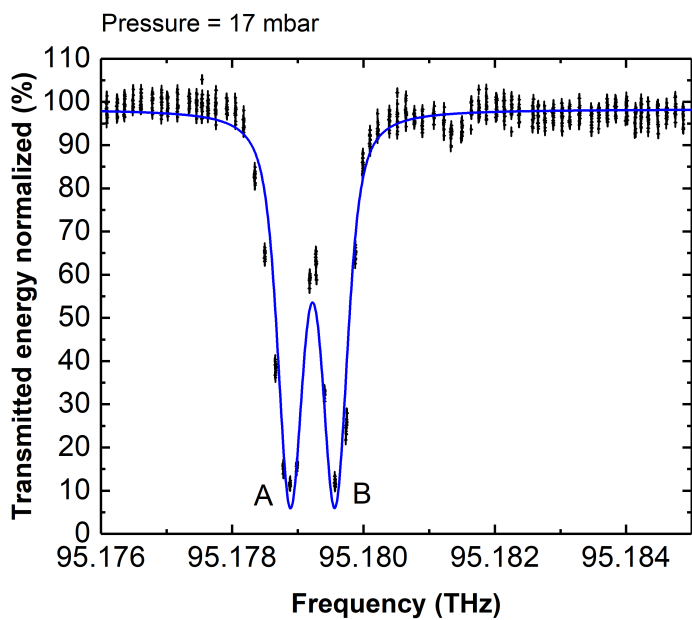
The central frequency of each peak was first extracted by fitting Eq. 6.48 to the data. These extracted values were compared to the HITRAN data to evaluate frequency shifts induced by pressure. The central frequencies showed good agreement between the HITRAN data and the values derived using the wavemeter ($f_{\text{pump}} - f_{\text{signal}}$), with deviations of ± 40 MHz and ± 20 MHz for peaks measured at pressures of 17 mbar and 1.2 mbar, respectively. These deviations align with the wavemeter's relative accuracy of ± 30 MHz, confirming that no intrinsic frequency shifts are induced by the OPO/OPA system.

The linewidth components of each peak include Doppler broadening (Gaussian profile), laser linewidth (assumed Lorentzian), and power broadening (Lorentzian) contributing to the natural linewidth. The Doppler broadening was calculated using

$$\Delta f_{FWHM}^{\text{Dop}} = \sqrt{\frac{8kT \ln 2}{mc^2}} f_c, \tag{6.49}$$



(a)



(b)

Figure 6.48: Measured CH_4 absorption lines at 95.1796 THz and 95.1789 THz, labeled as A and B, respectively. The Voigt fits to the measured absorption peaks are shown in blue. Measurements were conducted over a 2 m path length at two pressures: (a) 1.2 mbar and (b) 17 mbar.

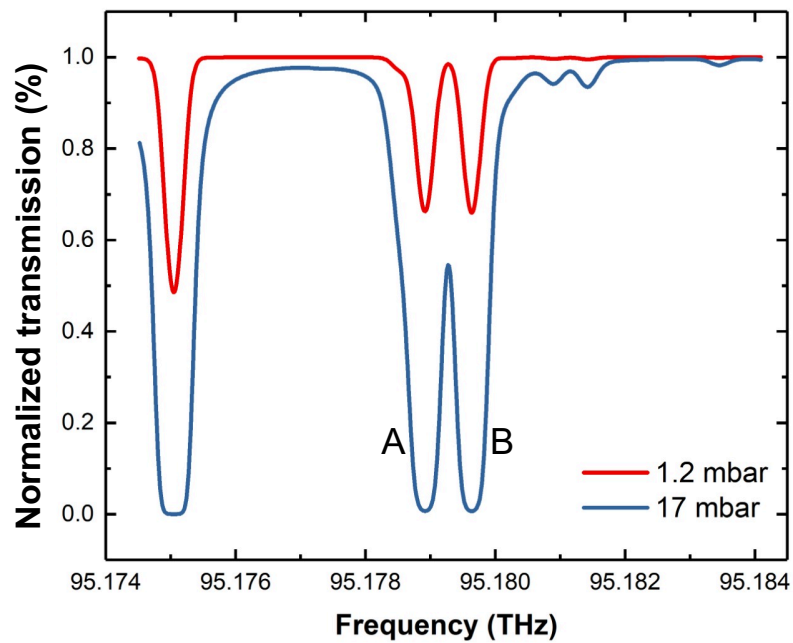


Figure 6.49: Simulated CH_4 absorption lines at 95.1796 THz and 95.1789 THz, labeled as A and B, respectively, using the HITRAN database. Simulations were performed for a 2 m path length at pressures of 1.2 mbar (red) and 17 mbar (blue).

where f_c is the central frequency of the peak. The calculated Doppler broadening, W_G , was 290.36 MHz for both peaks. Using this value, the FWHM of the total Lorentzian profile, W_L , was extracted. For peaks A and B at 1.2 mbar, W_L was determined to be 0.11(2) GHz and 0.12(2) GHz, respectively. At 17 mbar, W_L was 269(6) MHz and 258(6) MHz for peaks A and B, respectively. A plot of the extracted Lorentzian linewidths of the absorption lines as a function of pressure is shown in Fig. 6.50.

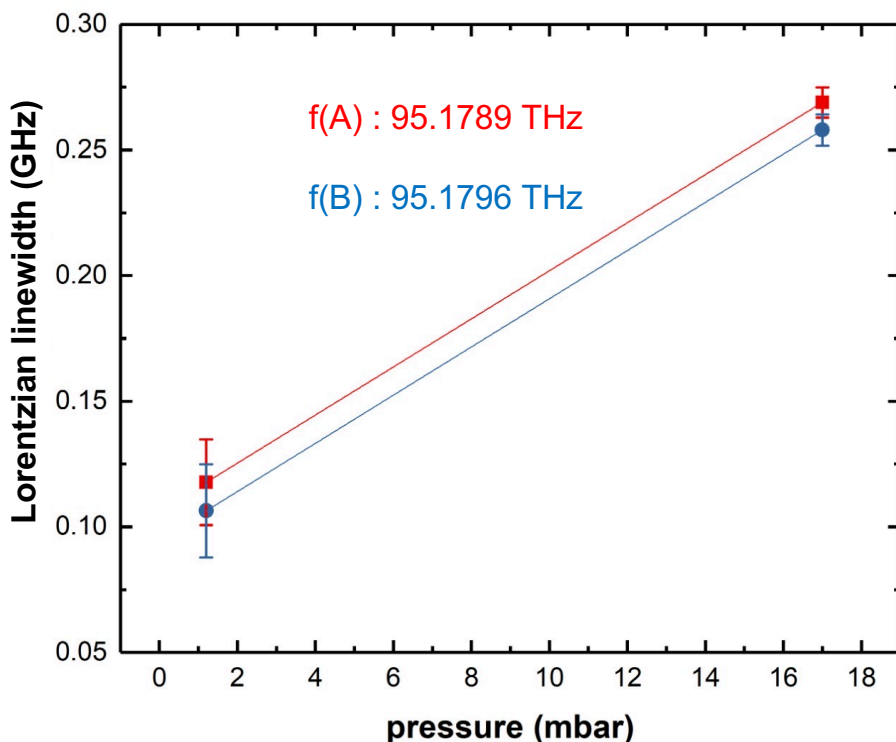


Figure 6.50: Pressure dependence of the Lorentzian linewidth extracted from Voigt fits to the CH_4 absorption lines at 95.1789 THz (red, labeled as A) and 95.1796 THz (blue, labeled as B). The linewidth values were obtained at pressures of 1.2 mbar and 17 mbar, with error bars representing the uncertainties in the fit parameters. The linear trend reflects the broadening due to pressure effects.

The natural linewidth of the Lorentzian profile was obtained through simulations at zero pressure. By combining the natural linewidth with the extracted Lorentzian linewidths at different pressure values, the power broadening was determined. The power-broadened linewidths obtained from the fits were then used to estimate the laser linewidth. The laser linewidths extracted at pressures of 17 mbar and 1.2 mbar were 110 ± 40 MHz and $90 \pm$

30 MHz, respectively. These values represent upper limits of the laser linewidth, constrained by saturation effects at 17 mbar. Nonetheless, the preliminary results confirm that the laser linewidth remains within the 100 MHz range required for the experiment.

Appendices

6.A Derivation of the reflectivity of the variable outcoupling OPO cavity

6.A.1 Reflection

Here we provide a full derivation of the reflectivity of the OPO cavity by tracking the beam propagation through Fig. 6.A.1. The field reflectivity of mirrors CM1 and CM2 mirrors are r_1 and r_2 , respectively, the field transmission and reflection of the TFP are $t_{\text{TFP}}, r_{\text{TFP}}$, respectively. The field transmission of the $\lambda/4$ – plate is t_λ . A beam crossing a quarter wave plate two times is equivalent to a single pass through a half wave plate, in terms of the Jones matrix this can be written as:

$$\begin{aligned} M_{\lambda/2} &= e^{-i\pi/2} \begin{pmatrix} \cos(\theta)^2 - \sin(\theta)^2 & 2 \cos(\theta) \sin(\theta) \\ 2 \cos(\theta) \sin(\theta) & \sin(\theta)^2 - \cos(\theta)^2 \end{pmatrix} \\ &\equiv e^{-i\pi/2} \begin{pmatrix} Q_{11} & Q_{12} \\ Q_{21} & Q_{22} \end{pmatrix}. \end{aligned} \quad (6.50)$$

The incoming laser field amplitude \vec{E}_{inc} is assumed to be linearly polarized with its polarization vector given by $\frac{|E_{\text{inc}}|}{\sqrt{2}} \begin{bmatrix} \cos(\beta) \\ \sin(\beta) \end{bmatrix}$ without any loss of generality.

The field amplitude of the beam propagating from point ①, $\lambda/4$ – plate then reflected by CM1 to pass through $\lambda/4$ – plate back to point ② is described by the product of the Jones matrices:

$$\vec{E}_2 = \frac{|E_{\text{inc}}|}{\sqrt{2}} \cos(\beta) r_1 e^{-2iL_1 k} t_\lambda^2 t_{\text{TFP}} M_{\lambda/2} \cdot \begin{pmatrix} 1 \\ 0 \end{pmatrix}. \quad (6.51)$$

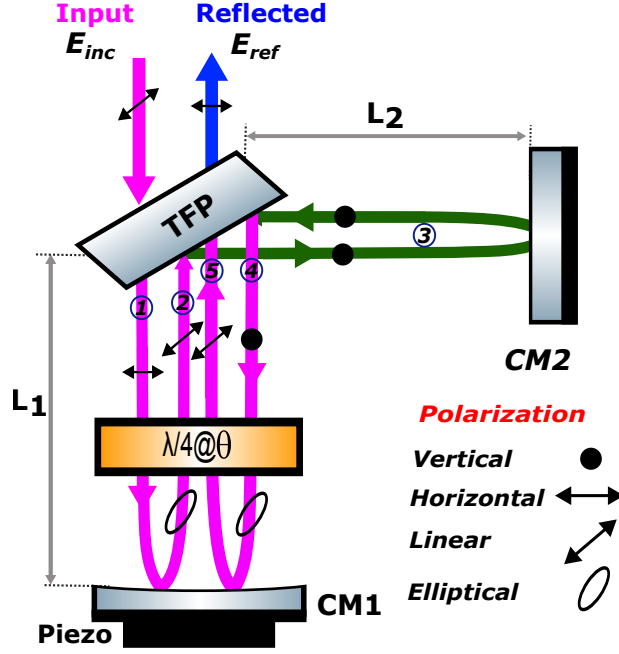


Figure 6.A.1: Sketch of the beam propagation within the OPO cavity. L_1 and L_2 correspond to the distance from the TFP to CM1 and CM2, respectively. The symbol $\lambda/4@θ$ corresponds to the $\lambda/4$ – plate being set to an arbitrary angle.

The propagation of the beam from point ② to ③ then to point ④ happening each round trip is described by the factor given in Eq. 6.52.

$$\begin{aligned}
 & r_{\text{TFP}} M_{\text{TFP}}(S) \cdot r_2 e^{-2iL_2 k} r_{\text{TFP}} M_{\text{TFP}}(S) \\
 &= r_{\text{TFP}} \begin{pmatrix} 0 & 0 \\ 0 & 1 \end{pmatrix} r_2 e^{-2iL_2 k} r_{\text{TFP}} \begin{pmatrix} 0 & 0 \\ 0 & 1 \end{pmatrix}, \tag{6.52}
 \end{aligned}$$

where, from right to the left, this factor describes the beam reflection off the TFP, the reflection from the mirror CM2, the phase shift acquired from the propagation of L_2 then another reflection off the TFP. The beam propagating from point ④ through the quarter wave plate, gets reflected by CM1 and travels a distance L_1 reaching point ⑤, completing a full roundtrip, will acquire a factor of:

$$r_1 e^{-2iL_1 k t_\lambda^2} \cdot M_{\lambda/2}. \tag{6.53}$$

For every round trip Eqs. 6.52 and 6.53 will be multiplied to the left of E_2 . Summing over each field amplitude going through a round trip to get the total field amplitudes at point ⑤

gives:

$$\begin{aligned} \sum \vec{E}_5 = & \sum_{n=1}^{\infty} \left[r_1 e^{-2i(L_1+L_2)k} t_{\lambda}^2 M_{\lambda/2} r_{\text{TFP}} \begin{pmatrix} 0 & 0 \\ 0 & 1 \end{pmatrix} r_2 r_{\text{TFP}} \begin{pmatrix} 0 & 0 \\ 0 & 1 \end{pmatrix} \right]^n \\ & \cdot \frac{|E_{\text{inc}}|}{\sqrt{2}} \cos \beta \cdot r_1 e^{-2iL_1k} t_{\lambda}^2 t_{\text{TFP}} M_{\lambda/2} \cdot \begin{pmatrix} 1 \\ 0 \end{pmatrix}. \end{aligned}$$

Then the total field amplitudes within the cavity is given by:

$$\begin{aligned} \vec{E}_{\text{circ}} &= E_2 + \sum E_5 \\ &= \sum_{n=0}^{\infty} \left[r_1 e^{-2i(L_1+L_2)k} \rho M_{\lambda/2} \begin{pmatrix} 0 & 0 \\ 0 & 1 \end{pmatrix} r_2 \begin{pmatrix} 0 & 0 \\ 0 & 1 \end{pmatrix} \right]^n \\ & \cdot r_1 e^{-2iL_1k} t_{\lambda}^2 t_{\text{TFP}} M_{\lambda/2} \cdot \begin{pmatrix} E_{\text{inc}} \\ 0 \end{pmatrix}, \end{aligned} \quad (6.55)$$

where $\rho = t_{\lambda}^2 r_{\text{TFP}}^2$ is the round trip field loss factor, and for simplification we write $E_{\text{inc}} = \frac{|E_{\text{inc}}|}{\sqrt{2}} \cos \beta$. Rearranging and simplifying the different terms gives:

$$\begin{aligned} \vec{E}_{\text{circ}} &= \\ & \sum_{n=0}^{\infty} \left[r_1 r_2 e^{-2i(L_1+L_2)k} \rho \right]^n \left[M_{\lambda/2} \begin{pmatrix} 0 & 0 \\ 0 & 1 \end{pmatrix} \right]^n \cdot r_1 e^{-2iL_1k} t_{\lambda}^2 t_{\text{TFP}} M_{\lambda/2} \cdot \begin{pmatrix} E_{\text{inc}} \\ 0 \end{pmatrix} \\ &= \sum_{n=0}^{\infty} \left[r_1 r_2 e^{-2i(L_1+L_2)k} \rho \right]^n \\ & \left[e^{-i\pi/2} \right]^n \left[\begin{pmatrix} Q_{11} & Q_{12} \\ Q_{21} & Q_{22} \end{pmatrix} \begin{pmatrix} 0 & 0 \\ 0 & 1 \end{pmatrix} \right]^n r_1 e^{-2iL_1k} t_{\lambda}^2 t_{\text{TFP}} M_{\lambda/2} \cdot \begin{pmatrix} E_{\text{inc}} \\ 0 \end{pmatrix} \\ &= \sum_{n=0}^{\infty} \left[r_1 r_2 e^{-2i(L_1+L_2)k} \rho \right]^n \\ & \left[e^{-i\pi/2} \right]^n \begin{pmatrix} 0 & Q_{12} \\ 0 & Q_{22} \end{pmatrix}^n r_1 e^{-2iL_1k} t_{\lambda}^2 t_{\text{TFP}} M_{\lambda/2} \cdot \begin{pmatrix} E_{\text{inc}} \\ 0 \end{pmatrix}. \end{aligned} \quad (6.56)$$

We now redefine

$$C = r_1 r_2 e^{-2i(L_1+L_2)k} \rho e^{-i\pi/2},$$

$$A = \begin{pmatrix} 0 & C \cdot Q_{12} \\ 0 & C \cdot Q_{22} \end{pmatrix},$$
(6.57)

and the matrix then the summation over n from Eq. 6.56 becomes

$$\sum_{n=0}^{\infty} \begin{pmatrix} 0 & C \cdot Q_{12} \\ 0 & C \cdot Q_{22} \end{pmatrix}^n = (\mathbf{I} - A)^{-1} = \begin{pmatrix} 1 & -C \cdot Q_{12} \\ 0 & 1 - C \cdot Q_{22} \end{pmatrix}^{-1}$$

$$= \frac{1}{1 - C \cdot Q_{22}} \begin{pmatrix} 1 - C \cdot Q_{22} & C \cdot Q_{12} \\ 0 & 1 \end{pmatrix}.$$
(6.58)

Where the result in Eq. 6.58 is obtained in the case of $|A| < 1$, which is the case given by calculating the eigen values.

Now Eq. 6.56 becomes,

$$\vec{E}_{\text{circ}} = \frac{1}{1 - C \cdot Q_{22}} \begin{pmatrix} 1 - C \cdot Q_{22} & C \cdot Q_{12} \\ 0 & 1 \end{pmatrix} \cdot (r_1 e^{-2iL_1 k} t_{\lambda}^2 t_{\text{TFP}}) M_{\lambda/2} \cdot \begin{pmatrix} E_{\text{inc}} \\ 0 \end{pmatrix}$$

$$= \frac{1}{1 - C \cdot Q_{22}} \begin{pmatrix} 1 - C \cdot Q_{22} & C \cdot Q_{12} \\ 0 & 1 \end{pmatrix} \cdot (r_1 e^{-2iL_1 k} t_{\lambda}^2 t_{\text{TFP}}) e^{-i\pi/2} \begin{pmatrix} Q_{11} & Q_{12} \\ Q_{21} & Q_{22} \end{pmatrix} \cdot \begin{pmatrix} E_{\text{inc}} \\ 0 \end{pmatrix}$$

$$= \frac{(r_1 e^{-2iL_1 k} t_{\lambda}^2 t_{\text{TFP,H}}) e^{-i\pi/2}}{1 - C \cdot Q_{22}} \begin{bmatrix} (1 - C \cdot Q_{22})Q_{11} + C \cdot Q_{12}Q_{21} \\ Q_{21} \end{bmatrix}.$$
(6.59)

To obtain an expression for the reflected field, one need to multiply E_{circ} by the field transmission and the polarization matrix of the TFP for the P-polarization, $t_{\text{TFP}} \begin{pmatrix} 1 & 0 \\ 0 & 0 \end{pmatrix}$.

The expression for the reflected field E_{ref} is then given by

$$\vec{E}_{\text{ref}} = \begin{bmatrix} E_{\text{ref}}(P) \\ E_{\text{ref}}(S) \end{bmatrix} = \frac{(r_1 e^{-2iL_1 k} t_{\lambda}^2 t_{\text{TFP}}) e^{-i\pi/2}}{1 - C \cdot Q_{22}} \begin{bmatrix} (1 - C \cdot Q_{22})Q_{11} + C \cdot Q_{12}Q_{21} \\ 0 \end{bmatrix} E_{\text{inc}}. \quad (6.60)$$

Substituting the polarization matrix elements of $M_{\lambda/2}$ from Eq. 6.50, and the value of C from Eq. 6.60, then by taking only the horizontally polarized component $E_{\text{ref}}(P)$ since the

other component is zero, E_{ref} becomes:

$$\begin{aligned}
E_{\text{ref}} &= \frac{(r_1 e^{-2iL_1 k} t_\lambda^2 t_{\text{TFP}}^2) e^{-i\pi/2}}{1 + C \cdot (\cos(2\theta))} [(1 + C \cdot \cos(2\theta)) \cos(2\theta) + C \cdot \sin(2\theta)^2] E_{\text{inc}} \\
&= \frac{(r_1 e^{-2iL_1 k} t_\lambda^2 t_{\text{TFP}}^2) e^{-i\pi/2}}{1 + r_1 r_2 e^{-2i(L_1+L_2)k} \rho e^{-i\pi/2} \cdot (\cos(2\theta))} (\cos(2\theta) + r_1 r_2 e^{-2i(L_1+L_2)k} \rho e^{-i\pi/2}) E_{\text{inc}}.
\end{aligned} \tag{6.61}$$

The ratio of the reflected intensity to the incident intensity is given by:

$$\begin{aligned}
\frac{I_{\text{ref}}}{I_{\text{inc}}} &= \frac{E_{\text{ref}} \cdot E_{\text{ref}}^*}{E_{\text{inc}} \cdot E_{\text{inc}}^*} \\
&= \frac{(r_1 t_\lambda^2 t_{\text{TFP}}^2)^2 [\cos^2(2\theta) + (r_1 r_2 \rho)^2 - 2r_1 r_2 \rho \cos(2\theta) \sin(2kL)]}{1 + r_1 r_2 \rho \cos^2(2\theta) - 2r_1 r_2 \rho \cos(2\theta) \sin(2kL)},
\end{aligned} \tag{6.62}$$

where $L = L_1 + L_2$ is the total length of the cavity.

6.B Active mixer for the PDH locking

The schematic and the PCB layout of the PDH active mixer is given in Fig. 6.B.2 and Fig. 6.B.3, respectively. The evaluation board (EVAL-ADL5387) has been reconfigured to utilize the full differential baseband outputs (see table 4 of the board datasheet). This configuration allows for precise selection and combination of the two in-phase and two quadrature output channels, enabling the desired phase shift in the output error signal. This functionality is achieved through the circuit design illustrated in Fig. 6.B.2, which facilitates gain control for each channel and provides the ability to switch between them.

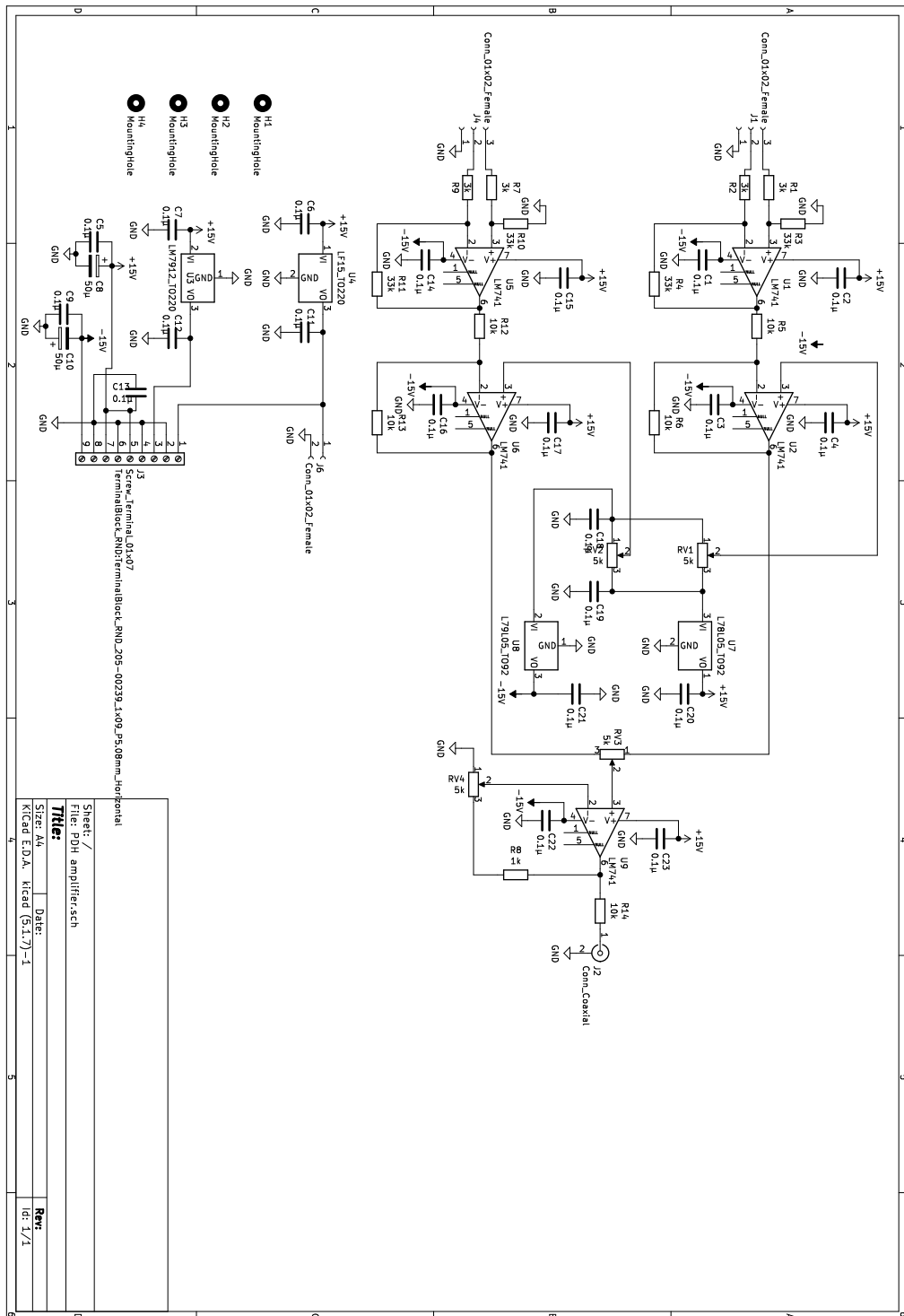


Figure 6.B.2: Circuit diagram of the PDH active mixer.

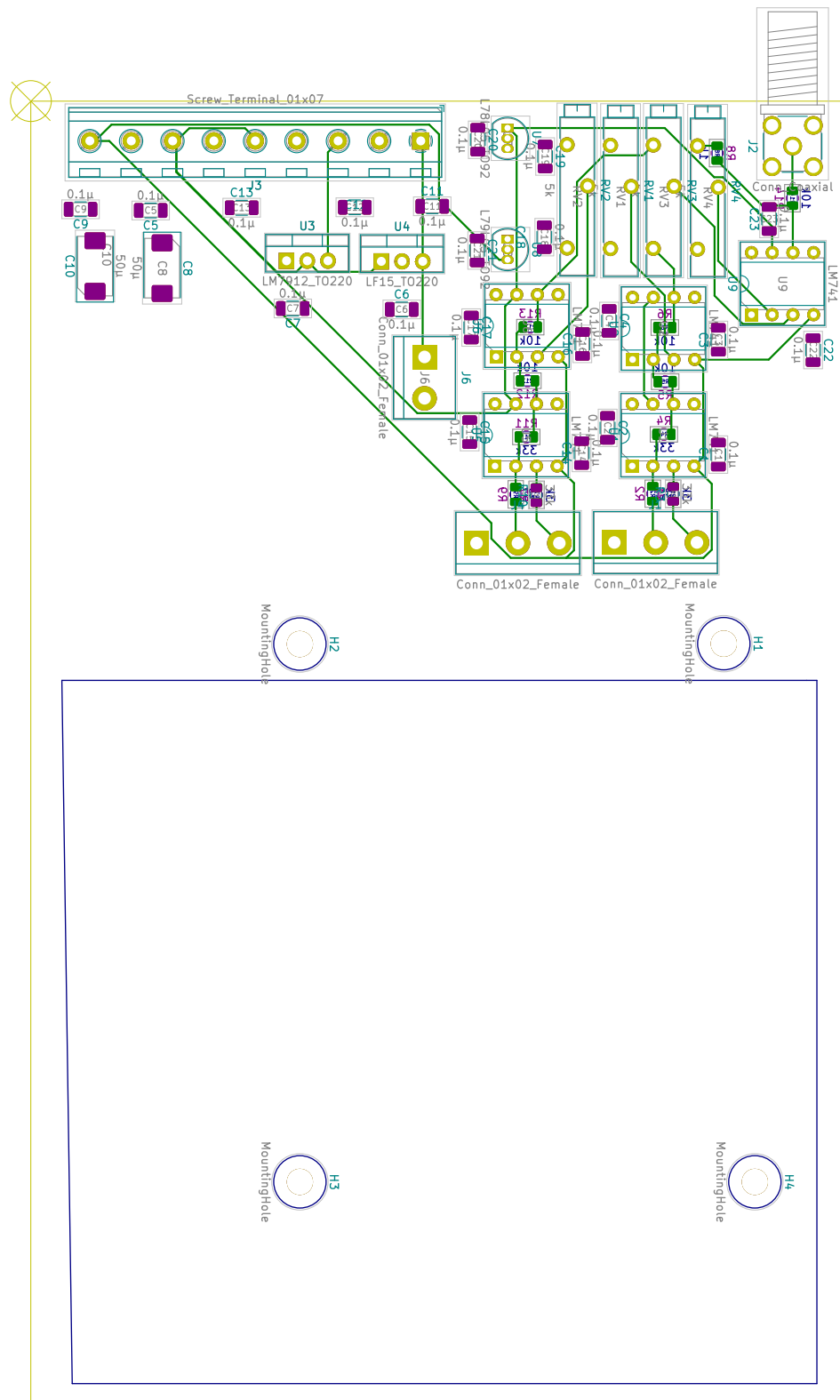


Figure 6.B.3: PCB layout of the PDH active mixer. The evaluation board is mounted using a set of screws through the holes (H1-4).

Conclusion

This thesis focused on the development of the down-conversion system for the HyperMu experiment, which aims to measure the ground-state hyperfine splitting in muonic hydrogen with 1 ppm precision. This measurement enables the precise extraction of the proton structure contributions, such as the Zemach radius and proton polarizability. A central focus of this work was the realization of a high-energy, narrow-bandwidth, single-frequency OPO/OPA system at $3.1 \mu\text{m}$, as well as an updated theoretical prediction for the HFS transition energy.

We successfully demonstrated a single-frequency OPO/OPA system at $3.1 \mu\text{m}$ with a narrow bandwidth of less than 100 MHz, achieving pulse energies of up to 3.4 mJ. The system exhibited excellent beam quality, characterized by $M^2 = 1.3$, and demonstrated continuous tunability over 20 GHz, extendable to a range of several nanometers.

Simulations were conducted to determine the pulse energies required for the difference frequency generation (DFG) stage. The analysis revealed that pulses with 2.5 mJ at $3.1 \mu\text{m}$ and 25 mJ at $2.1 \mu\text{m}$ are necessary to produce $6.8 \mu\text{m}$ pulses with a few mJ of energy. While the OPO/OPA1 branch at $3.1 \mu\text{m}$ successfully met these requirements, simulations for the OPO/OPA2 branch at $2.1 \mu\text{m}$ using a PPKTP crystal suggest a potential pulse energy of approximately 30 mJ. Efforts to experimentally realize this second branch are ongoing.

The realization of an OPO/OPA system delivering high-energy, narrow-bandwidth, single-frequency pulses in the 50 ns regime underscores the potential for further optimization. Extending the pulse length could mitigate challenges related to damage thresholds in the multi-pass cell surrounding the muon stopping volume.

Narrowing the theoretical uncertainty of the HFS transition energy is critical to reducing the resonance search range. Our updated theoretical compilation for the 1S-HFS transition

energy yielded $E_{1S\text{-HFS}} = 182.6389(163)$ meV, incorporating recent evaluations of the two-photon exchange (2PE) contribution from data-driven and chiral perturbation theory (χ PT) approaches. Additionally, higher-order QED corrections up to $\alpha^3 E_F$, as well as electronic vacuum polarization contributions of the same order, were included. While QED uncertainties are within 0.5 ppm, the 2PE contribution remains the largest source of theoretical uncertainty at approximately ± 60 ppm. We chose a search range of around 50 GHz, centered at 44.161 THz.

Resolving discrepancies in proton structure contributions—particularly between data-driven and χ PT methods on one side and χ PT and heavy baryon effective field theory on the other—is essential. Additionally, contributions from weak interactions and hadronic vacuum polarization, which are comparable in magnitude to higher-order electronic vacuum polarization effects, require re-evaluation. Reducing these uncertainties will directly minimize the resonance search range and optimize the required data-taking time.

Future work will focus on completing the OPO/OPA2 branch at $2.1 \mu\text{m}$ and finalizing the DFG stage to produce $6.8 \mu\text{m}$ pulses with the necessary properties. Optimizing the coupling of these pulses into the multi-pass cell and conducting spectroscopic characterization of the final output will ensure the laser system’s readiness for the first beam time.

Bibliography

- [1] A. Antognini, F. Hagelstein, and V. Pascalutsa, “The proton structure in and out of muonic hydrogen,” *Ann. Rev. Nucl. Part. Sci.*, vol. 72, p. 389, 2022.
- [2] J. Nuber, A. Adamczak, M. A. Ahmed, L. Affolter, F. D. Amaro, P. Amaro, A. Antognini, P. Carvalho, Y. H. Chang, T. L. Chen, W. L. Chen, L. M. P. Fernandes, M. Ferro, D. Goeldi, T. Graf, M. Guerra, T. W. Hänsch, C. A. O. Henriques, M. Hildebrandt, P. Indelicato, O. Kara, K. Kirch, A. Knecht, F. Kottmann, Y. W. Liu, J. Machado, M. Marszałek, R. D. P. Mano, C. M. B. Monteiro, F. Nez, A. Ouf, N. Paul, R. Pohl, E. Rapisarda, J. M. F. dos Santos, J. P. Santos, P. A. O. C. Silva, L. Sinkunaite, J. T. Shy, K. Schuhmann, S. Rajamohanan, A. Soter, L. Sustelo, D. Taqqu, L. B. Wang, F. Wauters, P. Yzombard, M. Zeyen, and J. Zhang, “Diffusion of muonic hydrogen in hydrogen gas and the measurement of the $1s$ hyperfine splitting of muonic hydrogen,” *SciPost Phys. Core*, vol. 6, p. 057, 2023.
- [3] M. Marszałek, *Multipass cell for laser spectroscopy of muonic hydrogen*. PhD thesis, ETH Zurich, 2022.
- [4] P. Amaro, A. Adamczak, M. A. Ahmed, L. Affolter, F. D. Amaro, P. Carvalho, T. L. Chen, L. M. P. Fernandes, M. Ferro, D. Goeldi, T. Graf, M. Guerra, T. W. Hänsch, C. A. O. Henriques, Y. C. Huang, P. Indelicato, O. Kara, K. Kirch, A. Knecht, F. Kottmann, Y. W. Liu, J. Machado, M. Marszałek, R. D. P. Mano, C. M. B. Monteiro, F. Nez, J. Nuber, A. Ouf, N. Paul, R. Pohl, E. Rapisarda, J. M. F. dos Santos, J. P. Santos, P. A. O. C. Silva, L. Sinkunaite, J. T. Shy, K. Schuhmann, S. Rajamohanan, A. Soter, L. Sustelo, D. Taqqu, L. B. Wang, F. Wauters, P. Yzombard, M. Zeyen, and A. Antognini, “Laser excitation of the $1s$ -hyperfine transition in muonic hydrogen,” *SciPost Phys.*, vol. 13, p. 020, 2022.

- [5] J. Nuber, *Studies of muonium emission into vacuum and diffusion of muonic hydrogen in the μp hyperfine splitting experiment at PSI*. PhD thesis, ETH Zurich, 2023.
- [6] R. W. Boyd, “Chapter 2 - wave-equation description of nonlinear optical interactions,” in *Nonlinear Optics (Third Edition)* (R. W. Boyd, ed.), pp. 69–133, Burlington: Academic Press, third edition ed., 2008.
- [7] G. I. Stegeman and R. A. Stegeman, *Nonlinear optics: phenomena, materials and devices*, vol. 78. John Wiley & Sons, 2012.
- [8] P. G. Schunemann, K. T. Zawilski, L. A. Pomeranz, D. J. Creeden, and P. A. Budni, “Advances in nonlinear optical crystals for mid-infrared coherent sources,” *JOSA B*, vol. 33, no. 11, pp. D36–D43, 2016.
- [9] A. Antognini, F. Nez, K. Schuhmann, F. D. Amaro, F. Biraben, J. M. Cardoso, D. S. Covita, A. Dax, S. Dhawan, M. Diepold, *et al.*, “Proton structure from the measurement of 2s-2p transition frequencies of muonic hydrogen,” *Science*, vol. 339, no. 6118, pp. 417–420, 2013.
- [10] D. Ruth *et al.*, “New spin structure constraints on hyperfine splitting and proton Zemach radius,” *Phys. Lett. B*, vol. 859, p. 139116, 2024.
- [11] F. Hagelstein, V. Lensky, and V. Pascalutsa, “Chiral perturbation theory of the hyperfine splitting in (muonic) hydrogen,” *The European Physical Journal C*, vol. 83, no. 8, p. 762, 2023.
- [12] V. L. Fitch and J. Rainwater, “Studies of X-rays from Mu-mesonic atoms,” *Physical Review*, vol. 92, no. 3, p. 789, 1953.
- [13] K. P. Jungmann, “Aspects of fundamental muon physics,” in *Muon Science*, pp. 405–461, Routledge, 2017.
- [14] B. Ohayon, Z. Burkley, and P. Crivelli, “Current status and prospects of muonium spectroscopy at psi,” *SciPost Physics Proceedings*, no. 5, p. 029, 2021.
- [15] F. Renga, “Experimental searches for muon decays beyond the standard model,” *Reviews in Physics*, vol. 4, p. 100029, 2019.
- [16] A. Antognini, “Muonic atoms and the nuclear structure,” in *Laser Spectroscopy: XXII International Conference on Laser Spectroscopy (ICOLS2015)*, pp. 17–29, World Scientific, 2017.

- [17] R. Pohl, A. Antognini, F. Nez, F. D. Amaro, F. Biraben, J. M. Cardoso, D. S. Covita, A. Dax, S. Dhawan, L. M. Fernandes, *et al.*, “The size of the proton,” *nature*, vol. 466, no. 7303, pp. 213–216, 2010.
- [18] M. Niering, R. Holzwarth, J. Reichert, P. Pokasov, T. Udem, M. Weitz, T. Hänsch, P. Lemonde, G. Santarelli, M. Abgrall, *et al.*, “Measurement of the hydrogen 1 s-2 s transition frequency by phase coherent comparison with a microwave cesium fountain clock,” *Physical Review Letters*, vol. 84, no. 24, p. 5496, 2000.
- [19] M. Fischer, N. Kolachevsky, M. Zimmermann, R. Holzwarth, T. Udem, T. W. Hänsch, M. Abgrall, J. Grünert, I. Maksimovic, S. Bize, *et al.*, “New limits on the drift of fundamental constants from laboratory measurements,” *Physical Review Letters*, vol. 92, no. 23, p. 230802, 2004.
- [20] J. C. Bernauer, P. Achenbach, C. Ayerbe Gayoso, R. Böhm, D. Bosnar, L. Debenjak, M. Distler, L. Doria, A. Esser, H. Fonvieille, *et al.*, “High-precision determination of the electric and magnetic form factors of the proton,” *Physical Review Letters*, vol. 105, no. 24, p. 242001, 2010.
- [21] P. G. Blunden and I. Sick, “Proton radii and two-photon exchange,” *Physical Review C—Nuclear Physics*, vol. 72, no. 5, p. 057601, 2005.
- [22] R. Pohl, R. Gilman, G. A. Miller, and K. Pachucki, “Muonic hydrogen and the proton radius puzzle,” *Annual Review of Nuclear and Particle Science*, vol. 63, no. 1, pp. 175–204, 2013.
- [23] A. Grinin, A. Matveev, D. C. Yost, L. Maisenbacher, V. Wirthl, R. Pohl, T. W. Hänsch, and T. Udem, “Two-photon frequency comb spectroscopy of atomic hydrogen,” *Science*, vol. 370, no. 6520, pp. 1061–1066, 2020.
- [24] N. Bezginov, T. Valdez, M. Horbatsch, A. Marsman, A. Vutha, and E. Hessels, “A measurement of the atomic hydrogen Lamb shift and the proton charge radius,” *Science*, vol. 365, no. 6457, pp. 1007–1012, 2019.
- [25] A. Beyer, L. Maisenbacher, A. Matveev, R. Pohl, K. Khabarova, A. Grinin, T. Lamour, D. C. Yost, T. W. Hänsch, N. Kolachevsky, *et al.*, “The Rydberg constant and proton size from atomic hydrogen,” *Science*, vol. 358, no. 6359, pp. 79–85, 2017.

- [26] A. Brandt, S. Cooper, C. Rasoar, Z. Burkley, A. Matveev, and D. Yost, “Measurement of the $2\text{S } 1/2\text{-}8\text{D } 5/2$ transition in hydrogen,” *Physical Review Letters*, vol. 128, no. 2, p. 023001, 2022.
- [27] S. Scheidegger and F. Merkt, “Precision-spectroscopic determination of the binding energy of a two-body quantum system: The hydrogen atom and the proton-size puzzle,” *Physical Review Letters*, vol. 132, no. 11, p. 113001, 2024.
- [28] H. Fleurbaey, S. Galtier, S. Thomas, M. Bonnaud, L. Julien, F. Biraben, F. Nez, M. Abgrall, and J. Guéna, “New measurement of the $1\text{S}\text{-}3\text{S}$ transition frequency of hydrogen: contribution to the proton charge radius puzzle,” *Physical review letters*, vol. 120, no. 18, p. 183001, 2018.
- [29] W. Xiong, A. Gasparian, H. Gao, D. Dutta, M. Khandaker, N. Liyanage, E. Pasyuk, C. Peng, X. Bai, L. Ye, *et al.*, “A small proton charge radius from an electron–proton scattering experiment,” *Nature*, vol. 575, no. 7781, pp. 147–150, 2019.
- [30] M. Belushkin, H.-W. Hammer, and U.-G. Meißner, “Dispersion analysis of the nucleon form factors including meson continua,” *Physical Review C—Nuclear Physics*, vol. 75, no. 3, p. 035202, 2007.
- [31] M. Horbatsch, E. A. Hessels, and A. Pineda, “Proton radius from electron-proton scattering and chiral perturbation theory,” *Physical Review C*, vol. 95, no. 3, p. 035203, 2017.
- [32] D. W. Higinbotham, A. A. Kabir, V. Lin, D. Meekins, B. Norum, and B. Sawatzky, “Proton radius from electron scattering data,” *Physical Review C*, vol. 93, no. 5, p. 055207, 2016.
- [33] Y.-H. Lin, H.-W. Hammer, and U.-G. Meißner, “New insights into the nucleon’s electromagnetic structure,” *Physical Review Letters*, vol. 128, no. 5, p. 052002, 2022.
- [34] P. Mohr, D. Newell, B. Taylor, and E. Tiesinga, “CODATA Recommended Values of the Fundamental Physical Constants: 2022,” *arXiv preprint arXiv:2409.03787*, 8 2024.
- [35] M. M. Sternheim, “Vacuum polarization corrections to hyperfine structure in muonic atoms,” *Phys. Rev.*, vol. 138, pp. B430–B432, Apr 1965.
- [36] M. I. Eides, H. Grotch, and V. A. Shelyuto, “Theory of light hydrogenlike atoms,” *Physics Reports*, vol. 342, no. 2-3, pp. 63–261, 2001.

- [37] G. Breit, “Possible effects of nuclear spin on X-ray terms,” *Physical Review*, vol. 35, no. 12, p. 1447, 1930.
- [38] D. Aguillard, T. Albahri, D. Allspach, A. Anisenkov, K. Badgley, S. Baekler, I. Bailey, L. Bailey, V. Baranov, E. Barlas-Yucel, *et al.*, “Detailed report on the measurement of the positive muon anomalous magnetic moment to 0.20 ppm,” *arXiv preprint arXiv:2402.15410*, 2024.
- [39] N. M. Kroll and F. Pollock, “Second-order radiative corrections to hyperfine structure,” *Phys. Rev.*, vol. 86, pp. 876–888, Jun 1952.
- [40] D. E. Zwanziger, “ α^3 corrections to hyperfine structure in hydrogenic atoms,” *Physical Review*, vol. 121, no. 4, p. 1128, 1961.
- [41] K. Jungmann, V. G. Ivanov, and S. G. Karshenboim, “Hyperfine structure in muonic hydrogen,” *The Hydrogen Atom: Precision Physics of Simple Atomic Systems*, pp. 446–453, 2001.
- [42] V. Ivanov and S. Karshenboim, “Radiative corrections for level widths in light muonic atoms,” *Journal of Experimental and Theoretical Physics*, vol. 85, pp. 435–440, 1997.
- [43] S. Karshenboim, U. Jentschura, V. Ivanov, and G. Soff, “Corrections to the wave function and the hyperfine structure in exotic atoms,” *The European Physical Journal D-Atomic, Molecular, Optical and Plasma Physics*, vol. 2, pp. 209–215, 1998.
- [44] U. D. Jentschura, G. Soff, V. G. Ivanov, and S. G. Karshenboim, “Bound $\mu^+\mu^-$ system,” *Phys. Rev. A*, vol. 56, pp. 4483–4495, Dec 1997.
- [45] S. Karshenboim, “Logarithmic radiative corrections to the dipole matrix elements in the hydrogen atom,” *Journal of Experimental and Theoretical Physics*, vol. 80, no. 4, pp. 593–602, 1995.
- [46] S. Karshenboim, E. Y. Korzinin, and V. Ivanov, “Hyperfine splitting in muonic hydrogen: QED corrections of the α^2 order,” *JETP Letters*, vol. 89, no. 4, pp. 216–216, 2009.
- [47] V. G. Ivanov, E. Y. Korzinin, and S. G. Karshenboim, “Second-order corrections to the wave function at the origin in muonic hydrogen and ponium,” *Physical Review D*, vol. 80, no. 2, p. 027702, 2009.

- [48] S. G. Karshenboim, E. Y. Korzinin, and V. G. Ivanov, “Hyperfine splitting in muonic hydrogen: QED corrections of the α^2 order,” *JETP letters*, vol. 88, no. 10, pp. 641–646, 2008.
- [49] W. H. Furry, “On bound states and scattering in positron theory,” *Phys. Rev.*, vol. 81, pp. 115–124, Jan 1951.
- [50] N. M. Kroll and F. Pollock, “Radiative corrections to the hyperfine structure and the fine structure constant,” *Phys. Rev.*, vol. 84, pp. 594–595, Nov 1951.
- [51] S. J. Brodsky and G. W. Erickson, “Radiative Level Shifts. III. Hyperfine Structure in Hydrogenic Atoms,” *Physical Review*, vol. 148, no. 1, p. 26, 1966.
- [52] T. Kinoshita and M. Nio, “Radiative corrections to the muonium hyperfine structure: The $\alpha^2(z\alpha)$ correction,” *Phys. Rev. D*, vol. 53, pp. 4909–4929, May 1996.
- [53] K. Pachucki, “ $\alpha(z\alpha)^2 E_F$ correction to hyperfine splitting in hydrogenic atoms,” *Physical Review A*, vol. 54, no. 3, p. 1994, 1996.
- [54] R. Karplus and A. Klein, “Electrodynamic displacement of atomic energy levels. i. hyperfine structure,” *Phys. Rev.*, vol. 85, pp. 972–984, Mar 1952.
- [55] S. G. Karshenboim, V. A. Shelyuto, and M. I. Eides, “First Corrections of Order $\alpha^2(Z\alpha)E_F$ to Muonium and Hydrogen Hyperfine Splitting. (In Russian),” *Sov. J. Nucl. Phys.*, vol. 50, pp. 1015–1020, 1989.
- [56] M. I. Eides, S. G. Karshenboim, and V. A. Shelyuto, “New contributions to muonium and hydrogen hyperfine splitting induced by vacuum polarization insertions in external photons,” *Physics Letters B*, vol. 229, no. 3, pp. 285–288, 1989.
- [57] M. Eides, S. Karsenboim, and V. Shelyuto, “Purely radiative contribution to muonium and hydrogen hyperfine splitting induced by light by light scattering insertion in external photons.(phys. lett. b 268 (1991) 433; b 316 (1993) 631 (e)),” *Physics Letters B*, vol. 319, no. 4, pp. 545–545, 1993.
- [58] M. I. Eides, S. G. Karshenboim, and V. A. Shelyuto, “Last vacuum polarization contribution of order $\alpha^2(Z\alpha)E_F$ to muonium and hydrogen hyperfine splitting,” *Phys. Lett. B*, vol. 249, pp. 519–522, 1990.

- [59] S. G. Karshenboim, V. A. Shelyuto, and M. I. Eides, “Yet another component on the order of $\alpha^2(Z\alpha)E_F$ in the hyperfine splitting in muonium and hydrogen,” *JETP Lett.*, vol. 52, pp. 317–319, 1990.
- [60] S. M. Schneider, W. Greiner, and G. Soff, “Vacuum-polarization contribution to the hyperfine-structure splitting of hydrogenlike atoms,” *Physical Review A*, vol. 50, no. 1, p. 118, 1994.
- [61] M. Nio and T. Kinoshita, “Radiative corrections to the muonium hyperfine structure. ii. the $\alpha(z\alpha)^2$ correction,” *Phys. Rev. D*, vol. 55, pp. 7267–7290, Jun 1997.
- [62] M. A. B. Beg and G. Feinberg, “Exotic Interactions of Charged Leptons,” *Phys. Rev. Lett.*, vol. 33, p. 606, 1974. [Erratum: *Phys.Rev.Lett.* 35, 130 (1975)].
- [63] M. I. Eides, “Weak Interaction Contributions in Light Muonic Atoms,” *Phys. Rev. A*, vol. 85, p. 034503, 2012.
- [64] R. L. Workman *et al.*, “Review of Particle Physics,” *PTEP*, vol. 2022, p. 083C01, 2022.
- [65] R. N. Faustov and A. P. Martynenko, “Contribution of hadronic vacuum polarization to hyperfine splitting of muonic hydrogen,” *Phys. Atom. Nucl.*, vol. 61, pp. 471–475, 1998.
- [66] C. Peset and A. Pineda, “Model-independent determination of the two-photon exchange contribution to hyperfine splitting in muonic hydrogen,” *JHEP*, vol. 04, p. 060, 2017.
- [67] G. T. Bodwin and D. R. Yennie, “Some recoil corrections to the hydrogen hyperfine splitting,” *Phys. Rev. D*, vol. 37, pp. 498–523, Jan 1988.
- [68] C. E. Carlson, V. Nazaryan, and K. Griffioen, “Proton-structure corrections to hyperfine splitting in muonic hydrogen,” *Physical Review A*, vol. 83, no. 4, p. 042509, 2011.
- [69] R. Faustov and A. Martynenko, “Proton polarizability contribution to hydrogen hyperfine splitting,” *The European Physical Journal C-Particles and Fields*, vol. 24, pp. 281–285, 2002.
- [70] A. C. Zemach, “Proton structure and the hyperfine shift in hydrogen,” *Phys. Rev.*, vol. 104, pp. 1771–1781, Dec 1956.

- [71] K. Borah, R. J. Hill, G. Lee, and O. Tomalak, “Parametrization and applications of the low- Q^2 nucleon vector form factors,” *Physical Review D*, vol. 102, no. 7, p. 074012, 2020.
- [72] A. Antognini, Y.-H. Lin, and U.-G. Meißner, “Precision calculation of the recoil–finite-size correction for the hyperfine splitting in muonic and electronic hydrogen,” *Physics Letters B*, vol. 835, p. 137575, 2022.
- [73] O. Tomalak, “Two-photon exchange correction to the Lamb shift and hyperfine splitting of S levels,” *The European Physical Journal A*, vol. 55, pp. 1–6, 2019.
- [74] S. G. Karshenboim, “Nuclear structure-dependent radiative corrections to the hydrogen hyperfine splitting,” *Physics Letters A*, vol. 225, no. 1-3, pp. 97–106, 1997.
- [75] J. S. Schwinger, *Particles, sources, and fields. Vol. 2*. IOP Publishing, 1989.
- [76] S. Karshenboim, V. Ivanov, U. Jentschura, and G. Soff, “Bound states of the muon-antimuon system: Lifetimes and hyperfine splitting,” *Journal of Experimental and Theoretical Physics*, vol. 86, pp. 226–236, 1998.
- [77] A. Martynenko and R. Faustov, “Hyperfine ground-state structure of muonic hydrogen,” *Journal of Experimental and Theoretical Physics*, vol. 98, pp. 39–52, 2004.
- [78] G. Fesenko and G. Y. Korenman, “New results in the theory of muonic atom formation in molecular hydrogen,” *Hyperfine interactions*, vol. 101, no. 1, pp. 91–96, 1996.
- [79] D. S. Covita, D. F. Anagnostopoulos, H. Fuhrmann, H. Gorke, D. Gotta, A. Gruber, A. Hirtl, T. Ishiwatari, P. Indelicato, T. S. Jensen, *et al.*, “Line shape analysis of the $k\beta$ transition in muonic hydrogen,” *The European Physical Journal D*, vol. 72, pp. 1–22, 2018.
- [80] E. Borie and M. Leon, “X-ray yields in protonium and mesic hydrogen,” *Phys. Rev. A*, vol. 21, pp. 1460–1468, May 1980.
- [81] A. Adamczak and J. Gronowski, “Diffusion radius of muonic hydrogen atoms in hd gas,” *The European Physical Journal D*, vol. 41, pp. 493–497, 2007.
- [82] V. Popov and V. Pomerantsev, “Isotopic effects in scattering and kinetics of the atomic cascade of excited μ^-p and μ^-d atoms,” *Physical Review A*, vol. 95, no. 2, p. 022506, 2017.

- [83] L. P. Sinkunaite, *Detection system for measuring the hyperfine splitting in muonic hydrogen*. PhD thesis, ETH Zurich, 2022.
- [84] M. Zeyen, L. Affolter, M. Abdou Ahmed, T. Graf, O. Kara, K. Kirch, A. Langenbach, M. Marszalek, F. Nez, A. Ouf, *et al.*, “Injection-seeded high-power Yb:YAG thin-disk laser stabilized by the Pound-Drever-Hall method,” *Optics Express*, vol. 31, no. 18, pp. 29558–29572, 2023.
- [85] A. V. Smith, *Crystal nonlinear optics: with SNLO examples*. AS-Photonics Albuquerque, NM, USA, 2018.
- [86] C. Fischer and M. W. Sigrist, “Mid-IR difference frequency generation,” in *Solid-state mid-infrared laser sources*, pp. 99–143, Springer, 2003.
- [87] R. L. Byer and R. L. Herbst, “Parametric oscillation and mixing,” *Nonlinear Infrared Generation*, pp. 81–137, 2005.
- [88] M. Broyer *et al.*, “Intracavity cw difference frequency generation by mixing three photons and using gaussian laser beams,” *Journal de Physique*, vol. 46, no. 4, pp. 523–533, 1985.
- [89] J.-J. Zondy, “The effects of focusing in type-I and type-II difference-frequency generations,” *Optics communications*, vol. 149, no. 1-3, pp. 181–206, 1998.
- [90] G. Boyd and A. Ashkin, “Theory of parametric oscillator threshold with single-mode optical masers and observation of amplification in LiNbO_3 ,” *Physical review*, vol. 146, no. 1, p. 187, 1966.
- [91] A. E. Siegman, “How to (maybe) measure laser beam quality,” in *Diode Pumped Solid State Lasers: Applications and Issues*, p. MQ1, Optica Publishing Group, 1998.
- [92] P. D. Mason and L. F. Michaille, “Review of the development of nonlinear materials for mid-IR generation,” in *Technologies for Optical Countermeasures V*, vol. 7115, pp. 184–193, SPIE, 2008.
- [93] K. Zhong, J.-s. Li, D.-g. Xu, J.-l. Wang, Z. Wang, P. Wang, and J.-q. Yao, “Tunable and coherent nanosecond 7.2–12.2 μm mid-infrared generation based on difference frequency mixing in ZnGeP_2 crystal,” *Optoelectronics Letters*, vol. 6, no. 3, pp. 179–182, 2010.

- [94] S. G. Grechin and I. A. Muravev, “Crystal ZnGeP_2 for Nonlinear Frequency Conversion: Physical parameters, phase-matching and nonlinear properties: Revision,” in *Photonics*, vol. 11, p. 450, MDPI, 2024.
- [95] J. Hellström, *Nanosecond optical parametric oscillators and amplifiers based on periodically poled KTiOPO_4* . PhD thesis, Fysiska institutionen, 2001.
- [96] R. S. Coetzee, N. Thilmann, A. Zukauskas, C. Canalias, and V. Pasiskevicius, “Nanosecond laser induced damage thresholds in KTiOPO_4 and $\text{Rb}:\text{KTiOPO}_4$ at $1\ \mu\text{m}$ and $2\ \mu\text{m}$,” *Optical Materials Express*, vol. 5, no. 9, pp. 2090–2095, 2015.
- [97] J. T. Verdeyen, *Laser electronics*. Prentice Hall, Englewood Cliffs, NJ, 1989.
- [98] A. E. Siegman, *Lasers*. University science books, 1986.
- [99] E. Collett, “Field guide to polarization,” Spie Bellingham, 2005.
- [100] *Polarization and Crystal Optics*, ch. 6, pp. 193–237. John Wiley Sons, Ltd, 1991.
- [101] K. Schuhmann, K. Kirch, M. Marszałek, M. Pototschnig, L. Sinkunaite, G. Wichmann, M. Zeyen, and A. Antognini, “Polarizing Gires-Tournois interferometer as intra-cavity frequency-selective element in high-power lasers,” in *Components and Packaging for Laser Systems IV*, vol. 10513, pp. 206–211, SPIE, 2018.
- [102] M. Pollnau and M. Eichhorn, “Spectral coherence, Part I: Passive-resonator linewidth, fundamental laser linewidth, and schawlow-townes approximation,” *Progress in quantum electronics*, vol. 72, p. 100255, 2020.
- [103] R. W. Drever, J. L. Hall, F. V. Kowalski, J. Hough, G. Ford, A. Munley, and H. Ward, “Laser phase and frequency stabilization using an optical resonator,” *Applied Physics B*, vol. 31, pp. 97–105, 1983.
- [104] A. Staley, *Locking the advanced LIGO gravitational wave detector: with a focus on the arm length stabilization technique*. Columbia University, 2015.
- [105] E. D. Black, “An introduction to Pound–Drever–Hall laser frequency stabilization,” *American journal of physics*, vol. 69, no. 1, pp. 79–87, 2001.
- [106] M. Zeyen, L. Affolter, M. A. Ahmed, T. Graf, O. Kara, K. Kirch, M. Marszałek, F. Nez, A. Ouf, R. Pohl, *et al.*, “Pound–Drever–Hall locking scheme free from Trojan operating points,” *Review of Scientific Instruments*, vol. 94, no. 1, 2023.

- [107] G. Boyd and D. Kleinman, “Parametric interaction of focused gaussian light beams,” *Journal of Applied Physics*, vol. 39, no. 8, pp. 3597–3639, 1968.
- [108] S. E. Harris, “Tunable optical parametric oscillators,” *Proceedings of the IEEE*, vol. 57, no. 12, pp. 2096–2113, 1969.
- [109] E. Granot, S. Pearl, and M. M. Tilleman, “Analytical solution for a lossy singly resonant optical parametric oscillator,” *JOSA B*, vol. 17, no. 3, pp. 381–386, 2000.
- [110] S. Brosnan and R. Byer, “Optical parametric oscillator threshold and linewidth studies,” *IEEE Journal of Quantum Electronics*, vol. 15, no. 6, pp. 415–431, 1979.
- [111] L. R. Marshall and A. Kaz, “Eye-safe output from noncritically phase-matched parametric oscillators,” *JOSA B*, vol. 10, no. 9, pp. 1730–1736, 1993.
- [112] J. Terry, Y. Cui, Y. Yang, W. Sibbett, and M. H. Dunn, “Low-threshold operation of an all-solid-state KTP optical parametric oscillator,” *JOSA B*, vol. 11, no. 5, pp. 758–769, 1994.
- [113] A. Smith, W. Alford, T. Raymond, and M. S. Bowers, “Comparison of a numerical model with measured performance of a seeded, nanosecond KTP optical parametric oscillator,” *JOSA B*, vol. 12, no. 11, pp. 2253–2267, 1995.
- [114] R. T. White, Y. He, B. J. Orr, M. Kono, and K. Baldwin, “Control of frequency chirp in nanosecond-pulsed laser spectroscopy. 1. optical-heterodyne chirp analysis techniques,” *JOSA B*, vol. 21, no. 9, pp. 1577–1585, 2004.
- [115] R. T. White, Y. He, B. J. Orr, M. Kono, and K. Baldwin, “Pulsed injection-seeded optical parametric oscillator with low frequency chirp for high-resolution spectroscopy,” *Optics letters*, vol. 28, no. 14, pp. 1248–1250, 2003.
- [116] R. T. White, Y. He, B. J. Orr, M. Kono, and K. G. H. Baldwin, “Control of frequency chirp in nanosecond-pulsed laser spectroscopy. 2. a long-pulse optical parametric oscillator for narrow optical bandwidth,” *J. Opt. Soc. Am. B*, vol. 21, pp. 1586–1594, Sep 2004.
- [117] M. S. Fee, K. Danzmann, and S. Chu, “Optical heterodyne measurement of pulsed lasers: Toward high-precision pulsed spectroscopy,” *Physical Review A*, vol. 45, no. 7, p. 4911, 1992.

- [118] W. J. Smith, *Modern optical engineering: the design of optical systems*. McGraw-Hill Education, 2008.
- [119] G. Arisholm, Ø. Nordseth, and G. Rustad, “Optical parametric master oscillator and power amplifier for efficient conversion of high-energy pulses with high beam quality,” *Optics express*, vol. 12, no. 18, pp. 4189–4197, 2004.
- [120] L. Behnke, E. J. Salumbides, G. Göritz, Y. Mostafa, D. Engels, W. Ubachs, and O. Versolato, “High-energy parametric oscillator and amplifier pulsed light source at 2- μm ,” *Optics Express*, vol. 31, no. 15, pp. 24142–24156, 2023.
- [121] G. Arisholm, R. Paschotta, and T. Südmeyer, “Limits to the power scalability of high-gain optical parametric amplifiers,” *JOSA B*, vol. 21, no. 3, pp. 578–590, 2004.
- [122] I. Standard *et al.*, “Test methods for laser beam widths, divergence angles and beam propagation ratios,” 2021.
- [123] I. E. Gordon, L. S. Rothman, e. R. Hargreaves, R. Hashemi, E. V. Karlovets, F. Skinner, E. K. Conway, C. Hill, R. V. Kochanov, Y. Tan, *et al.*, “The HITRAN2020 molecular spectroscopic database,” *Journal of quantitative spectroscopy and radiative transfer*, vol. 277, p. 107949, 2022.
- [124] M. Zeyen, L. Affolter, M. Abdou Ahmed, T. Graf, O. Kara, K. Kirch, M. Marszalek, F. Nez, A. Ouf, R. Pohl, *et al.*, “Compact 20-pass thin-disk multipass amplifier stable against thermal lensing effects and delivering 330 mJ pulses with $M^2 < 1.17$,” *Optics Express*, vol. 32, no. 2, pp. 1218–1230, 2024.
- [125] L. Antwis, S. Bara, C. Bruhn, T. E. Cocolios, M. Deseyn, A. Doinaki, C. E. Düllmann, J. Fletcher, M. Heines, R. Heller, *et al.*, “A comparative study of target fabrication strategies for microgram muonic atom spectroscopy,” 2024.
- [126] A. Adamczak, A. Antognini, N. Berger, T. E. Cocolios, N. Deokar, C. E. Düllmann, A. Eggenberger, R. Eichler, M. Heines, H. Hess, *et al.*, “Muonic atom spectroscopy with microgram target material,” *The European Physical Journal A*, vol. 59, no. 2, p. 15, 2023.

List of Publications

- M. Zeyen, L. Affolter, M. Abdou Ahmed, T. Graf, O. Kara, K. Kirch, M. Marszalek, F. Nez, A. Ouf, R. Pohl, *et al.*, “Compact 20-pass thin-disk multipass amplifier stable against thermal lensing effects and delivering 330 mJ pulses with $M^2 < 1.17$,” *Optics Express*, vol. 32, no. 2, pp. 1218–1230, 2024
- L. Antwis, S. Bara, C. Bruhn, T. E. Cocolios, M. Deseyn, A. Doinaki, C. E. Düllmann, J. Fletcher, M. Heines, R. Heller, *et al.*, “A comparative study of target fabrication strategies for microgram muonic atom spectroscopy,” 2024
- M. Zeyen, L. Affolter, M. Abdou Ahmed, T. Graf, O. Kara, K. Kirch, A. Langenbach, M. Marszalek, F. Nez, A. Ouf, *et al.*, “Injection-seeded high-power Yb:YAG thin-disk laser stabilized by the Pound-Drever-Hall method,” *Optics Express*, vol. 31, no. 18, pp. 29558–29572, 2023
- M. Zeyen, L. Affolter, M. A. Ahmed, T. Graf, O. Kara, K. Kirch, M. Marszalek, F. Nez, A. Ouf, R. Pohl, *et al.*, “Pound–Drever–Hall locking scheme free from Trojan operating points,” *Review of Scientific Instruments*, vol. 94, no. 1, 2023
- A. Adamczak, A. Antognini, N. Berger, T. E. Cocolios, N. Deokar, C. E. Düllmann, A. Eggenberger, R. Eichler, M. Heines, H. Hess, *et al.*, “Muonic atom spectroscopy with microgram target material,” *The European Physical Journal A*, vol. 59, no. 2, p. 15, 2023
- J. Nuber, A. Adamczak, M. A. Ahmed, L. Affolter, F. D. Amaro, P. Amaro, A. Antognini, P. Carvalho, Y. H. Chang, T. L. Chen, W. L. Chen, L. M. P. Fernandes, M. Ferro, D. Goeldi, T. Graf, M. Guerra, T. W. Hänsch, C. A. O. Henriques, M. Hildebrandt, P. Indelicato, O. Kara, K. Kirch, A. Knecht, F. Kottmann, Y. W. Liu, J. Machado, M. Marszalek, R. D. P. Mano, C. M. B. Monteiro, F. Nez, A. Ouf, N. Paul,

- R. Pohl, E. Rapisarda, J. M. F. dos Santos, J. P. Santos, P. A. O. C. Silva, L. Sinkunaite, J. T. Shy, K. Schuhmann, S. Rajamohanan, A. Soter, L. Sustelo, D. Taqqu, L. B. Wang, F. Wauters, P. Yzombard, M. Zeyen, and J. Zhang, “Diffusion of muonic hydrogen in hydrogen gas and the measurement of the $1s$ hyperfine splitting of muonic hydrogen,” *SciPost Phys. Core*, vol. 6, p. 057, 2023
- P. Amaro, A. Adamczak, M. A. Ahmed, L. Affolter, F. D. Amaro, P. Carvalho, T. L. Chen, L. M. P. Fernandes, M. Ferro, D. Goeldi, T. Graf, M. Guerra, T. W. Hänsch, C. A. O. Henriques, Y. C. Huang, P. Indelicato, O. Kara, K. Kirch, A. Knecht, F. Kottmann, Y. W. Liu, J. Machado, M. Marszalek, R. D. P. Mano, C. M. B. Monteiro, F. Nez, J. Nuber, A. Ouf, N. Paul, R. Pohl, E. Rapisarda, J. M. F. dos Santos, J. P. Santos, P. A. O. C. Silva, L. Sinkunaite, J. T. Shy, K. Schuhmann, S. Rajamohanan, A. Soter, L. Sustelo, D. Taqqu, L. B. Wang, F. Wauters, P. Yzombard, M. Zeyen, and A. Antognini, “Laser excitation of the $1s$ -hyperfine transition in muonic hydrogen,” *SciPost Phys.*, vol. 13, p. 020, 2022

Acknowledgement

I am deeply grateful to my Master studies supervisor, Dr. Sebastian Wuester, for his unwavering support and encouragement, without which I would not have had the adventure of spending an Erasmus semester in 2017 at LMU. A series of fortunate events following that experience led me to join my PhD project, for which I am forever thankful.

Randolf, I sincerely appreciate the opportunity you gave me since the day we first met at the “Christmas party.” You often encouraged me to take on challenges I was not sure I could overcome. I value the trust and care you show to all your students.

Aldo, you have been more than a supervisor to me—you have shown me how genuine a person can be while working tirelessly toward their goals. You taught me how to turn stressful and difficult moments into motivation, and to focus on “scoring the goal” rather than showing off mid-field. Thank you for the endless support and the joyful discussions about every aspect of life.

My mother, my first teacher, has always encouraged me to pursue knowledge and supported me through every stage of my life. Her unlimited care has been invaluable. No words can express the immense support and patience I have received from my wife throughout this difficult journey. She has softened my hard days, putting up with my randomness and obsession with work at times. Büşra, “seni seviyorum.”

Siddharth, my wise lab and group friend, it has been an absolute joy working with you. I hope it was the same for you! Thank you for your support and for putting up with my endless complaints.

Karsten, there are special moments in life, and watching something work in the lab for the first time is one of them. Thank you for sharing your knowledge and being my first laser teacher. Thank you for the very random and joyful discussions about a lot of topics.

Thanks to Oguzhan Kara (Ozzy), the magic hand in the lab. Many things would not have happened without your continuous support to everyone. Your help with nonlinear process simulations was very appreciated.

Manu, thank you for sharing your knowledge about the disk laser. It was a pleasure working

with you, even if only for a short time.

Wei-Ling, I deeply appreciate your assistance with the simulations and data analysis for the spectroscopy.

Lukas, thank you for your help with beam quality data analysis and for being a precise and reliable partner in the lab.

To the entire muon group at PSI—Giuseppe, Stella, Lukas, Mirek, Jonas, Giovanni, and Azziza—you all have shown remarkable kindness and care, and I am grateful for being part of such a supportive group.

Special thanks to Dr. Marcos Gaspar for his help with electronics and for always lending devices and components spontaneously. Our lively and joyful discussions about various aspects of life made those moments even more special.

Dr. Anna Soter, thank you for your advice from time to time and for lending us the oscilloscope for the chirp measurement.

Thanks to Annita Van Loon for her administrative support and to Gisela Rasmussen for the hospitality she showed during my stay at PSI.

I am very grateful to the PRISMA internship program for the opportunity through which I have come to Mainz and then joined my PhD project. Special thanks to Kevin Anding and Snjezana Teljega.

Steffi Wortman, thank you for all the assistance and help you have given me during this project.

Many thanks to the group in Mainz—Marcel for helping bring the setup to PSI in 2021, Henderik and Gregor for transporting the Toptica laser to PSI, and Merten and Hannah for their care.

I am especially grateful to Dr. Franziska Hagelstein for the continuous and timeless discussions we had about the theory and her feedback on my writing, which greatly helped refine my understanding.

I would like to thank Prof. Krzysztof Pachucki for his patience in explaining the intricacies of QED corrections and our detailed discussions, and Prof. Michael Eides for his elaborations on QED corrections.

Special thanks to Prof. Carl Carlson for his insights on proton structure contributions, and to Dr. Savely G. Karshenboim for his patience in replying to my many emails filled with questions about his work.

To Aya, Alaa, and Abdulrahman, your unwavering support and care mean the world to me. Just picking up the phone and talking to one of you always brings back the joy of life. Muhittin, my little cat, I have missed your warm “meowing” behind the door when I worked from home.

To my aunt Mona and my uncles Tamer, Yasser, and Ashraf, thank you for showing care and support throughout the writing of this thesis, even when I disappeared for months on end.

Salman and Elif, they say that close friends become family when you are far from home. Thank you for everything you have done for me—I am beyond grateful for your help, especially during the final months of my PhD. To Melis, the honey sweetening life around her, your favorite uncle will soon have more time to play with you.

Tarek, thank you for helping me at the beginning of my stay in Mainz, without your help it would have been very difficult to get to start my PhD. Fate finds its way to bring us together. I am deeply grateful to Nafisa Motti for her help and genuine support during a challenging time last year.

Heartfelt gratitude to the place and time that brought me together with Ahmed Al Hasanat. Our long night discussions and meals made the tough days more bearable. May the seeds one day flourish again in their own home.

Mujahid and Murod, even though we are separated by continents and fields of physics, our conversations always revive the spirit of “Dorm 15” over tea. Thank you for always caring and checking in.

To Hasan and Adam, Nour and Mohamed, Thank you for the warm hospitality at your home during the PSI beamtime. One day, we will gather together back home.

Curriculum Vitae

Ahmed Ouf

Institut für Physik
Staudingerweg 7, 05-525,
55128 Mainz, Deutschland.

Ahmedouf@uni-mainz.de



ACADEMIC POSITIONS

Post-Doc laser spectroscopy of exotic atoms group, Institute of physics, Mainz university.	February 2025 -
Research assistant laser spectroscopy of exotic atoms group, Institute of physics, Mainz university.	January 2019 – January 2025
Research and Teaching Assistant Department of Physics Bilkent University, Ankara, Turkey	Sep 2015 – June 2018

EDUCATION

Johannes Gutenberg universität , Mainz, Germany PhD in Physics	January 2025
Bilkent University , Ankara, Turkey M.Sc. in Physics CGPA: 3.4	June 2018
Zagazig University , Sharkia, Egypt B.Sc. in Electrical Engineering (Electronics and Telecommunications) 7.6/10, Ranked the 6 th out of 86 students	July 2014
Elsadat Secondary School , Sharkia, Egypt High School Diploma, in the highest 0.6% of roughly half a million students nationwide 98.5%	July 2009

RESEARCH EXPERIENCE

- **Paul Scherrer institute**, Villigen, Switzerland. July 2021-

Visiting researcher, ground Hyperfine splitting in muonic hydrogen experiment.

- **University of Munich**, Munich, Germany. Nov 2017–Feb 2018
Intern, experimental quantum physics group, Prof. Harald Weinfurter.
- **Bilkent University**, Ankara, Turkey June 2016 – June 2018
Research Assistant, Quantum Dynamics of complex systems Group (PI: **Sebastian Wuster**)
- **Indian Institute of Science Education and Research Bhopal, India** June 2017 – Aug 2017
Visiting Researcher, part of master thesis research, Quantum Dynamics of Complex Systems Group
- **Middle East Technical University**, Ankara, Turkey January 2016 – June 2016
Research Assistant, Experimental Space Radiation and Particle Physics Group

TEACHING EXPERIENCE

- **Johannes Gutenberg universität**, Mainz, Germany Winter 2024
Teaching Assistant of “_Technische Mechanik und Konstruktionsmethodik_”
 - Tutoring students on exercises.
- **Johannes Gutenberg universität**, Mainz, Germany Winter 2019,2020,2021
Teaching Assistant of experimental physics-5a: Atomic physics
 - Tutoring students on exercises on the subject of atomic physics.
- **Bilkent University**, Ankara, Turkey Fall 2017
Teaching Assistant of Phys 252-1: Introduction to Astronomy
 - Conducted Telescopic observation sessions of planets, and nebulas using equatorial mount telescope
- **Bilkent University**, Ankara, Turkey Spring 2016 – Summer 2016
Teaching Assistant of Prof. Coşkun Kocabaş at Phys 102: electricity and magnetism
 - Gave tutorials on problem solving
 - Conducted lab experiments for the students, graded quizzes, project proposals, and posters presentations

RESEARCH PROJECTS

PhD Project : Jan 2019 –
Development of the laser system for the hyperfine splitting experiment at PSI, Switzerland

Developing the down-conversion scheme consisting of two branches of optical parametric oscillators (OPO) and amplifiers (OPA) at $3.1 \mu\text{m}$. And $2.1 \mu\text{m}$.

- Built a novel OPO at $3.1 \mu\text{m}$ with variable out-coupling enabling optimization of the nonlinear conversion.
- Built a single frequency, 50 ns long pulsed OPO/OPA at $3.1 \mu\text{m}$ with total pulse energy of 3.4 mJ, tunable over few nanometers, and with a narrow bandwidth.
- Designed the down-conversion scheme optical layout.

M.Sc. Project : June 2016 – June 2018
Investigation of Hawking Radiation from a Sonic Black hole in Atomic Bose Einstein Condensate (BEC)

Investigating the proposed spontaneous emission of phonon pairs from the horizon of a sonic black-hole (BH) created by accelerating BEC to higher than speed of sound.

- Using the truncated Wigner method we numerically looked at the density-density correlation function of the phonon flux emitted from the horizon of sonic BH.
- Analyzed the experimental results reported from Jeff Steinhaur's Group in Haifa about the observation of Analog Hawking Radiation in Bose-Einstein Condensate.
- Implementation of numerical simulation is done via XMDS software.

Internship Project: Nov 2017 – Feb 2018
Characterization of the factors affecting laser (at 850nm) polarization inside a fiber optic for QKD purposes

B.Sc. Project: Sep 2013 – July 2014
Design for fabrication of 8bit Digital-to-Analog Converter (DAC) in 130-nm CMOS technology

AWARDS, SCHOLARSHIPS AND FELLOWSHIPS

- Bilkent University Full Scholarship September 2015
- EgScience Week Best Projects of the year August 2014

LANGUAGES

1. Arabic (Native)
2. English (Fluent)
3. German (Intermediate)

COMPUTER SKILLS

1. Python
2. XMDS
3. Matlab
4. LATEX

